Computational Modelling and EXAFS Studies of Electrolytic Manganese Dioxide

A thesis presented by

Rapela Regina Maphanga

In fulfillment of the requirements for the degree of Doctoral of Philosophy to the Faculty of Sciences, Health and Agriculture in the School of Physical and Mineral Sciences, Discipline of Physics

at the

University of Limpopo
Turfloop Campus, South Africa

2005

Supervisor: Professor P.E. Ngoepe
Co-Supervisors: Professor A.V. Chadwick
Professor S.C. Parker

Declaration

I declare that the thesis hereby submitted to the University of Limpopo, Turfloop campus for the degree of Doctor of Philosophy has not previously been submitted by me for a degree at this or any other university that is my own work in design and execution that all material contained therein has been duly acknowledged.

……

Rapela Regina Maphanga

Abstract

Electrolytic Manganese Dioxide (EMD) is an important material for manufacturing alkaline electrolyte in commercial batteries. The structure of this material, which tends to be an intergrowth of pyrolusite and ramsdellite polymorphs, is very complex. The current study combines the computational modelling and EXAFS (used to investigate the local structure) studies to gain a better understanding of the structure.

We have studied structural and electronic properties of pyrolusite and ramsdellite using the density functional technique (DFT) where pseudopotential plane wave methods have been invoked. In particular, the equations of states (EOS) are determined and bulk moduli predicted. The partial density of states (PDOS) and charge deformations of pyrolusite and ramsdellite, provide information on the bonding at different pressures. Atomistic simulation techniques, based on interatomic potentials, are used to investigate the surface structures, stability and reactivity of pyrolusite and ramsdellite polymorphs. The flat surfaces {001}, {010}, {011}, {100}, {101}, {110} and {111} were modelled for both pyrolusite and ramsdellite using the shell and the rigid ion models. For pyrolusite, $\{110\}_a$ surface is found to be the most stable surface with the relaxed surface energies 2.54 and 2.07 $J.m^{-2}$ for the shell model and the rigid ion model respectively. For ramsdellite, the rigid ion model predicted $\{111\}_a$ surface to be the most stable with surface energy of 1.51 Jm^{-2}.

Molecular dynamics (MD) study on the effect of temperature on pyrolusite and ramsdellite structures was carried out. The bulk structures of pyrolusite and ramsdellite and the low index surfaces of pyrolusite were described using the Radial Distribution Functions (RDFs). The structures show that as the temperature is increased the height of peaks (pair distribution function) is decreased and the peaks become broader. An Extended X-ray Absorption Fine Structure (EXAFS) spectroscopy is used to investigate the local structure of EMD, pyrolusite and ramsdellite. The local structure is described using the RDFs and compared with the results obtained using the MD technique. Equivalent surface energies of pyrolusite and ramsdellite structures provided guidance in building various intergrowths, which

tend to occur in natural EMD. Changes of RDF peak widths and positions with temperature were studied by the MD method.

Amorphization and recrystallization simulation technique has been used to generate pyrolusite-ramsdellite interface models. The evolutionary method was applied to study large simulation cells of pyrolusite and ramsdellite interfaces. For pyrolusite MnO_2/MnO_2(001) interface +10% and +13% lattice misfit were applied to the thin film whereas for ramsdellite MnO_2/MnO_2(100) interface –6% lattice misfit was applied. Generated ramsdellite interface yielded a model composed of pyrolusite (1 x 1) single chains and ramsdellite (2 x 1) double chains after partial amorphization and recrystallization. Structural descriptions of the models, in particular RDFs, show an excellent correlation with our experimental and literature results. Furthermore, the methodology generated models, which reveal the atomic structure and give information on the defects (vacancies and clustering), grain boundary structures and epitaxial relationships. A simulated amorphization and recrystallization methodology has also been used to generate atomistic models of MnO_2 nanoparticles. The morphologies of the resulting nanoparticles are spherical for both pyrolusite and ramsdellite. The morphologies exhibit {110}, {100} and {010} faces for pyrolusite and {110}, {100} and {001} for ramsdellite. This shows that the surface properties have an influence on the structural morphology of the system.

Acknowledgements

I would like to thank my supervisor Prof. P.E. Ngoepe for all the unconditional support, guidance, encouragement, mentoring and initiation of the project. Thanks for introducing me into research field. My gratitude also goes to my co-supervisors, Prof. A.V. Chadwick and Prof. S.C. Parker for their contribution throughout this study. I am forever grateful for their mentoring and steady encouragement at all the times.

I fully acknowledge the financial support that I got from the following institutions: Delta EMD in SA, National Research Foundation (South Africa)/Royal Society (United Kingdom) Collaboration and National Research Foundation/Department of Labour Scarce Skills Scholarship. This research was possible due to the financial support they offered me, without the support I would not have been able to do all this work. I am grateful for having had the opportunity to carry out this research from the following institutions: Daresbury SRS Laboratory (UK) for the EXAFS experiments facilities, University of the North (SA), University of Bath (UK), University of Kent (UK) and Cranfield University (UK) for computational modelling facilities.

My sincere gratitude goes to the following individuals Dr. H.M. Sithole, Dr. D.C. Sayle and Prof. C.R.A. Catlow for their valuable inputs and discussions. You made a huge contribution towards my understanding on most of the things. Many thanks to all members of Materials Modelling Center whose friendship and support had made the center more than an area to study at; “I enjoyed working with you guys”. Thanks are due also to several researchers, students and staff at all other institutions (in UK) that I visited during the study.

Finally, many thanks to my parents Maria Mantši and Mokatšhane George Maphanga for a warm support, constant encouragement and love they showed during my entire study and life. It is because of them that I am now who I am. My brothers (John, Magick and Sello) and sisters (Annastacia and Dameline), thanks a lot for being there for me at all the times and for your understanding. Most importantly, lots of thanks to my daughter (Tsakane Vanessa Mathilda) for being able to stand all my absences in her life during the study. This is for you my girl. Ke a leboga Bakone. Thanks to God.

Dedication

This is fully dedicated to my parents and my daughter.

Contents

List of Figures

List of Tables

Chapter 1

Introduction

1.1 General Introduction

The need for a portable power supply has increased significantly and this gave a large incentive for research in understanding and improving the properties of manganese dioxide in battery applications. A substantial amount of work has been done on manganese dioxide since its introduction as a depolarizing agent in zinc/ammonium chloride/carbon battery by Leclanchè in 1866. A significant development occurred with the usage of electrochemically active forms of manganese dioxide with the alkaline electrolyte in commercial batteries. An expanding semiconductor industry with the need of portable power sources has driven the importance of these materials. In spite of the importance of manganese dioxides, their atomic scale structure and their structural evolution upon proton intercalation and heat treatment is still not understood. With the advent of affordable increasing computational power, materials modelling techniques are being used successfully in studying structural, electronic, optical, magnetic, transport of bulk and surface properties on different types of materials. In

particular, studies of metal oxides on a wide variety of simple and complex structures including MnO_2 using both classical and quantum mechanical approaches have been reported [Catlow 1996].

Recently, detailed structural studies of EMD (Electrolytic Manganese Dioxide) were carried out in three phases by Accelrys, where experimental XRD (X-ray Diffraction) patterns were compared with those calculated using the structures containing different types of defects [Delta Report 1999]. The first two phases concentrated on extended defects in γ-MnO_2. In phase I the intergrowth of pyrolusite and ramsdellite, in the form of de Wolff disorder, was studied. In phase II microtwinning of ramsdellite was the main area of simulation. In both cases the structures that produced calculated XRD patterns that gave a good agreement with the experimental results were identified. The last phase III, focussed on the effects of introducing the defects, such as Mn^{4+} vacancies, in ramsdellite and pyrolusite. Charge compensation was achieved by replacing some of the oxygens surrounding Mn^{4+} vacancies by OH^- ions. The model explains several properties of γ-MnO_2 but there has been no comprehensive description of the structural arrangement of γ-MnO_2 that explains both their scattering function and their physico-chemical behaviour. The vacancies increased the stability of both structures, while the substitution of Mn^{4+} by Mn^{3+} cations reduces. It could be surmised that manufactured EMD with more Mn^{4+} vacancies should be more stable. On the contrary this is not so owing to de Wolff disorder and/or microtwinning.

Furthermore, the presence of Na^{+}, K^{+}, Mg^{2+} and Ca^{2+} on the stability of pyrolusite and ramsdellite structures was studied. The calculations show that the favoured locations of these cations are in Mn^{4+} vacancy sites replacing charge compensation protons. Defect energies of these defects are relatively high hence proposing small concentrations of such defects. Microtwinned structures from a de Wolff disordered structure was created although this presented a significant challenge. The structures that produced XRD patterns that compared best with the experimental values were identified. Lastly, XRD patterns from a combination of point defects and de Wolff microtwinned structures were studied and compared with the experimental.

Although XRD data offers by far the quickest and most convenient route to determine P and T parameters, the limited accuracy of current analysis methods are known. An extensive review by Chabre and Pannetier [1995] on structural and electrochemical properties of the proton/γ-MnO_2 systems has pointed out a need for alternate methods to check and complement diffraction techniques. Among the possible techniques, EXAFS (Extended X-ray Absorption Fine Structure) spectroscopy, which probes Mn-Mn distances [Manceau and Combes 1988] and vibrational spectroscopies (IR and Raman) were mentioned. As an example a combination of molecular dynamics (MD) and EXAFS methods have provided useful information of cation-cation and cation-anion radial distances in metal fluorides [Cox et al. 1994 and Netshisaulu et al. 1999]. The results identified cations with a more disordered neighbourhood. Furthermore, fluorine ion migration mechanisms were clearly identified.

1.2 Historical Overview of MnO_2

Many research projects over the past fifty years have focussed on manganese dioxide. Research on these materials has been done in both industrial and academic laboratories, and has mainly focussed on chemical, physical and electrochemical properties. The main interest of battery industry in relation to manganese dioxide has been its electrochemical behaviour under a wide range of conditions. The ways of improving its electrochemical performance through development and implementation of new materials and electrode designs were also included in the area of research. Initial work on studying manganese dioxide in alkaline electrolytes was carried out by Herbert [1952, 1953 and 1956], Cahoon and Korver [1959] Bell and Huber [1964] and Boden et al [1967]. Several investigations have been performed on manganese dioxides in terms of their crystallographic structure [Fernandes et al 1985a], chemical composition, thermal behaviour [Giovanoli 1994], magnetic properties [Fernandes et al 1985bc] and electrical resistivity [Stephan et al. 1997]. Manganese dioxides are promising cathode materials because of their high specific energy, low toxicity and low cost, and have stable structures and good electrochemical lithiation properties [Pistoia and Antonini 1997]. Tools for analysis of XRD patterns of disordered manganese dioxides were developed by Pannetier in the early nineties. They gave access to a comprehensive description of the structure of γ-MnO_2 in terms of intergrowth of pyrolusite and ramsdellite domains and microtwinning [Ripert et al. 1991a, Pannetier 1992, 1993]. In the very same years, the structural changes upon proton intercalation and upon heat treatment were studied using in situ neutron powder

diffraction [Ripert et al. 1991b]. Hence the electrochemical and structural studies have been extended since then.

de Wolff [1959] proposed that γ-MnO_2 is a random intergrowth of pyrolusite and ramsdellite structures. Chabre and Pannetier [1995] used an XRD simulation package called DIFFAX to show that de Wolff disorder cannot account for many features of the X-ray diffraction data of EMD. However, de Wolff disorder is being supported by several experimental observations, including HRTEM images and X-ray diffraction lines. In particular, it cannot explain the broad and diffuse diffraction peaks in the system. To explain the broadness of the diffusion peaks, they introduced the additional concept of microtwinning. The XRD patterns obtained by incorporating both de Wolff disorder and microtwinning closely match those obtained experimentally and hence Chabre and Pannetier classified all possible EMD structures with two variables, thus, percent of de Wolff disorder and percent of microtwinning. Refined Rietveld model was developed to explain the characteristics of the XRD patterns for a wide variety of EMD samples [Simon 2000]. In contrast to the Chabre and Pannetier model, which disregarded ε-MnO_2 as a component of EMD, Simon's incorporated it as one of the possible phases in the Rietveld model, their model describes EMD as a binary mixture of ε-MnO_2 and pyrolusite and ramsdellite intergrowth (which they call γ-MnO_2) crystals with different crystal domain sizes. The model agrees with that of Chabre and Pannetier in the sense that it incorporates both the de Wolff disorder and microtwinning in the intergrowth phase. Heuer [2000] studied the microstructure and crystallography of EMD using Transmission Electron Microscopy (TEM). In

contrast to previous TEM studies of EMD that used powder prepared from bulk material by grinding [Charenton 1988], Heuer et al used TEM thin foils that were prepared by ion beam milling from the bulk. Their TEM data described EMD as a heterogeneous phase system, partially consistent with Simon's results. They found that EMD material contains approximately 50% ramsdellite, 30% ε-MnO_2 and 15% pyrolusite. However, no evidence for microtwinning was found in their EMD samples. An alternative interpretation of EMD structure was provided by Bowden et al. [2000]. They performed Convergent Beam Electron Diffraction (CBED) experiments on EMD samples. The CBED patterns revealed streaks of intensity in the reciprocal space, which is interpreted to be resulting from the two-dimensional sheets of scattered intensity perpendicular to the c-axis. The results of Bowden et al are consistent with those of Chabre and Pannetier since the combination of de Wolff defects and extensive twin defects produces the linear disorder that results in the observed sheets of intensity in the reciprocal space. Thus, their results show that EMD consists of randomly oriented homogeneous ramsdellite crystals distorted by the presence of one-dimensional pyrolusite defects and extensive twin defects.

1.3 MnO_2 Applications

Manganese dioxide is the positive active material used in Leclanche and alkaline manganese batteries, which together dominate the primary battery market. MnO_2 is an important substance used widely as cathodic material, catalyst and magnetic material [Tarascon 1993]. Synthetic manganese dioxides and particularly those made by electro deposition are used in high performance batteries. Manganese

dioxide is a very important active material widely used in the battery industry because of its many applications in different types of power sources such as the dry cells (alkaline primary and rechargeable versions), magnesium- and lithium based cells and in electronic materials such as ferrites. MnO_2 is a complex material and exists in different crystallographic structures that enable it to exhibit a varied battery performance in different systems [Ananth 1998]. Among the different battery applications of MnO_2, the latest popular application is in alkaline batteries due to a strong market presence in pagers and photoflash sectors [Tye et al 1980]. Therefore, manganese dioxide samples intended for use in alkaline electrolytes requires intensive characterization to optimize their performance.

Electrolytic Manganese Dioxide is the most common variety of manganese dioxide used in primary Zn-MnO_2 batteries as the major component of composite cathodes. The rechargeability of the material batteries depends on the partial discharge of the manganese dioxide cathode to avoid problems associated with the manganese dioxide deep discharge [Jantscher et al 1999]. Despite the success of EMD as a primary battery material, the use of manganese dioxide as a secondary battery constituent has, for a few decades, met little success [Binder et al 1998].

In a battery, the anode and cathode are in contact with an electrolyte solution. During discharge process hydrogen is generated and tends to coat the cathode with a gas film, which cuts the electrical generation. The main role of manganese in the battery is to depolarize the system by oxidizing the hydrogen to form water that is bringing the cathode into contact with the electrolyte. Therefore, EMD is used as a

depolarizing agent in four types of batteries: zinc-carbon cells, magnesium-manganese dioxide cells, alkaline manganese dioxide cells and lithium-manganese dioxide cells. The characteristics that make MnO_2 desirable for battery use are its: crystal structure, surface area, pore size distribution and particle shape. The success of manganese dioxide as a cathode material in primary alkaline dry cell batteries can be attributed to a combination of its electrochemical, chemical and economic properties. Such features include (i) its ability to sustain high currents for prolonged periods of time, (ii) an ambudance of the reagents necessary to synthesized manganese dioxide, and (iii) the low cost production of primary alkaline Zn-MnO_2 batteries requires up to 10 times the energy of its expected energy output. The main limitation of manganese dioxide electrode system is its poor performance in secondary battery systems.

1.4 Properties of MnO_2

Manganese dioxide exists only below 1080°C; above this temperature the dioxide form dissociates to release its oxygen. The cathode MnO_2 can be found in its mineral form of ramsdellite, but it is very rare to find. Manganese (IV) oxide, MnO_2 is deep black to dark brown in colour and practically it is insoluble in water. It is more commonly referred to as manganese dioxide. Pure manganese dioxide corresponds closely to the formula MnO_2 that occurs as the β- modification. The compositions of other natural or synthetic manganese dioxide range from $MnO_{1.7}$ to $MnO_{<2.0}$, with varying contents of lower valence manganese foreign, cations like K^+, Na^+, Ba^{2+}, hydroxyl ions and water molecules. MnO_2 modifications like α,

β, γ, and δ have been characterized, they differ according to their degree of crystallization and their content of foreign ions. The β-MnO_2 modification is known to be the least reactive and most highly crystalline form of manganese dioxide. By contrast, γ-MnO_2 is nearly amorphous and much reactive both chemically and electrochemically. When γ-MnO_2 is heated up to 500°C it frequently releases water and/or undergo phase transition. Above 500°C it liberates oxygen. Between 500°C and 600°C MnO_2 is converted into Mn_2O_3 and above 890°C is converted into Mn_3O_4. Manganese dioxide acts as oxidant toward readily oxidizable materials, its valency changing from +4 to +3 to +2. MnO modifications have sorptive and ion-exchange capabilities and catalytic and electrochemical activities. The density of EMD ranges from 4.0 to 4.3 g/cm³.

1.5 Computational Modelling

As computer power has increased the range of systems available for study and the techniques available has also grown tremendously. The growth has led to an increase in the importance of computer simulations. This means that the calculations, which were not possible few years ago, are now trivial to perform. Despite this, computational techniques such as Energy Minimization (EM), Molecular Dynamics (MD), Molecular Mechanics (MM), Monte Carlo (MC) and electronic structure techniques are used to fill the information gap between fundamental materials-science and industrial applications. The techniques can be applied to a wide variety of systems. Computational techniques can help to understand and design complex materials and offer an attractive approach in many

fields where experimental data are rare and difficult to obtain. Consequently, using the computational methods, alone or in combination with experiments, it is possible to model and predict structures, characterize bonding in solids, model surfaces and interfaces, atomic transport and defect structures, chemical reactions, phase transformations, docking or predict reaction mechanisms [Catlow 1987, 1990, 1994ab, 1997ab, Hafner 2000 and Allan et al 2000].

Surfaces and interfaces occur in many aspects of science from catalysis to device fabrication. Moreover, with the advent of new preparative methods in conjunction with high-resolution techniques for structural characterization, the field of surfaces and interfaces has enjoyed explosive growth during the past few years [Chambers 2000]. Atomistic simulation is widely used in the modelling of surfaces and interfaces. Sithole [2000] calculated the modelled planar surfaces and surface defects such as facets and steps of FeS_2 and found that {100} surface is the dominant surface and is virtually bulk-terminated, in agreement with experiment. Its dominance is further confirmed by the stabilization of {110} surface through faceting into {100} planes. The surfaces containing lower-coordinated surface sites are less stable compared to the planar {100} surface containing five-coordinated surface atoms. Oliver et al [1997] calculated the surface energies of TiO_2 and found that the relaxed crystal morphologies agreed closely with experimental observed crystals. The surface energies were found to be in good agreement with experimental and electronic structure calculations. Computer simulation was also used to study steps on the MgO(100) surface [Harding 1999], $SrTiO_3$ and $BaTiO_3$(110) surface relaxation [Heifets 2000] and mineral

(magnesium silicate and magnesium aluminite) surfaces including stability and growth [Parker 1997]. Other studies range from simple binary oxides such as NiO [Oliver et al 1993] to more complex structures as calcium carbonate polymorphs [de Leeuw and Parker 1998]. Crystal surfaces observed in nature are not only contaminated, but will also contain structural defects. The defects may include point defects, vacancies, dislocations or steps.

Techniques such as molecular beam epitaxy have enabled one to exercise control over the thin film structure at the atomic scale. Experimentally, it is very difficult to obtain a complete structural characterization of a supported thin film. Structural characterization of interface requires knowledge of the precise atomic positions of all the atoms within a particular system including their evolution with time. High-resolution electron microscopy can provide images at the atomic level of specific regions of the material, but a complete three-dimensional description of the atomic structure is difficult or even not possible at present. Accordingly, atomistic computer simulation offers a unique opportunity to complement experiment in the exploration of interfacial structures since the positions of all the atoms is explicitly defined [Sayle 2001]. All the atomistic simulations start by defining the basic configuration of the interface, which is then simulated using static or dynamical methods. Sayle [1997, 1998] developed an approach called amorphization and recrystallization technique, which includes energy minimization and dynamical simulation. For example, he explored SrO thin film supported on an MgO(001) substrate. The SrO thin film was placed directly on top of the MgO(001) support such that the ions of the thin film lied directly above their respective counterions

of the underlying MgO. Another example is the study of CeO_2 thin films supported on an YSZ (yttrium-stabilized zirconia) substrate [Maicaneanu et al 2001a]. They explored the influence YSZ support may have with respect to the overlying CeO_2 and characterized the structural defects, which evolve within CeO_2. Since it has been shown that by supporting CeO_2 on a substrate material, the catalytic properties may be enhanced, elucidating the structural features which evolve upon supporting the material will have important implications for catalytic systems. In summary, Sayle et al [2002a] have explored the growth, nucleation and thin film structures of oxides supported on an oxide substrate. They observed that the structure of the substrate surface exacts a critical influence on the thin film deposited thereon and they also observed that the defects, dislocations and grain boundaries evolve to help accommodate the associated lattice misfit.

To generate models of supported oxide thin films that are more realistic, various structural features, including the epitaxial relationships, various defects and reduced interfacial ion densities must also be introduced within the model. The defects, which evolve in response to misfit accommodation, may include dislocation arrays, vacancies, substitutions and interstitials. All these types of defects will evolve and act to reduce the lattice misfit thereby stabilizing the thin film [Sayle 2001]. When modelling supported thin film, there are two primary requirements, (i) the simulation cell must be sufficiently large to accommodate the incommensurate nature of the system and include misfit-induced structural modifications such as dislocations [Schnitker 1998] and (ii) the final structure must not be influenced by the starting structure. In particular, since the elucidation

of the precise atomistic structure of an interface is, at present, intractable experimentally, assumptions must be made with regard to the initial structure for the simulation model. For example, if the initial configuration was erroneous, any final structure, which reflects structurally the (erroneous) preparatory configuration, would also be suspect. Accordingly, simulated 'amorphization and recrystallization' methodology [Sayle 1999 and 2001] which resolves each of the problems discussed above is employed. A detailed description of the technique, which will also be used in the present work to generate the MnO_2/MnO_2 interfaces and nanoparticles, will be presented in Chapter 2. In reality, crystal surfaces found in nature are not clean, but covered with an adsorbed layer. The structure of the thin film and the substrate interface can be difficult to study using experimental methods. Still computer simulation has proved to be an invaluable tool in this area.

Atomistic simulation techniques have also been used in the design and refinement on industrial processes. This role illustrates their potential and practicality even further. Their major disadvantage is their inability to explicitly model electronic properties. This problem is overcome by the use of electronic structure calculation. Ab initio methods offer a complete theoretical framework of describing the motions of electrons and ensembles of atoms. In the past decade, it has become possible to compute with great accuracy a number of electronic and structural properties of solids from ab initio calculations [Benosman 2001]. Among the quantities obtainable form this kind of calculations are crystal structures, phonon spectra, lattice constants, bulk and shear moduli, density of states, charge density difference, band structures and other static and dynamical properties. This

development has opened up many exciting possibilities for the study of condensed matter, since at present it is possible to predict the properties of a solid, which were formerly inaccessible to the experiment. One of the triumphs of quantum mechanics in the area of solid-state materials was the ability to explain why some materials are metallic conductors while others are insulators or semiconductors. The density of state, band structure and charge density differences can be calculated using ab initio method and they provide access to the electronic properties of the materials. The ground state self-consistent all-electron total energy calculations on structural, electronic and cohesive properties of BeS were performed [Benosman 2001]. Also, the band structure calculation was performed using the self-consistent full-potential linear augmented plane wave band method. Obtaining highly converged total energies and stresses in BeS, they successfully calculated the elastic moduli, cohesive energy, band structure, density of states and the pressure dependences of the gap. Detailed analysis of the valence charge distribution and the calculated value of the fractional ionic character confirm that BeS is a covalent binary compound. Computer simulation was also used to study electronic properties of correlated perovskites, K_2NiF_4 and K_2CoF_4 using local spin density approximation [Punkkinen 2001]. The electronic structure calculations are discussed in Chapter 3. However, the calculations are not based on the surfaces but on bulk crystal structures of pyrolusite and ramsdellite.

1.6 Structural Aspects

Polymorphism is common among binary metal oxides, MO_2 (M = metal) but MnO_2 is the dioxide that exhibits the largest structural complexity. This could result from the small ionic radius of Mn^{4+} (r = 0.53 Angstroms), which brings MnO_2 to the lower limit of stability of the rutile structure. However, this small ionic radius could favour tetrahedral coordination. Manganese (IV) oxides have a versatile chemistry with many parent structures. It is a non-stoichiometric compound and has many crystalline forms such as α-, β-, γ- and δ- type [Kordesch 1974]. Beside layered δ-MnO_2 and λ-MnO_2 phases there are a large number of tunnel structures that involve packed oxide lattices. The most commercially important form, γ-MnO_2 is the cathode material of choice for aqueous zinc batteries. Based on the production method, γ-MnO_2 can be categorized into three forms, namely:

(i) Natural Manganese Dioxide (NMD)

(ii) Chemically prepared Manganese Dioxide (CMD) and

(iii) Electrolytic Manganese Dioxide.

The structural peculiarities, whose details are still largely not known, as well as the poor quality XRD patterns obtained from most samples, explain why manganese dioxide in general are poorly characterized materials. The basic framework for all manganese oxide structures is a hexagon closed-packed array of oxygen ions (OH^-, O^{2-}, H_2O) depending on the oxidation state of the manganese ion [Giovanoli 1980]. Manganese dioxide structure is generated if half of the octahedral sites within the framework were to be filled with Mn^{4+} ions. A number of different names have been given to specific arrangements of the manganese

atoms in such a close-packed oxygen framework, and they are outlined in the following sections.

1.6.1 Pyrolusite

Pyrolusite is one of the known crystalline polymorphs of manganese dioxide [Wells 1984]. Pyrolusite structure is intimately related to the ramsdellite structure due to the similarity of their oxygen framework. The pyrolusite structure is described as an infinite tetragonal single chains of MnO_6 of edge sharing octahedral, which are connected to other single chains by corners whilst ramsdellite structure has double chains connected to other double chains by corners [MacLean and Tye 1996]. This sort of arrangement leads to formation of a tunnel, and pyrolusite is said to contain (1 x 1) tunnels.

Pyrolusite is the most stable polymorph of manganese dioxide and it has the rutile structure [Baur 1976]. The oxygen atoms form a slightly distorted hexagonal close packed (hcp) array; half the close packed rows of octahedral interstices are occupied by Mn^{4+}. The average distance between Mn-O atoms is 1.88Å. Pyrolusite structure is analogous to that of rutile TiO_2. Figure 1.1 below shows a schematic representation of the pyrolusite structure.

1.6.2 Ramsdellite

Ramsdellite is very closely related to rutile structure as it has been discussed in section 1.2.1. The ramsdellite structure also consists of a hexagonal closed packed lattice but the ordering of Mn^{4+} cations is different from the arrangement of cations in pyrolusite, is said to contain (1 x 2) tunnels. It occurs as a mineral and is

often mixed with pyrolusite, it is very rare to find pure ramsdellite mineral. All attempts of synthesizing pure ramsdellite have been unsuccessful [Klingsberg and Roy 1959].

The ramsdellite structure possesses a disorder where some double chains of octahedra are being replaced by the single pyrolusite -like chains, this structural defect was suggested by Byström and Byström in 1950 and was explained quantitatively by de Wolff in 1959. de Wolff disorder is a partial or totally random distribution of two kinds of structural units; pyrolusite layers, **r**, of single chains of edge-sharing octahedra and ramsdellite layer, **R**, of double chains of edge-sharing octahedra. Another type of defect that occurs in synthetic ramsdellite is the lattice twinning referred to as microtwinning disorder. Microtwinning of pyrolusite or ramsdellite lattice on the planes 021 and/or 061 of the orthorhombic lattice are the growth faces of electrochemical manganese dioxide and twinning faults are incorporated during growth of MnO_2 crystallites [Pannetier 1992]. The schematic representation of the ramsdellite structure is shown in figure 1.2. Ramsdellite and pyrolusite structures are chemically pure and structurally well-characterized forms of manganese dioxide. Ramsdellite is a relatively rare mineral, usually occurring in low temperature hydrothermal deposits and commonly associated with, and probably altering to, pyrolusite. Ramsdellite is isostructural to goethite (FeOOH) and gibbsite (AlOOH).

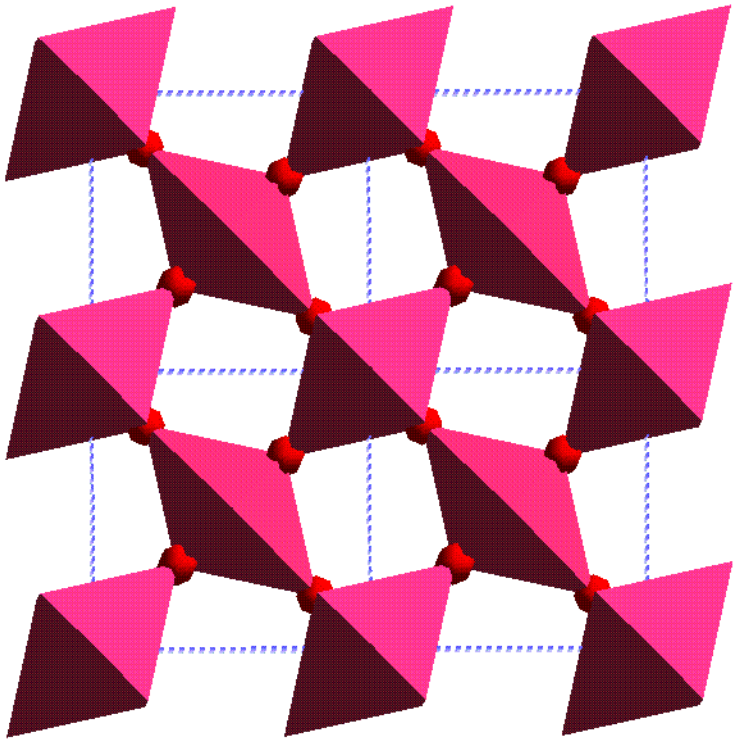

Figure 1.1: Pyrolusite crystal structure showing single chains connected to other chains by corners

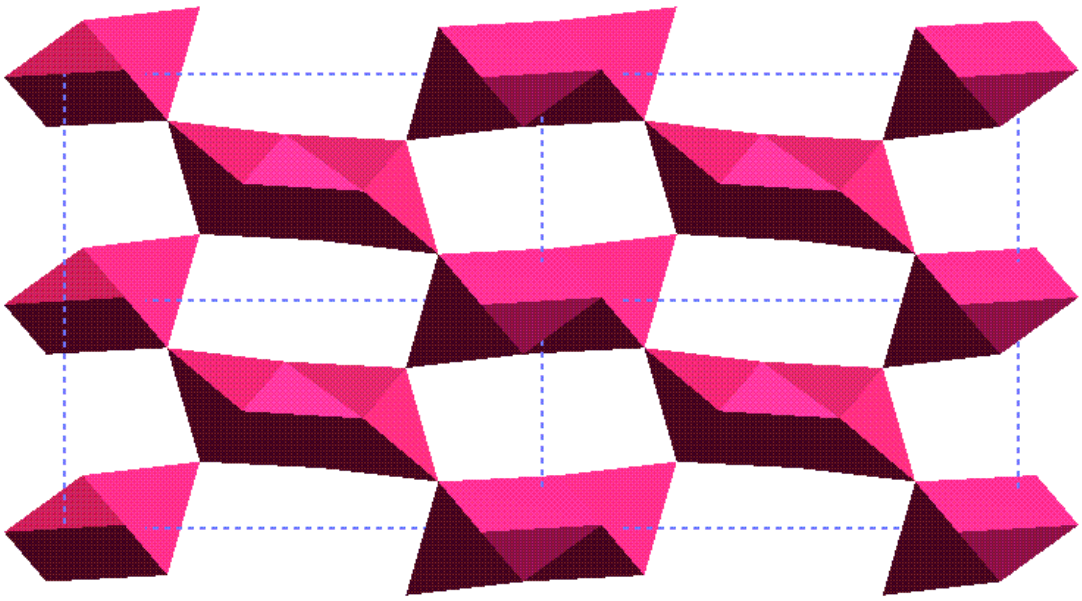

Figure 1.2: Ramsdellite crystal structure showing double chains connected to other double chains by corners

1.6.3 EMD

Manganese dioxide polymorphs bear, collectively a tunnel structure as a common structure unit, which is formed by edge-sharing or corner-sharing of (MnO_6) octahedra [Burns 1983]. The polymorphs are distinguished from each other by the tunnel sizes that are defined by the product of the numbers of (MnO_2) octahedra on the abscissa and on the ordinate (number of ordinate multiply by the number of abscissa) as (1 x 1), (1 x 2) in the cross-section. Pyrolusite has a relatively stoichiometric composition and isostructure with rutile TiO_2 consists almost of (1 x 1) tunnels and ramsdellite consists of (1 x 2) tunnels. The width of the species of tunnels are similarly in one dimension and the phases easily form domain intergrowth [Li 1988a].

Another common polymorph, γ-MnO_2 that is used as an oxidizing agent for dry cells, consists of irregular random intergrowth of the (1 x 1) tunnel units and (1 x 2) tunnel units. Such tunnel structures and their intergrowths have recently been noted, because the difference in the tunnel size may affect unique material characteristics such as electrical conductivity [Li 1988b], the discharge of dry cell [Brenet 1985], ion-exchange [Wadsley 1950], ion-absorption [BigLiocca 1967], gas reactivity [Li 1988c], etc. Besides structural complexity of manganese dioxide, these compounds are known to be non-stoichiometric and to contain substantial amounts of protonic species, in particular, electrolytic manganese dioxide. This was elucidated by Ruetschi in 1984 [Ruetschi 1984], that non-stoichiometry originates from the Mn^{4+} vacancies that are compensated by 4 OH^- in the lattice. This model explains several properties of electrolytic manganese dioxide, but, up

to now, there has been no comprehensive description of the structural arrangements of electrolytic manganese dioxide, which explains both their scattering function and their physico-chemical behaviour [Chabre 1995]. The electrochemically active forms of MnO_2 (usually known as γ- and/or ε-MnO_2) are structurally related to the mineral ramsdellite and they are difficult to characterize. Their structure incorporates defects. ε-MnO_2 is a highly textured fibrous samples of manganese dioxide that are prepared electrochemically and γ-MnO_2 is a disordered material due to a variety of structural features. de Wolff has characterized the difference between γ- and ε-MnO_2 as a difference in the manganese ion distribution in the same hexagonal close packed oxygen sublattice of manganese dioxide. The γ-MnO_2 exhibit an intergrowth structure of ramsdellite and pyrolusite domains whilst in ε-MnO_2 the manganese atoms are randomly distributed on all available octahedral sites in the a,b-plane of the oxygen sublattice atoms of the ramsdellite and hence achieve hexagonal symmetry. Besides intergrowth of pyrolusite and ramsdellite, γ-MnO_2 has Mn(III) sites and cation vacancies [Ruetschi 1984]. The boundary between the two component phases is referred to as de Wolff defect. Also there is a significant amount of twinning in the material. Cole et al. [1947] noted that γ-MnO_2 is closely related to ramsdellite from the comparison of their powder diffraction patterns. The crystal structure of ramsdellite was determined by Byström in 1949. It was soon realized that the structure of γ-MnO_2 always contains water or at least protonic species [Sasaki and Kozawa 1957]. Manganese dioxide structure always exhibits several defects that are related to the method of preparation of the manganese dioxide and that modify their X-ray diffraction patterns as well as their electrochemical

behaviour. The latter family of manganese dioxides is usually termed γ-MnO_2 when they are synthetic, and is of considerable technological importance. Consequently, it is rather unexpected that there is no accepted method to characterize the structural features of commercial γ-MnO_2.

1.6.4 MnO_2 Nanoparticles

EMD can be nanocrystalline and microporous and contains microcavities probably ranging in dimension from the structural nano-sized channels between the octahedral, via grain and crystallite structural misfits (grain boundaries) to regular cracks and pores [Donne 2002]. Different synthetic conditions yield MnO_2 with different physical and chemical properties such as crystallinity, amount of combined water, specific surface area, conductivity, magnetic and electrochemical performance. And physical and chemical properties of a material can be changed dramatically when the size of the particles is reduced to the nanometre scale. [Pardoe 2001, Petroski 2001, Kruis 1998 and Khan 2000].

In recent years intense interest has been paid to the preparation of various ultrafine particles, since nanoparticles can exhibit unique or improved mechanical, electronic, magnetic and optical properties owing to the effects of their small size and high surface area [Henlein 1984]. Particularly, the synthesis of nano-sized metal oxides is of great significance in application fields. Nanoparticles of metal oxides can usually be prepared with gas condensation, hydrothermal, sol-gel and micro-emulsion methods [Li 2003]. In particular, as the size of the material reduces to the nanometer scale, the properties change uniquely in comparison with the bulk characteristics of the parent material [Pardoe 2001 and Gleiter 2000]. The

origins of which maybe attributed to the dimensions of the particles being comparable to the length scales of the basic quanta in solids (phonon invalency, de Brogile wavelengths of electrons). Moreover, since most of the ions comprising the materials are located at the surface or near surface regions, surface effects dominate the thermodynamics and energetics of the particle (crystal structure, morphology, reactivity, etc).

1.7 Objectives of this Study

Various authors used different techniques and samples of diverse origins to study the properties of Electrolytic Manganese Dioxide. In this thesis, computational modelling studies and EXAFS experiment will be combined to study properties of EMD, ranging from structural, electronic and surface properties, interfaces/intergrowths and nanoparticle properties. While γ-MnO_2 has been a subject of experimental investigation for many years, little is known about its structure and other relevant properties. In our literature review EMD has been described as an intergrowth of pyrolusite and ramsdellite and other authors have proposed that it includes a partially ordered version of ε-MnO_2 in addition to pyrolusite and ramsdellite structures. The structural perculiarities, whose details are largely unknown, as well as the poor quality of X-ray diffraction patterns obtained explains why EMD in general is a poorly characterized material. In this work, *ab initio* and atomistic simulations and EXAFS experiments will be used to investigate polymorphs of γ-MnO_2 and to understand their structural complexity.

Brief summaries of the simulations and experimental outcomes are outlined below.

We will carry out *ab initio* electronic structure calculations to study the structural and electronic properties of pyrolusite and ramsdellite polymorphs of MnO_2. The lattice parameters and bondlengths and the effect of pressure on them will be predicted, since there are no experimental results to compare with. Also the pressure-volume dependences will be predicted. In order to understand the density of states and charge density differences of both systems, the predicted structural parameters will be used to calculate the aforementioned electronic properties. Charge distributions and differences explain the nature of bonding in these materials.

Classical energy minimization methods will be used to study structural properties of bulk pyrolusite and ramsdellite systems, so as to test the validity of the potential model to be used. The validated potentials will then be used to study surface properties of both systems, such as surface stability and reactivity. The calculated surface energies will play a very important role in constructing pyrolusite-ramsdellite interfaces.

Amorphization and recrystallization technique will be used to generate MnO_2 interfaces and nanoparticles, and the resulting structural properties where possible, will be compared with those of EXAFS experiments.

1.8 Outline of the Study

The thesis is organised into nine chapters as follows:

Chapter 1 contains a general introduction to the study, applications, properties, structural aspects and background on computational modelling of materials and intentions of the current study.

Chapter 2 reviews the theoretical methodologies and the EXAFS method. Theoretical methods include both the quantum and classical mechanical methods.

Chapter 3 presents the calculation details, results and discussion on structural and electronic properties of pyrolusite and ramsdellite structures, where ab initio methods have been invoked.

Chapter 4 presents surface properties of pure pyrolusite and ramsdellite structures determined by atomistic simulations (energy minimization technique) using interatomic potentials.

Chapter 5 discusses the molecular dynamic simulations performed on bulk pyrolusite and ramsdellite systems. Details on molecular dynamic simulations are given and followed by results and discussions based on the simulations.

Chapter 6 discusses the EXAFS experiments on pyrolusite, ramsdellite and EMDs. The results are compared with those obtained in Chapter 5, particularly in terms of radial distances.

Chapter 7 uses the surface energies obtained in Chapter 4 to construct interfaces between pyrolusite and ramsdellite models. Structural properties on interfaces are compared with EXAFS experimental results.

Chapter 8 uses the amorphization and recrystallization technique to generate MnO_2 interfaces and nanoparticles. Furthermore, structural properties of interfaces are compared with EXAFS results.

Chapter 9 summarises the results and offer suggestions for future work on Electrolytic Manganese Dioxide.

Chapter 2

Theoretical and Experimental Methodologies

The developments of new theoretical concepts and computational approaches for atomistic simulations have been a major part of solid-state physics, chemistry and materials science. There are two types of atomistic computation methodologies which are used for the prediction of material properties, thus;

(i) Empirical potential or force field approach, which describe the interactions between the atoms in a quasi-classical from avoiding any details of the electronic structure.

(ii) Non- empirical quantum mechanical methods that take into account the motion and interactions of the electrons in the system. Quantum mechanical method is one of the methods that are widely used in computations since it captures the essential aspects such as the electronic levels, charge transfer and spin polarization. It provides geometric structures, heats of formation, optical spectral, electronic charges and electrostatic potentials.

2.1 *Ab initio*

Methods that require only a specification of the ion present (by their atomic number) are referred to as the *ab initio* of first principle methods. Unlike either molecular mechanics or semi-empirical quantum mechanics methods, ab initio techniques use no experimental parameters in their computations. Instead, these computations are based on the laws of quantum mechanics and on the values of a small number of physical constants. *Ab initio* computations provide high quality quantitative predictions for a broad range of systems. They can handle any type of atom, including metals. The *ab initio* method can use a quantum mechanical approach to calculate interatomic potentials [Elliot 1998]. The advantage of these methods is that potential parameters can be calculated for systems where there is insufficient or unavailable experimental data.

2.1.1 Density Functional Theory

Density Functional Theory (DFT) is an extremely powerful approach but its success depends upon a good parametric description of the problem. DFT has emerged as a principal quantum mechanical many-electron approach in solid-state physics and is also being used increasingly to address chemical questions. The major disadvantage of present DFT is the lack of systematic improvements towards the exact solution. Density Functional Theory has been developed by Hohenberg and Kohn [1964] and Kohn and Sham [1965]. They proved that the total energy including the exchange and correlation, of an electron gas (even in the presence of a static external potential) is a unique functional of the electron

density. The minimum value of the total energy functional is the ground state energy of the system, and the density that yields this minimum value is the exact single particle ground state density. Kohn and Sham showed how it is possible to replace the many electron problems by an exactly equivalent set of self-consistent one electron equations.

An important advance in the calculation of the energy of electrons of the atoms and the forces on each atom was made by Kohn-Sham [1965], who showed how a mean field theory could be applied to problems. In their method, the electron density plays a crucial role so that although the term has more general applicability, the Kohn-Sham method is commonly referred to as the DFT. This has since advanced to become a very important method for determining the energy of many-electron, and therefore many atom systems. Density Functional Theory is based on concepts by Thomas [1926] and Fermi [1928], who introduced the idea of expressing the total energy of a system as a functional of the total electron density. In DFT, the energy is not written in terms of the many-electron wave function as is conventional in quantum chemistry, but is written as a functional of the electron density, which in turn depends on the positions of the atoms, that is;

$$E = E\left[\rho(r), R_x\right] \tag{2.1}$$

Then the total energy is decomposed into three contributions, the kinetic energy, Coulomb energy and the exchange-correlation energy due to classical electrostatic interactions among all charged particles in the system. The Kohn-Sham total energy functional for a set of doubly occupied electronic states can be written as

$$E = -\frac{1}{2}\sum_i \int \psi_i^*(r)\psi_i(r)dr + \int \rho(r)V_{ext}(r)dr + \frac{1}{2}\int\left\{\frac{\rho(r)\rho(r')}{|r-r'|}\right\}drdr' + \int \rho(r)\varepsilon_{XC}[\rho(r)]dr \quad (2.2)$$

where $\rho(r)$ is the electron charge density and ε_{XC} is the exchange correlation energy (is a function of the density). The kinetic energy of the system is written as a kinetic energy of a gas of independent electrons, with the same density as the interacting system. This is achieved by the introduction of Kohn-Sham orbitals, $\psi_i(r)$, which fulfil the orthonormality constraints

$$\int \psi^*{}_i(r)\psi_i(r)dr = \delta_{ij} \quad (2.3)$$

these orbitals are obtained by minimizing the total energy of the system. The minimization problem is equivalent to the solution of the Kohn-Sham equations which are derived from the total energy given in equation 2.2 and is given by the expression

$$\left[\frac{1}{2}\nabla^2 + V(r) + \int\left\{\frac{\rho(r')}{|r-r'|}\right\}dr' + \mu_{xc}\rho(r)\right]\psi_i = \varepsilon_i\psi_i(r) \quad (2.4)$$

Corresponding to three terms in the total energy expression, equation 2.2, that is the kinetic energy, Coulomb energy and the exchange-correlation energy; the effective one particle Hamiltonian of the Kohn-Sham equations contains a kinetic energy operator, Coulomb potential operator and the exchange-correlation operator. The exchange correlation potential μ_{xc} is given by

$$\mu_{xc}[\rho(r)] = \frac{d[\rho\varepsilon_{xc}(\rho)]}{d\rho} \quad (2.5)$$

The charge density is related to Kohn-Sham orbital by the relationship

$$\rho(r) = \sum_i |\psi_i(r)|^2 \qquad (2.6)$$

with the constraints

$$\int \rho(r) dr = N \qquad (2.7)$$

where N is the number of electrons of the system. The total charge density given in equation 2.6, together with the one-particle wave functions allows the calculations of the total energy of the system.

2.1.2 Local Density Approximation

Local Density Approximation (LDA) is the simplest method of describing the exchange correlation energy of an electronic system [Kohn and Sham 1965] and its approximation is always used in the total energy pseudopotential calculations. LDA assumes that the exchange-correlation energy functional is purely local. In principle, the local density approximation ignores corrections to the exchange-correlation energy at a point r due to nearby inhomogeneities in the electron density. Considering the inexact nature of the approximation, it is remarkable that the calculations performed using the LDA have been so successful. Recent work has shown that this success can be partially attributed to the fact that the LDA gives the correct sum rule for the exchange-correlation hole [Harris and Jones 1974, Gunnarsson and Lundquist 1976 and Langreth and Perdew 1977]. In LDA the exchange-correlation energy of an electronic system is constructed by assuming that the exchange-correlation energy per electron is at point r in the electron gas, $\varepsilon_{XC}(r)$, is equal to the exchange correlation energy per electron in a homogeneous gas that has the same density as the electron gas at point r_i thus

$$E_{XC}[n(r)] = \int \varepsilon_{XC}(r) n(r) d^3 r \tag{2.8}$$

and

$$\frac{\delta E_{XC}[n(r)]}{\delta n(r)} = \frac{\partial [n(r)\varepsilon_{XC}(r)]}{\partial n(r)} \tag{2.9}$$

with

$$\varepsilon(r) = \varepsilon_{XC}^{\text{hom}}[n(r)] \tag{2.10}$$

LDA a gives a single well-defined global minimum for the energy of a non-spin polarized system of electrons in a fixed ionic potential.

2.1.3 Local Spin Density Approximation

The density functional theory shows that it is possible to determine the total energy using functional that depends on the density alone and not on the spin densities. The task of finding good approximations to the exchange-correlation energy is greatly simplified if the functional is expressed in terms of spin densities. This is the simplest way of satisfying the requirement (Hund's rule), which a state with a larger spin tends to be favoured energetically. The inclusion of the spin dependence by using the Local Spin Density Approximation (LSDA) is found to be improving the description of unpaired electrons, thereby improving the cohesive energy of the solid. LSDA is the approximation used in total energy calculations and the total energy is given by

$$E_{XC}^{LSD} = \int dr n(r) \varepsilon_{XC}[n_{\uparrow}(r), n_{\downarrow}(r)] \tag{2.11}$$

where $\varepsilon_{XC}[n_\uparrow, n_\downarrow]$ is the exchange and correlation energy per particle of a homogeneous, spin-polarized electron gas with spin-up and spin down densities $n_\uparrow$ and $n_\downarrow$ respectively.

2.1.4 Generalised Gradient Approximation

A large number of total energy calculations have shown that LDA gives interatomic bond lengths within ± 0.05 Å of experiment or better for a great variety of solids, surfaces and molecules. However, two systematic trends have been found, that is (i) weak bonds are too short and (ii) binding energies calculated with LDA are typically too large [Wimmer 1998]. Gradient-corrected density functional, suggested by Perdew [1986] and Becke [1988], seems to have offered a remedy. The terms in the exchange-correlation expressions which depend on the gradient of the electron density, and not only on its value at each point in space, are included in the scheme of Perdew and Becke. Generalized Gradient Approximation (GGA) includes the gradient as the only new variable. The GGA exchange energy is written as

$$E_{XC}^{GGA}(n) = \int dr n(r) \varepsilon_{XC}^{GGA}[n(r), \nabla n(r)] \qquad (2.12)$$

where ε_{XC} is the exchange correlation energy and $\nabla n(r)$ is the gradient term.

2.1.5 Plane-Wave Pseudopotential Method

The pseudopotential approximation [Phillips 1958, Cohen and Heine 1970, Yin and Cohen 1982] allows the electronic wave functions to be expanded using much smaller number of plane-waves basis states. It is well known that most physical

properties of solids depend on the valence electrons to a much greater extent than on the core electrons. The pseudopotential approximation exploits this by removing the core electrons and replaces them and the strong ionic potential by a weaker pseudopotential that acts on a set of pseudo wave functions rather than the true valence wave functions. Generally, the pseudopotential is given by the form;

$$V_{NL} = \sum_{lm} |l_m\rangle V_i \langle l_m| \tag{2.13}$$

where $|l_m\rangle$ are the spherical harmonics and V_i is the pseudopotential for angular momentum. A pseudopotential that uses the same potential for all the angular momentum components of the wave function is normally called a local pseudopotential. A local pseudopotential is a function of the distance from the nucleus. It is possible to produce arbitrary, predetermined phase shifts for each angular momentum state with a local potential.

2.1.6 Solution of the Kohn-Sham Equations

The Kohn-Sham equations represent a mapping of the interacting many-electron systems onto a system of non-interacting electrons moving in an effective potential due to all other electrons. If the exchange-correlation energy is known exactly, then taking the functional derivative with respect to the density would produce an exchange-correlation potential that includes the effects of exchange and correlation exactly. The Kohn-Sham equations must be solved self consistently so that the occupied electronic states generate a charge density that produces the electronic potential that was used to construct the equations. The set of wave functions minimizes the Kohn-Sham energy functional. These wave

functions are given by the self-consistent solutions to the Kohn-Sham equations [Kohn and Sham 1965];

$$\left[-\frac{\hbar^2}{2m}\nabla^2 + V_{ion}(r) + V_H(r) + V_{XC}(r)\right]\psi_i(r) = \varepsilon_i\psi_i(r) \tag{2.14}$$

where ψ_i is the wave function of the electronic state i, ε_i is the Kohn-Sham eigenvalue and V_H is the Hatree potential of the electrons and is given by

$$V_H(r) = e^2\int\frac{n(r')}{|r-r'|}d^3r' \tag{2.15}$$

The exchange-correlation potential V_{XC} is given by the functional derivative

$$V_{XC}(r) = \frac{\delta\varepsilon_{XC}[n(r)]}{\delta n(r)} \tag{2.16}$$

2.2 Potential Models

Atomistic simulation techniques based on the Born model of solids is described. Atomistic simulation techniques use analytic functions to describe interactions between the ions in the crystal. The basis of this method is to calculate the total interaction energy, often called the lattice energy of the system under study. The technique use simple, parameterized analytical functions to describe the interactions between all species in the system. This enables the lattice energy of the system to be calculated. And this is defined as the energy released when the component ions at infinity are brought together on their lattice sites. To ensure that the surface or interface calculations reflect the system under study, it is necessary to use an appropriate potential model to describe the interactions in the system. The interactions between ions constitute of two parts; (i) short-range interactions

which involve the attractions and repulsions of the ions and (ii) long-range interactions which describe the Coulombic interactions. **Born model of solids** [Born and Huang 1954] assumes that the lattice energy of a system is given by the sum of all pair wise interactions between the atoms i and j, and lattice energy is given by

$$U(r_{ij}) = \sum_{i}^{N}\sum_{j_{j\neq i}}^{N}\frac{q_i q_j}{r_{ij}} + \sum_{i}^{N}\sum_{j_{j\neq i}}^{N}\phi_{ij}(r_{ij}) \qquad (2.17)$$

where the first term represents the long-range electrostatic interactions and the second term represents the short-range interactions. The parameters q_i and q_j represent the charges for ions *i* and *j* respectively, r_{ij} is the distance between ions *i* and *j* and ϕ_{ij} refers to all pairs of ions *i* and *j* interactions. This is for two-body term.

2.2.1 Long-Range Interactions

The lattice energy of a system is released when two atoms are brought from infinity to their lattice sites positions within the crystal. The lattice energy corresponds to the potential energy of the long-range electrostatic interactions and is given by

$$\psi = \sum_{l,i,j}\frac{q_i q_j}{4\pi\varepsilon_0(r_{ij}+l)} \qquad (2.18)$$

where q_i and q_j are the charges on the ions i and j, r_{ij} is the displacement of ion i from ion j and l is the set of lattice vectors representing the periodicity of the crystal lattice. The equation above converges slowly with r and therefore it

cannot be used directly. Consequently, much work has been done and quicker methods of deriving the equation [Parry 1975, 1976 and Ewald 1921] are presented in Appendix B.

2.2.2 Short-Range Interactions

The short-range repulsive and attractive interactions are described using simple parameterized models. It is essential that this model accurately describes the lattice properties if reliable, quantitative, results are to be obtained. In particular, for surfaces studies it is necessary to describe the interaction at distances possibly far removed from those found in bulk lattice. The Ewald sum accounts for the long-range, attractive Coulomb interaction, but is unable to describe what occurs when two charged atoms brought near one another.

The charge distributions of two adjacent atoms are able to overlap if they are brought near enough to one another. This causes two repulsive interactions, which if the distance between these atoms become sufficiently small causes the overall force between them to become repulsive, even if the ions are oppositely charged. The two terms, (i) the Pauli term which is a result of the Pauli Exclusion Principle and (ii) the nuclear-nuclear repulsion. The generalized statement of the Pauli Exclusion Principle is that no two fermions can occupy the same quantum state. When electron clouds overlap, for the Pauli Exclusion Principle to be satisfied, the ground state charge distribution of an electron is forced to occupy a higher energy state, thus creating an increase in electron energy. This increase in energy gives rise to the repulsion.

At small internuclear distances there also exist attractive forces, the van der Waals-London interaction. This is relatively weak spontaneously induced dipole on each of the interacting species, as was postulated by Debye. In the case of two identical atoms, this force varies proportionally to r^{-6}. Although this is a quantum mechanical effect, the r^{-6} dependency can be derived from classical electrostatics. Given this broad description of the short-range repulsive energy, the functional of forms can be used to describe various terms can now be explained and they are given by:

$$\phi_{s-r} = \sum_{ij} \phi_{ij} + \sum_{ijk} \phi_{ijk} + \sum_{ijkl} \phi_{ijkl} + ... \qquad (2.19)$$

where *ij* refers to all pair interactions, *ijk* refers to all three-body interactions, and so on. Fortunately, the work in this thesis considers only two-body interactions (i.e. the first term of equation 2.19). Careful consideration must therefore be made on the suitability of any function for modelling the interactions of a particular system. With that establishment, the most commonly used potentials are described below; Lennard-Jones potential, Buckingham potential, Morse potential, Harmonic potential, Shell model potential, etc.

2.2.2.1 Lennard-Jones Potential

The Lennard-Jones potential was developed to describe the interactions on noble gases and it was later applied to intermolecular interactions in molecular systems. It is an approximation that describes the complicated nuclear and electronic repulsions, which dominate the attractive interactions at short separations. The potential is given by the form

$$\phi_{ij}\left(r_{ij}\right)=\frac{A}{r_{ij}^{12}}-\frac{B}{r_{ij}^{6}} \qquad (2.20)$$

where the first term is the repulsive term dominating at short distance and the second term represents the attractive forces dominating at large distances. The repulsive term is related to the Pauli principle: when the electronic clouds surrounding the atoms start to overlap, the energy of the system increases abruptly. The attractive term is originated by van der Waals dispersion forces, originated by dipole-dipole interactions due to fluctuating dipoles. They are weak interactions.

2.2.2.2 Buckingham Potential

The Buckingham potential is similar to the Lennard-Jones potential. It has the form

$$\phi_{ij}\left(r_{ij}\right)=A_{ij}e^{-\left(\frac{r_{ij}}{\rho_{ij}}\right)}-\frac{C}{r_{ij}^{6}} \qquad (2.21)$$

where A, ρ and C are the parameters which differ for each pair of interacting ions. Thus, they are the adjustable parameters whose descriptions of the short-range interactions largely determine the success of the calculations described later in this thesis. A and ρ are related to the size and the hardness of the ion respectively. The parameters A, ρ and C can be derived for each material. The repulsive r^{-12} term of Lennard-Jones potential is replaced by an exponential repulsive term (equation 2.20). This potential is widely used in simulation of polar solids where the repulsive terms are more significant since it has more flexible repulsive components than the Lennard-Jones.

2.2.2.3 Harmonic Potential

Modelling interaction between bonded ions can be achieved using harmonic potential form, which has the analytical form as:

$$U(r_{ij}) = \frac{1}{2} k_{ij} (r_{ij} - r_0)^2 \qquad (2.22)$$

where the parameters k_{ij} represent the force constant associated with the deviation from the equilibrium bond separation and r_0 the equilibrium bond separation. This potential is harmonic due to the energy being dependent on the square of the displacement of the current bond length (r_{ij}) from the equilibrium bond length, and is used only when the bond length does not vary much from the equilibrium. For interactions where the bond stretching is larger, Morse potential discussed in the following section can be used.

2.2.2.4 Morse Potential

The Morse potential is used to model covalently bonded interactions where the separations vary from equilibrium, such as atoms in the molecular ions. The potential is given by the from;

$$V(r_{ij}) = A_{ij} \left[1 - e^{B_{ij} [r_{ij} - \phi_{ij}]} \right]^2 - A_{ij} \qquad (2.23)$$

where A_{ij} is the bond dissociation energy, ϕ_{ij} is the equilibrium bond distance and B_{ij} is related to the curvature of slope of the potential energy.

2.2.2.5 Shell Model Potential

The shell model was developed by Dick and Overhauser [1958] and describes the ion as being divided into two components, core of charge X in which the mass

is concentrated and charge Y (massless shell) surrounding the core. The shell represents the valence electrons. Core and shell are linked by a harmonic spring, which has the spring constant k (equation 2.24). The total of core and shell charges, X and Y, are considered to represent the total charge of the ion whereas positions of the core represent the position of the ion. The interaction of core and shell is given by

$$\phi_i(r_i) = \frac{1}{2} k_i r_i \qquad (2.24)$$

where r_i is the distance between the core and the shell. The schematic representation of shell model is shown in figure 2.1. The polarizability of a free ion is given by

$$\alpha = \frac{Y^2}{4\pi\varepsilon_0 k} \qquad (2.25)$$

The parameters Y and k are obtained by empirical fitting to dielectric constants, elastic constants or phonon dispersion curves. The disadvantage of using the shell model is that the calculations become considerably computationally expensive since the number of species in the system is effectively doubled.

Although the shell model is phenomenological in nature, its use is warranted by its success in previous studies (see for example [Catlow 1987]). The strength of this model is that any force acting on an ion is assumed to do so via the shell, thus coupling short-range interactions to the polarizability see figure 2.1. Clearly, this provides a framework by which it is possible to model more of the interactions occurring between species than if the shell model was not used (i.e. the rigid ion

model alone). There are, however, limitations to this model mostly that the shell model does not account for the Cauchy violation and is computationally expensive.

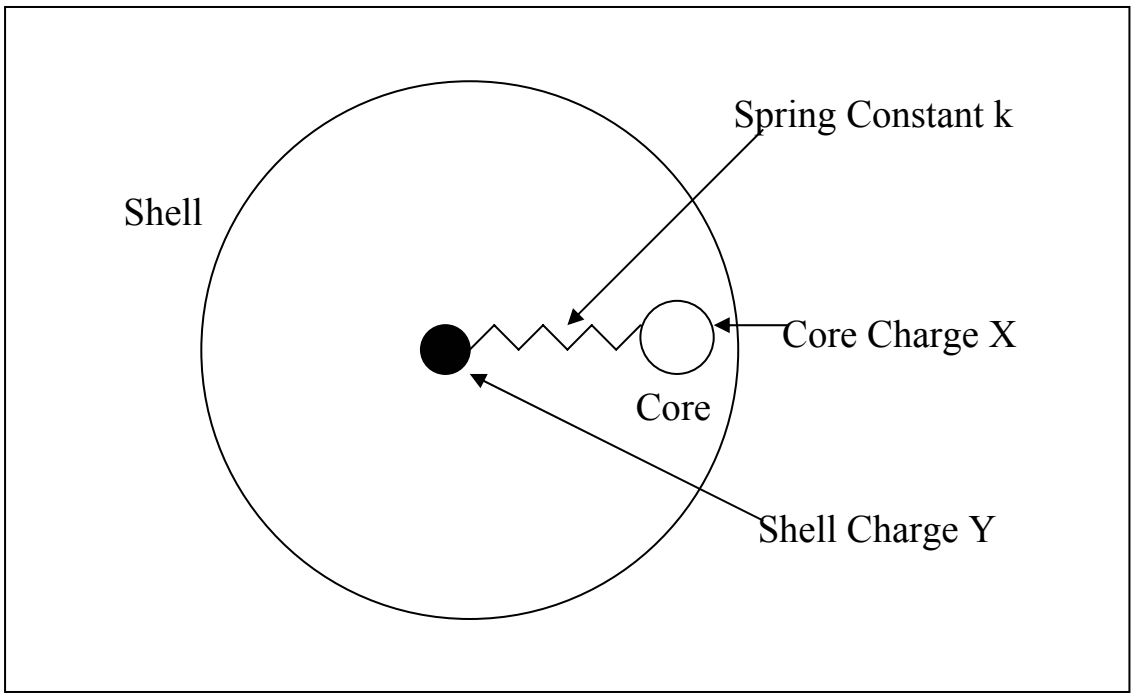

Figure 2.1 Schematic representation of the shell model

2.2.2.6 Rigid ion model

The simplest form of potential is one in which electronic polarizability is neglected; the rigid ion model. This model is good in reproducing structural parameters for static systems. However, lattice vibrations are poorly modelled as they are so strongly coupled to polarizability. Also, once a defect is introduced, polarization will be expected to occur around a defect so as to stabilize it. The problem of defect energies in static conditions can be handled by refitting short-range potential parameters to model the static dielectric constants, overestimating

the polarization due to lattice relaxation to compensate for the short fall to the neglect of electronic polarizability and thus obtain correct defect energies.

2.3 Energy Minimization

In molecular modelling the interest is especially in minimum points on the energy surface. Minimum energy arrangements of the atoms correspond to stable states of the system; any movement away from a minimum gives a configuration with a higher energy. There maybe very large number of minima on the energy surface. The minimum with the very lowest energy is known as the global energy minimum. Minimization algorithm is used to identify those geometries of the system that correspond to the minimum points on the energy surface. The highest point on the pathway between minima is of special interest and is known as the saddle point with the arrangement of atoms being the transition structure.

In order for the aforementioned potential models to be useful in predicting perfect lattice properties, it must be combined with an energy minimization technique to bring the system to a state of mechanical equilibrium. All ionic interactions are calculated and each ion subsequently moves a distance proportional to the force acting on the particle in the direction of the overall field. There are two approaches that are in common use for minimising the lattice energy, either at constant volume or constant pressure. During constant volume minimization the cell dimensions are fixed but the ions are allowed to move in space. This means that no consideration is made of the bulk lattice strain. For constant pressure techniques, it is necessary to determine the minimum energy not only through adjustment of

ionic coordinates, but also unit cell dimensions, accounting for the strains both on individual ions as well as the unit cell. Thus, in case of constant pressure minimization both the cell dimensions and ion coordinates are allowed to change.

Static energy minimization can be used to obtain bulk and surface properties of a system. The energy of the systems considered in this work are not harmonic, thus the energy minimum cannot be arrived at in single step. Rather, subsequent displacements, in general, results in lower energy configurations. Thus, the atom positions are adjusted iteratively until the forces on the atoms are zero (equation 2.26). Thus achieving the minimum value of the lattice energy, U:

$$\bar{g} = \frac{\partial U}{\partial \bar{r}} \tag{2.26}$$

where $\bar{g}$ is the force, U is the total lattice energy and $\bar{r}$ is the vector describing the configuration of the system. There are two methods of energy minimization employed in this work: Newton-Raphson and Conjugate-Gradient. A brief outline of the both methodologies is described below.

2.3.1 Constant Volume Minimization

Consider a lattice of N atoms per unit cell and lattice energy $U_L(\bar{r})$. Expanded U about a point $\bar{r} + \bar{\delta r}$ to the second order using Taylor expansion gives:

$$U_L(\bar{r} + \bar{\delta r}) \approx U_L(\bar{r}) + \bar{\delta r}.\bar{g r}^T + \frac{1}{2}\left(\bar{\delta r}^T . W \bar{\delta r}\right) \tag{2.27}$$

where $\bar{\delta r}$ is the displacement ions from their original positions, $\bar{g}$ is the first derivative of the energy (equation 2.26), W is the second derivative matrix $\left(\frac{\partial^2 U_L(\bar{r})}{\partial \bar{r}}\right)$. Making the assumption that the minimum energy occurs at the

equilibrium position, when the change in energy caused by changing the coordinates by an amount δr is zero, it can be seen by differentiating equation 2.27 that the minimum energy occurs when equation 2.28 is satisfied.

$$\frac{\partial U_L\left(\bar{r}+\bar{\bar{\delta r}}\right)}{\partial \bar{\bar{\delta r}}} = g + W\bar{\bar{\delta r}} = 0 \qquad (2.28)$$

rearranging this in terms of $\bar{\bar{\delta r}}$ gives

$$\bar{\bar{\delta r}} = W^{-1}\bar{g} \qquad (2.29)$$

If the system was perfectly harmonic in nature, the minimum energy structure would be calculated in one step. This is not however, the case. To achieve the minimum energy structure, several iterations are usually performed. There are many methods available for optimizing a matrix equation and it is important to select the most appropriate technique for being considered. Failure to do this can add greatly to computational time. All Newton-Raphson type formulae (e.g. the Borgden, Fletcher, Goldfard, Shanno) formula serve to iteratively update the Hessian matrix, H, from equation 2.30

$$\delta = -H.g \qquad (2.30)$$

$$r_{n+1} = r_n - H_i.g_i \qquad (2.31)$$

This however requires the storage of the Hessian matrix of the second derivatives, which is computationally expensive. Furthermore, solving for the second derivative matrix at each step would result in less expeditious overall calculations. For this reason, Conjugate Gradient type minimizations are also employed. These only require the calculations of the first derivatives of the lattice energy:

$$\beta = \frac{g_{i-1}^{T} \cdot g_{i-1}}{g_{i-2}^{T} \cdot g_{i-2}} \tag{2.32}$$

Conjugate Gradient calculations are computationally less expensive compared to Newton-Raphson variety and converge quickly when far from the lattice energy minimum. However, when near the minimum, the Conjugate Gradient technique becomes less efficient due to the small gradients. Thus, a combination of these two techniques is used during the minimization process, beginning with Conjugate Gradient as a coarse refinement until a certain small gradient is met and the switching to Newton-Raphson type methods in order to finalize the minimization.

2.3.2 Constant Pressure Minimization

Once constant volume minimization has been carried out the vectors are adjusted to remove the bulk strains. To achieve this, Hooke's law is applied to the system so that the lattice vectors are adjusted according to the bulk lattice strain ε.

$$\varepsilon = C^{-1}\overline{\sigma} \tag{2.33}$$

where the stress is the sum of the applied and static pressure $\left(P_{static} + P_{applied}\right)$. The static pressure is given by the expression:

$$P_{static} = \frac{1}{V}\frac{\partial U_L}{\partial \varepsilon} \tag{2.34}$$

and C is the compliance matrix. This is the second order derivatives of lattice energy with respect to strain. Again because the systems are not completely harmonic the system is minimized by an iterative process.

2.4 Molecular Dynamics

Molecular dynamic simulation is a powerful tool in materials science. It can be used to study time dependent properties such as diffusion [Fisher 1998, Suzuki 1998ab, Khan 1998 and Karakasidis 1999] phase stability, melting, defects [Jacobs 1997 and reference therein] and to elucidate structural evolution of a thin film grown by atom deposition [Sayle 2000a and 2001] or evolution from an amorphous structure to a crystalline one with structural modifications that arise [Sayle 2000b, 2001 and Maicaneanu 2001ab].

Molecular dynamics is a computer simulation technique where the time evolution of a set of interacting atoms is followed by integrating their equations of motion. Molecular dynamics calculates `real' dynamics of the system from which time averages of properties can be calculated. The major disadvantage however, is that, it is time consuming and can be computationally expensive. To a large extent this has been offset with the development of more efficient simulation packages and the advancement of computer technology. This makes it possible to undertake molecular dynamic simulations on a desktop PC.

In MD, atoms interact with each other, the forces acting upon the atoms are originated by the interactions and the atoms move under the action of the instantaneous forces. As the atoms are moving, their relative positions and forces change. Sets of atomic positions are derived in sequence by applying Newton's equations of motion. MD is a deterministic method, thus, the state of the system at any future time can be predicted from its current state. In MD laws of classical

mechanics are followed and notably Newton's law for each atom i in the system constituted by N atoms:

$$\overline{F}_i = m_i \overline{a}_i \tag{2.35}$$

where m_i is the atom mass, $\overline{a}_i$ is the acceleration of the atom and $\overline{F}_i$ is the force acting upon the atom, due to interactions with other atoms. The force, **F**, on an atom can be evaluated directly from the first derivative of the potential energy, E, with respect of the coordinates, r, and can be implemented in Newton's second law of motion (2.35). The equation becomes

$$-\frac{\partial E}{\partial r} = m\frac{\partial^2 r}{\partial t^2} \tag{2.36}$$

The acceleration is given by

$$a_i = \frac{d^2 r_i}{dt^2} \tag{2.37}$$

In practice molecular dynamics is run with finite time steps. Using the equations above would therefore lead to the introduction of inaccuracies [Biesiadecki and Skeel 1993]. A number of algorithms have been developed to overcome this difficulty. There are many ways for integrating the equations of motion, such as the Verlet, verlet leap-frog, velocity verlet, Beeman or Gear predictor-corrector algorithms [Leach 1996]. It has been shown that for short time steps, the predictor-corrector method may be more accurate, but for longer time steps the Verlet algorithm may be better [Leach 1996]. The Verlet Leapfrog Algorithm (VLA) is a modification of Verlet's original algorithm [Verlet 1967]. VLA is the basis of the algorithms used in DL_POLY [Smith 1999], the simulation package used in this

work. All the algorithms assume that the position and dynamical properties (e.g. velocity, acceleration) for each atom can be approximated as Taylor expansion series:

$$r_i(t+\delta t) = r_i(t) + v_i(t)\delta t + \frac{\delta t^2}{2} \qquad (2.38)$$

$$v_i(t+\delta t) = v_i(t) + \bar{a}_i(t)\delta t \qquad (2.39)$$

Moreover, in the leap-frog algorithm it is assumed that the velocity, v(t), is changing linearly during δt, therefore it can be calculated as an instantaneous velocity at δt/2. The VLA can be expressed mathematically by equations 2.40 and 2.41 below:

$$\bar{r}(t+\delta t) = \bar{r}(t) + \bar{v}\left(t+\frac{1}{2}\delta t\right)\delta t \qquad (2.40)$$

$$\bar{v}\left(t+\frac{1}{2}\delta t\right) = \bar{v}\left(t-\frac{1}{2}\delta t\right) + \bar{a}(t)\delta t \qquad (2.41)$$

The quantities to be stored for each step are therefore the position $\bar{r}(t)$ and the acceleration $\bar{a}(t)$. In addition to those quantities the mid-step velocity $\bar{v}\left(t-\frac{1}{2}\delta t\right)$. The equation 2.40 is implemented first and the next mid-step velocity $v\left(t+\frac{1}{2}\delta t\right)$ is calculated. If the velocities for the current step are required they can be calculated at this point using equation 2.42. This in turn allows the energy at time *t* and other quantities that are functions of position and velocity to be calculated. Equation 2.40 is used to calculate the new positions of all the particles. After which the accelerations may be calculated ready for the next iteration.

$$\bar{v}(t) = \frac{1}{2}\left[\bar{v}\left(t+\frac{1}{2}\delta t\right) + \bar{r}\left(t-\frac{1}{2}\delta t\right)\right] \qquad (2.42)$$

In order to make molecular dynamics simulations more comparable with experiment much time has been spent developing various conditions or ensembles under which MD can be run [Allen and Tildesley 1989]. Normally, the simulation temperature fluctuates at the beginning of the run. In order to take consideration of this the velocities are rescaled at regular intervals throughout the initial run. In doing so it enables the kinetic energy of the system to converge to a point where it corresponds to the chosen temperature [Jacobs and Rycerz 1997]. This process is termed equilibrium. Once the system has achieved the required Maxwell-Boltzmann distribution of velocities the simulation begins.

In dynamical simulation the choice of a time step in accord with the type of system and motion present is critical. A timestep must be chosen such that it is shorter than the period of any lattice vibrations. If this is not done vibrations will not be fully tracked by the MD and will lead to inaccuracies when calculating the systems properties. When the time step is quite small (T/8) there is still a good agreement with the true oscillation but as the time step becomes large the simulated curve follows the true curve less and less and hence would lead to larger errors in any calculations whereas if the time step is too small the simulation will exceed the available computer time before the ions have moved a significant distance. Consequently the time step is required to be as small as possible. This however, leads to an increase in the number of iterations over which the simulation run in order for the total sampling time to be of the desired length. In this study a time step of 5×10^{-3} ps was used in all calculations, which means that

after each iteration, $5x10^{-3}$ ps, the coordinates, velocities, accelerations and energies are recalculated.

MD methods are used in solid-state physics, with applications in studies of ionic properties, modelling of phase transition and elucidating the structure and dynamical correlations. Molecular dynamics has a kinetic energy that contributes to the total energy of the system. The simulations are traditionally performed under conditions of constant number of particles (N), volume (V) and energy (E) (the constant NVE or microcanonical ensemble). But it can also be adapted to simulate from the canonical ensemble, and two other common ensembles, which is isothermal-isobaric (fixed NPT) and grand canonical (fixed μVT). Thermodynamic averages are obtained from MD simulation as time averages using the numerical integration of the equation

$$\langle A \rangle = \iint dp^N dr^N A\left[p^N, r^N, \rho\left(p^N, r^N\right)\right] \qquad (2.43)$$

where p^N and r^N represent the N momenta and positions respectively, $A\left(p^N, r^N\right)$ is the instantaneous value of the property A, $\rho\left(p^N, r^N\right)$ is the probability density of the ensemble, that is the probability of finding a configuration with momenta p^N and positions r^N and $\langle\ \rangle$ is an ensemble average or expectation value; that is the average value of the property A over all replications of the ensemble generated by the simulation. Thus, thermodynamic averages are given by the relation;

$$\langle A \rangle = \frac{1}{M} \sum_{i=1}^{M} A\left(p^N, r^N\right) \qquad (2.44)$$

where M is the number of steps. Despite the traditional use of MD, nowadays is also used for other purposes, such as studies of non-equilibrium processes and as an efficient tool for structure optimizations overcoming the local energy minima.

2.4.1 Energy

The internal energy is easily obtained from a simulation as the ensemble average of the energies of the states that are examined during the course of the simulation and is given by

$$\begin{aligned} U &= \langle E \rangle \\ &= \frac{1}{M} \sum_{i=1}^{M} E_i \end{aligned} \tag{2.45}$$

The average potential energy V is obtained by averaging its instantaneous value, which is obtained at the same time as the force computation is made. Thus the potential energy is given by

$$V(t) = \sum_{i} \sum_{j>1} \phi\left(\left| r_i(t) - r_j(t) \right| \right) \tag{2.46}$$

The kinetic energy is given by

$$K(t) = \frac{1}{2} \sum_{i} m_i \left[v_i(t) \right]^2 \tag{2.47}$$

where m_i is the mass of atom i and v_i is the velocity of atom i. The total energy of the system can be represented as the sum of the kinetic energy and the potential energy. With the kinetic energies defined in terms of velocities (2.47). The total energy of a system with a given set of positions and velocities is represented by

$$E_{tot} = K(t) + V(t) \tag{2.48}$$

2.4.2 Pressure

The pressure is calculated in a computer simulation via the virial theorem of Claussius. The virial theorem is defined as the expectation value of the sum of the products of the coordinates of the particles and forces acting on them. It is written as

$$W = \sum x_i p_{xi} \tag{2.49}$$

where xi is the coordinate and p_{xi} is the first derivative of the momentum along the coordinate. The virial theorem states that the virial is equal to $-3Nk_BT$. In an ideal gas, forces are those due to interactions between the gas and the container and in this case the virial theorem is equal to $-3PV$. These results can be obtained from

$$PV = Nk_BT \tag{2.50}$$

Forces between the particles in a real gas or liquid affect the virial and thence the pressure. The total virial for a system equals the sum of an ideal gas part $(-3PV)$ and contribution due to interactions between the particles. The result obtained is

$$P = \frac{1}{V}\left[Nk_BT - \frac{1}{3k_BT}\sum_{i=1}^{N}\sum_{j=i+1}^{N} r_{ij} f_{ij} \right] \tag{2.51}$$

The forces are calculated as part of molecular dynamics simulation, and so little additional effort is required to calculate the virial and thus the pressure.

2.4.3 Temperature

It is necessary to assign initial velocities to each atom before the iterative process can be started. This can be done by random selection from a Maxwell-Boltzmann distribution at the temperature of interest:

$$P(v)\partial v = \left(\frac{m}{2\pi kT}\right)^{\frac{3}{2}} \exp\left(\frac{-mv^2}{2kT}\right) 4\pi v^2 \partial v \qquad (2.52)$$

where *P(v)* is the probability of velocity v, m is the mass of particle, v is the velocity of particle, T is temperature and k is Boltzmann constant.

In the microcanonical ensemble, the temperature is fluctuating whilst in the canonical total temperature is constant. Since the system is in motion, the temperature is directly related to the kinetic energy of the system as follows

$$\chi = \sum_{i=1}^{N} \frac{|p_i|^2}{2m_i}$$

$$= \frac{k_B T}{2}(3N - N_c) \qquad (2.53)$$

where p_i is the total momentum of particle i and m_i is the mass. N_c is the number of constraints and $3N - N_c$ is the total number of degrees of freedom. According to equipartition theorem of energy, each degree of freedom contributes $\frac{k_B T}{2}$. If there are N particles, each with three degrees of freedom, then the kinetic energy equals $\frac{3Nk_B T}{2}$. N is the number of constraints on the system. An expression for temperature in terms of velocity can be derived:

$$K = \frac{3}{2}kT \qquad (2.54)$$

$$T = \frac{mv^2}{3k} \qquad (2.55)$$

2.4.4 Radial Distribution Functions

The Radial Distribution Functions (RDFs) are a very useful way of describing the structure of a system [Leach 1999] and the information can be extracted from MD simulations via the pair distribution function, $g(r)$, which is given by

$$g_{ij}(r) = \left\{ \frac{\langle n_{ij}(r) \rangle}{4\pi r^2 (n_i n_j)^{\frac{1}{2}}} \right\} \qquad (2.56)$$

where $\langle n_{ij}(r) \rangle$ is the ensemble average of the number of species of type j in a radial shell of $r \to r + dr$ with a species of type i at the centre, n is the bulk density of ion type i [Islam et al 1996]. The pair distribution function, $g(r)$, is the probability of finding an atom or molecule at a distance r from another atom or molecule compared to the ideal gas distribution. Thus $g(r)$ is dimensionless. Higher radial distribution functions like the triplet radial distribution function can also be found, but they are rarely calculated and so in most cases the references to the RDFs are usually taken to mean the pair wise version. In a crystal RDFs has an infinite number of sharp peaks whose separations and heights are characteristics of the lattice structure. RDFs can be measured experimentally using the X-ray diffraction where a regular arrangement of the atoms in a crystal gives the characteristics x-ray diffraction pattern with bright and sharp spots.

2.4.5. Periodic Boundary Conditions

Periodic boundary conditions (PBC) describe periodicity in solids modelling and ensure the removal of the problems associated with edge effects. PBC enable a simulation to be performed using a relatively small number of particles in such a way that the particles from the edges experience forces as if they were in the bulk. In simulating ionic crystals, there is a finite size of the simulation cell. There are constraints of the simulation, which are, processing power, computer memory and the length of the time allowed for the simulation. This leads to atoms in the crystal lattice being exposed to different environments and interactions, e.g., atoms at the edge of the simulation will experience different interatomic forces than those in the centre of the simulation cell [Elliot 1998]. To overcome this problem periodic boundary conditions are imposed on the simulation cell. With repeating boundary conditions, one typically conducts a simulation within a box. The simulation box containing particles is replicated periodically through the space in all the directions to give an infinite lattice. As an ion moves during the simulation, its image in all the other replicated cells move also. Even when an ion leaves the central cell its image enters the box through the opposite side-conserving the number of ions in each image [Elliot 1998]. Figure below shows an example of periodic boundary conditions.

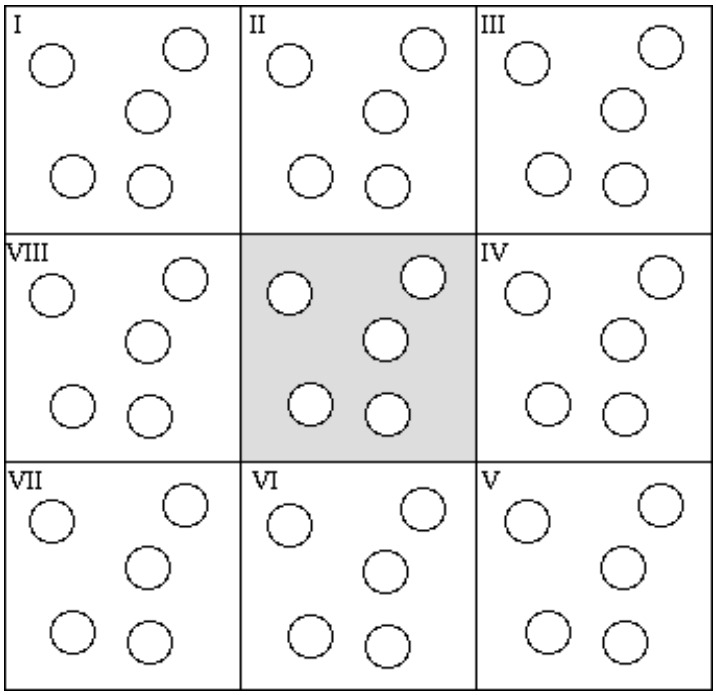

Figure 2.2: Schematic representation of two-dimensional boundary conditions employed in simulations.

2.5 Computer Codes

To investigate the behaviour of ions in the bulk, and at the surfaces and interfaces the GULP [Gale 1997], MARVIN [Gay 1995], METADISE [Watson 1996] DLPOLY [Smith 1999] and MDPREP [Watson 2002] codes were used.

2.5.1 GULP (General Utility Lattice Program)

GULP is a code used to simulate three-dimensional periodic systems (bulk crystal structures), to calculate material properties and conversely to derive empirical potential parameters through least-square fitting. This can be used to create crystals, optimise the crystals, study defect structures in solid solutions [Balducci 1997] and calculate many properties in solid state for comparison with

experiments. Also it can be used to derive interatomic potentials. In this work, GULP code was used to calculate lattice parameters for MnO_2 systems based on the values of the potential available and create unit cells of the required support crystals of MnO_2.

2.5.2 MARVIN (Minimization And Relaxation of Vacancies and Interstitials Near Surface Program)

MARVIN is a computer code designed specifically for simulations of surfaces and interfaces employing two-dimensional PBC figure 2.2. Periodic Boundary Conditions enable a simulation to be performed using a relatively small number of particles in such a way that particles from the edges experiences forces as if they were in the bulk. PBC describe periodicity in solids modelling and ensure the removal of the problems associated with the edge effects. Graphical representation of the simulation box containing the particles under study is shown in figure 2.3 and is replicated periodically through space to give an infinite lattice. MARVIN can perform both energy minimization and dynamical simulations.

Figure 2.3 shows the simulation cell used, consisting of one block for surface simulations and two blocks A and B for interface simulations, where block B contains the supported thin film. Each block is divided into two regions: region I in which the ions form are allowed to move under dynamics, or to relax under energy minimization and region II in which the ions are held fixed relative to one another, but allowed to move as a whole in response to region I. Ions included in region II ensure the correct crystalline environment for the lower ions in region I.

The code was used to create surfaces of MnO_2 and the surface is made up two different regions, regions I and II. Ions in region I are allowed to move during dynamical simulation whereas those in region II are kept fixed to reproduce the potential of the bulk lattice on region I. Figure 2 shows an illustration of regions I and II in a typical MnO_2 support. In thesis, {100} and {001} surfaces of MnO_2 pyrolusite and {100} surface for MnO_2 ramsdellite were used for interface generation. Other surfaces were also investigated but they didn't work. If a particle is moving in the simulation box during the simulation under the action of interatomic forces, its image in all other boxes moves in exactly the same way.

2.5.3 METADISE (Minimum Energy Techniques Applied to Dislocations, Interfaces and Surface Energies)

METADISE is a computer code that can be applied to dislocations, interfaces and surface energies. This programme was in part derived from MIDAS code developed by Tasker in 1978 [Tasker 1978]. The crystal is considered to consist of a series of charged planes parallel to the surface and periodic in 2D. The bulk is made up of two regions blocks each of which is divided into two regions, region I and region II (figure 2.3). The ions in region II are held fixed at their equilibrium position whilst the ions in region I are allowed to relax relative to region II.

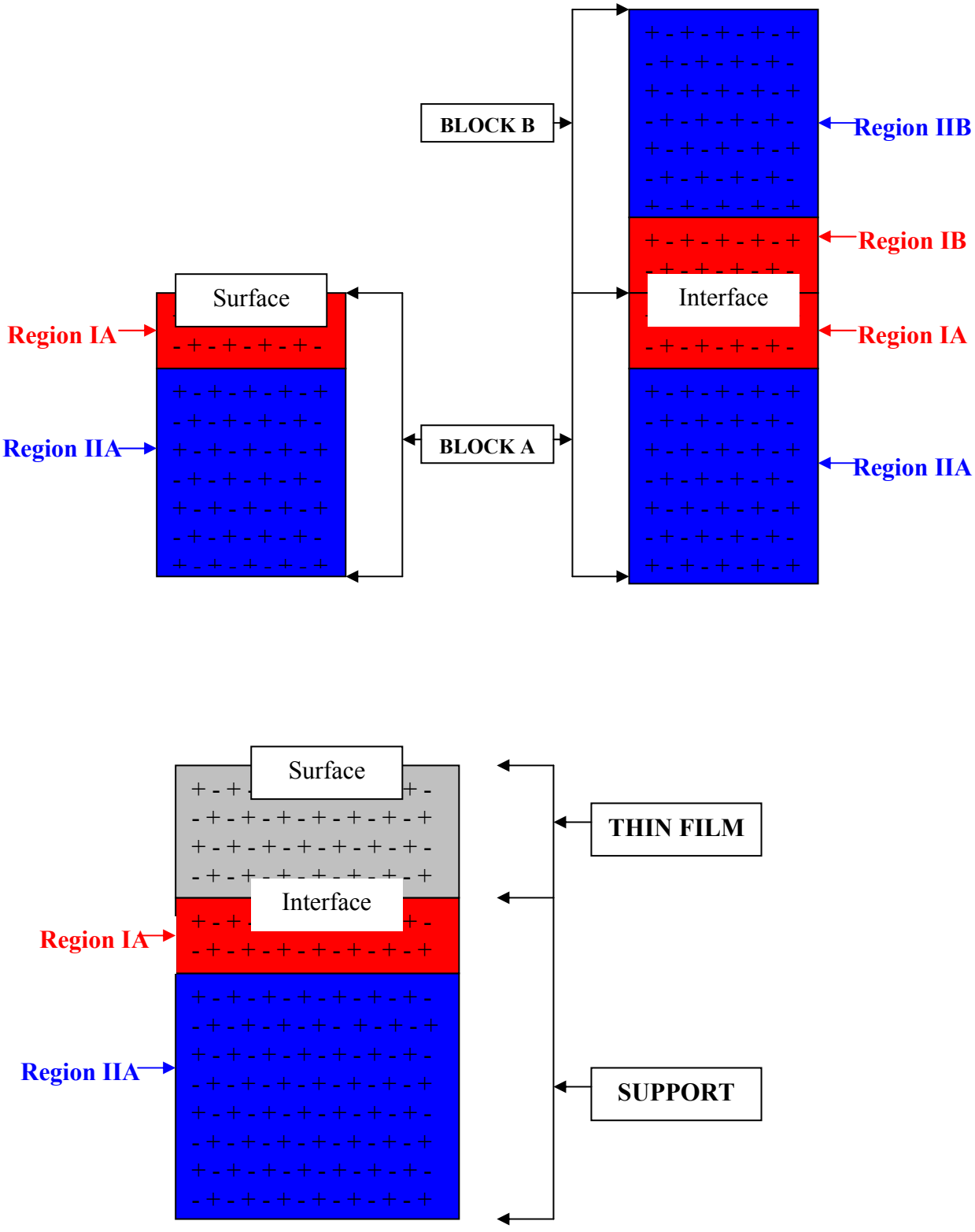

Figure 2.3: Schemamatic representation of approach for calculating surfaces (top) and interfaces (bottom) in a crystal.

A surface is created when the blocks are separated. The energy of the crystal is made up of two parts such that

$$E_{tot} = E_1 + E_2 \tag{2.57}$$

where E_1 and E_2 are the energies of the ions in region I and region II respectively. The energy of region I is given by equation 2.58 below

$$E_1 = \sum_{\substack{i\in I \\ j\in I}} \sum_{l} \psi_{ij}\left(\left|r_{ij} - r_l\right|\right) + \frac{1}{2}\sum_{\substack{i\in I \\ j\in II}} \sum_{l} \psi_{ij}\left(\left|r_{ij} - r_l\right|\right) \tag{2.58}$$

where the first term includes interactions between the ions in region I and second term the interactions between the ion in region I and region II. The energy of the region II consists of only the second term as the ions are kept fixed and hence the interactions between the ions in region II is uncharged. The energy contribution is therefore given by the equation 2.59

$$E_2 = \frac{1}{2}\sum_{\substack{i\in I \\ j\in II}} \psi_{ij}\left(\left|r_{ij} - r_l\right|\right) \tag{2.59}$$

When calculating the surface energy of a crystal it is necessary to perform two METADISE calculations, one for the surface block and one for a bulk block. The surface energy is described using the following method. If the energy of the surface block is E_s and the bulk block is E_B then these energies can be broken down into the following components:

$$E_S = E'_{I-II} + E'_{I-I} + E'_{II-I} + E'_{II-II} \tag{2.60}$$

$$E_B = E''_{I-II} + E''_{I-I} + E''_{II-I} + E''_{II-II} \tag{2.61}$$

where $E_{I\text{-}I}$ is the interaction energy of the ions in region I with others in region I, $E_{II\text{-}I}$ is the interaction energy of all the ions in region I with all the ions in region II, etc. It can be shown that the surface energy of the crystal face is described by equation

$$\gamma = \frac{E_S - E_B}{Area} \qquad (2.62)$$

Since the ions in region II do not relax, the total interaction energy, $E_{II\text{-}II}$, of all the ions in region II with all the other ions in region II does not change, these will cancel in the surface energy calculation.

In this thesis, METADISE code has been used to calculate surface properties of electrolytic manganese dioxide. Also the code was used to generate MnO_2 interfaces, by placing MnO_2 thin film on top of MnO_2 (hkl) supports of both pyrolusite and ramsdellite polymorphs. The size of the cell is specified in the x and y directions using the METADISE code, and also the number of layers in the thin film and the support. The layers occurring in region I and II were specified, with the support regions being designated IA or IIA. The ions in the thin film are all situated in region I and are designated as region IB. Figure 2.3 shows a simulation cell illustrating all the regions defined above.

2.5.4 DLPOLY

DLPOLY is a code designed to perform molecular dynamics simulations of macromolecules and biological systems, polymers, ionic systems, simple atomic systems and solutions on distributed memory parallel computers. The code was

written to accommodate three-dimensional periodic boundary conditions, cubic, orthorhombic, parallelepiped, truncated octahedral, rhombic dodecahedral, slab and hexagonal prism. The DL_POLY code was used in this study to perform all the dynamical simulations. Since the code utilizes three-dimensional periodic boundary conditions the surface is simulated using a periodic array of slabs with a void (ca. 50-75 Å in size) introduced perpendicular to the interfacial plane to represent the vacuum above the surface of the thin film. The size of the void is, of course, suitably large to ensure that the interactions between the slabs are negligible. In addition, a standard two-region approach [Watson 1996] is employed. Region I contains the MnO_2 thin film and one repeat unit of MnO_2, and ions in this region are allowed to move within the dynamical simulation. Ions in region II are held fixed during the simulation to reproduce the potential of the bulk lattice in region I. The reason for using DL_POLY (code using two-dimensional periodicity are available [Gay 1995]), is that it offers a considerable speed advantage for our particular simulations. In particular, for simulating interfaces, one must be able to accommodate many structural features including the epitaxial relationships, grain boundaries, dislocations, and a range of defects including vacancies, interstitials, and substitutionals including clustering-all within a single simulation cell. And while vacancies can be accommodated within a small simulation cell, dislocations and grain boundaries are much larger structurally, and to ensure their evolution, a much large simulation cell is required. Finally, to ensure a reasonable distribution of oriented grains within a crystalline material, the interfacial area of the simulation cell must be larger still. Accordingly, the vector introduced perpendicular to the surface to generate the vacuum above the thin film, while being sufficiently large to prohibit any artificial interactions between the system and its periodic images, is also our smallest vector that facilitates a very efficient

three-dimensional simulation. Many simulations of the surfaces performed using the three-dimensional codes are inefficient owing to the large sampling of reciprocal lattice vectors perpendicular to the surface in the Ewald sum compared with the other two directions. In addition, by performing the dynamical simulations on a parallel computer (typically such calculations require 10 days using 16 processors of an Origin 2000), we benefit also from the efficiency of the DL_POLY code when run in parallel.

Simulations were performed within the NVE ensemble for both pyrolusite and ramsdellite interfaces and NPT for ramsdellite interface. NVE considers constant number of particles, constant volume and constant energy with instantaneous velocity scaling to the simulation temperature throughout. This prevents the rapid and large build up of excess kinetic energy as the thin film evolves from the high strained initial configuration, via an amorphous (or molten) transition, to a crystalline phase with reduced strain and a range of defects.

2.5.5 MDPREP

MDPREP code is used to analyze the simulation cell after dynamical simulation is applied. It was used to convert atomic positions from a DLPOLY output file called HISTORY, to a graphical format that can be recognized by a computer graphics program called cerius^2 from Accelrys. Then the graphical representation of the atom position can be used to characterize defects such as vacancies and dislocation in a simulation cell. MDPREP can perform different calculations to show what happened to the simulation cell after simulation dynamics was applied to it. It can

calculate RDFs, Directional Densities (DDEN), Mean Square Displacements (MSD), etc.

2.6 Interface Construction

There are several approaches of constructing thin film interfaces, namely, (i) atom deposition, (ii) layer-by-layer and (iii) cube-on-cube construction. In atom deposition, an interface is generated by a sequential deposition of atoms onto the surface of the support until a thin film of required thickness is achieved; figure 2.4(a) [Sayle 1998]. In the layer-by-layer approach, the thin film interface is created by sequential deposition of monolayers onto the support until the required thickness for the thin film is reached; figure 2.4(b) [Sayle 2000a]. In the case of cube-on-cube construction, the interface is generated by placing the whole thin film directly onto the support followed by dynamical simulation and energy minimisation; figure 2.4(c). In this case larger simulation cell may be used, allowing the formation and evolution of many misfit induced defects, such as dislocations, lattice slip and twist boundaries, because, unlike in other approaches, only a single dynamical simulation is performed. Since the simulation cell used in atom deposition or layer-by-layer growth is too small to accommodate such defects, the cube-on-cube methodology offers a viable approach for elucidating their structure [Sayle 2000b]. Consequently in this work a cube-on-cube approach was used to perform all the simulations, enabling larger simulation cells to be considered. The approach is less computationally expensive compared to other two approaches mentioned above. It is very expensive to create a thicker thin film

with atom deposition or layer-by-layer approach, as after every deposition of atom or layer, a dynamical simulation is performed.

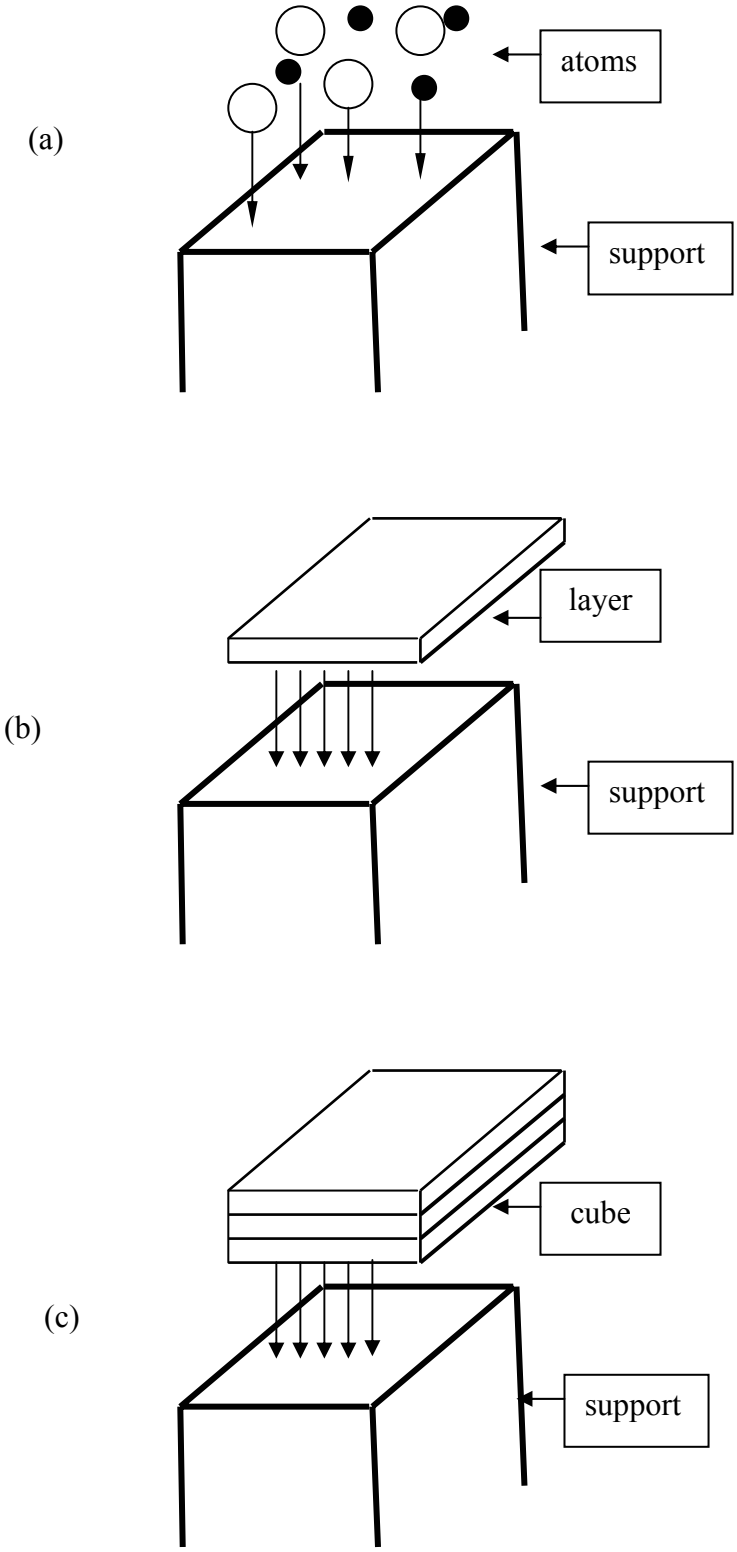

Figure 2.4: Schematical representation of (a) atom deposition, (b) layer-by-layer and (c) cube-on-cube approaches for interface construction.

2.7 Amorphization and Recrystallization

To generate models of supported oxide thin films that are more realistic, various structural features, including epitaxial relationships and various defects must be introduced within the model. The defects, which evolve in response to misfit accommodation, include dislocations arrays, vacancies, substitutions and interstitials including clustering of such defects. All these type of defects will evolve and act to reduce the lattice misfit thereby stabilizing the thin film. The simulated amorphization and recrystallization technique allows a natural evolution of all structural features that would exist within a real system. The technique involves forcing the overlaying material to undergo, under dynamical simulation, a controlled amorphization prior to recrystallizing. The recrystallization process is controlled by the interaction between the amorphous thin film and the substrate, which does not undergo an amorphous transition. Prolonged dynamical simulation results in recrystallization of the amorphous thin film together with the evolution of the structural features relating to the grain boundaries, dislocations, defects, and reduced interfacial ion densities. The final thin film structure is therefore governed solely by the interfacial interaction and lattice misfit associated with the system rather than the (perhaps artificial) starting configuration. Central to this methodology is that dynamical simulation, as applied to an amorphous structure, allows the ions to evolve or assemble into an appropriate (low energy) configuration owing to the much higher ionic mobility of species within an amorphous compared with a crystalline structure.

The initial strain under which the thin film is constrained is critical in generating the desired high-energy amorphous transition. If the strain is too low, the system may not go amorphous and therefore no structural modifications will evolve. Alternatively, for greater but still inadequate initial strain the system will go amorphous, although the amorphous structure may have insufficient energy to allow complete exploration of the potential hypersurface [Sayle 2001]. On the other hand, if the initial amorphous inducing strain is too large, the velocities of the ions will be so high such that the thin film will loose integrity and the dynamical simulation will fail. The very short time scales accessible to atomistic dynamical simulations (typical 1 ns) are a major limitation within the dynamical simulations. Consequently, for highly crystalline materials, in which ionic migration is slow, dynamical simulation is not an appropriate technique to explore the energy barriers for migration because no migration would be observed within the time scales accessible. However, owing to high ion mobility in an amorphous material, they can migrate more quickly (within the time scales available) to low-energy positions compared with performing similar simulations without the amorphous transition. The amorphization and recrystallization strategy provides therefore a mechanism for overcoming, in part, the considerable (time) limitation associated with dynamical simulation.

To induce the initial amorphization, the supported material can be constrained under either high-compressive or tensile stresses. The subsequent application of high-temperature dynamical simulation to the system then results in its amorphization. Trial starting structures calculations have to be performed for both

systems since it was observed that the initial strain required to induce adequate amorphization is system dependent. In this work strains ranging from -25 to +25 % were tried for both pyrolusite and ramsdellite. It was found that the lattice misfit associated with $MnO_2/MnO_2(001)$ and $MnO_2/MnO_2(100)$ systems is +10% and 13% for pyrolusite and –6% for ramsdellite. Figure 2.5 shows a graphical representation of the compressive and tensile stress in thin films.

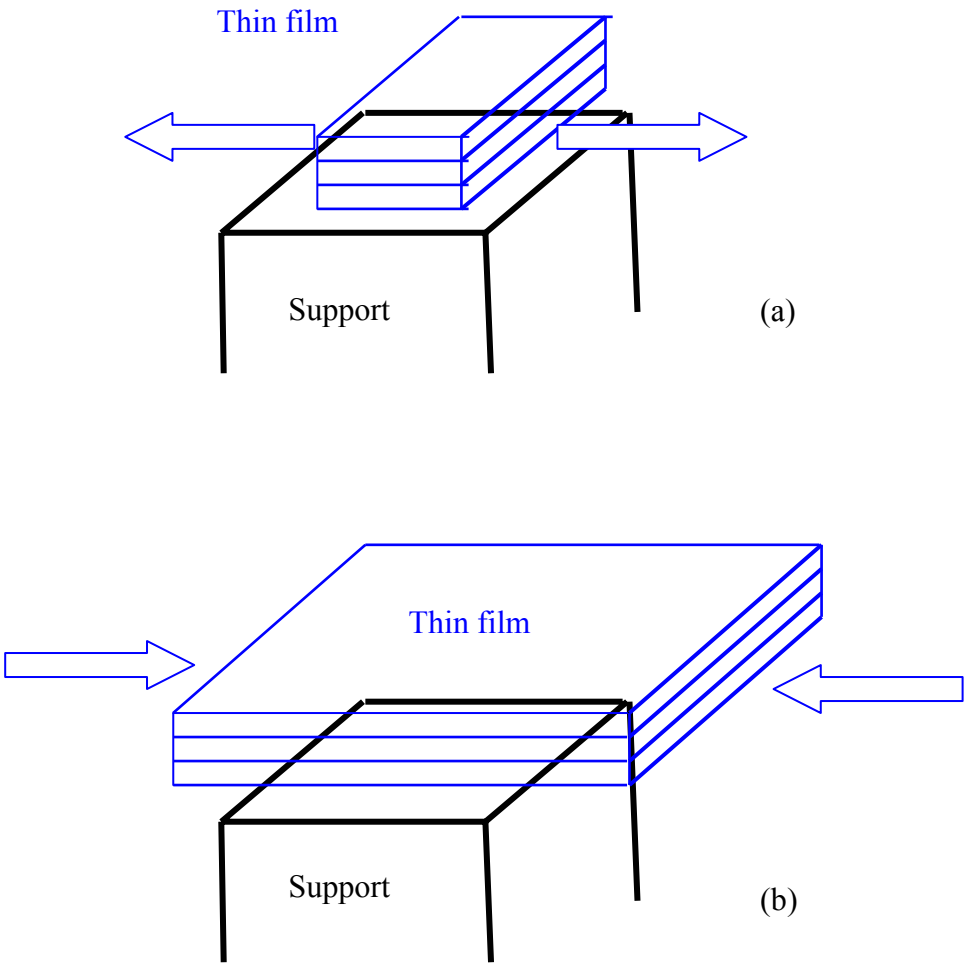

Figure 2.5: Schematic representation of (a) negative, tensile and (b) positive, compressed misfit between thin film and support.

Preliminary calculations, using various trial starting structures have to be performed for each system, since it was observed that the initial strain required to induce adequate amorphization is system dependent. Although the initial strain imposed upon the supported thin film is the main driving force to amorphization, the temperature at which dynamical simulation is performed plays an additional important role. As an example, the procedure can be performed equally at 50K as at 2000K. However, the recrystallization process at 50K is much slower. Essentially, the optimum temperature is one that allows the structure to evolve but that falls short of melting the thin film. This would be detrimental as it would prevent recrystallization and require an additional quenching step [Sayle 2001].

2.8 Extended X-ray Absorption Fine Structure

In recent years advances in theory and analysis methods have revolutionized the technique of Extended X-ray Absorption Fine Structure for local structure determinations. Structural information is most often obtained from the use of X-ray Diffraction (XRD), but it has been realized that techniques based on X-ray absorption spectroscopy, such as Extended X-ray Absorption Fine Structure and X-ray Absorption Near Edge Structure (XANES) may provide important possibilities for structure characterization. For example, many systems that cannot be structurally characterized by XRD due to the presence of microcrystalline structures or amorphous phases are conveniently studied by EXAFS. The phenomenon of Extended X-ray Absorption Fine Structure refers to the oscillation of x-ray absorption coefficient as a function of x-ray energy above threshold. The

physical origin of this phenomenon is due to the final state interference, i.e., the final state is modified by the presence of the surrounding atoms [Azaroff 1963]. EXAFS contains structural information that can be extracted using Fourier-transform techniques. However, the extraction of structural information from EXAFS requires a precise knowledge of the functional behaviour of the x-ray absorption coefficient against incident x-ray energy. EXAFS is a structural technique that originated in 1970's and is now widely used by physicists, chemists and biologists. It offers the potential of providing direct information on the local environments, specifically the bond distances or radii of coordination shells, coordination number and elements in the coordination shell around a particular atom. XRD and EXAFS can be regarded as complimentary techniques since XRD probes structures with long-range order whilst EXAFS is sensitive mainly to the local surrounding of the atom in a system. Therefore a combination of the two techniques offers new possibilities for obtaining a more complete structural description [Clausen et al 1994, 1996, 1998].

2.8.1 EXAFS Applications

The determination of the positional coordinates of major elements within crystalline materials where specific site coordinates or occupancies are not well resolved by XRD alone, EXAFS application is of considerable importance. In such cases EXAFS may provide significant additional information allowing a unique determination of the structure where ambiguities occur in XRD data. EXAFS is highly selective since the edge of various elements in the compound is excited separately. In a binary compound AB the pairs BB are not involved when

the edge of A is studied. EXAFS can be used to analyze dilute systems and in particular to determine chemical impurities. It can also be used provided there is a local radii order, but long order range is not needed. However, the fluctuations in the radial order strongly dampen the signal and generally in disordered media only the first shell is visible. The technique is used to study amorphous substances, glasses, solutions, catalysts and crystal defects.

2.8.2 EXAFS Spectrum

The basic EXAFS experiment involves measuring the X-ray absorption spectrum of a thin sample as a function of X-ray energy. This involves the measurement of the incident X-ray, I_o, and the transmitted intensity, I_t, and evaluating the coefficient, μ from the equation

$$\mu = \ln \frac{I_0}{I_t} \tag{2.63}$$

A well resolved EXAFS spectrum yield (a) the distance between the excited atom and its neighbours, $\Delta r \approx 0.01$ Å., (b) the number N of nearest-neighbour scatters, $\Delta N \approx 0.2$ to 0.5 and (c) an estimate of the fluctuations in the values of R_i, $\Delta\sigma \approx 0.01$ Å. Since the coordination number is strongly coupled to Debye-Waller factor its determination is less accurate. The attenuation of X-ray by matter obeys the equation

$$I_t = I_0 e^{-\mu x} \tag{2.64}$$

where I_t is the intensity after transmission through the sample, I_0 is the intensity of the incident ray , μ is the X-ray absorption coefficient of the material and x is

the thickness of the material. X-rays pass right through the sample at low energies and μ becomes close to zero. As the energy is increased a point where the X-ray has sufficient energy to eject an electron from the atoms of one of the elements in the sample is reached. The electron is an inner core electron either K or L shell. The point where there is a sharp rise in u, is referred to as the absorption edge and X-ray energy $h\nu$ is equal to the binding energy of the electron in its initial state. Increasing the X-ray energy further does not change absorption edge since the extra energy is transformed into the kinetic energy of the photoelectron. The adsorption spectrum is predicted to be a simple step function and the final energy state E_f of the photoelectron is given by

$$E_f = E - E_b \tag{2.65}$$

where E_b is the binding energy and E is the X-ray energy given by

$$E = h\nu \tag{2.66}$$

The equation for the absorption spectrum is simply the kinetic energy and linearly depends on $h\nu$. Figure 2.4 shows a typical EXAFS spectrum. The EXAFS spectrum is divided into three regions, that is, the pre-edge region, near-edge structure (XANES) and EXAFS structure. The near-edge structures are the oscillations extending over around 50eV and EXAFS structure extending out at about 1000eV beyond the edge. The pre-edge features originate from the excitation of electrons from a core level to an outer level. They vary in terms of position, height and breadth as the local symmetry and oxidation state of the atom changes. An example of EXAFS spectrum is shown in figure 2.6.

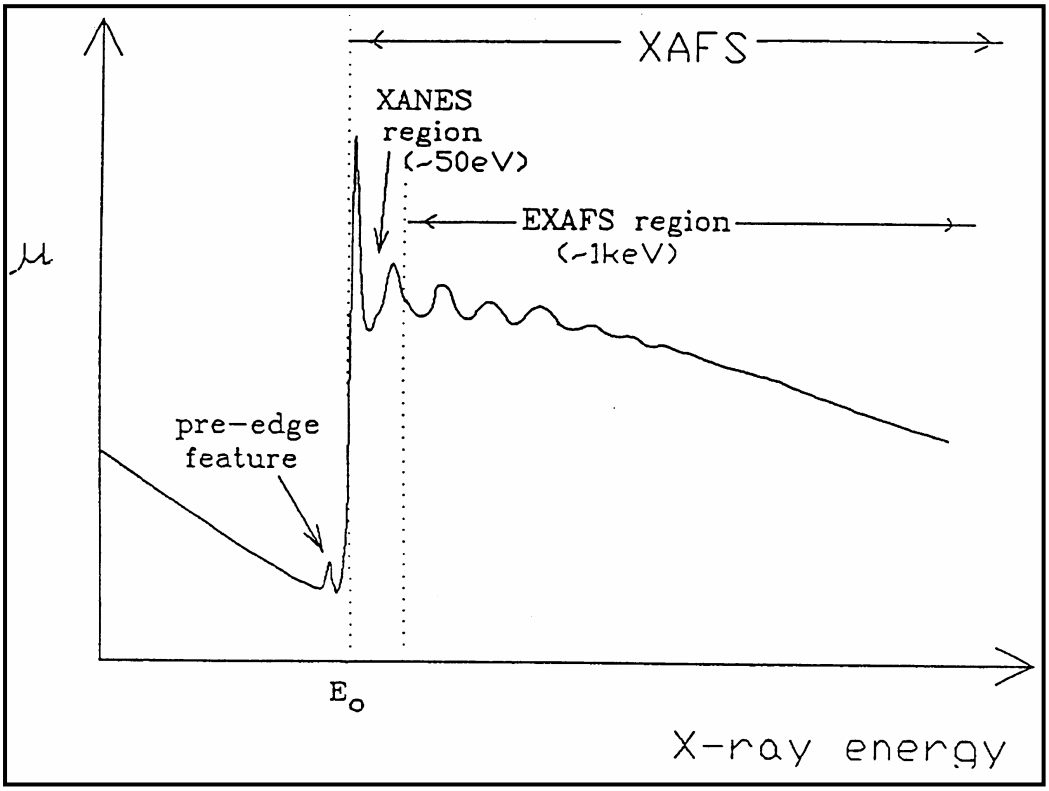

Figure 2.6: X-ray absorption spectrum from a condensed phase sample

EXAFS spectrum originates from the explanation that follows. An electron is a quantum mechanical particle having particle properties and when it moves out of the excited atom it appears as a spherical wave. When the wave encounters a neighbouring atom it is reflected back on itself and the backscattered wave undergoes an interference with outgoing wave. The interference is either constructive or destructive depending on the distance between the excited atom and the scattering atom. Thus, the intensity of the oscillations depends on the atom type acting as the backscatterer, where higher atomic weight atoms produce more intense oscillations and the number of backscattering atoms. As the energy varies, the wavelength of the electron also varies and the interference passes through constructive, destructive, constructive, destructive, etc. This gives rise to

oscillations in the probability of the absorption process and hence oscillations in μ. An illustration of EXAFS origin is shown in figure 2.7.

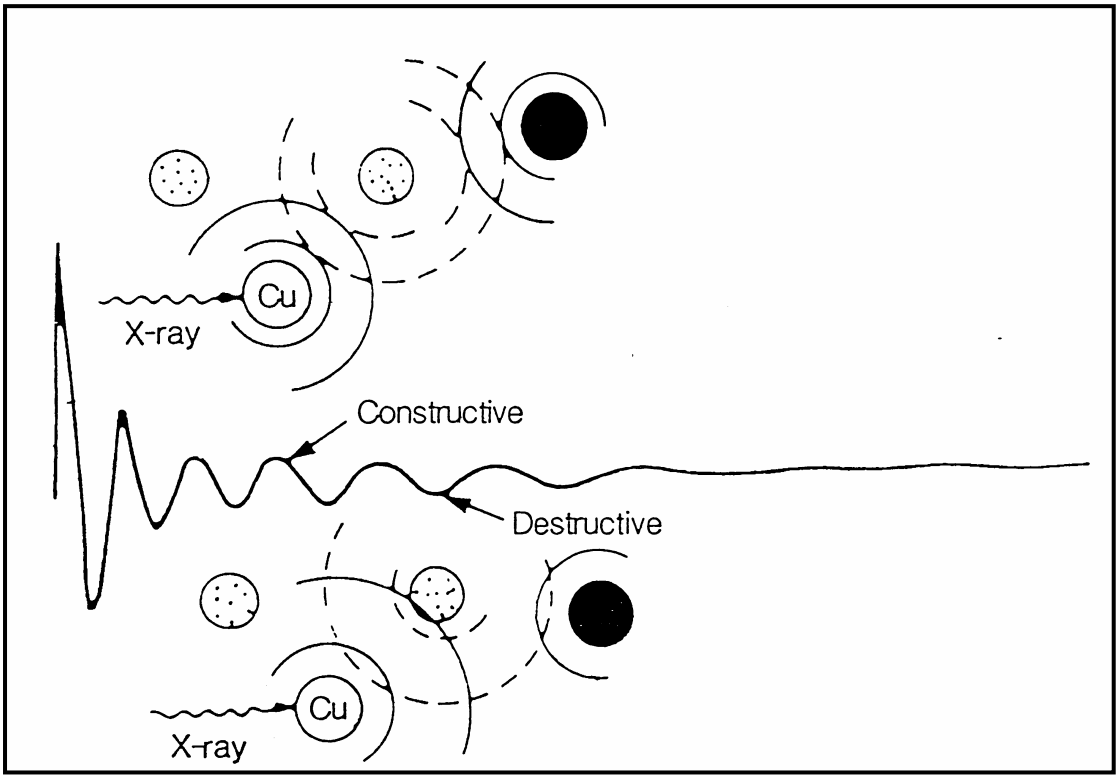

Figure 2.7: Schematic representation of the origin of EXAFS

2.8.3 The EXAFS equation

The oscillations $\chi(k)$ arise from the backscattering of the photoelectron from the atoms around the excited central atom. The neighbouring atoms are considered to be in a series of shells going out of the central atom. The EXAFS equation is given by

$$\chi(k) = \frac{\Delta\mu}{\mu_0} \tag{2.67}$$

$$\chi(k) = \sum_j \frac{N_j}{kr_j^2} \left| f_j(k,\pi) \right| \sin\left(2kr_j + \psi_j + 2\delta\right) \tag{2.68}$$

Thus,

$$\chi(k) = -\sum_j \frac{N}{kr_j^2} \left| f_j(\pi) \right| e^{\frac{-2r_j}{\lambda}} e^{-2\delta_j^2 k^k} \sin\left(2kr_j + \psi_j + 2\delta\right) \qquad (2.69)$$

where N_j is the number of atoms in the jth shell, all of the same type, at a distance r_j from the central atom. The first term $\frac{N_j}{kr_j^2}$ explains that the more the atoms in a shell and closer they are to the central atom, then the greater is the amplitude of the backscattering. The term $\left| f_j(k,\pi) \right|$ is the backscattering factor for the elements in the jth shell. Backscattering factor varies with atomic number and the variation is used to identify the atoms in the EXAFS spectroscopy. $e^{-2\delta^2 k^2}$ is the Debye-Waller factor and δ_j^2 is the mean square variation in r_j. It varies from thermal vibrations of the atoms and/or due to the static disorder leading to differences in bond lengths, $e^{\frac{-2r_j}{\lambda}}$ is the term that allows inelastic scattering of the photoelectron, λ is the mean free path of the electron, $\sin\left(2kr_j + \psi_j + 2\delta\right)$ is the sine function that depends on kr_j, the bigger r_j the more closely spaced are the oscillations. However, ψ_j and 2δ are the phase shifts terms. The photoelectron wave suffers these phase shifts as it interacts with the electrons of the scattering atoms ψ_j and the central atoms 2δ. The most important use of the EXAFS equation is that Fourier transform with respect to $\sin(2kr)$ or e^{-2ikr}, yields the radial distribution functions (RDFs) in real space with peak areas proportional to N_j. The phase factors maybe obtained either from theoretical calculations or fitted from the EXAFS of a compound chemically similar to the sample with known r_j and N_j. If r_j and N_j are known, the radial distances can be determined.

Chapter 3

Ab initio Calculations

3.1 Introduction

In this chapter we report the results based on *ab initio* calculations. DFT has provided a convenient first principle framework for studying the structural and electronic properties of a wide range of materials. The main aim of this chapter is to present a theoretical study of electronic and structural properties of pyrolusite and ramsdellite polymorphs of MnO_2. Brief discussions on the methods used are given and finally the results are presented. The total geometry optimization is performed using the computer code CASTEP (Cambridge Serial Total Energy Package) [CASTEP Users Guide 1998]. Calculated structural (lattice parameters and equation of states) and electronic properties (density of states, charge differences and deformations) calculated are presented. The charge deformations give information on the type of bonding in the systems.

3.2 Methodology

Plane wave pseudopotential (PWP) method is used to perform calculations on pyrolusite and ramsdellite structures. Within the Density Functional Theory,

LSDA simulation was performed. In PWP plane wave basis set is used for expanding electronic states. In order to reduce the number of plane waves required, chemically inactive core electrons are effectively replaced with ultrasoft pseudopotentials, usp [Vanderbilt 1990 and Kresse et al 1994], which were taken from the CASTEP database in this work. There are two parameters that affect the accuracy of the calculations, that is, kinetic energy cut-off, which determines the number of plane waves in the expansion and the k-points used for the Brillouin zone integration. Therefore it is very important to ensure that appropriate energy cut-off and k-points used.

3.2.1 Plane-Wave Pseudopotential

A theoretical background of this method is fully discussed in Chapter 2. The lattice parameters, pressure-volume (PV) dependences of the equation of states (EOS) and the bond lengths for pyrolusite and ramsdellite structures are predicted using the PWP method. Geometry optimization was achieved by varying the hydrostatic pressure and allowing the lattice to relax using Broyden-Fletcher-Goldfarb-Shano (BFGS) minimization method. Electronic minimization was performed using band-by-band conjugate gradient (CG) method. Pyrolusite model is tetragonal, that is a = b, ≠ c; α= β = γ = 90° and has the space group $P4_2/mnm$ whereas ramsdellite is orthorhombic, that is a ≠ b ≠ c; α = β = γ = 90° and has the space group *Pbnm* [Miura et al 1990] and each Mn^{4+} atom is surrounded by six O^{2-} atoms. Figures 3.1 and 3.2 show the crystal structures of pyrolusite and ramsdellite respectively. In figure 3.1, oxygens have a primitive tetragonal packing [West and Bruce 1982] and in figure 3.2 oxygens have the same packing

arrangement based on a combination of body centred tetragonal packing [David et al 1983] and hexagonal close packing [MacLean and Tye 1996].

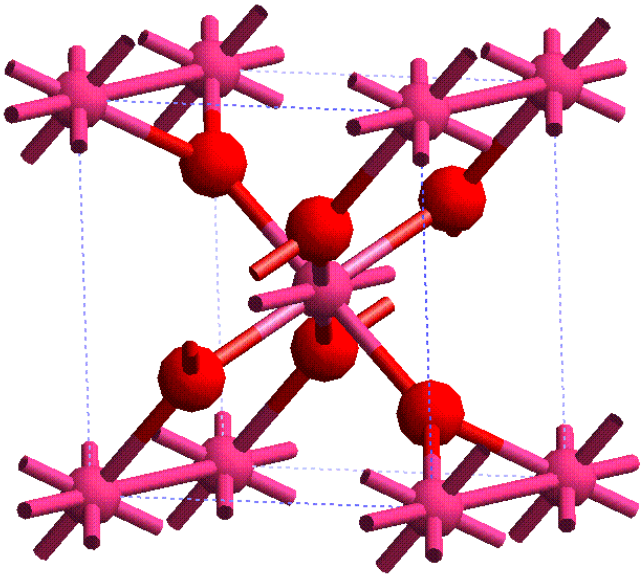

Figure 3.1: Pyrolusite crystal model.

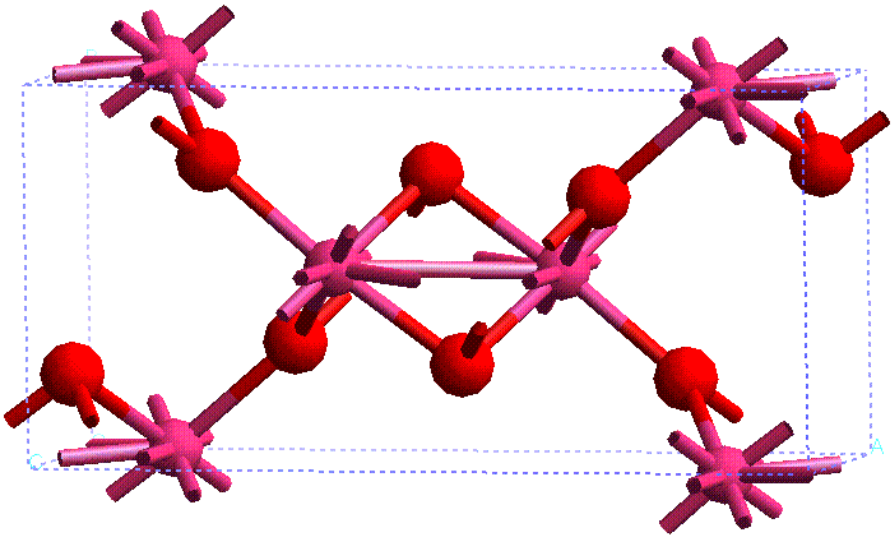

Figure 3.2: Ramsdellite crystal model.

3.2.2 K-points sampling

The Monkhorst-Pack scheme of the k-points sampling was used to select an optimal set of special k-points of the Brillouin zone such that the greatest possible accuracy is achieved from the number of k-points used [Hohenberg and Kohn 1964, Kohn and Sham 1965]. The number of k-points was determined by running SCF calculations for different k-points. The k-points that gave the minimum total energy of the system was chosen and used in all calculations. In this work, 4 x 4 x 8 and 2 x 4 x 8 were obtained for pyrolusite and ramsdellite respectively.

3.2.3 Energy cut-off

Energy cut-off is the important parameter in PWP calculations because it determines the number of plane waves required in a calculation. Calculations on different values of energy cut-off were performed until a constant minimum energy is obtained, thus the energy becomes stable and the cut-off energy that corresponds to the minimum total energy is recorded. For pyrolusite and ramsdellite, the energy cut-off used is 600eV. The graph of total energy versus energy cut-off for pyrolusite is shown in figure 3.3. The cut-off energies correspond to Fast Fourier Transform (FFT) grid of 30 x 30 x 20 and 74 x 52 x 24 for pyrolusite and ramsdellite respectively. The total number of plane waves used is 1000 for pyrolusite and 2000 for ramsdellite. Pullay correction on forces was included to compensate the energy cut-off. In all optimizations, the tolerance in total energy and pressure change before self-consistency was 2×10^{-5} eV/atom and 0.1GPa respectively. The RMS tolerance for the atoms displacement was restricted to 0.001Å. Within the LSDA, spin of 6 and 12 were used for pyrolusite and ramsdellite respectively.

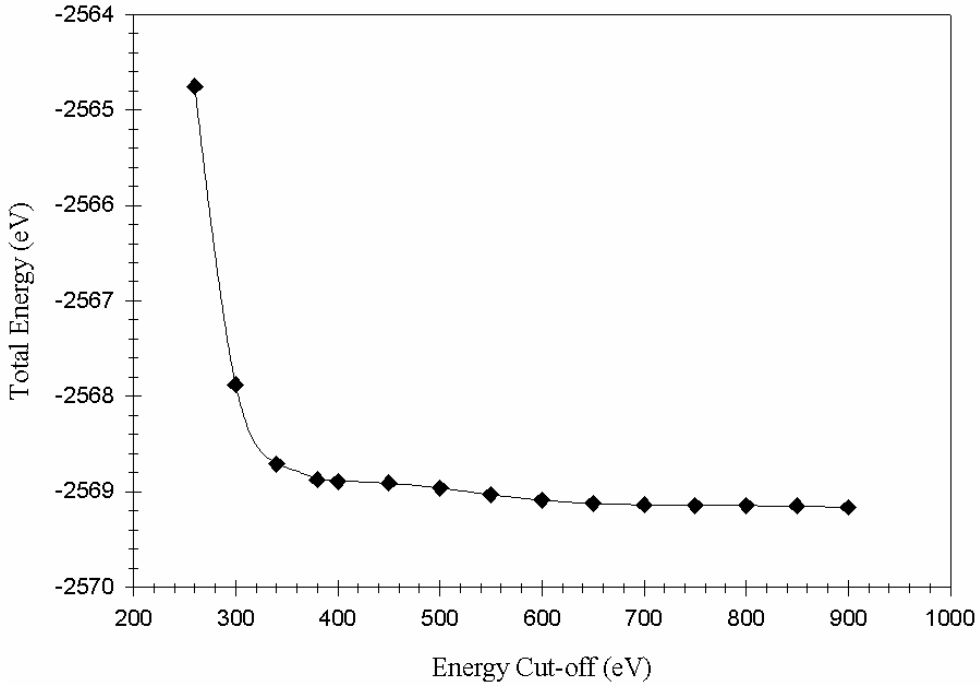

Figure 3.3: Energy versus energy cut-off graph for pyrolusite structure.

3.2.4 Equation of state

At a given volume the positions of the atoms are determined by minimizing the forces on the ions, and the unit cell edges by equalizing the stress on the cell. Calculations were performed for various pressures ranging from -20GPa to 50GPa in steps of 5. The calculations were considered converged when the residual forces were less than $0.05 eVÅ^{-1}$, the displacement of atoms during the geometry optimization steps were less than 0.001Å and the residual bulk stress was less than 0.1GPa.

3.3 Results and Discussions

Structural and electronic properties of pyrolusite and ramsdellite are presented in this section. The effect of pressure on the systems is discussed and particular, the equation of states, density of states and charge differences, at pressures ranging from -20GPa to 50GPa, were determined.

3.3.1 Structural Properties

Prediction of the geometric and electronic structures of a solid requires a calculation of the total energy of the system and subsequent minimization of that energy with respect to nuclear coordinates and electronic coordinates.

3.3.1.1 Pyrolusite Structural Parameters

The results of the equilibrium lattice parameters and bond lengths for pyrolusite are listed in Table 3.1. The results are based on LSDA forms of exchange correlation interaction using the computer code CASTEP. The lattice parameters and bondlengths were calculated for each hydrostatic pressure. Figure 3.4 shows the bond lengths of pyrolusite as a function of pressure. Bond lengths between Mn-O and O-O are shown. The application of pressure to the system shows a relative shortening of the bond lengths. At a low pressure, 0GPa, the bond lengths are in reasonable agreement with the experimental values. As expected, they are reduced significantly at higher pressure. The Mn-Mn bond length decreases more rapidly than the one for O-O interactions. The lattice parameters are reduced as the pressure is increased. The total energy minimization gives results which are in good experimental as they are listed in Table 3.1.

	Lattice Parameter a (Å)	Lattice Parameter c (Å)	Volume V (Å^3)	Bond Length Mn-O (Å)	Bond Length O-O (Å)	Bulk Modulus GPa
Calculated	4.52	3.00	61.54	1.95	2.76	156.9
Experimental*	4.41	2.86	55.81	1.87	2.68	

Table 3.1: Pyrolusite structural properties obtained for LSDA and experimental values by *[Brenet 1950].

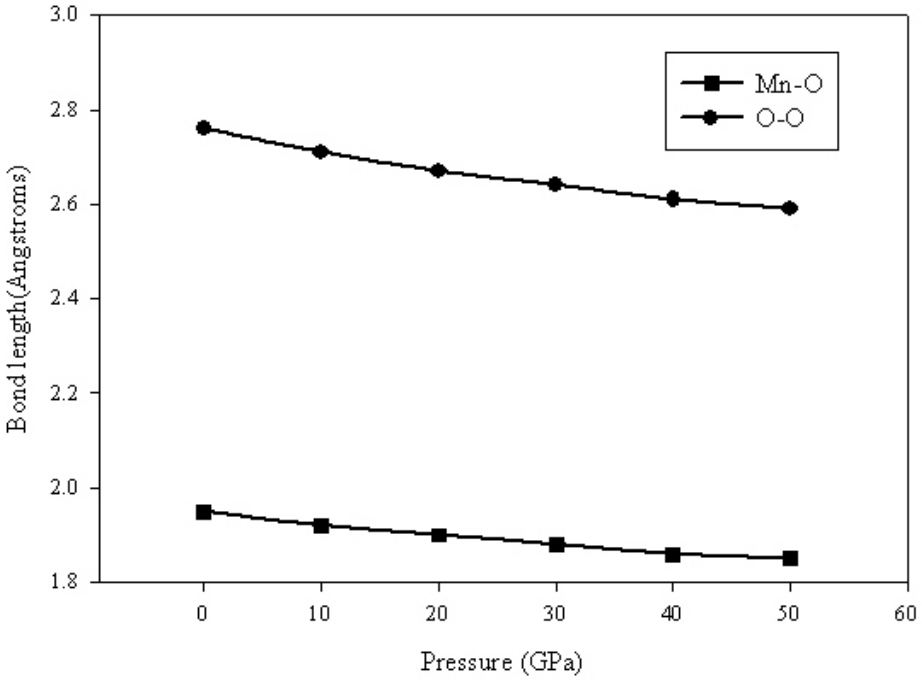

Figure 3.4: Pyrolusite LSDA bond length versus pressure graph.

3.3.1.2 Pyrolusite Equation of State

The equation of state (EOS) of pyrolusite is given in figure 3.5 showing the LSDA simulation results. Compressibility of pyrolusite is illustrated by the change in relative volume with pressure. The bulk modulus of the system is defined by equation 3.1 below:

$$\overline{B} = -V_0 \frac{\partial P}{\partial V} \qquad (3.1)$$

The bulk modulus was deduced from figure 3.5 by fitting the Murnaghan's third order equation of state and it was found to be 156.9 GPa. Presently there are no experimental results to compare with.

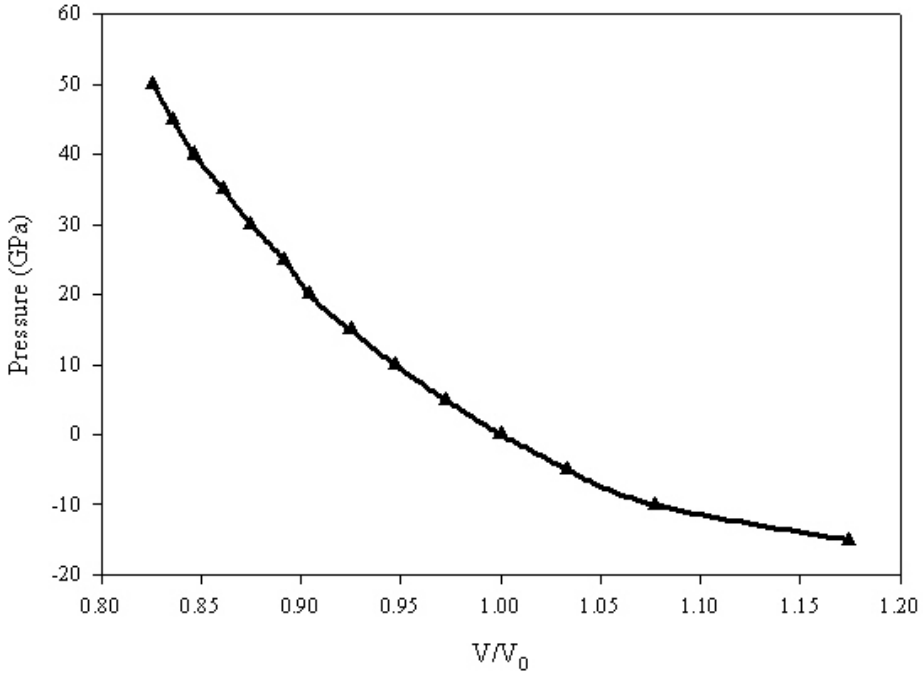

Figure 3.5: Pressure versus V/V_0 graph for pyrolusite.

3.3.1.3 Ramsdellite Structural Parameters

Prediction of the volume of a system indicates how accurate the system is being modelled. The structural properties of ramsdellite structure at 0GPa are listed in Table 3.2 showing the lattice parameters, bond lengths and bulk modulus. The results were obtained using the Local Spin Density Approximation. The approximation underestimated the total volume of the system. The system relaxes

more along the b-direction. The atoms are moving out along this direction. The results are within the acceptable margins of error. The Mn-O and O-O bond lengths are well reproduced. Figure 3.6 shows the equation of state plot for ramsdellite, from which the bulk modulus was deduced. The bulk modulus is lower than that predicted for the pyrolusite structure.

	Lattice Parameters				**Bond Lengths**		**Bulk Modulus (GPa)**
	a (Å)	**b (Å)**	**c (Å)**	**V (Å^3)**	**Mn-O (Å)**	**O-O (Å)**	
Calculated	9.573	4.055	2.876	111.62	1.884	1.881	73.07
Experimental*	9.355	4.479	2.854	119.55			
Experimental**	9.37	4.467	2.850	119.29	1.915	1.903	

Table 3.2: Structural parameters for ramsdellite structure, calculated and experimental by *[Abou-El-Sherbini 2002], **[Konddrasev 1951].

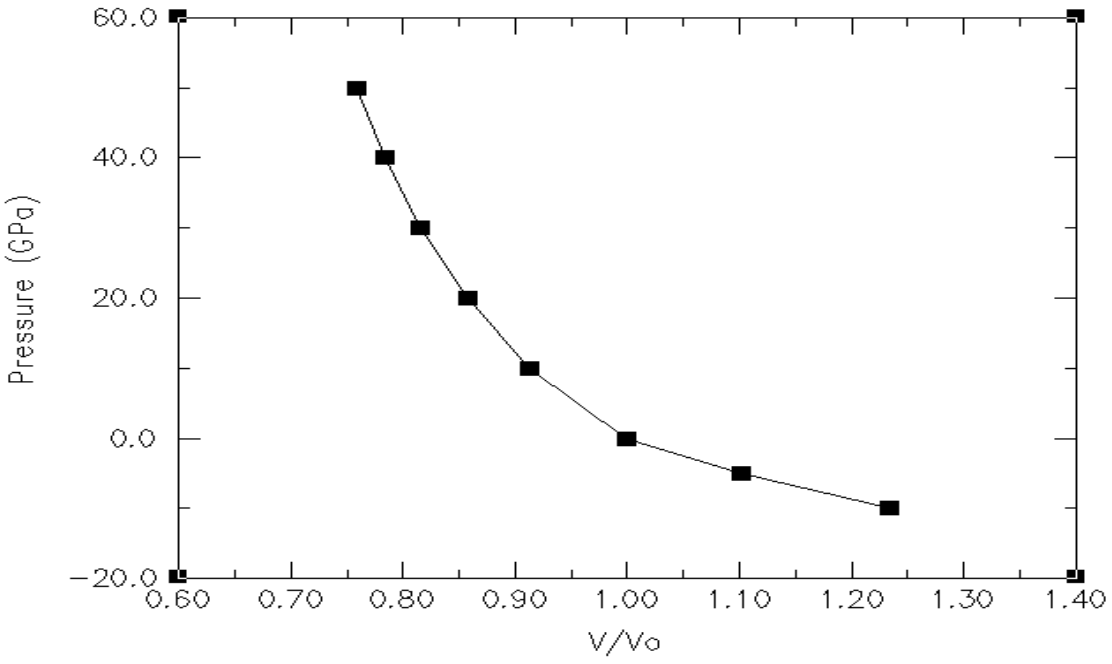

Figure 3.6: Pressure versus V/V_0 graph for ramsdellite

3.3.2 Electronic Properties

The electronic properties of a material help in understanding the classification of the material under three main categories, i.e., metals, semiconductors and insulators. The type of material is determined by the size and existence of the energy gap between the highest occupied orbitals (conduction band) and the lowest unoccupied orbitals (valence band). In metals, the occupied and unoccupied orbitals overlap, therefore no gap between the bands is noted. In semiconductors and insulators the gap is present which tends to be larger for insulators.

3.3.2.1 Charge density differences

Charge density differences (crystal minus superposition of atoms) are of immense interest since they inform us on the nature of bonding between the oxygen and manganese atoms and also play a major role in determining the electronic properties of MnO_2. Some features of charge density differences can be linked to the information obtained from the total and partial density of states. The charge density differences for pyrolusite are shown in figures 3.7 and 3.8 for the pressure at 0GPa and 50GPa respectively. The magnitude of charge is shown by different colours with the red and blue indicating gain and loss respectively. It is noted that four lobes of Mn have depleted charge (blue). Two lobes with charge gain are seen around Mn. Since charge differences show how charge is shared among the atoms during bonding, it is evident that charge is transferred from O^{2-} to Mn^{4+}. At 0GPa, relatively more covalent bond is noted between oxygen and manganese with the polarization of the oxygen electron cloud towards manganese. At 50GPa the Mn-O

bonds appear to be ionic, with the oxygen charge more spherically concentrated on the oxygen 2p lobes.

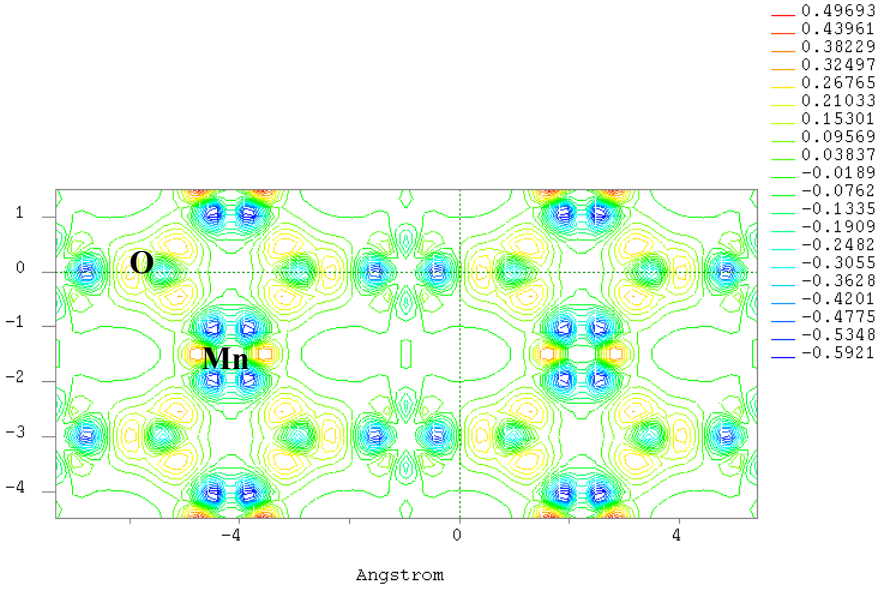

Figure 3.7: Charge density difference for pyrolusite at 0GPa.

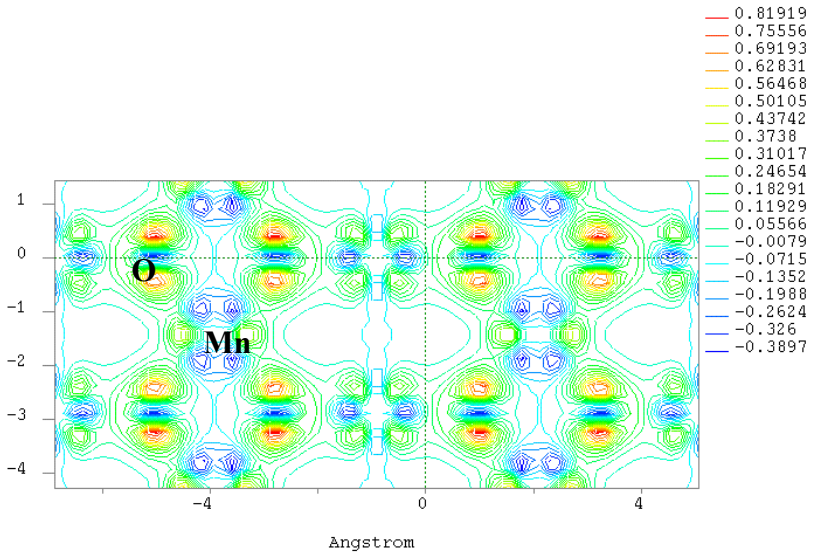

Figure 3.8: Charge density difference for pyrolusite at 50GPa.

The charge density differences for ramsdellite are shown in figures 3.9 and 3.10 for 0GPa and 50GPa respectively. At 0GPa, the charge differences for ramsdellite appear to be a mixture of covalent and ionic bonding between manganese and oxygen. The directionality of the oxygen charge distribution indicates the presence of covalent bonding. It is noted that at both pressures there is ionicity between manganese and oxygen atoms.

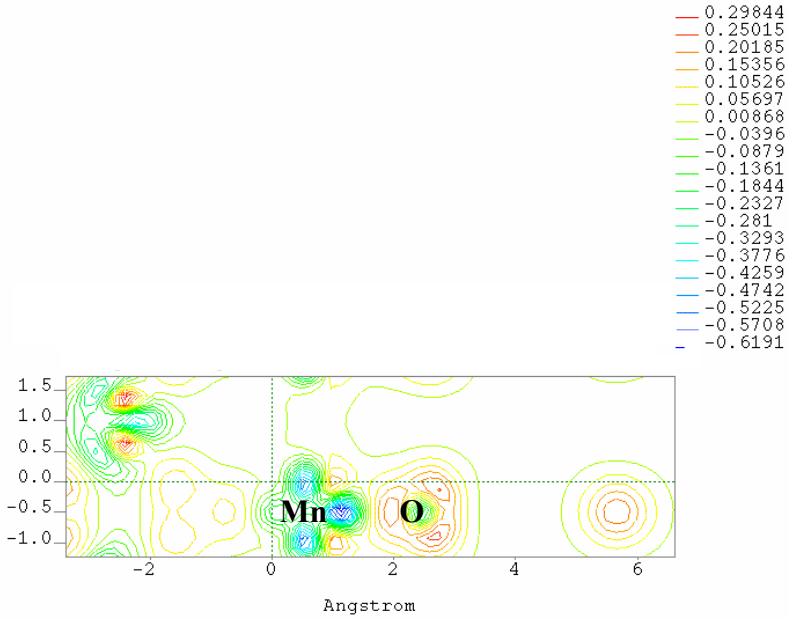

Figure 3.9: Charge density difference for ramsdellite at 0GPa.

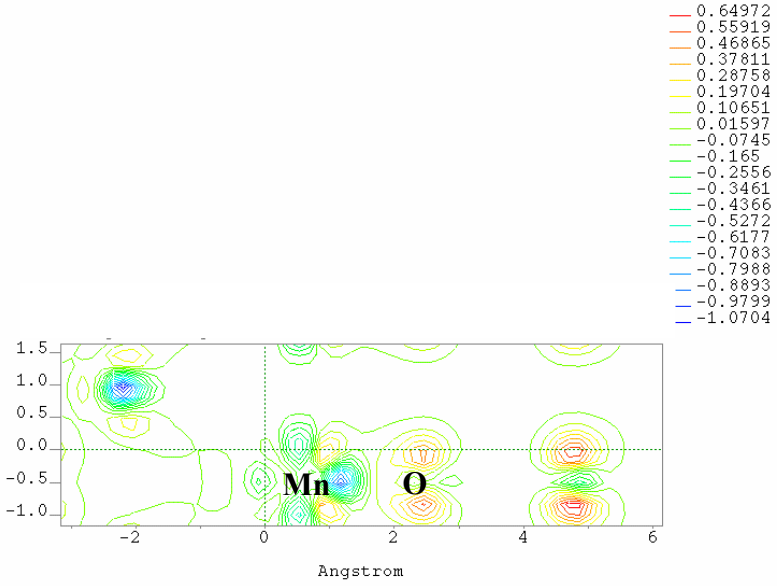

Figure 3.10: Charge density difference for ramsdellite at 50GPa.

3.3.2.2 Density of states

Figures 3.11-3.14 give the partial density of states (PDOS) for pyrolusite and ramsdellite structures. PDOS gives the atomic contributions of a material. Considering the projections over atomic orbitals, the sequence of peaks appearing from the valence band to the conduction band can be interpreted as follows.

For pyrolusite, the first double peak in the valence band corresponds to 5d(Mn) and also the first maximum peak in the conduction band (figure 3.11-3.12 top). The first peak at approximately -14eV in figure 3.11-3.12 bottom is 2s(O). This is followed by a broad peak that corresponds to 2p(O). There is small contribution of s and p orbitals for manganese in the valence band and a strong contribution in the conduction band. The valence band is dominated by the 5d contribution. Oxygen shows no d-orbital contribution, it is dominated by s and p orbitals in the low energy band and a small contribution of p orbital in the high energy band.

The pyrolusite system appears to be metallic at 0GPa and becomes an insulator under 50GPa. The band gap at 50GPa is estimated as 2.8 eV for pyrolusite. This behaviour tends to agree with the observation noted on the charge density differences where the covalent and ionic bondings are dominant at 0 and 50GPa respectively.

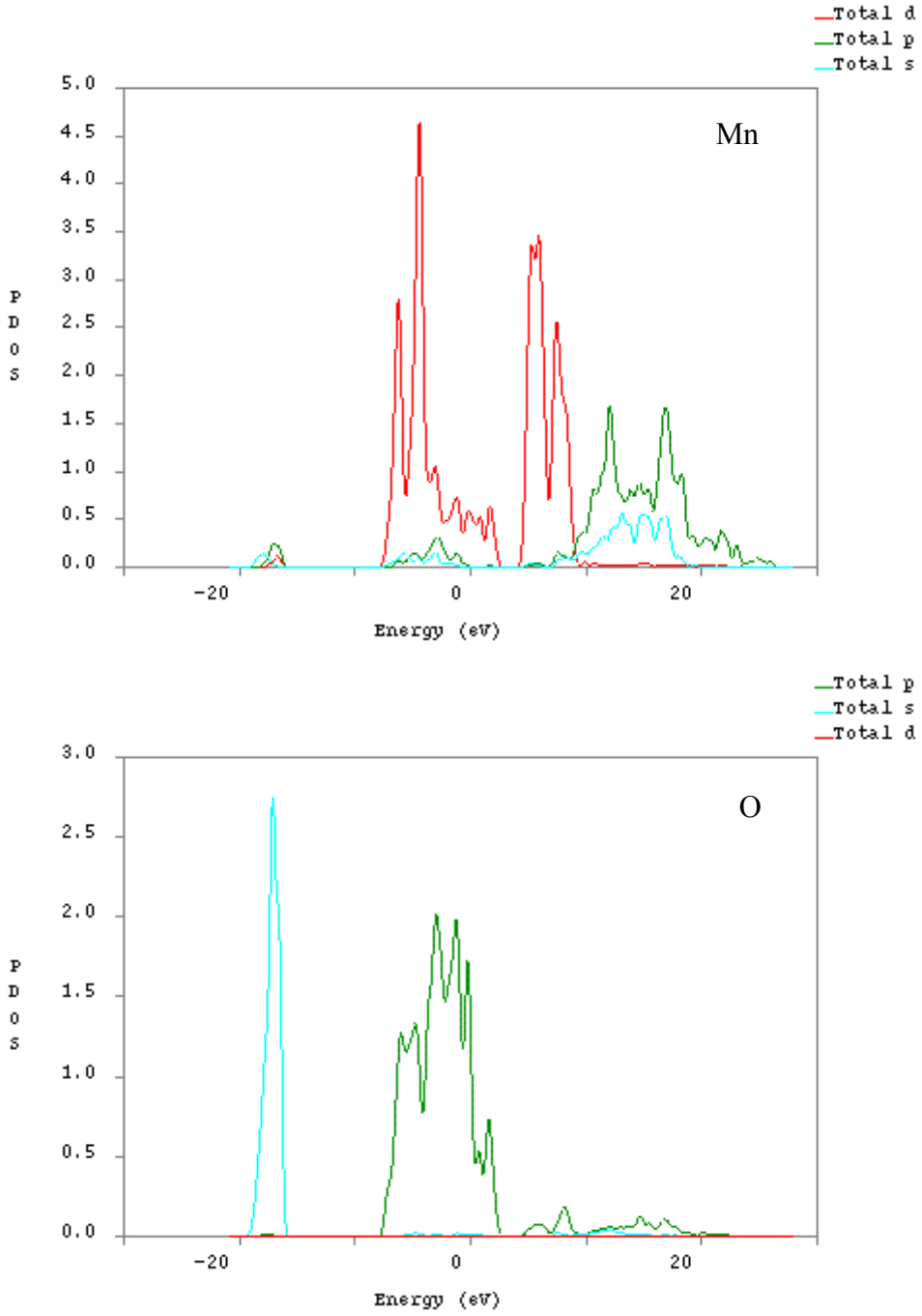

Figure 3.11: PDOS for pyrolusite at 0GPa obtained using LSDA Mn at the top and O at the bottom.

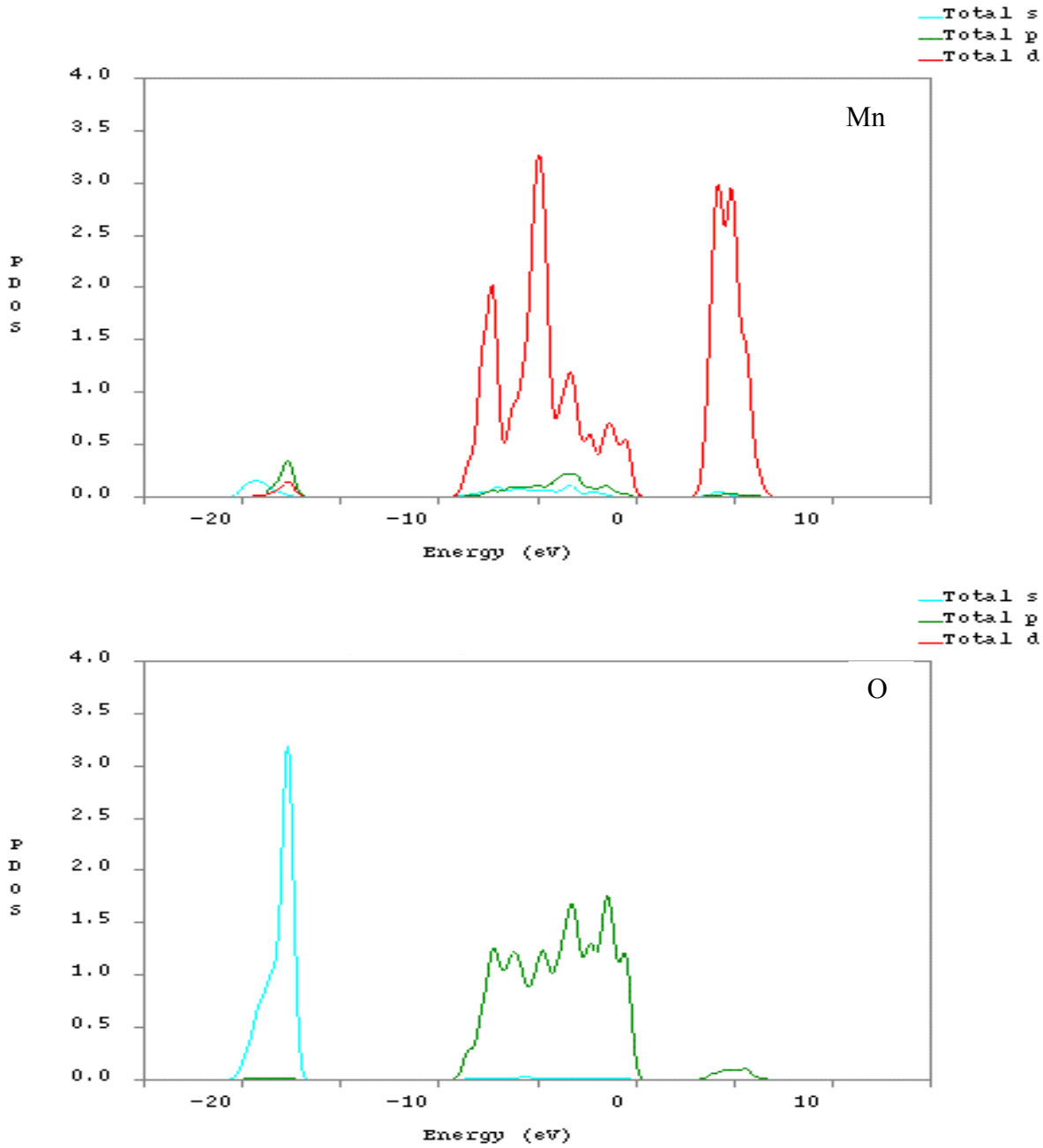

Figure 3.12: PDOS for pyrolusite at 50GPa, Mn at the top and O at the bottom.

For ramsdellite, at approximately -17eV, we note a small contribution of all the orbitals. The Mn 5d orbital dominates the contribution in both the valence and conduction bands (figure 3.13-3.14 top). The bottom PDOS show peaks of non-bonding O s orbital at energy of -17eV. It is followed by a wide band with low

contribution from the p orbital. The low contribution of O p orbital is noted at the top of the valence band and lastly a very small contribution in the conduction band. The figures show that the system is an insulator at both 0GPa and 50GPa. Application of pressure to the system results in no closure of the gap as indicated in the PDOS plots. However, it reduces the band gap from 4.8 eV at 0 GPa to 2.5 eV at 50GPa respectively. Hence ramsdellite remains in an insulating state.

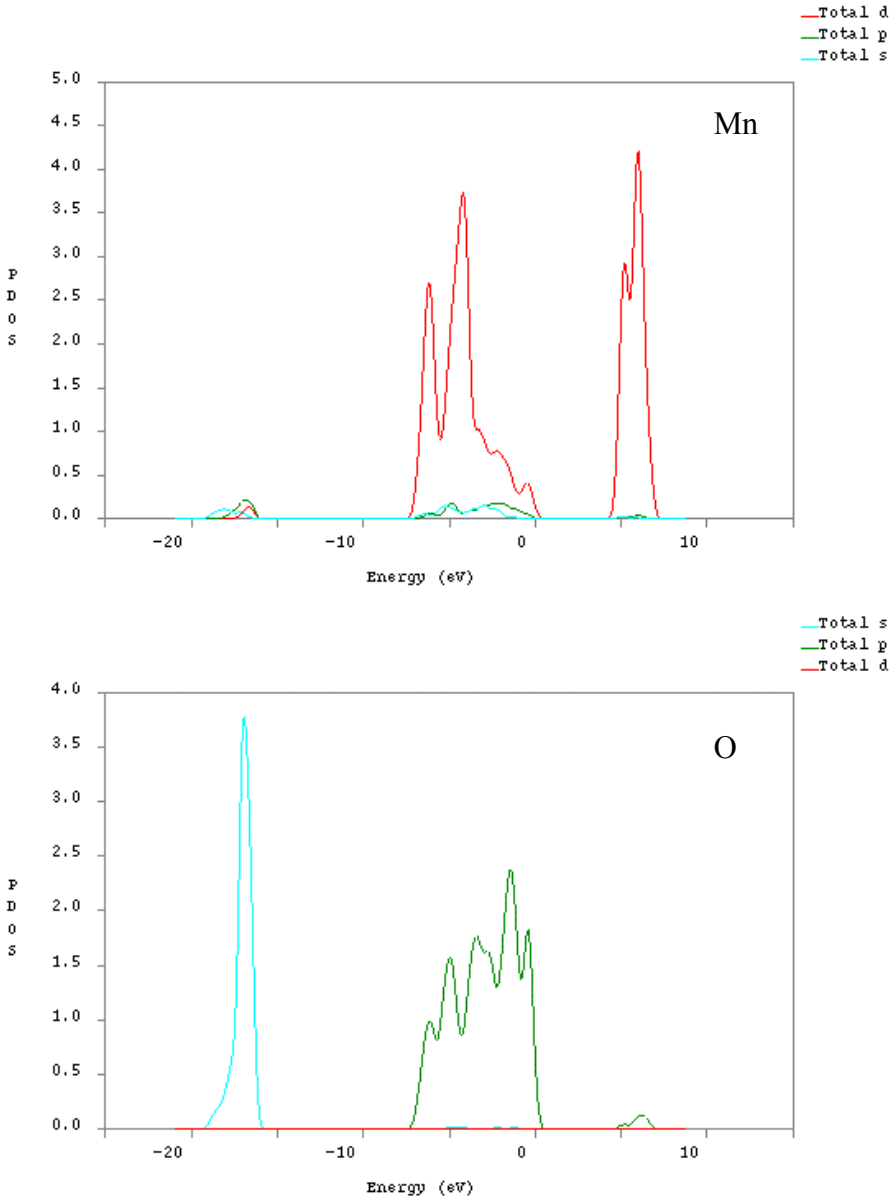

Figure3.13: PDOS for ramsdellite at 0GPa, Mn at the top and O at the bottom.

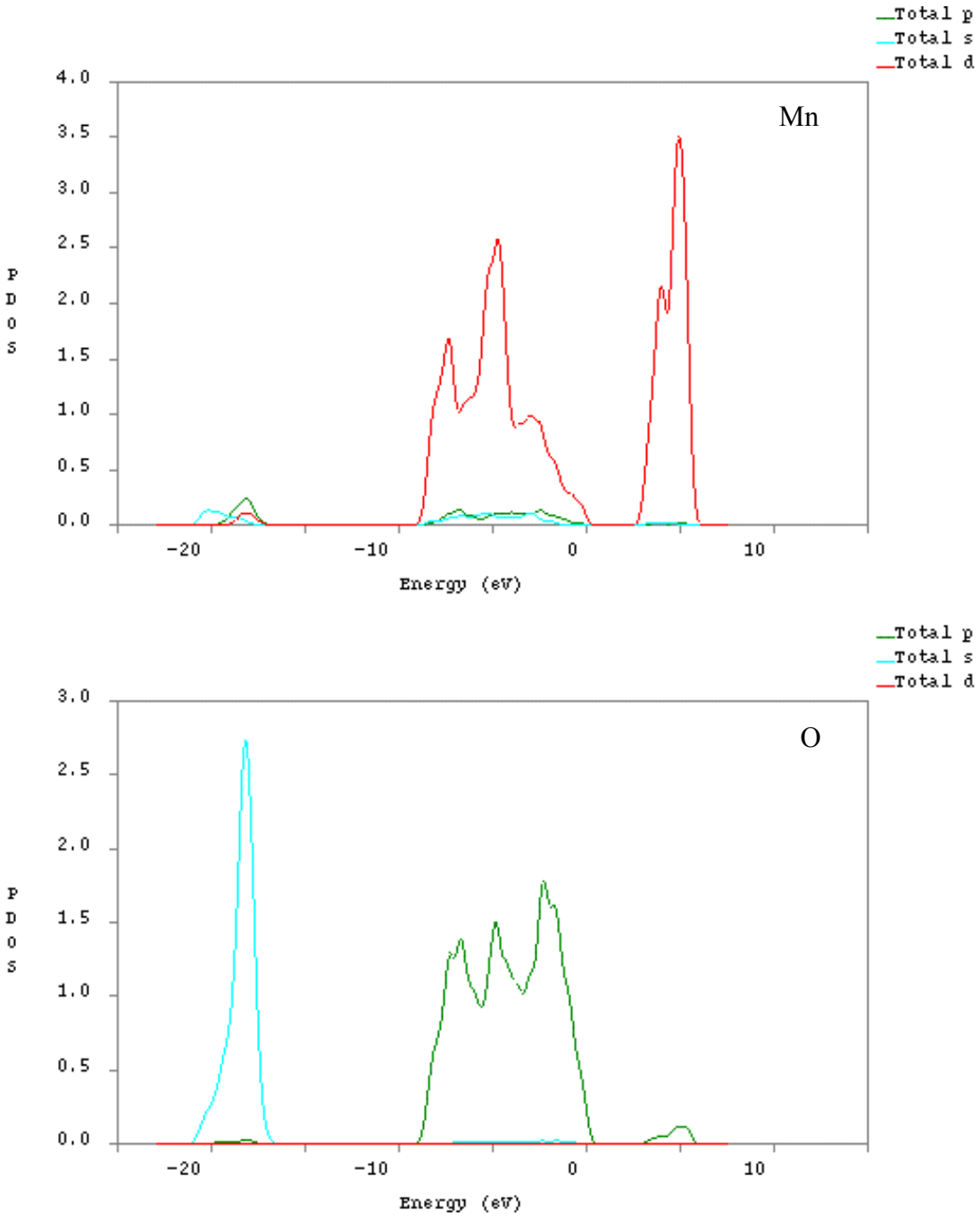

Figure 3.14: PDOS for ramsdellite at 50GPa, Mn at the top and O at the bottom.

3.4 Conclusion

The ab initio quantum mechanical method treatment has been applied successfully to the study of structural and electronic properties of pyrolusite and ramsdellite systems. We have determined a suitable energy cut-off, which is 600 eV, for both systems and the k-points 4 x 4 x 8 for pyrolusite and 2 x 4 x 8 for ramsdellite. We have also shown the P versus V/V_0 curve from which the bulk moduli has been determined. The results will be compared with the experimental results once available. The equation of state has been calculated for each of the systems involved, pyrolusite and ramsdellite, including the structure optimization and derivation of the bond lengths changes with pressure up to 50GPa. The charge density difference and the partial density of states showed the nature of bonding in both compounds.

Chapter 4

Energy Minimization

4.1 Introduction

In this chapter, an energy minimization technique is used to study the surfaces of pyrolusite and ramsdellite structures. Atomistic simulation methods can be used to calculate the forces and energies of a particular system. Low index Miller planes are the common surfaces of a crystal and generally they have the lowest surface energies, that is, they are the most stable surfaces. The results presented are based on Born model of solids, and yield surface energies, surface structures, surface stabilities and surface reactivity of pyrolusite and ramsdellite structures. The technique uses known data in the form of interatomic potentials, which include the long-range interactions (Coulombic and Van der Waals) and short-range interactions (Lennard-Jones and Buckingham).

Classical calculations are far more efficient and less computationally demanding, allowing for a larger number of atoms to be considered. Eventually, when processing power has substantially increased, quantum mechanical simulations will be much more amenable to larger systems.

4.2 Methodology

The calculations were carried out using atomistic simulation techniques based on Born model of solids [Born and Huang 1954], in which the ions interact via a long-range Coulombic interactions, calculated using the Ewald summation [Ewald 1921], and short-range parameterized interactions. The surface energies and structures of pyrolusite and ramsdellite were obtained using the computer code METADISE [Watson et al. 1996]. The code is designed for modelling dislocations, interfaces and surface energies. The crystal is divided into two blocks (block I and block II), each consisting of two regions, region I and II. Region I contains ions close to the interface and are allowed to relax whereas region II contains ions further away from the surface and are held fixed. During the minimization process, the ions in region I are allowed to relax relative to region II. Region I and II need to be sufficiently large for the energy to converge. In this work Region I consists of six basis lattice units whereas Region II consists of sixty repeated units. The surfaces were generated from the bulk structures of pyrolusite and ramsdellite. The surfaces were minimised using the conjugate gradient and Newton-Raphson methods (see Chapter 2). The energies of the block are the sum of the energies of the interaction between the ions. The surface energy, E, of a particular Miller index is given by

$$E = \left[\frac{E_{surface} - E_{bulk}}{A} \right] \tag{4.1}$$

where $E_{surface}$ is the energy of the surface block of the crystal, E_{bulk} is the energy of the same number of bulk ions and A is the surface area. It is necessary to ensure that a sufficient number of layers are modelled so that the energy of the

block has converged. In the calculation of a particular Miller index there may be multiple unique repeat units. The surfaces are classified according to the scheme identified by Tasker [1979] (Appendix C), i.e., Type I where the surface unit cell has cations and anions in stoichiometric ratio, Type II is comprised of a stack of charged planes where the repeat unit has no dipole moment perpendicular to the surface and Type III has a stack of charged planes where the repeat unit cell has a dipole moment perpendicular to the surface. However, the Coulombic sum for such a surface cannot be evaluated, as it is divergent [Bertant 1958], and if such surfaces are to be studied then the surface must be reconstructed such that the dipole is cancelled [Olivier et al. 1993]. Thus for each surface different terminations are identified and if it is a Type III, the surface is further reconstructed to remove the dipole moment perpendicular to the surface. If there are multiple unique repeat units, then the lowest energy cut should be most representative of the experimental surface structure. This is further complicated by the presence of asymmetric cuts. Symmetric repeat unit $(hkl)_{sym}$ has the same surface at the top and bottom whereas asymmetric repeat unit $(hkl)_{asym}$ has different surface at the top and bottom. If the crystal space group has a centre of inversion then each asymmetric surface will have its own inverse $(hkl)_{iasym}$ and the asymmetric cut is treated independently.

The success of the calculations described in this study depends critically upon the quality of the short-range potentials. The reliability of any atomistic simulation rests ultimately with the potential parameters. Therefore it is essential that these terms are derived carefully in order to create an accurate description of our system.

There are two principal methods of deriving potentials, that is, empirically or by direct calculation. The empirical fitting of potentials has historically involved varying the short-range parameters until the structural and lattice properties agree with experimental observations. Potentials are now chosen to reproduce a variety of properties, such as, elastic constants, high frequency and static dielectric constants and lattice energies. Any of the mentioned properties can be used in conjunction with the crystal structure for fitting. Initial values for the parameters are selected and adjusted systematically via a least square procedure.

The energy of a crystal is described via an interatomic potential. The potential is comprised of parameterized analytical expression describing the interactions between the atoms. We considered two models; first Dick and Overhauser [1958] shell model where the atoms are assigned full valence charges and the shell model potential parameters used in this study are listed in Table 4.1. For Mn^{4+}-O^{2-} interactions, the potential parameters derived by Ammundsen, Roziere and Islam [1997] were adjusted until they fitted pyrolusite and ramsdellite structures using the computer code GULP [Gale 1997]. The second model is a partially charged (rigid ion) model where the potentials used were obtained by modifying the parameters developed by Matsui and Akoagi [1991] for isostructural TiO_2 so that they gave good agreement with the crystal structure. Pyrolusite possesses a rutile structure, and is reasonably well lattice matched to TiO_2 [Chambers and Liang 1999]. The rigid ion potential parameters employed in the study are listed in Table 4.1. The analytical form of the force field is simple and readily suited to

numerically demanding dynamical simulations that is a two-body rigid ion potential. The

analytical expression, including electrostatic terms and short-range Buckingham potentials, was discussed in Chapter 2 and is shown in equation 4.2

$$U_{ij} = \left[\frac{q_i q_j}{r_{ij}} + A_{ij} e^{-\frac{r_{ij}}{\rho_{ij}}} - \frac{C_{ij}}{r_{ij}^6} \right] \tag{4.2}$$

where the parameters for ions i and j, separated by a distance r_{ij} are A_{ij}, ρ_{ij} and C_{ij} and q_i and q_j represent the charges. The second term using A_{ij} and ρ_{ij} represent the short-range repulsive interaction between the ions and the third term represents the attractive van der Waals forces. In addition, for the shell model the polarizability of the free ion is given by

$$\alpha_i = \left[\frac{Y^2}{4\pi\varepsilon_0 k_i} \right] \tag{4.3}$$

where Y is the shell charge and k is a parameter representing the force constant between the nucleus and the core electrons. The crystal structures were used in the derivation of the parameters and it is not surprising that the agreement is good, especially the pyrolusite structural parameters. However, we note that as with the TiO_2, the *c/a* ratio is reproduced better using the partially ionic, rigid ion description than using the fully charge shell model. Similarly, the rigid ion model gives better results as compared to the shell model. The lattice parameters of pyrolusite and ramsdellite are listed in Tables 4.2 and 4.3 respectively.

Short-Range Interactions						
	A (eV)	**ρ (Å)**	**C (eV^6)**	**Species**	**Y (e)**	**k (eV^{-2})**
Shell Model						
Mn^{4+}….O^{2-}	2000.986	0.3180	0.000	Mn^{4+}	4.00	95.0
O^{2-}……O^{2-}	22764.30	0.1490	43.000	O^{2-}	-2.24	9.85
Rigid ion model						
$Mn^{2.2+}$….$O^{1.1-}$	15538.20	0.195	22.00	$Mn^{2.2+}$	2.20	
$Mn^{2.2+}$…$Mn^{2.2+}$	23530.50	0.156	16.00			
$O^{1.1-}$……$O^{1.1-}$	11782.76	0.234	30.22	$O^{1.1-}$	-1.10	

Table 4.1: Interatomic potentials for pyrolusite and ramsdellite (shell and rigid ion models). The potential parameters describe the short-range potential terms between the component ions species of MnO_2. The cut-off of 10.0Å was used.

	Shell Model Calculated	Rigid ion model Calculated	Experimental*
Lattice Parameter			
a (Å)	4.464	4.401	4.414
b (Å)	4.464	4.401	4.414
c (Å)	3.227	2.925	2.860
α, β, γ (˚)	90.00	90.00	90.00
Fractional coordinates			
Mn core	0.000 0.000 0.000	0.000 0.000 0.000	0.000 0.000 0.000
O core	0.311 0.311 0.311	0.302 0.302 0.302	0.306 0.306 0.306
O shell	0.312 0.312 0.312		0.306 0.306 0.306

Table 4.2: Calculated and experimental *[Brenet 1950] lattice parameters and structural parameters of pyrolusite.

	Shell Model Calculated	Rigid ion model Calculated	Experimental*
Lattice Parameter			
a (Å)	9.580	9.181	9.264
b (Å)	3.234	2.965	2.859
c (Å)	4.774	4.345	4.513
α, β, γ (˚)	90.00	90.00	90.00
Fractional coordinates			
Mn core	0.142 0.250 0.691	0.132 0.250 0.112	0.139 0.250 0.029
O core	0.790 0.250 0.271	0.763 0.250 0.062	-0.209 0.250 0.215
O core	0.933 0.250 0.841	0.988 0.250 0.783	-0.055 0.250 -0.277
O shell	0.787 0.250 0.265		-0.209 0.250 0.215
O shell	0.936 0.250 0.881		-0.055 0.250 -0.277

Table 4.3: Calculated and experimental*[Miura et al 1990] lattice parameters and structural parameters of ramsdellite.

In order to understand the surface reactivity of MnO_2, atomistic simulation technique was used to model defects in the surfaces. The calculations are based on energy minimization procedure where all the ions are relaxed using a Newton-Raphson method for which both the first and second derivatives of the energy with respect to strain must be calculated. For the study of Mn^{3+} defects, the interactions were modelled using the Buckingham potential for which the parameters are listed in Table 4.4. Mn^{3+} is represented by Mnt for its parameters to be differentiated to those of Mn^{4+}.

Short-Range Interactions						
	A (eV)	**ρ (Å)**	**C (eV^6)**	**Species**	**Y (e)**	**k (eV^{-2})**
Shell Model						
Mnt^{3+}….O^{2-}	1267.5	0.3231	0.000	Mn^{3+}	3.00	95.0
O^{2-}……O^{2-}	22764.30	0.1490	43.000	O^{2-}	-2.24	9.85
Rigid ion model						
$Mn^{2.2+}$….$O^{1.1-}$	15538.20	0.195	22.00	$Mn^{2.2+}$	2.20	
$Mn^{2.2+}$…$Mn^{2.2+}$	23530.50	0.156	16.00			
$O^{1.1-}$……$O^{1.1-}$	11782.76	0.234	30.22	$O^{1.1-}$	-1.10	
$Mnt^{1.65+}$…..$O^{1.1-}$	18645.84	0.195	22.00	$Mnt^{1.65+}$	1.65	
$Mn^{2.2+}$…$Mnt^{1.65+}$	28707.21	0.156	16.00			
$Mnt^{1.65+}$..$Mnt^{1.65+}$	33883.92	0.156	16.00			

Table 4.4: Interatomic potentials for pyrolusite and ramsdellite (shell and rigid ion models). The potential parameters describe the short-range potential terms between the component ions species of Mn_2O_3. The cut-off of 10.0Å was used.

4.3 Results and Discussions

A surface can be thought of as a large defect. Several methods can be employed in modelling surfaces. For surface calculations, a unit cell is defined, cut in a specified orientation and duplicated via periodic boundary conditions in two-dimensions (see figure 2.3). In three-dimensions the repeat block of material including the surface extending approximately by 30Å in the bulk constitutes region I. Beneath that surface is an additional 30Å of material, region II, in which the ions retain their perfect lattice positions. Interactions between the ions are treated the same as when considering bulk defects. Thus the long-range Coulomb interaction and short-range interaction are considered.

4.3.1 Pyrolusite Surface Energies

The most stable surfaces of pyrolusite were investigated using the energy minimization technique. The calculations on the lower index surfaces were performed for both rigid ion model and shell potential model. The {110} surface is the most stable surface for pyrolusite with the surface energies 2.54 $J.m^{-2}$ for shell potential model and 2.07 $J.m^{-2}$ for rigid ion model. The {010} and {100} surfaces have the same surface energies and surface structures for both shell model and rigid ion model. Thus, surface {010} also implies {100}. The same behaviour has been found for isostructural of TiO_2. The {010} surface has the relaxed surface energies 3.06 $J.m^{-2}$ and 2.43 $J.m^{-2}$ for shell model and rigid ion model respectively. However, {001} surface is the most unstable surface with the surface energies 4.50 $J.m^{-2}$and 2.74 $J.m^{-2}$ for shell model and rigid ion model respectively. The surface energies for rigid ion model and shell model for pyrolusite structure are listed in Table 4.5 and 4.6 respectively.

The figures showing the most stable and most unstable relaxed surfaces are given in figures 4.1, 4.2 and 4.3. In addition to the study of low index surfaces, stepped surfaces of pyrolusite were investigated and their structures are shown in figure 4.4. Steps and kinks are common defects occurring in surfaces.

Miller index	Area (Å^2)	E_{unrel} (J.m^{-2})	E_{rel} (J.m^{-2})	Symmetry	Termination
{001}	19.37	3.21	2.74	symm	MnO
{010}	12.87	2.80	2.43	symm	O
$\{101\}_a$	23.25	2.38	2.15	asymm	O
$\{101\}_b$	23.25	6.54	3.93	symm	Mn
$\{110\}_a$	18.20	2.40	2.07	asymm	O
$\{110\}_b$	18.20	10.43	2.88	asymm	O
$\{111\}_a$	26.79	4.46	3.02	asymm	MnO
$\{111\}_b$	26.79	4.46	3.32	asymm	O
{102}	40.82	7.31	3.35	symm	O
$\{120\}_a$	28.78	6.87	2.99	asymm	O
$\{120\}_b$	28.78	6.87	4.11	asymm	MnO
$\{210\}_a$	28.78	6.87	2.99	asymm	O
$\{210\}_b$	28.78	6.87	4.11	asymm	MnO
$\{310\}_a$	40.70	6.87	4.30	asymm	O
$\{310\}_b$	40.70	9.54	4.04	symm	Mn
$\{320\}_a$	46.41	8.17	2.32	asymm	MnO
$\{320\}_b$	46.41	8.17	3.66	asymm	O

Table 4.5: Surface energies (before and after minimization) for pyrolusite obtained using the rigid ion model, showing the area, unrelaxed and relaxed surface energies, symmetry and surface termination. The subscripts after the surfaces are indicating different orientations in one surface, and different orientations have different terminations.

Miller index	Area (Å^2)	E_{unrel} (J.m^{-2})	E_{rel} (J.m^{-2})	Symmetry	Termination
{001}	19.93	6.33	4.50	symm	MnO
{010}	14.41	4.48	3.06	symm	O
$\{101\}_a$	24.59	4.33	3.10	asymm	Mn
$\{101\}_b$	24.59	4.33	3.30	symm	O
{110}	20.37	3.85	2.54	asymm	O
{111}	28.50	9.22	4.02	asymm	O
{102}	42.38	18.01	5.39	symm	O
{120}	32.21	14.34	3.57	asymm	O
$\{210\}_a$	32.21	14.34	3.88	asymm	MnO
$\{210\}_b$	32.21	14.34	6.80	asymm	O
{310}	45.56	21.39	3.81	symm	Mn
{320}	51.94	18.42	5.84	asymm	MnO

Table 4.6: Surface energies (before and after minimization) for pyrolusite obtained using the shell model, showing the area, unrelaxed and relaxed surface energies, symmetry and surface termination. The subscripts after the surfaces are indicating different orientations in one surface.

4.3.2 Pyrolusite Surface Structures

Pyrolusite surfaces for both models are discussed in this section. Selected structures are shown, especially for the most stable and unstable surfaces.

{110} Surface

The relaxed {110} surfaces are shown in figures 4.1 and 4.2 for the shell model and rigid ion model respectively. The {110} surface is asymmetric and is terminated by the bridging oxygens which are linked to six or five coordinate manganese atoms. For both models there is an oxygen movement, where the shell

model predicts that the bridging oxygen is relaxed out of the surface by 0.2Å whereas the rigid ion model predicts that it is slightly moved out of the surface by 0.003Å and there are no lateral relaxations. Again both models predict that there is movement for six coordinate manganese atom which is moved out of the surface by 0.2Å. The manganese relaxations predicted by the two models agree very well. Finally, the shell model shows that there is a five coordinate manganese atom, which is slightly relaxed into the surface by 0.1Å.

{101} Surface

This surface has two different orientations, one is symmetric and manganese terminated and the other surface is asymmetric and oxygen terminated. Both models suggest that there is bridging oxygen movement out of the surface and into the surface. The shell model predicts that the bridging oxygen is relaxed out of the surface by 0.01Å whereas the rigid ion model suggests that a movement into the surface of 0.1Å. The six coordinate manganese atom is relaxed into the surface by 0.2Å for the shell model and out of the surface by 0.1Å for the rigid ion model.

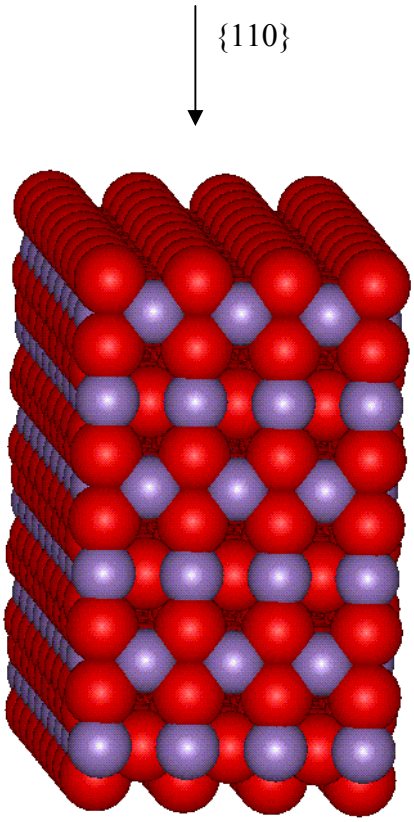

Figure 4.1: Pyrolusite {110} surface structure for the shell potential model.

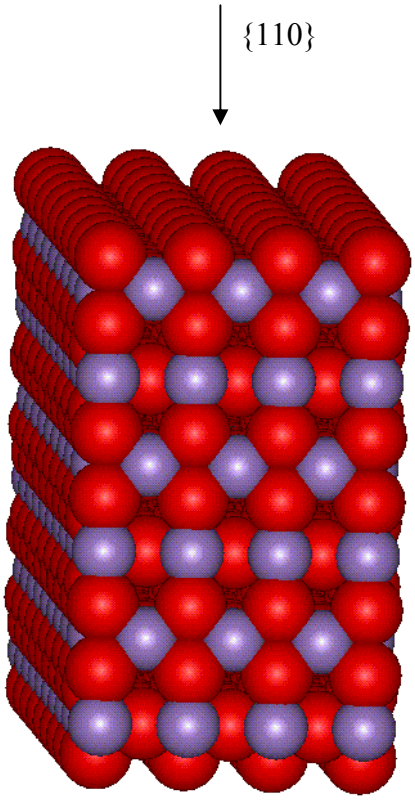

Figure 4.2: Pyrolusite {110} surface structure for the rigid ion model.

{010} Surface

The surface is symmetric and oxygen terminated. The surface is composed of bridging oxygen atoms linked to five coordinate manganese atoms. The shell model and the rigid ion models both suggest that there is an oxygen movement out of the surface and in the surface plane. They agree for the in plane movement of 0.2Å but differ in the extent of relaxation out of the surface, the shell model suggests 0.2Å while rigid ion model gives 0.01Å. The same behaviour has been found for {100} surface, which agrees very well with results obtained for the surface energies.

{001} Surface

The {001} surface has a symmetric arrangement and is terminated by MnO_2. Both models predict that after minimization the six coordinate manganese is relaxed into the surface by 0.2Å, with no lateral relaxations. The surface oxygen atoms relax to a smaller extent with the shell model predicting a 0.1Å movement out of the surface compared to 0.01Å yielded by the rigid ion model. The surface structure for the rigid ion model is shown in figure 4.3 amongst other low index surfaces.

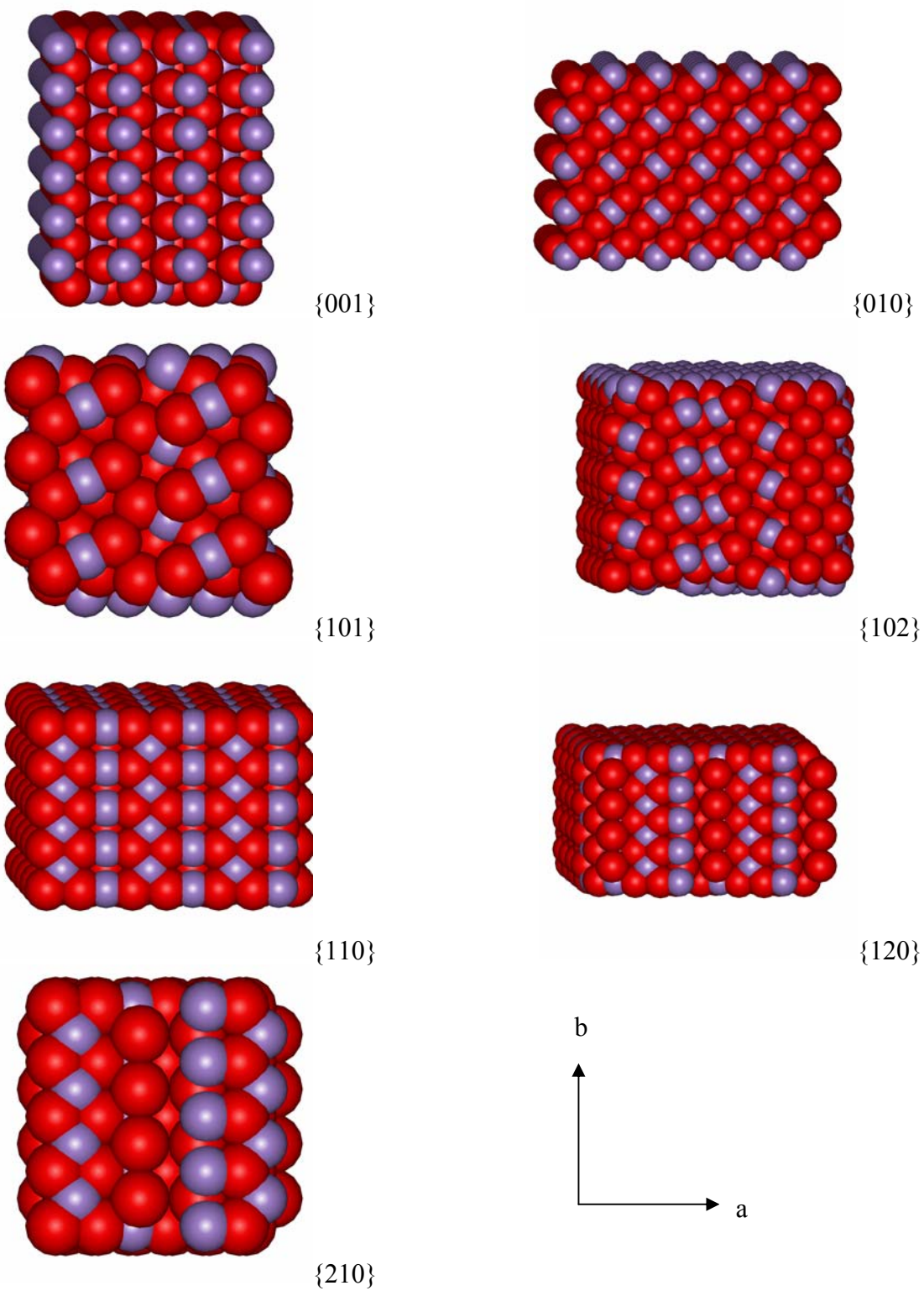

Figure 4.3: Low index pyrolusite surfaces, corresponding to the rigid ion model and have the same structure as the shell potential model surfaces. Red balls represent oxygen atoms and purple balls represent manganese atoms.

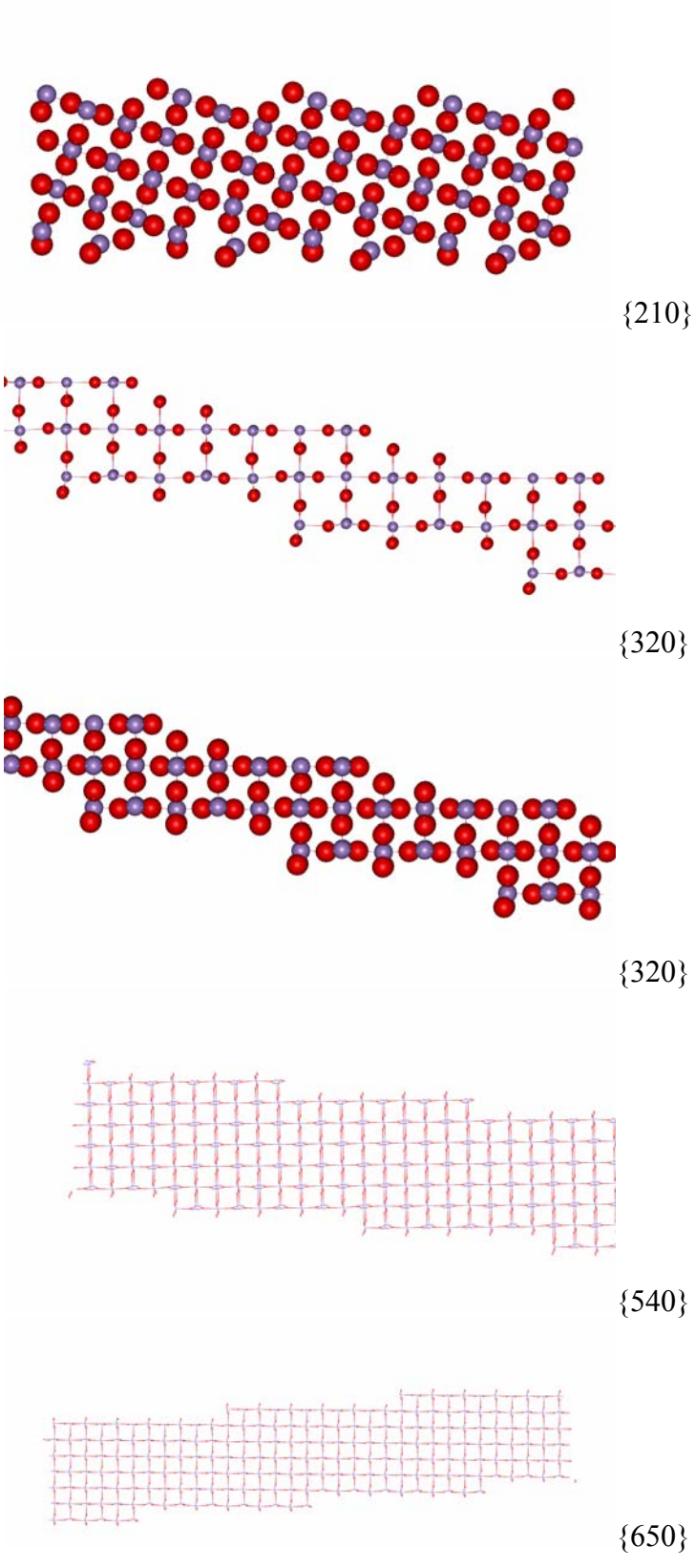

Figure 4.4: Pyrolusite stepped surfaces showing steps.

4.3.3 Ramsdellite surface energies

The most stable low index surfaces of ramsdellite were also investigated using the energy minimization technique. For the rigid ion model $\{111\}_a$ surface was found to be the most stable surface with the relaxed surface energy 1.51 $J.m^{-2}$. For the shell model $\{001\}_b$ surface was found to be the most stable surface with the least surface energy of 1.12 $J.m^{-2}$. There is not much correlation between the surface energies of ramsdellite rigid ion model and shell potential model. Relaxed and unrelaxed surface energies for both models are listed in Tables 4.7 and 4.8.

Miller index	Area ($Å^2$)	E_{unrel} ($J.m^{-2}$)	E_{rel} ($J.m^{-2}$)	Symmetry	Termination
$\{001\}_a$	27.22	2.33	1.69	asymm	O
$\{001\}_b$	27.22	6.69	6.06	asymm	O
$\{010\}_a$	39.89	2.95	2.49	asymm	MnO
$\{010\}_b$	39.89	7.42	2.83	asymm	MnO
$\{011\}_a$	48.29	9.23	1.76	asymm	O
$\{011\}_b$	48.29	3.67	1.95	symm	O
$\{100\}_a$	12.88	2.19	1.79	symm	O
$\{100\}_b$	12.88	2.97	2.45	symm	O
$\{101\}_a$	30.11	2.14	1.60	asymm	O
$\{101\}_b$	30.11	6.46	1.52	asymm	O
$\{110\}_a$	41.92	2.99	2.45	symm	O
$\{110\}_b$	41.92	6.88	2.43	symm	Mn
$\{111\}_a$	49.98	3.00	1.51	asymm	O
$\{111\}_b$	49.98	3.00	1.82	symm	O
$\{201\}_a$	37.48	5.56	3.23	asymm	O
$\{201\}_b$	37.48	5.83	2.94	asymm	MnO
$\{210\}_a$	47.48	5.70	3.94	asymm	O
$\{210\}_b$	47.48	2.06	1.81	symm	Mn_2

Table 4.7: Surface energies (before and after minimization) for ramsdellite obtained using the rigid ion model, showing the area, unrelaxed and relaxed surface energies, symmetry and surface termination.

Miller index	Area (Å^2)	E_{unrel} (J.m^{-2})	E_{rel} (J.m^{-2})	Symmetry	Termination
$\{001\}_a$	30.98	14.4	2.74	asymm	O
$\{001\}_b$	30.98	5.97	1.12	asymm	O
$\{010\}_a$	45.74	5.87	4.07	asymm	Mn_2O
$\{010\}_b$	45.74	19.32	3.24	asymm	Mn_2O
$\{011\}_a$	55.24	3.74	2.54	asymm	O
$\{011\}_b$	55.24	10.40	2.34	asymm	O
{100}	15.44	4.25	-28.63	symm	O
{101}	34.61	2.78	1.59	asymm	O
$\{110\}_a$	48.27	18.71	3.41	asymm	O
$\{110\}_b$	48.27	15.20	4.13	asymm	Mn
$\{111\}_a$	57.37	6.32	1.52	asymm	Mn
$\{111\}_b$	57.37	8.19	4.12	asymm	O

Table 4.8: Surface energies (before and after minimization) for ramsdellite obtained using the shell model, showing the area, unrelaxed and relaxed surface energies, symmetry and surface termination. The subscripts after the surfaces are indicating different orientations in one surface.

4.3.4 Ramsdellite surface structures

{101} Surface

The {101} surface has asymmetric arrangement and is oxygen terminated. After minimization both models predicted that there is oxygen movement. The oxygen atom is moved out of the surface by 0.2Å and moved into the surface by 7.7Å for the rigid ion model and the shell model respectively. The rigid ion model predicts that the manganese atom is relaxed into the surface by 0.2Å to a smaller extent as compared to the 4.6Å movement predicted by the shell model. The surface structure is shown in figure 4.6 for the shell potential model.

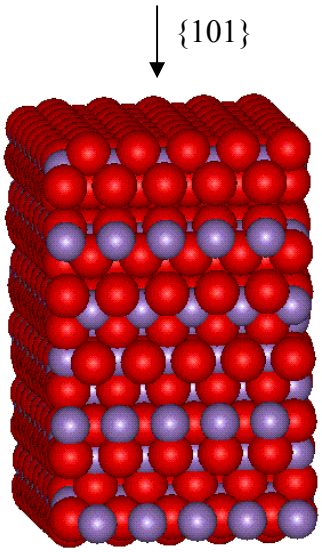

Figure 4.5: Ramsdellite {101} surface structure for the shell potential model.

{100} Surface

Surface {100} is symmetric and oxygen terminated. For the shell model the atoms are relaxed to a big extent as compared to the atoms of the rigid ion model. Thus the oxygen atom is moved into the surface by 6.5Å for the shell model while is moved into the surface by 0.1Å for the rigid ion model and the manganese atom is moved into the surface by 5.7Å for the shell model and moved out of the surface by 0.1Å for the rigid ion model.

{011} Surface

The {011} surface has an asymmetric arrangement and is oxygen terminated. The bridging oxygen is moved into the surface by 0.3Å and out of the surface by 0.02Å for the rigid ion model and shell model respectively. Both models predicted that there is a slight movement of the bridging oxygen. The four coordinate

manganese atom is relaxed into the surface by 2.7Å for the rigid ion model as compared to a small movement of 0.1Å predicted by the shell model.

{110} Surface

For {110} surface, models produce two different surfaces, thus symmetric and oxygen terminated surface for the rigid ion model and asymmetric surface terminated by oxygens for the shell model. Both models suggested that the oxygen is moved into the surface, 1.5Å movement for the shell model and 0.5Å movement for the rigid ion model. Shell model predicted 2.0Å movement into the surface whereas the rigid ion model predicted 0.5Å movement for the manganese atom.

{010} Surface

The {010} surface is asymmetric and is terminated by Mn_2O_4. Both models predicted a 0.1Å movement of the five coordinate manganese atom into the surface. Again they predicted that there is a slight relaxation on the oxygen, 0.1Å movement out of the surface for the shell model and 0.1Å movement into the surface for the rigid ion model.

{001} Surface

{001} surface is asymmetric and is oxygen terminated. There is an oxygen movement for both models, out of the surface by 0.1Å for the rigid ion model and into the surface by 2.2Å for the shell model. Both models suggest that there is a movement for the manganese atom into the surface; rigid ion predicts 0.2Å

movement whereas shell model predicts 2.5Å. The surface structure for the rigid ion model is shown in figure 4.7.

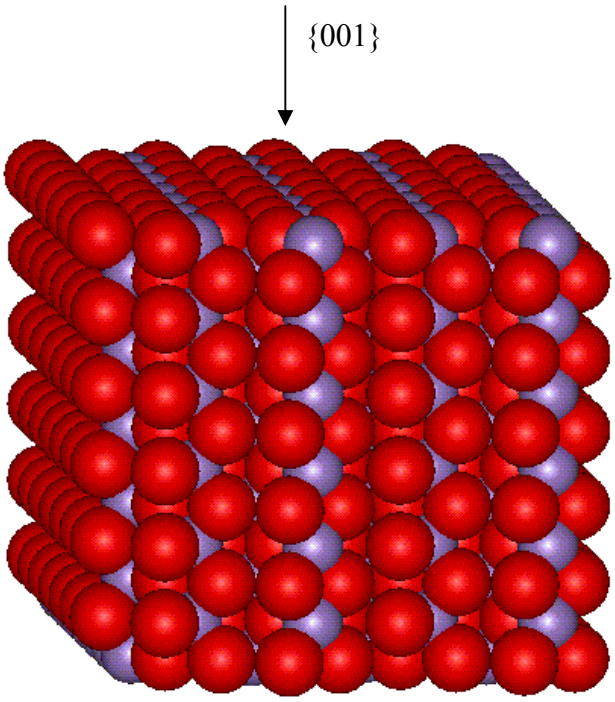

Figure 4.6: Ramsdellite {001} surface structure for the rigid ion model.

4.3.5 Surface Reactivity

As a way of examining the surface reactivity we considered the reduction of the surface. The approach was to replace the Mn^{4+} ions on the top layer of various MnO_2-pyrolusite Miller planes by Mn^{3+} and compensating the charge by removing oxygen atom. The first layer contained either oxygen or Mn^{4+} depending on the surface termination. The energies are given in Tables 4.9 and 4.10 for pyrolusite and ramsdellite respectively, one oxygen vacancy was created by removing an oxygen ion on the top layer and replacing two Mn^{4+} by two Mn^{3+}. Then two oxygen vacancies were created by removing two oxygen ions and replacing four Mn^{4+} by four Mn^{3+}. Removal of oxygen and compensating the Mn^{4+} charge by

Mn^{3+} leads to lattice rearrangement under the formation Mn_2O_3. For one oxygen vacancy, 17% of the Mn^{4+} in the surface was replaced by Mn^{3+} and for two vacancies, 33% of Mn^{4+} in the surface was replaced by Mn^{3+} for both models. The {101} surface is the most reactive surface with surface energy -0.49 eV for the rigid ion model and -1.59 eV for the shell model. Figures 4.8, 4.9 and 4.10 show the surface structures of {101} and {110} surfaces. Surface structure of {101} surface shows the vacancy created, the vacancy is on the top layer of the surface and seems to be a step like. A two vacancies surface is shown in figure 4.8, where there are vacancies on the top layer looking like those in one oxygen vacancy structure and also on the second layer. Vacancies on the second layer can be seen very well. For the least reactive surface, {110}, there seems to be spacing amongst the atoms all over the structure except mainly on the first two top layers.

	Miller Index	Energy (eV) One oxygen vacancy	Energy (eV) Two oxygen vacancies
Rigid ion model	{001}	1.693	6.258
	{010}	2.167	6.334
	$\{101\}_a$	1.534	3.627
	$\{101\}_b$	-0.489	0.776
	$\{110\}_a$	0.605	1.538
	$\{110\}_b$	3.274	2.672
Shell model	{001}	1.426	5.495
	{010}	0.502	…
	$\{101\}_a$	1.558	2.932
	$\{101\}_b$	-1.586	3.201
	{110}	0.538	1.764

Table 4.9: Surface energies of pyrolusite defects (oxygen vacancies) for rigid ion and shell models. Surfaces with the same indices but different surface energies correspond to different terminations.

Shown in Table 4.9 are the surface energies of reduced surfaces of ramsdellite. For the rigid ion model, $\{110\}_a$ is the most reactive surface with surface energy of 0.426 eV whereas in the case of shell model the most reactive one is $\{101\}_a$ with a negative surface energy of -16.184 eV. In contrast to pyrolusite results, there is no correlation between rigid ion and shell model results.

	Miller Index	Energy (eV) One oxygen vacancy	Energy (eV) Two oxygen vacancies
Rigid ion model	$\{001\}_a$	3.033	2.653
	$\{001\}_b$	1.162	4.695
	$\{010\}_a$	1.639	4.121
	$\{010\}_b$	0.559	1.605
	$\{011\}_a$	1.628	0.852
	$\{011\}_b$	0.724	1.387
	$\{100\}_a$	3.118	6.941
	$\{100\}_b$	3.333	6.607
	$\{101\}_a$	0.856	3.948
	$\{101\}_b$	1.047	5.225
	$\{110\}_a$	0.426	2.142
	$\{110\}_b$	1.257	2.965
Shell model	$\{001\}_a$	0.555	-14.09
	$\{001\}_b$	0.687	2.770
	$\{010\}_a$	1.408	4.543
	$\{010\}_b$	2.521	5.312
	$\{011\}_a$	2.379	3.095
	$\{011\}_b$	2.693	5.790
	$\{100\}$	2.788	10.448
	$\{101\}_a$	-16.184	-12.827
	$\{101\}_b$	1.863	1.651
	$\{110\}_a$	1.256	4.601
	$\{110\}_b$	-2.432	2.851

Table 4.10: Surface energies of ramsdellite defects (oxygen vacancies) for rigid ion and shell models. Surfaces with the same indices but different surface energies correspond to different terminations.

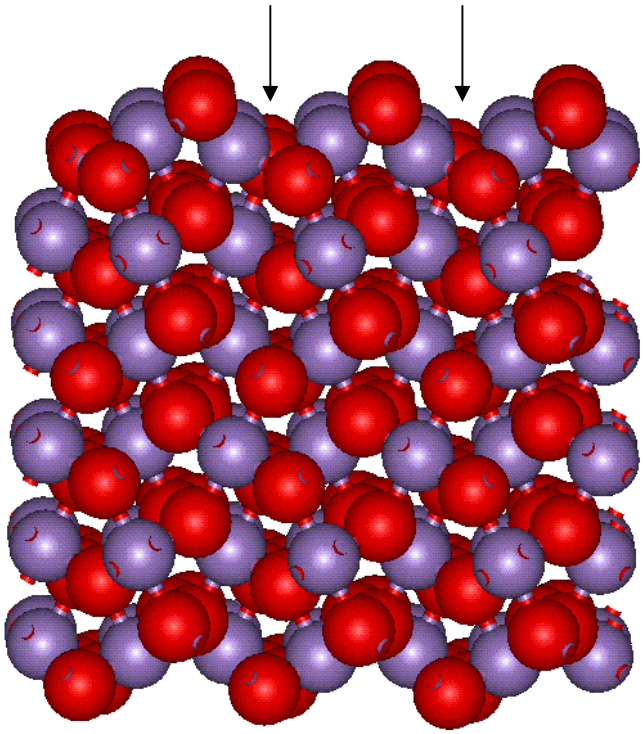

Figure 4.7: Pyrolusite {101} defects surface structure for the rigid ion model (one oxygen vacancy). Arrows indicates where the vacancies are located.

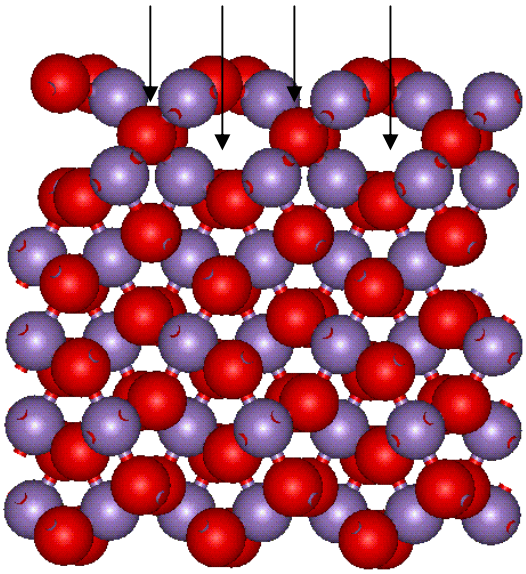

Figure 4.8: Pyrolusite {101} defects surface structure for the rigid ion model (two oxygen vacancies). Arrows indicates where the vacancies are located.

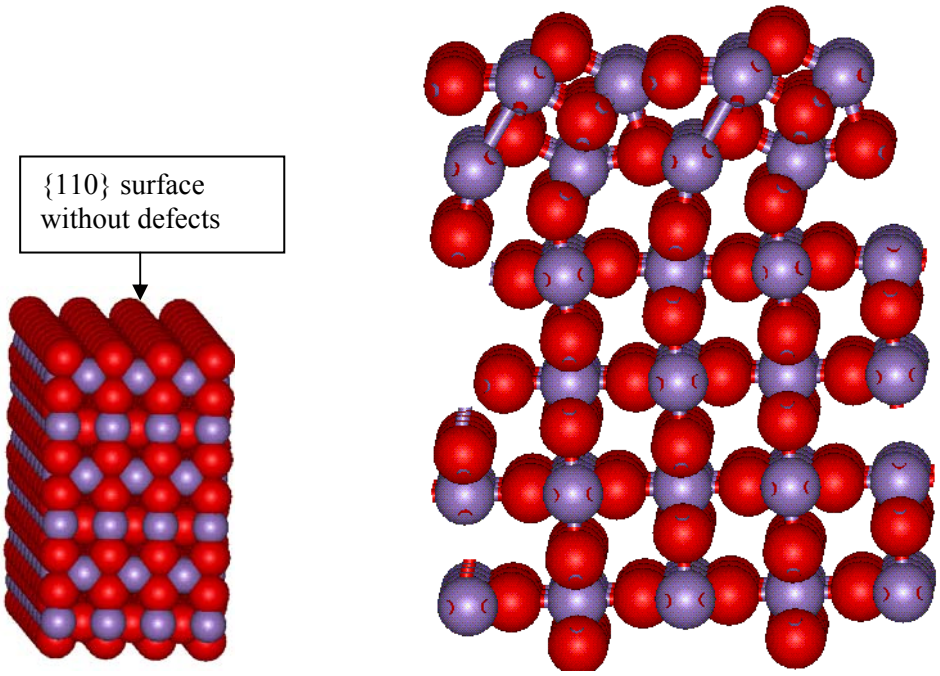

Figure 4.9: Pyrolusite {110} defects surface structure for the rigid ion model (two oxygen vacancies).

4.4 Conclusion

Energy minimization technique, using interatomic potentials, is the cost effective computational modelling technique and it is used to determine the minimum energy of the system. The surface energies, structures, stabilities and reactivities of pyrolusite and ramsdellite structures have been calculated using the energy minimization technique and two different models were considered, that is the shell model and the rigid ion model. The $\{110\}_a$ surface was found to be the most stable surface for pyrolusite, for both models, with the surface energy 2.54 $J.m^{-2}$ and 2.07 $J.m^{-2}$ for the shell model and rigid ion model respectively. Surfaces {100} and {010} were identical, they had the same surface energy and surface structure for both models and this is owing to the tetragonal structure for pyrolusite. For ramsdellite, the $\{111\}_a$ surface is predicted to be the most stable surface with

surface energy 1.51 $J.m^{-2}$ for the rigid ion model and $\{001\}_b$ is the most stable surface for the shell model with the surface energy of 1.12 $J.m^{-2}$. Using the models mentioned above, no match was found amongst ramsdellite surfaces (energies and structural relaxations) since pure ramsdellite does not occur in nature and it is very rare to find except with inclusion of impurities. The presence of defects in the system reduces the surface energy of each orientation. Thus the surface energies of pure pyrolusite and ramsdellite are larger than the surface energies for the defect crystal surfaces. However, as the defects content is increased in the system the surface energies also increase. The negative surface energy implies that the surface is more reactive. For pyrolusite, surface {101} is the most reactive surface; irrespective of the defects content. Interestingly, the $\{101\}_a$ is the second most stable surface in the case of pyrolusite.

Thus far the rigid ion potential model has yielded more consistent bulk and surface properties of MnO_2 than the shell model. As an example, it reproduces lattice parameters that are in good agreement with experimental results. Furthermore, it predicts reasonable surface energies for both pyrolusite and ramsdellite polymorphs. In particular, it depicts equivalent surface energies for {100} pyrolusite and $\{100\}_b$ ramsdellite, which are surface on which intergrowths naturally occur. The shell model did not predict this equivalence and in certain instances gives negative surface energies.

Chapter 5

Molecular Dynamics Simulations

5.1 Introduction

Molecular dynamics is a long established simulation technique that has been used extensively to investigate structural and dynamical properties of solids, liquids and gases at the atomic scale [Allen and Tildesley 1989 and Meyer et al 1992]. The main objective of this chapter is to use molecular dynamics simulations to study the structural properties of Electrolytic Manganese Dioxide over a wide range of temperatures in order to monitor the effect of temperature on structural properties. The structures of different varieties have been well established: tetragonal rutile/pyrolusite [Baur 1976] and orthorhombic ramsdellite [Byström 1949].

5.2 Methodology

The molecular dynamics technique consists of an explicit dynamical simulation of the ensemble of particles, for which Newton's equation of motion are solved. The forces acting on the ions are described by the Born model of solids. The ions were assigned their formal valence charges with a Buckingham potential to model the short range interaction which model the overlap repulsion and dispersion forces

between neighbouring ions and the interatomic forces of the solid are represented by the pair potential of the Buckingham form, expressed analytically by

$$U_{ij}(r) = \left\{ \frac{q_i q_j}{r_{ij}} + A_{ij} e^{-\frac{r_{ij}}{\rho_{ij}}} - \frac{C_{ij}}{r_{ij}^6} \right\} \qquad (5.1)$$

where q_i and q_j are the charges of ions i and j separated by a distance r_{ij} and A_{ij}, ρ_{ij} and C_{ij} are the potential parameters for interaction for $i - j$. The potential model used was developed by Matsui and Akaogi [1991] for isostructural TiO_2 and the parameters were modified so that they are in good agreement with the crystal structures of pyrolusite and ramsdellite. The potentials are listed in Table 4.1.

MD simulation results presented in this chapter were performed using the computer code DL_POLY [Smith 1999] with a simulation box comprising of 1050 atoms for pyrolusite bulk structure and 840 atoms for ramsdellite bulk structure. The simulations of {100}, {111}, {101} and {001} surfaces of pyrolusite were performed using a cell containing 1008, 576, 720 and 1296 atoms respectively. In each simulation, velocity scaling was undertaken for the first 10001 steps, scaling every 0.005 pico seconds time steps. The ensemble used imposes the NVE condition. Cut-offs of 10.0Å and 9.0Å were used for pyrolusite and ramsdellite respectively.

5.3 Results and Discussions

5.3.1. Pyrolusite Bulk

The radial distribution functions at different temperatures for pyrolusite bulk structure are given in figures 5.1-5.3 and the radial distribution functions for Mn-Mn, Mn-O and O-O pairs at temperatures between 300K and 3500K are shown. The figures reveal a series of well-defined peaks corresponding to successive nearest neighbour distances. The plots are showing pair distribution functions as a function of distance where maximum and minimum peaks of the system can be defined. At temperature 300K shown in figure 5.1, the first maximum peak occurs at approximately r = 3.4Å for Mn-Mn pair, and the pair distribution function g(r) = 10.6. For Mn-O pair, the maximum peak occurs at r =1.9Å and g(r) = 16.3. Lastly, for O-O pair the maximum peak occurs at r = 2.9Å and g(r) = 7.7. The RDFs for all these three pairs show an increase in peak broadening as the temperature is increased. The profile of peak broadening indicates a greater degree of disorder at higher temperatures. As the temperature is increased the pair distribution function decreases, this can be easily seen at temperature 3500K shown in figure 5.3. Thus for Mn-Mn pair the maximum peak occurs at r = 3.4Å and g(r) = 4.9 and for Mn-O pair the peak occurs at g(r) =7.6. The same behaviour of g(r) decreasing with increase in temperature applies to O-O pair with g(r) = 3.9. The first peaks occur almost at the same distances no matter what the temperature is. Therefore temperature has an effect on pyrolusite structure; the higher the temperature the higher the disorder in the system and the broader is the peak (figures 5.4-5.6). Figure 5.7 depicts the total energy versus temperature graph, with a phase transition at about 2500K.

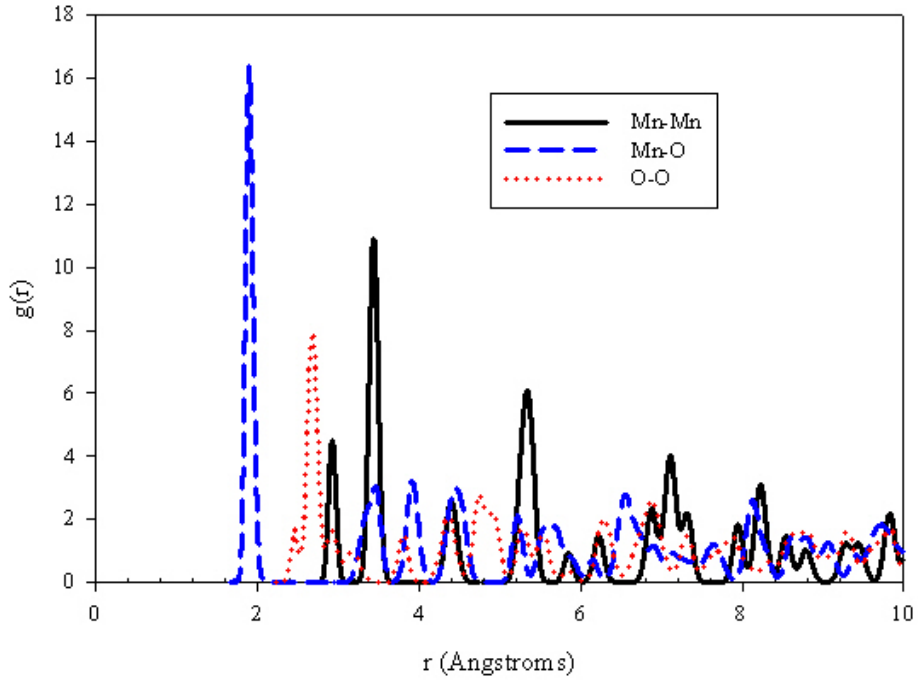

Figure 5.1: Radial Distribution Functions for pyrolusite structure showing Mn-Mn, Mn-O and O-O pairs at 300K.

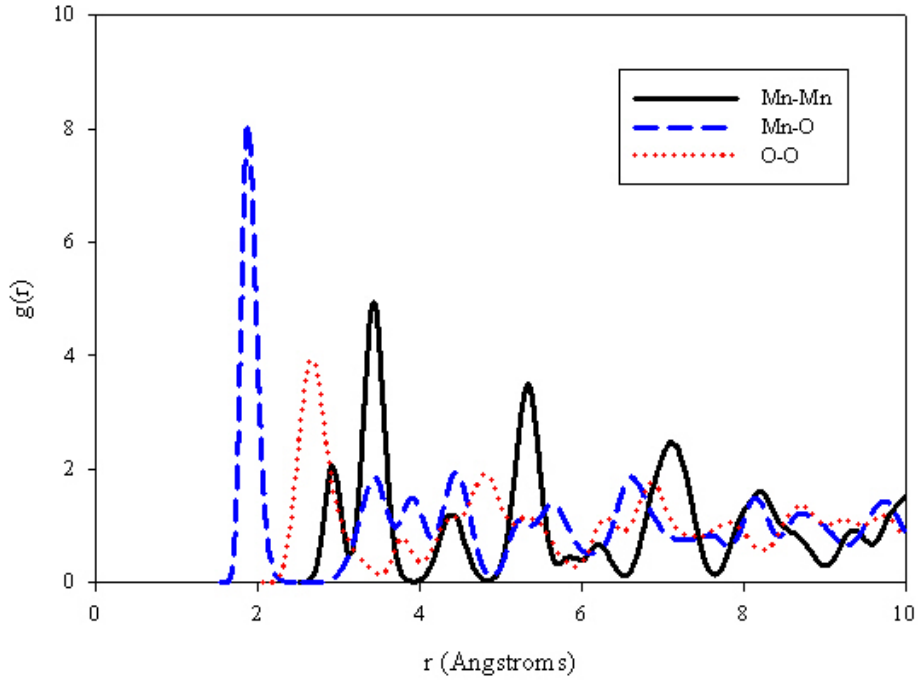

Figure 5.2: Radial Distribution Functions for pyrolusite structure showing Mn-Mn, Mn-O and O-O pairs at 1500K.

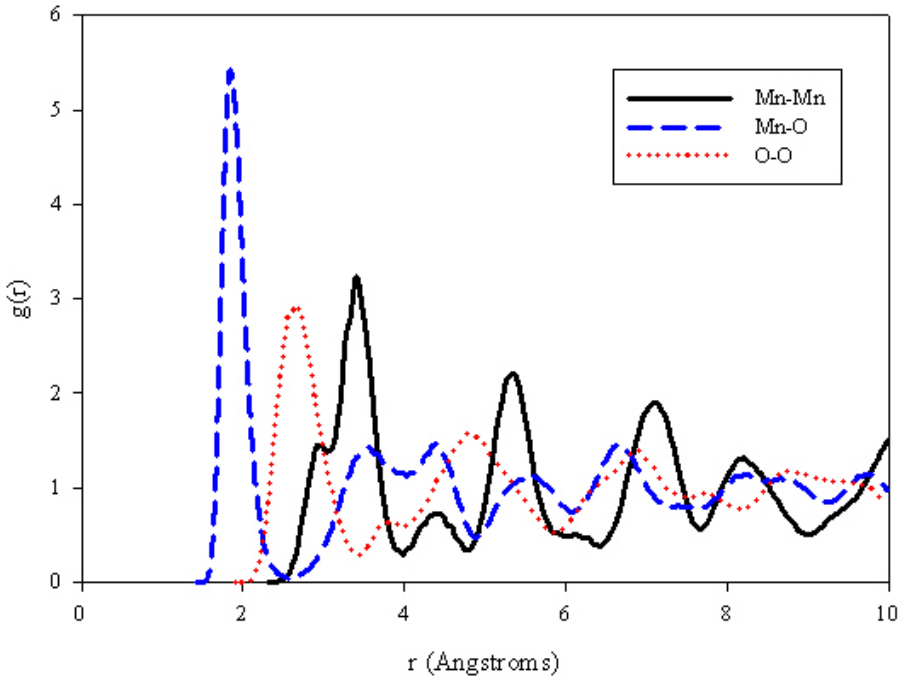

Figure 5.3: Radial Distribution Functions for pyrolusite structure showing Mn-Mn, Mn-O and O-O pairs at 3500K.

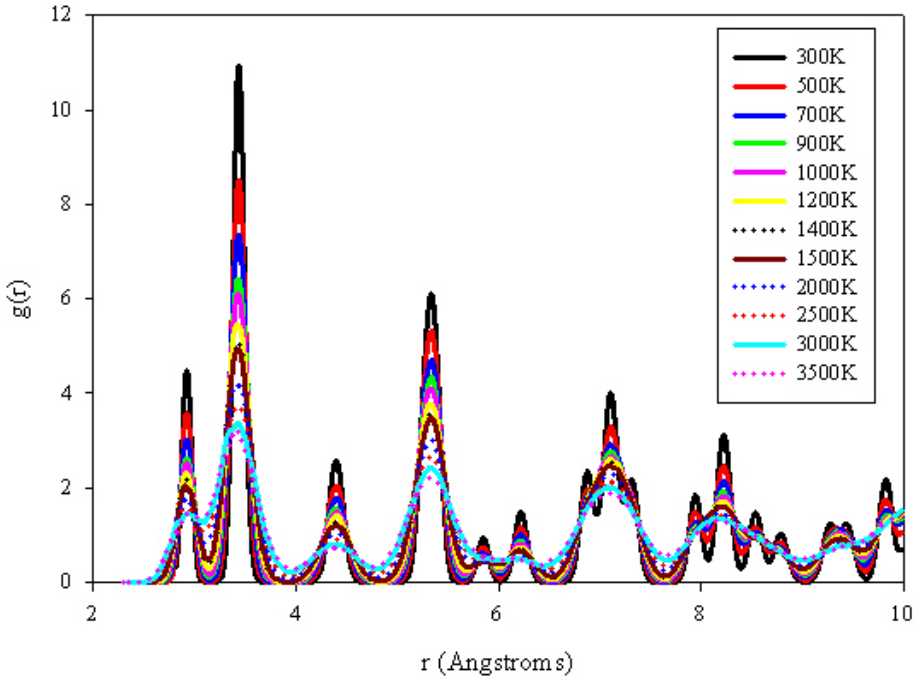

Figure 5.4: Radial Distribution Functions for pyrolusite structure showing Mn-Mn pair at different temperatures.

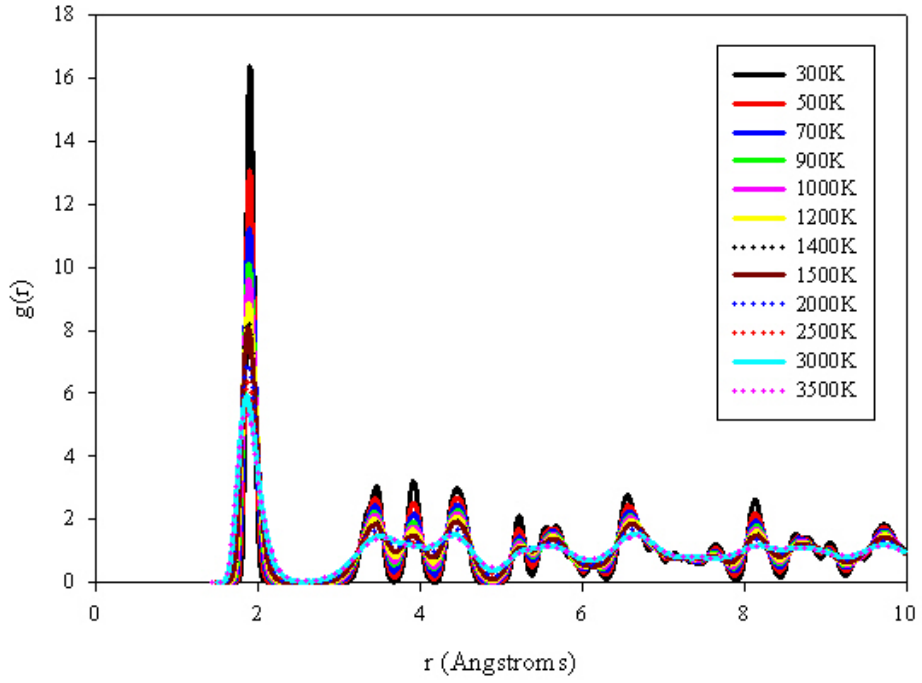

Figure 5.5: Radial Distribution Functions for pyrolusite structure showing O-Mn pair at different temperatures.

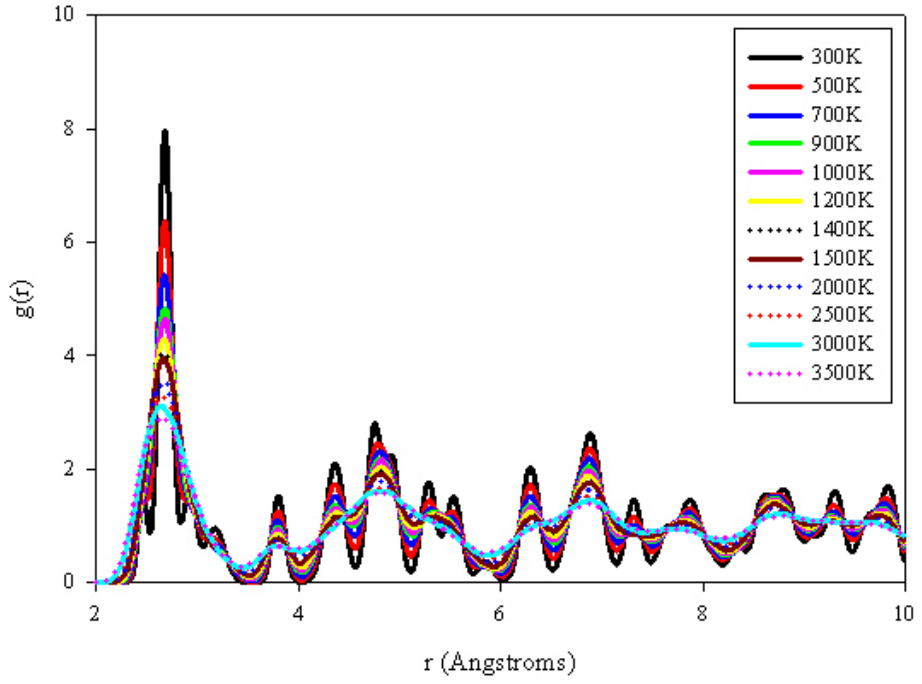

Figure 5.6: Radial Distribution Functions for pyrolusite structure showing O-O pair at different temperatures.

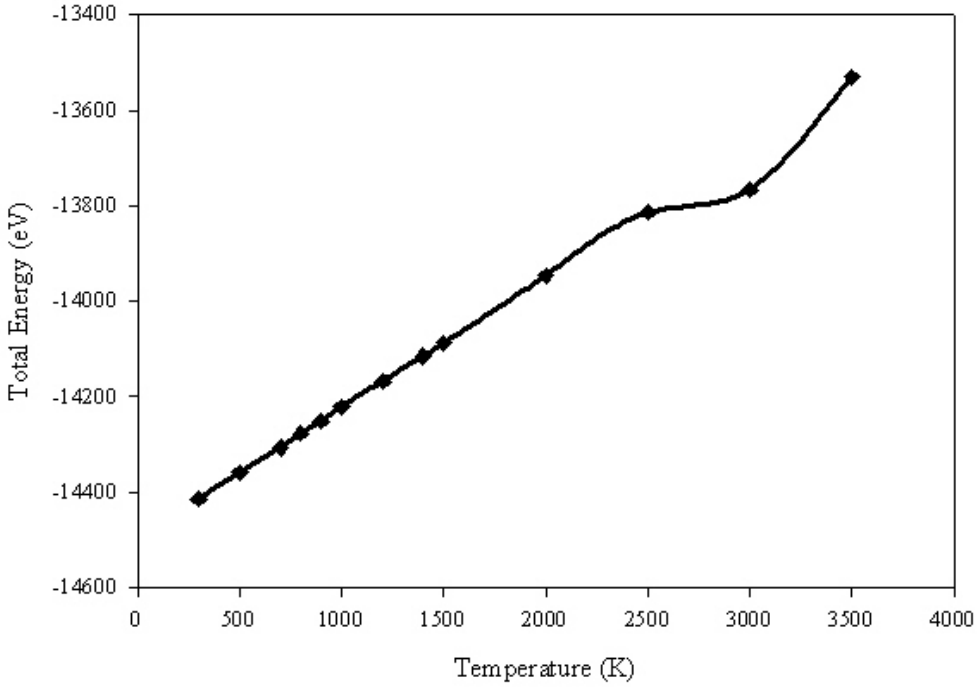

Figure 5.7: Total energy versus temperature graph for pyrolusite bulk.

5.3.2 Pyrolusite Surfaces

Pair distribution functions have been calculated for four orientations corresponding to the {110}, {101}, {111} and {001} Miller indices for pyrolusite. Only the room temperature effect was investigated. The MD results predict that all the surfaces have more or less the same structure with Mn-Mn pairs all being the first maximum peaks occurring at approximately distance r = 3.4Å and g(r) approximately equals 15.6, 1.8, 11.0 and 15.0 for {101}, {110}, {111} and {001} surfaces respectively. The {111} surface has the lowest value for pair distribution function g(r), which means that there are few atoms in the surface whereas the surface with the highest value is {110}, which has many atoms. Similarly, other two pairs (Mn-O and O-O) have the same structure but differ in values of g(r). All

the surfaces have the same behaviour for all pairs; they look the same but differ in peak height's. The first maximum peaks occur at the same distance in all surfaces.

MD simulation technique was used to calculate the surface energies for four pyrolusite surface mentioned above. The surface energies are listed in table 5.1 below together with the corresponding energies obtained using atomistic simulation technique. Generally, equivalent surface energies from the two techniques agree well. Surface {110} is the most stable surface for both methods. Unlike atomistic simulation, the surface energy was calculated using the equation

$$\gamma = \left[\frac{E_s - \left(\frac{n_s}{n_b} \right) E_b}{2A} \right] \qquad (5.2)$$

where E_s is the energy of the surface, n_s is the total number of atoms in the surface, n_b is the total number of atoms in the bulk, E_b is the energy of the bulk crystal and A is the surface area.

Miller Index	Molecular Dynamics Surface Energy ($J.m^{-2}$)	Energy Minimization Surface Energy ($J.m^{-2}$)
{110}	1.96	2.07
{101}	2.14	2.15
{001}	2.77	2.74
{111}	3.18	3.02

Table 5.1: Comparison of surface energies of pyrolusite obtained using molecular dynamics and energy minimization techniques.

5.3.3 Ramsdellite Bulk

The radial distribution functions for Mn-Mn, Mn-O and O-O pairs at 300K 1500K and 3500K are given in figures 5.8, 5.9 and 5.10 respectively. O-O pair possesses double peak as the first maximum peak at approximately distance 2.4-2.9Å for all temperatures. However, it is noted that, as the temperature is increased the peak collapses into a single peak, as observed at temperature 1500K. The peak is becoming broader also. All atom pairs of ramsdellite behave similarly to pyrolusite structure.

Thus the higher the temperature the broader is the peak which depicts more disorder in the system. As the temperature is increased in a system the height of the pair distribution function decreases. The temperature does not have much effect on the bond distance. At 300K the first maximum peaks were at 3.0Å and the pair distribution functions were 7.8, 13.4 and 4.6 for Mn-Mn, Mn-O and O-O pairs respectively. At 1500K the first peaks were still located at 3.0 Å and g(r) were 3.5, 7.2 and 2.8 for Mn-Mn, Mn-O and O-O respectively. The variation of RDFs with temperature for the ramsdellite structure is shown in figures 5.11 to 5.13.

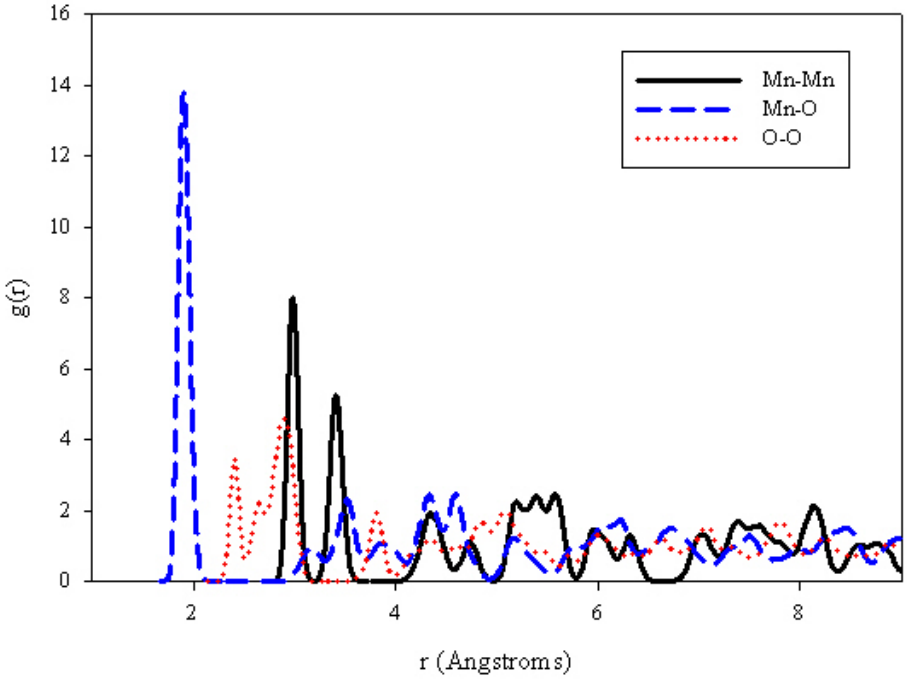

Figure 5.8: Radial Distribution Functions for ramsdellite structure showing Mn-Mn, Mn-O and O-O pairs at 300K.

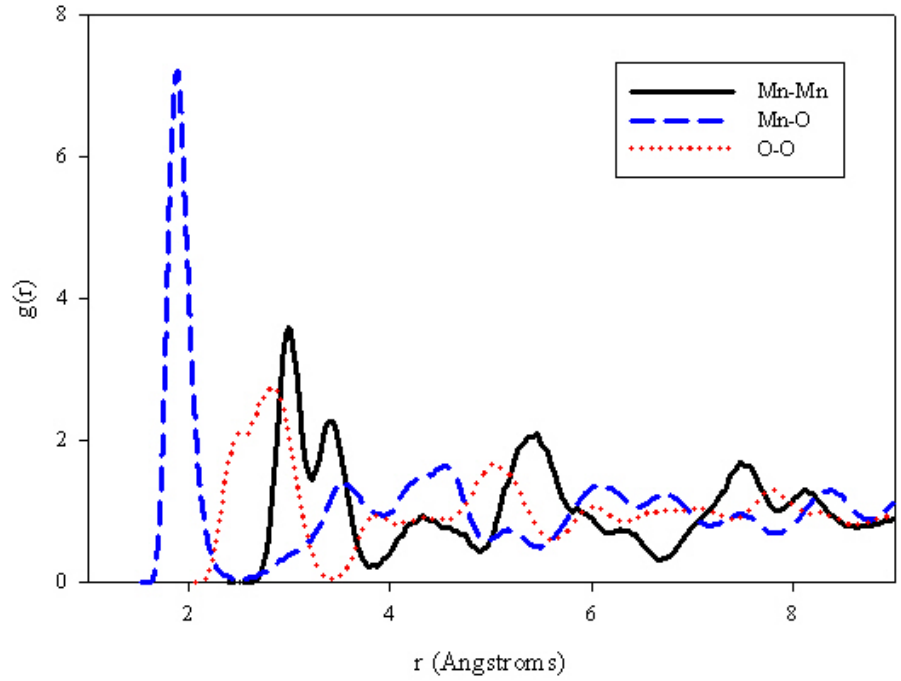

Figure 5.9: Radial Distribution Functions for ramsdellite structure showing Mn-Mn, Mn-O and O-O pairs at 1500K.

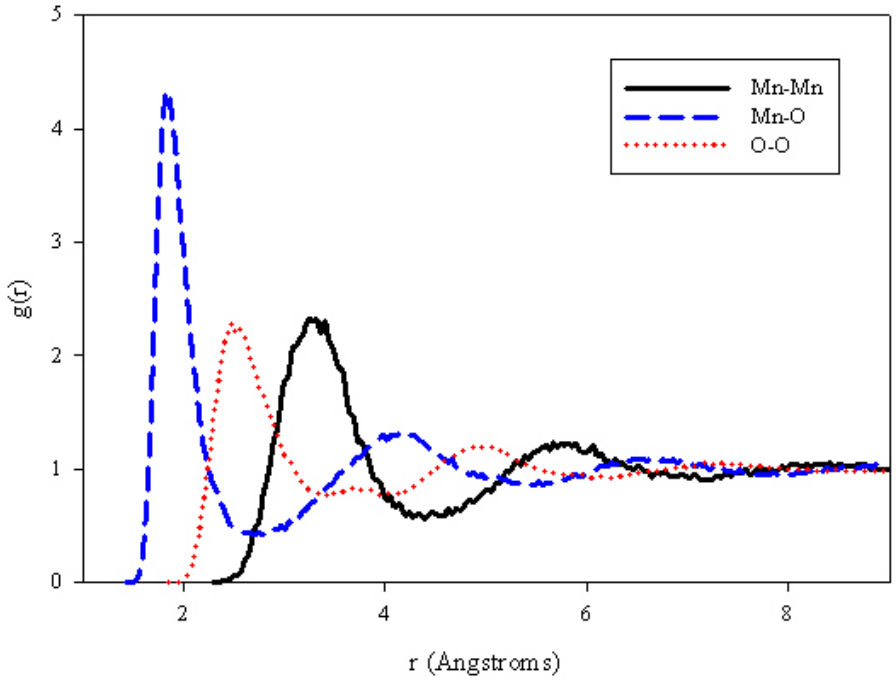

Figure 5.10: Radial Distribution Functions for ramsdellite structure showing Mn-Mn, Mn-O and O-O pairs at 3500K.

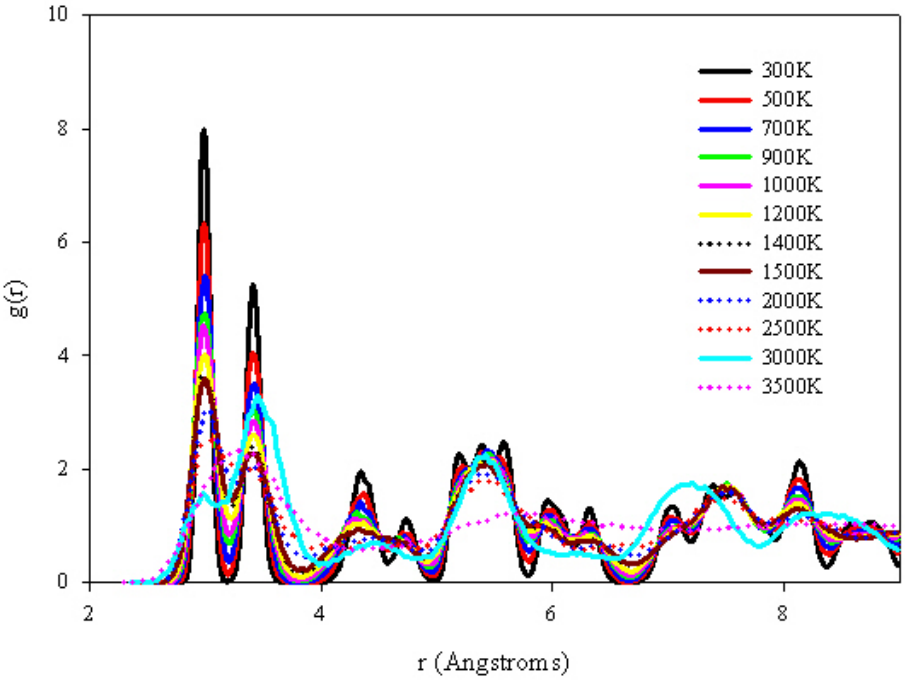

Figure 5.11: Radial Distribution Functions for ramsdellite structure showing Mn-Mn pair at different temperatures.

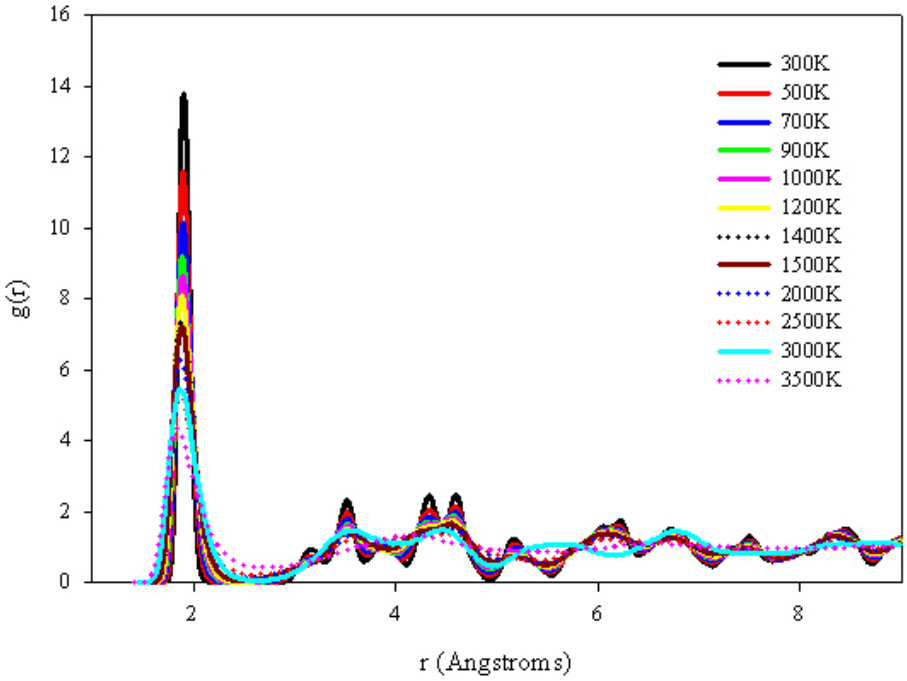

Figure 5.12: Radial Distribution Functions for ramsdellite structure showing Mn-O pair at different temperatures.

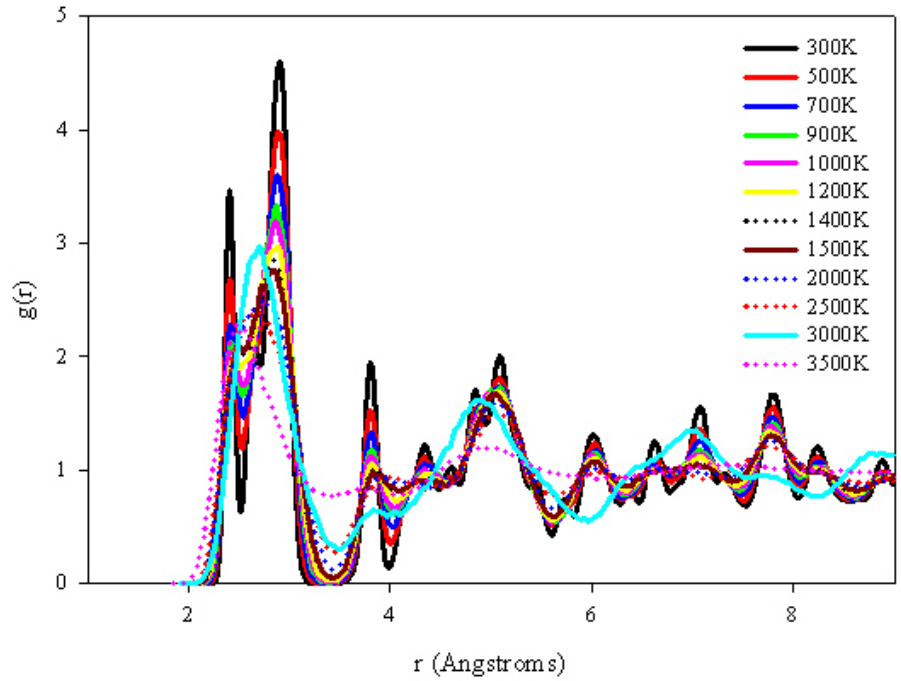

Figure 5.13: Radial Distribution Functions for ramsdellite structure showing O-O pair at different temperatures.

	Temperature (K)	Pair-interaction	Height of the peak
Pyrolusite	300	**Mn-Mn**	**10.6**
		Mn-O	**16.3**
		O-O	**7.7**
	1500	**Mn-Mn**	**4.9**
		Mn-O	**7.6**
		O-O	**3.9**
Ramsdellite	300	**Mn-Mn**	**7.8**
		Mn-O	**13.4**
		O-O	**4.6**
	1500	**Mn-Mn**	**3.5**
		Mn-O	**7.2**
		O-O	**2.8**

Table 5.2: Peak's height for pyrolusite and ramsdellite structures.

5.4 Conclusion

The dynamics of the atoms in matter is the key to understanding many physical properties and processes involving structural rearrangements. Especially at higher temperatures, the classical picture of atoms moving according to the Newton's equations of motion is an adequate description of the physics involved. Molecular dynamics technique was used to explore the structures of pyrolusite and ramsdellite at different temperatures. The Radial Distribution Function is a pair correlation function, which was used to describe the structure of the systems under study. It describes how the atoms in a system are radially packed around each other. The effect of temperature on the systems was investigated and it was found

that as the temperature increases, the heights of the peaks decrease and the peaks become broader. The bond lengths for Mn-Mn, Mn-O and O-O have been determined and they are in good agreement with the experimental values except in the case pyrolusite for one interaction, Mn-Mn. The surfaces energies of pyrolusite calculated from MD are in good agreement with those calculate using the atomistic simulation technique. According to the surface energies calculated using MD simulation and atomistic simulation techniques, surface {110} is the most stable surface for pyrolusite. The total energy of the system is directly proportional to the temperature, thus as the temperature increases the total energy of the system increases. There is a transition at around 2500K; the system changes from solid to liquid. RDFs can be deduced experimentally from X-ray or neutron diffraction studies, and it provides a direct comparison between experiment and simulations.

Chapter 6

EXAFS Experiments

6.1 Introduction

In other varieties, the structures are much more complicated and generally undetermined. For instance EMD and CMD γ- MnO_2 are generally poorly crystallized and their X-ray diffraction patterns may look different from one sample to another. A model has been proposed by De Wolff [1959] to explain such diffraction patterns on the basis of intergrowth domains of pyrolusite and ramsdellite types. An extension of this model including microtwinning has been recently proposed by Ripert [1991a]. It has been claimed that EXAFS spectroscopy is sensitive to the nature of inter-polyhedron linkages of the MnO_2 and can differentiate structures with contrasted edge-over corner sharing ratio like pyrolusite or domains [Gordart et al 1992]. In this chapter, structural aspects of Electrolytic Manganese Dioxide are studied using the Extended X-ray Absorption Fine Structure spectroscopy and compared with results obtained using the molecular dynamics technique.

6.2 Experimental Procedure

The EXAFS experiment measures the variation of a material X-ray energy up to typically 1000 eV beyond the absorption edge. Beyond the edge, oscillations are observed which arise from the interference involving the photoelectron wave ejected from the absorbing atom and the fraction of the photoelectron wave backscattered by atoms surrounding the absorbing atom. Fourier transformation of the oscillatory fine structure (obtained after background subtraction) yields a radial distribution function in real space with peaks corresponding to peaks in the electron density about emitting atom, revealing the local environment of specific atom types such as dopants.

EXAFS spectra were collected on station 8.1 (room temperature) and 9.2 (higher temperature) at the CCLRC Daresbury Synchrotron Radiation Source (SRS). The arrangement of the station is shown in figure 6.1. The synchrotron has electron energy of 2 GeV with an average current of 150 mA during measurements. Station 8.1 is a high bending magnet station, which is designed primarily for dilute sample studies in the energy ranging from 3.5-11 KeV [Davies et al 2000]. The station is equipped with an order-sorting bent double Si(111) crystal monochromator to allow rejection of harmonic contaminants from the monochromatic beam. All the stations have ion chambers for transmission experiments and multi-element solid state detectors (Canberra) for fluorescence experiments. There are order-sorting monochromators on the stations which allow higher harmonics to be rejected from the incident beam.

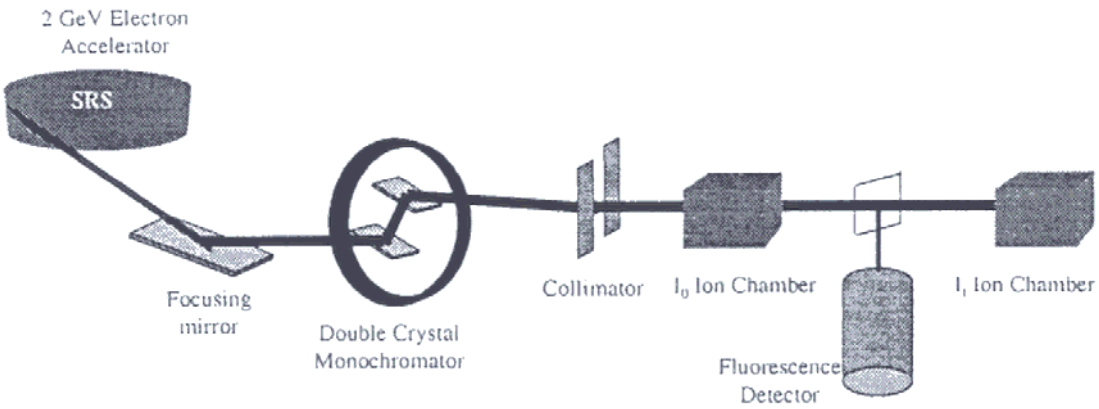

Figure 6.1: Schematic representation of CCLRC Daresbury Synchrotron Radiation Source (SRS) station 9.2

A beam of approximately 1mm high-10mm wide is shaped by passing the white light beam from the synchrotron through lead slits. The beam of the required length is obtained by diffraction from the first crystal and returned to the horizontal direction by diffraction from the second crystal in a double monochromator. The beam then passes through the first chamber called the reference chamber to measure I_0 and the second ion chamber called signal chamber to measure I_t. The ion chambers are partially filled with a rare gas to detect the X-rays, the pressure is adjusted in each chamber so that the reference chamber is 80% transmitting and the signal chamber is 80% absorbing. In the case where samples are powders, they are mixed with a light element non-adsorbing diluents, such as silica or polythene and pressed into a 13mm radius pellet. The sample thickness is adjusted so that the change in absorbance before and after the absorption edge is approximately one.

In this work, the samples were prepared by Delta EMD Pty Ltd Company (South Africa). They were pyrolusite (r107), ramsdellite (r102 and r106) and mixture of the two (RG and RC). For EXAFS experiments, the samples were further prepared by mixing the material (50 mg) with an equal amount of polythene, followed by pressing into a 13mm diameter pellets. EXAFS spectra were collected in a fluorescence mode at room temperature and for higher temperature experiments at 300ºC, 600ºC and 1000 ºC. Multiple EXAFS scans were collected and averaged in order to improve the signal-to-noise ratio.

The data was analyzed using the Daresbury suite of EXAFS analysis programs: EXCALIB, EXBACK and EXCURV98 [Binstead 1998], employing rapid curved wave theory [Gurman et al 1984] and assuming single scattering processes. Phase shifts were derived using Hedin-Lunqvist [Hedin and Lundqvist 1969] excited state and von Barth and Hedin [1972] ground exchange potentials within EXCURV98. EXCALIB is used to calibrate the experimental data by converting the monochromator angle and allows for background counts in the ion chambers. It is also used to add multiple spectra and from which the same sample run to improve the signal-to-noise ratio. EXBACK is used to produce the normalized EXAFS, $\chi(k)$ as a function of k, the X-ray wave vector. This involves the conversion to k-space, fitting and subtraction of the background and normalization of the edge step height. It also carries out the Fourier transform, enabling the interpretation of the oscillations in terms of radial distributions. EXCURV98 is used to perform the least-square fitting of the data to the EXAFS expression equation 2.69. It is least-square fitting of the data to the model of the local

structure with parameters such as N_j, r_j and A_j as variables. The iterative least-square fitting provides the best fit to the normalized absorption plot.

For each back transformed spectrum, a theoretical fit was obtained by adding shells of atoms around the central excited atom and allowing Fermi energy a correction to the absolute edge position (Fermi energy, Radial distance, and Debye-Waller Factors to float). The parameters defined in the fitting are number of shells, *i,* the coordination numbers of the shell, N_i, the type of atom in the shell, T_i, the distance of the shell from the central atom, r_i, and the Debye-Waller factor, A_i, of the shell. The Debye-Waller type factors contain contributions from thermal disorder and static vibrations in radial distances. The potentials and the phase shifts are calculated theoretically by the programmes. The theoretical model is the compared to the experimental data and refined until the parameters obtained are consistent and produce the best fit. The quality of the fit is measured by an R-factor, which is defined as the sum of the differences between the experimental $\chi(k)$ and the calculated $\chi(k)$ at each data point in k [Binstead 1998], which is given as a percentage:

$$R_{EXAFS} = \sum_{i}^{n} \left[\sigma_i \left| \chi_i^{\exp er}(k) - \chi_i^{theo}(k) \right| \right]^{-1} x100\% \qquad (6.1)$$

where

$$\left[\frac{i}{\sigma_i} \right] = \frac{k(i)^n}{\sum_j k(j) \left| \exp^{(i)} \right|} \qquad (6.2)$$

The Fourier transformation has to be performed with a phase-shift, usually the one for the atom in the first coordination shell. Tabulated output from EXCURVE contains the best-fit parameters, errors on the parameters, the correlation matrix for the parameters and quality of the fit.

6.3 Results and Discussions

In this section Fourier transformation plots are used to describe the structural properties of pyrolusite, ramsdellite and the mixture of the two. Fourier transform is corrected with the phase shift of the first shell, in this case manganese. It should be noted that the quantitative data presented in the tables has been derived from fitting to the normalized EXAFS spectra using EXCURVE programme. An initial structural model is required for the EXAFS fitting, in this thesis, crystallographic data for pyrolusite and ramsdellite were used.

6.3.1 Pyrolusite

The Mn K-edge EXAFS spectrum was collected in transmission model at room temperature on station 8.1 at Daresbury SRS. The structural parameters extracted from the EXAFS spectrum are average atomic distance, average coordination number, mean-square variation of bond length or relative to Debye-Waller factor broadening and the type of atomic species around the central atom. The parameters are listed in table 6.1. Radial Distribution Functions extracted from the EXAFS spectra of pyrolusite are presented in figure 6.2 and they are obtained from Fourier transformation function, $\chi(k)$ defined under methodology (Chapter2).

They are characterized by three peaks with different intensities. The first peak is due to the oxygen octahedron, located at 1.899 Å surrounded by six atoms. The second peak is due to the cation neighbours, located at 2.885 Å in edge sharing octahedra. The third peak is due to the second oxygen shell located at 3.620 Å and the second cationic neighbours, located at 3.457 Å.

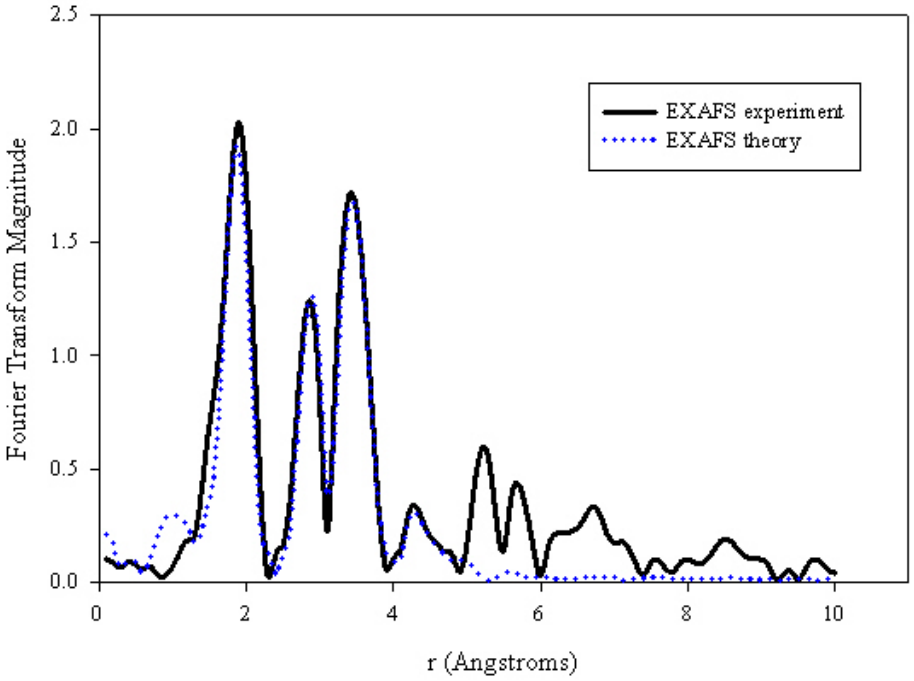

Figure 6.2: The Mn-K edge EXAFS for pyrolusite (r107 sample) shown by the corresponding Fourier Transform. The solid line is the experimental data and the dashed line is the theoretical data.

Number of Atoms	Type	Radial Distances	D-W Factor
6	O	1.899	0.007
2	Mn	2.885	0.004
8	O	3.620	0.010
8	Mn	3.457	0.008
8	O	4.029	0.031

Table 6.1: The Mn-K edge EXAFS structural properties for pyrolusite at room temperature.

6.3.2 Ramsdellite

The results are based on two different samples of ramsdellite (r102 and r107). Fourier transformations produce the radial distribution function of the local atomic environment around the probe element. The structural properties of the samples r102 and r106 are listed in Table 6.2 and 6.3 respectively. The EXAFS spectra and the corresponding Fourier transforms were corrected with the phase shifts and they were obtained after the background subtraction, they yield the radial distribution functions in real space with peaks corresponding to the peaks in electron density revealing the local environment of the system. The spectra of the two samples do not differ that much and they look similar to the one of pyrolusite sample. For r102 the first peak corresponding to the oxygen octahedrum is located at 1.898 Å whereas the one for r106 is at 1.899 Å. They also have the same number of atoms at a particular distance. EXAFS results agree very well with the results obtained with molecular dynamics calculations and the available results from other publications. For example the radial distance for the oxygen octahedrum obtained using EXAFS is 1.898 Å compared to 1.891 Å obtained using the molecular dynamics technique. The RDFs graphs are shown in figures 6.3 and 6.4 for r102 and r106 samples respectively.

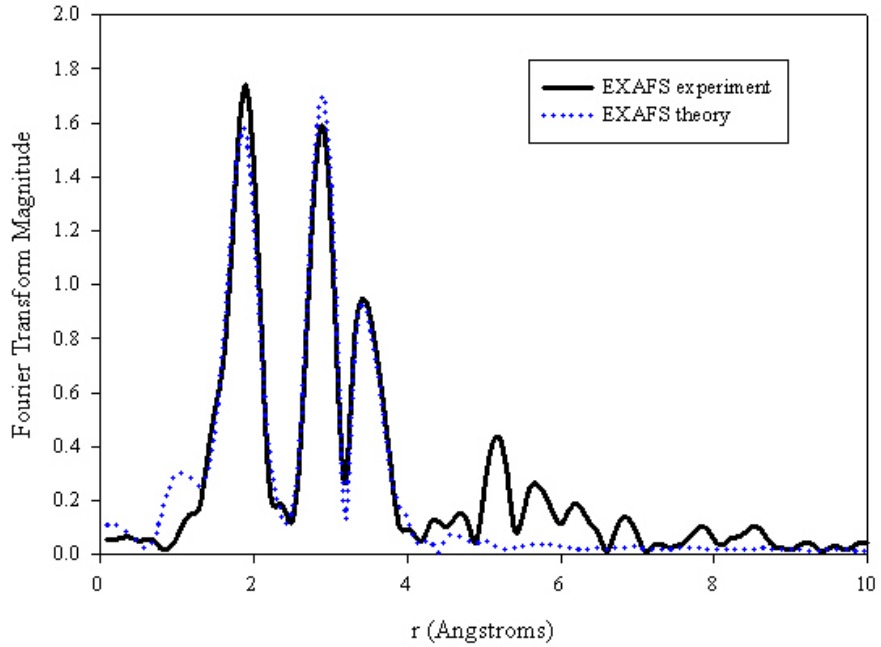

Figure 6.3: The Mn-K edge EXAFS for ramsdellite (r102 sample) shown by the corresponding Fourier Transform. The solid line is the experimental data and the dashed line is the theoretical data.

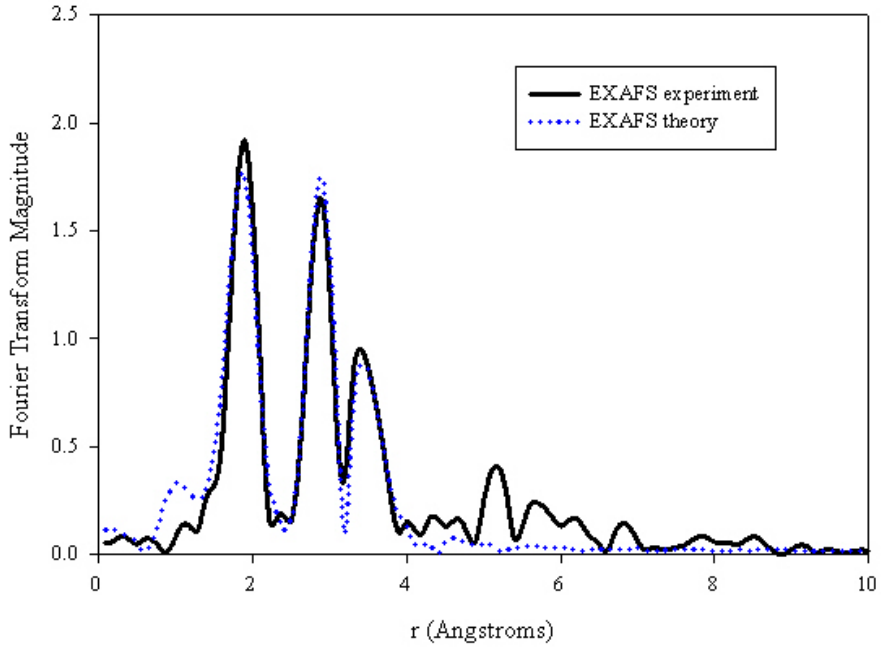

Figure 6.4: The Mn-K edge EXAFS for ramsdellite (r106 sample) shown by the corresponding Fourier Transform. The solid line is the experimental data and the dashed line is the theoretical data.

Number of Atoms	Type	Radial Distances	D-W Factor
8	O	1.898	0.015
4	Mn	2.886	0.008
7	O	3.597	0.018
4	Mn	3.448	0.007

Table 6.2: The Mn-K edge EXAFS structural properties for ramsdellite (r102 sample) at room temperature.

Number of Atoms	Type	Radial Distances	D-W Factor
8	O	1.899	0.013
4	Mn	2.883	0.008
7	O	3.604	0.022
4	Mn	3.445	0.007

Table 6.3: The Mn-K edge EXAFS structural properties for ramsdellite (r106) at room temperature.

6.3.3 Electrolytic Manganese Dioxide

The Fourier transformation as a function of the radial distance and the EXAFS experimental results as a function of curved wave SS theory are presented for two different samples, RC, and RG and two best fit parameters were considered for each sample. The EXAFS experimental and theoretical fittings are shown in figures 6.5-6.8. All the systems reveal a presence of four peaks corresponding to the first shell cation-anion and the second cation-cation radial distances. The first peaks result from the backscattering corresponding to the first shell cation-anion interactions, Mn-O whereas the second peaks correspond to the backscattering

from the second cation-cation interactions, Mn-Mn. The best fit values for radial distances; Debye Waller factors and number of nearest neighbouring atoms obtained from the EXAFS spectra are presented in Tables 6.6-6.9. Bond lengths obtained using the molecular dynamics technique and EXAFS spectroscopy are compared in Table 6.8.

Number of Atoms	Type	Radial Distances	D-W Factor
6	O	1.899	0.011
2	Mn	2.889	0.008
8	O	3.661	0.005
8	Mn	3.476	0.017
8	O	4.205	0.031
2	Mn	4.533	0.014
4	O	4.453	0.028

Table 6.4: The Mn-K edge EXAFS structural properties for EMD (RC1 sample) at room temperature.

Number of Atoms	Type	Radial Distances	D-W Factor
8	O	1.896	0.023
4	Mn	2.880	0.018
7	O	3.622	0.010
4	Mn	3.456	0.008

Table 6.5: The Mn-K edge EXAFS structural properties for EMD (RC2 sample) at room temperature.

Number of Atoms	Type	Radial Distances	D-W Factor
6	O	1.900	0.009
2	Mn	2.885	0.005
8	O	3.659	0.005
8	Mn	3.471	0.016
8	O	4.194	0.030
2	Mn	4.634	0.049
4	O	4.472	0.025

Table 6.6: The Mn-K edge EXAFS structural properties for EMD (RG1 sample) at room temperature.

Number of Atoms	Type	Radial Distances	D-W Factor
8	O	1.895	0.019
4	Mn	2.879	0.014
7	O	3.626	0.016
4	Mn	3.452	0.009

Table 6.7: The Mn-K edge EXAFS structural properties for EMD (RG2 sample) at room temperature.

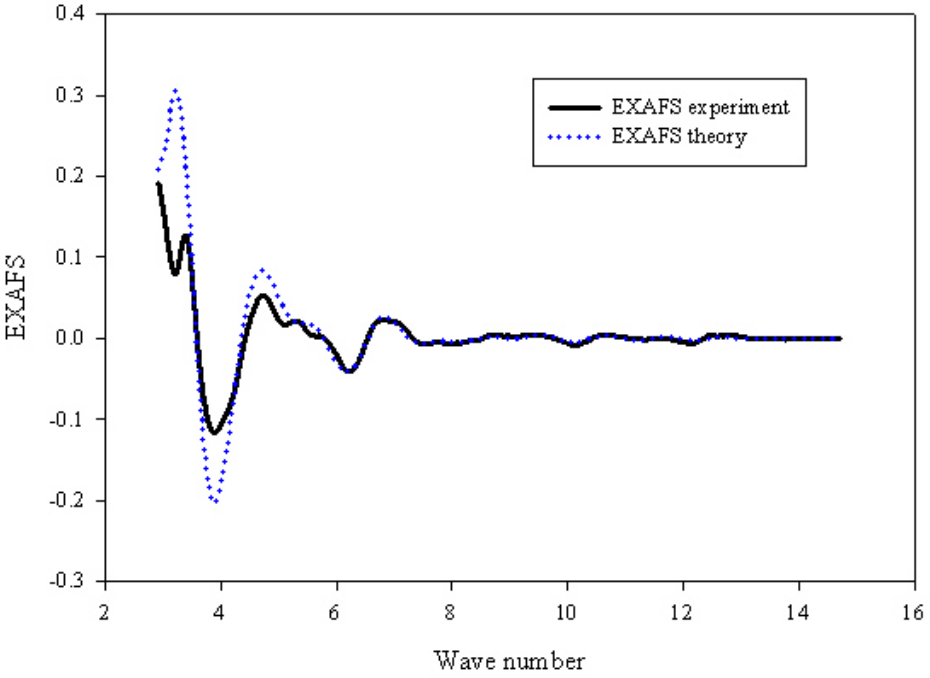

(a)

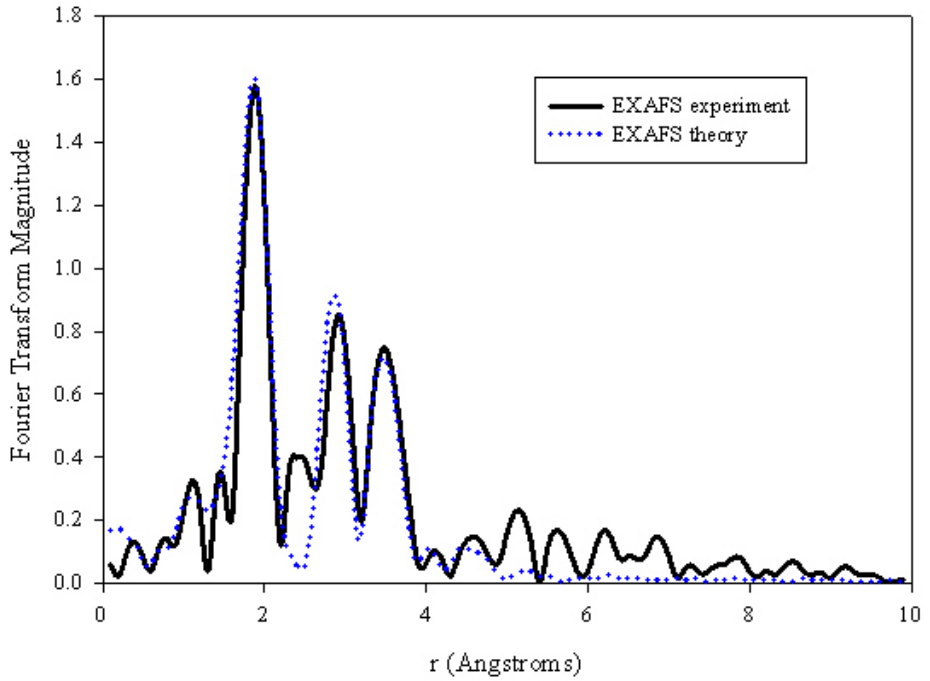

(b)

Figure 6.5 (a) and (b): The Mn-K edge EXAFS for EMD (RC1 sample) shown in (a) is the EXAFS and (b) is the corresponding Fourier Transform. The solid line is the experimental data and the dashed line is the theoretical data.

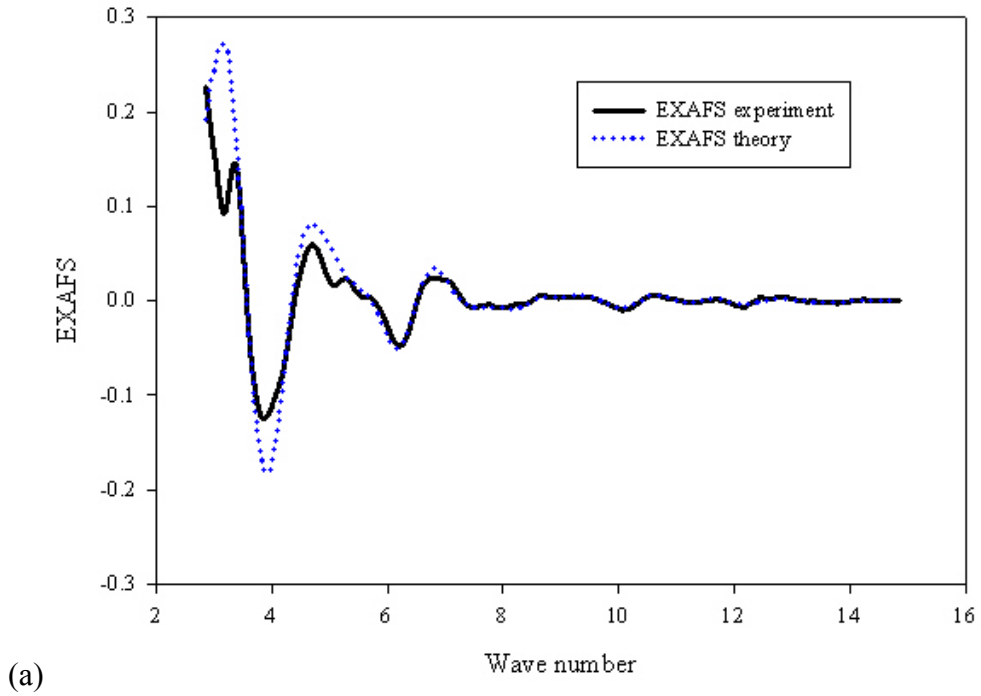

(a)

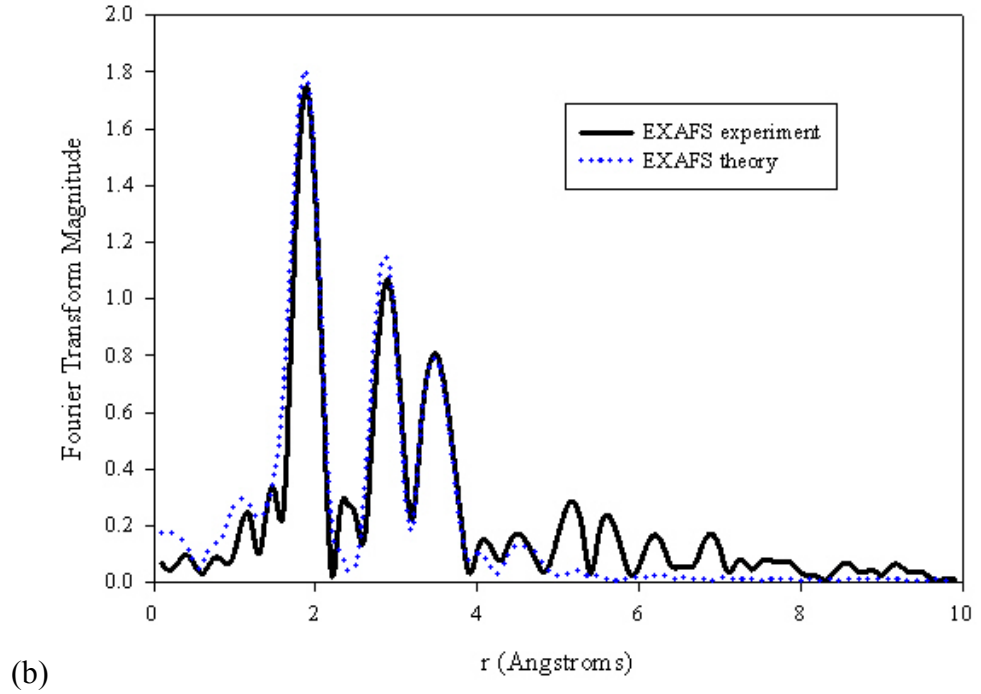

(b)

Figure 6.6 (a) and (b): The Mn-K edge EXAFS for EMD (RG1 sample) shown in (a) is the EXAFS and (b) is the corresponding Fourier Transform. The solid line is the experimental data and the dashed line is the theoretical data.

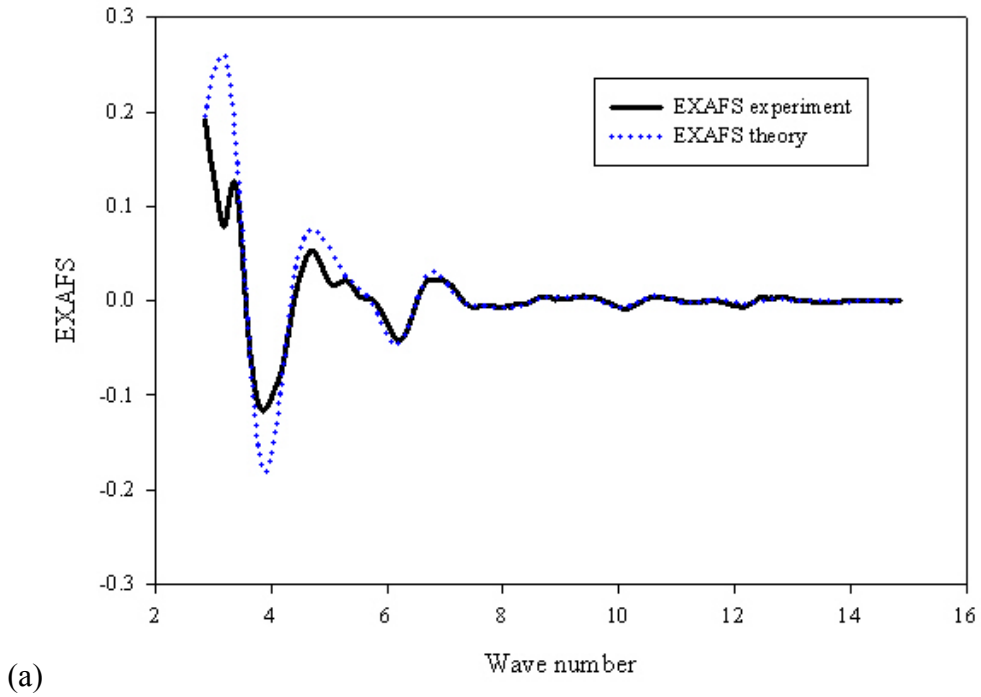

(a)

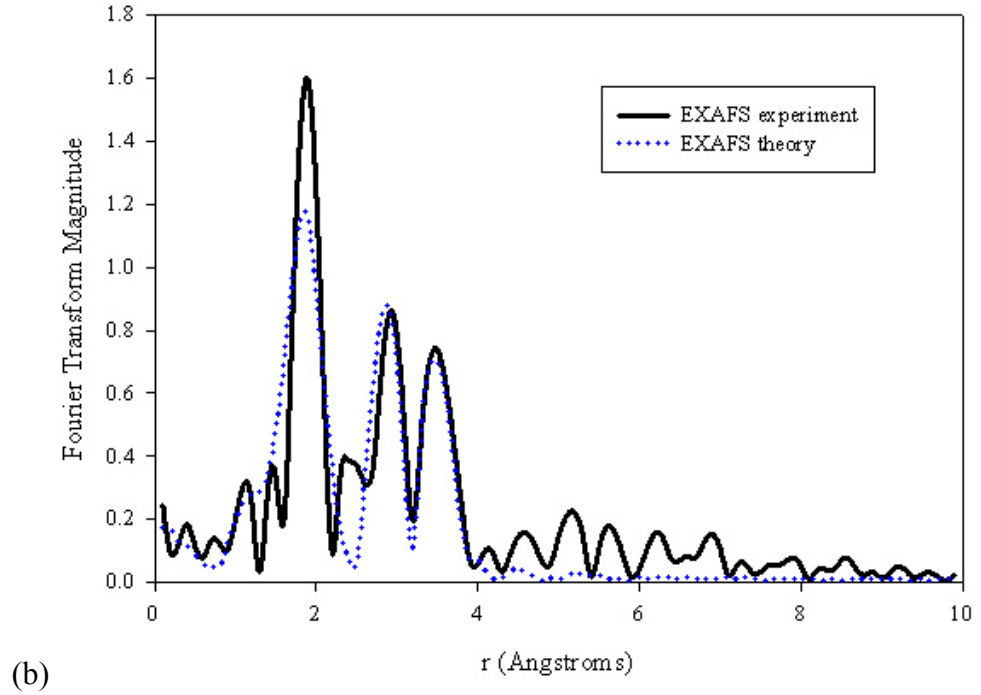

(b)

Figure 6.7 (a) and (b): The Mn-K edge EXAFS for EMD (RG2 sample) shown in (a) is the EXAFS and (b) is the corresponding Fourier Transform. The solid line is the experimental data and the dashed line is the theoretical data.

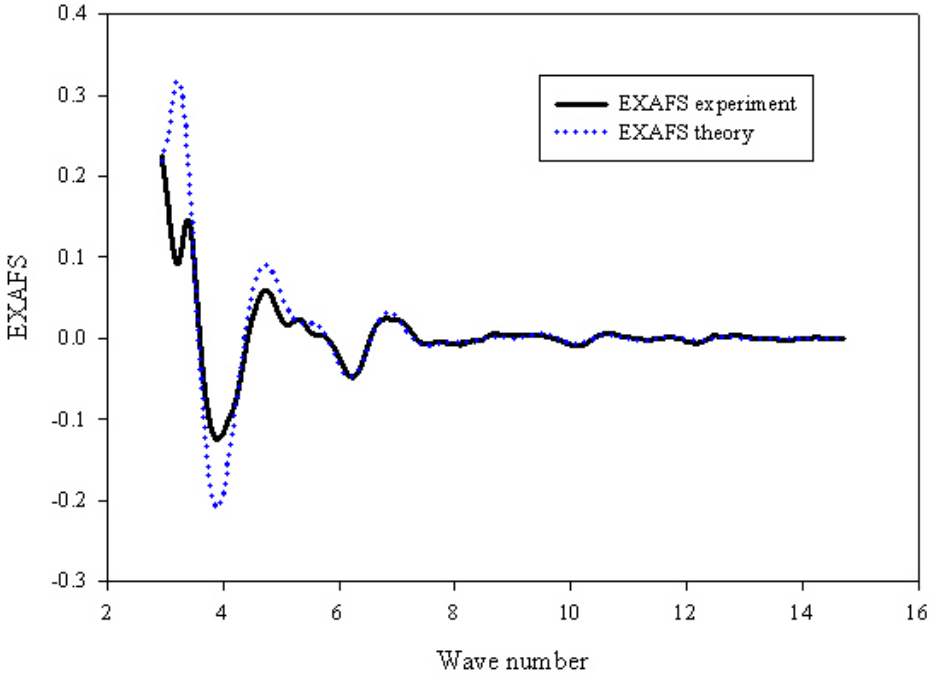

(a)

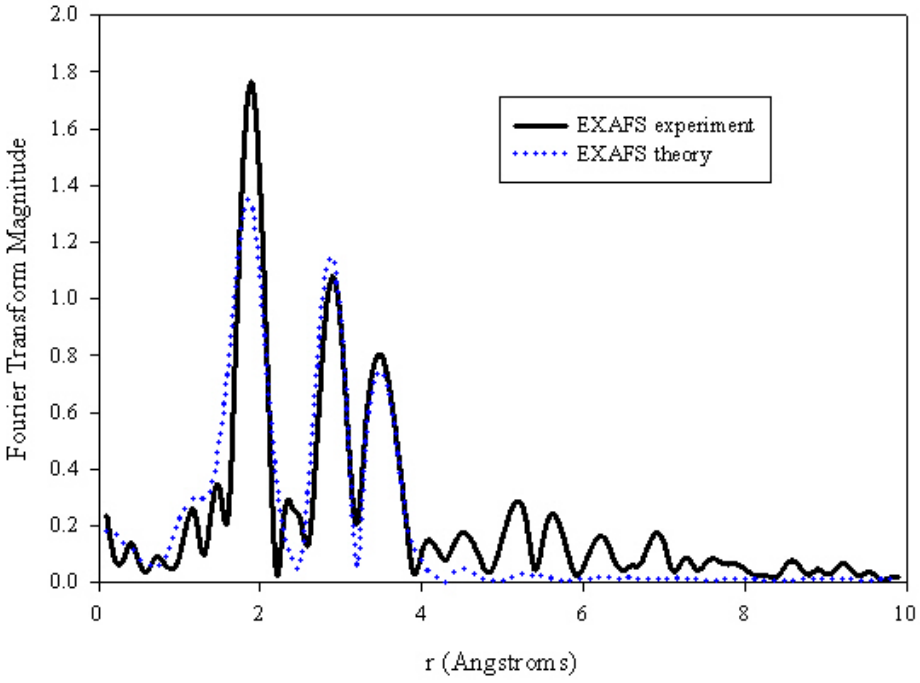

(b)

Figure 6.8 (a) and (b): The Mn-K edge EXAFS for EMD (RC2 sample) shown in (a) is the EXAFS and (b) is the corresponding Fourier Transform. The solid line is the experimental data and the dashed line is the theoretical data.

		EXAFS	MD	Petit'98	Manceau'88	Godart'92	Li'88
Pyrolusite	O	1.899	1.911		1.9	1.90, 1.86	1.88
	Mn	2.885	2.954	2.8	2.88	2.87, 2.87	2.87
	Mn	3.620	3.937	3.4		3.40, 3.44	
	O	3.457	3.445	3.4	3.45	3.44, 3.44	4.06
	O	4.029	....				
Ramsdellite	O	1.898	1.891			1.90, 1.88	1.894
	Mn	2.886	2.973	2.86	2.90	2.90, 2.88	2.833
	Mn	3.597	3.505			3.40, 3.46	
	O	3.448	3.406	3.44	3.48	3.41, 3.42	4.082

Table 6.8: Comparison of EXAFS, molecular dynamics and available radial distances results for pyrolusite and ramsdellite MnO_2.

6.4 Conclusion

Extended X-ray Absorption Fine Structure spectroscopy has been used to study different structures of manganese dioxide. Radial Distribution Functions were used in defining the structures, in particular the radial distances, number of neighbouring atoms/coordination number and the type of atoms. The RDF is an example of pair correlation function, which describes how the atoms in a system are radially packed around each other. It is an effective way of describing the average structure of disordered systems. Structural information is being obtained by analyzing the Extended X-ray Absorption Fine Structure, which extends up to 1000 eV above the absorption edge energy. EXAFS results are in good agreement with the molecular dynamics results. Thus, the radial distances obtained from the EXAFS experiments accord with those obtained from molecular dynamics simulations.

Chapter 7

Ramsdellite-Pyrolusite Interfaces

7.1 Introduction

In this Chapter we build various types of intergrowths of pyrolusite and ramsdellite structures and compare associated calculated radial distribution functions with experimental results.

7.2 Methodology

The interface is built by specifying the left and right sides of the interface using the Interface Left side and Interface Right side control panels of the Accelrys cerius^2 Interface Builder. Pyrolusite was specified as the crystal model for the right side and ramsdellite was specified as the one for the left side. Usually the crystal used for the left side is different from the crystal for the right side. However, to model a twinning or fault in a crystal, the same crystal model is used. The interface plane is specified by the Miller indices h,k,l in this case the planes were specified guided by the surface energies obtained using the atomistic simulation technique. Thus, surfaces with more or less the same surface energies were matched to build an interface. The {010} surface for pyrolusite has the

surface energy 2.43 $J.m^{-2}$ and was matched with {100} surface for ramsdellite with the surface energy of 2.45 $J.m^{-2}$. Table 7.1 gives the matching surface energies of pyrolusite and ramsdellite structures obtained using METADISE code for atomistic simulations in section 2.5.3. The depth for the interface is specified as the length of the pure crystal on a particular side, that is, the thickness of the slab. The parameters used for the left and right sides are listed in Table 7.2.

Pyrolusite			**Ramsdellite**		
Surface	Energy ($J.m^{-2}$)	Symmetry	Surface	Energy ($J.m^{-2}$)	Symmetry
{100}	2.43	symm	{100}	2.45	symm
			{010}	2.49	asymm
			{110}	2.45	symm
			{210}	2.43	symm
{110}	2.88	symm	{010}	2.83	asymm
{120}	2.99	symm	{201}	2.94	asymm
{101}	3.93	symm	{210}	3.94	symm

Table 7.1: Energetically equivalent surfaces for pyrolusite and ramsdellite.

The interfacial separation used was 0 Å so that the models will become one model. Second side of the Interface Mesh used is 5.00 Å perpendicular to the first side for both Left and Right Side. The match points used were 0.0, 22.555, 0.00 [u v w] and 37.883, 1.423, 0.00 [u v w] for Right Side and Left Side respectively. The interface is built using ATOMIC cleave, that is, is being built by cutting atoms from the crystal regardless of how they form molecules. Since the interface is defined on both sides, the Interface Building control panel is used to build the

interface and finally the crystal is being built using the Crystal Building control panel. The models built are shown under results and discussions section.

Right Side (Pyrolusite Model)		Left Side (Ramsdellite Model)	
Plane (hkl)	{100}	Plane (hkl)	{100}
Depth	4.414 Å	Depth	9.370 Å
[0 0 1]	2.861 Å	[0 0 1]	2.850 Å

Table 7.2: Parameters used for the Left Side and Right Side Interface builder.

The plane wave pseudopotential method is used to perform structural optimizations of the intergrowths. The lattice parameters of the intergrowths were determined using the LSDA version within the CASTEP code and details of the calculations are given in Chapter 3.

A wide range of observed powder X-ray diffraction patterns with a new structural model which incorporates two types of defects into an idealized ramsdellite structure was successfully explained [Pannetier 1991, Pannetier 1992, Ripert 1991a, Ripert 1991b, Chabre 1995]. The first type is a random planar fault based on the model originally constructed by de Wolff [1959] which exploits the fact that pyrolusite and ramsdellite possess intimately related structures due to the similarity of their oxygen frameworks. The intergrowth structures constructed in this study may be described as a random distribution of pyrolusite (P) layers formed from single chains and ramsdellite (R) layers formed from double chains [MacLean 1996]. Possible de Wolff intergrowth structures formed from a random sequence of layers derived from pyrolusite and ramsdellite structures were

obtained from MacLean [1996] and Hill et al. [2004]. Hill et al identified EMD structures that produced XRD patterns that compared best with the experimental values. This type of random planar defect has been given the de Wolff disorder. The second type of defect is that of random microtwinning of the ramsdellite structure on the (021) or (061) planes [Chabre 1995].

7.3 Results and Discussions

7.3.1 R1P1(Ramsdellite-Pyrolusite Interface)

The ramsdellite-pyrolusite interface is shown in figures 7.1 and 7.2. Figure 7.1 shows a crystal structure of R1P1 whereas figure 7.2 shows the visualized (increased in x, y, and z by one unit cell) structure of R1P1. Ramsdellite had twelve atoms whilst pyrolusite had six atoms, which results with the interface having total number of atoms equals eighteen. The parameter of the interface are $a = 14.0439$ Å, $b = 4.6352$ Å, $c = 2.9878$ Å and α, β, and $\gamma = 90°$, and the structure is relaxed using the energy minimization technique. The rigid ion model interatomic potentials, used for pyrolusite and ramsdellite crystals in surface energy (Chapter 4) calculations, were employed and are listed in Table 4.1. The system is minimized in order to verify the validity of the potential used. The minimized lattice parameters are given in Table 7.3 and they show that the structure is well minimized and thus the potentials perform well on the ramsdellite-pyrolusite interface as expected. The crystal appears to relax relatively more along the *a* lattice parameter.

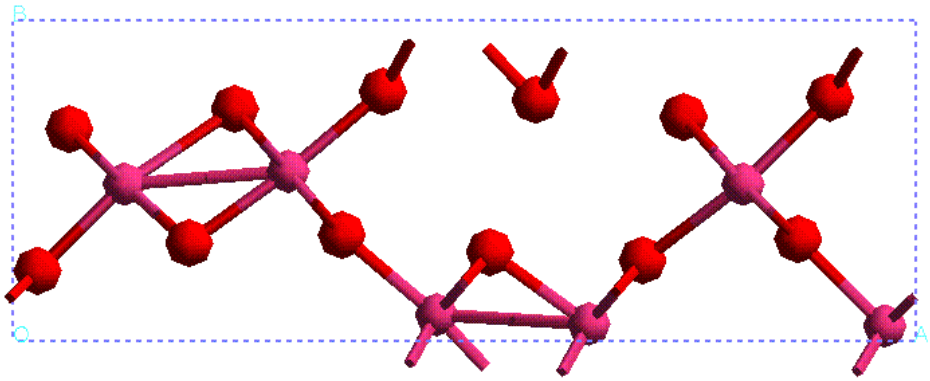

Figure 7.1: Ramsdellite-pyrolusite intergrowth with the half of pyrolusite on the left, ramsdellite part on the centre and other part of pyrolusite on the right hand side.

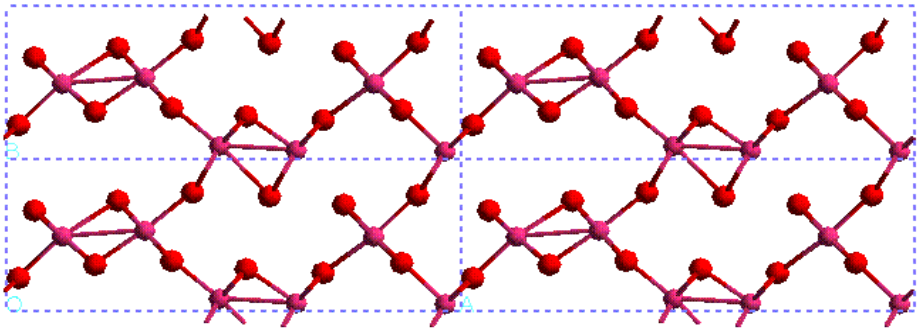

Figure 7.2: Visualized picture of figure 7.1 above.

Lattice Parameter	Unrelaxed	Relaxed	Difference
a (Å)	14.044	13.599	0.445
b (Å)	4.635	4.393	0.242
c (Å)	2.988	2.950	0.038
α, β, γ (˚)	90.000	90.000	0.000

Table 7.3: Unrelaxed and relaxed lattice parameters for the R1P1 interface.

Molecular dynamics calculations were carried out on the intergrowth structure. Figures 7.3, 7.4 and 7.5 depict the radial distribution functions, for Mn-Mn, Mn-O and O-O pairs, of the R1P1 structure at 300K 1500K and 3500K, and figures 7.6 to 7.8 show the radial distribution functions at different temperatures (from 300K

to 3500K). The graphs are showing pair distribution functions as a function of the radial distance where the minimum and maximum peaks can be defined. In a crystal RDFs have an infinite number of sharp peaks whose separation and heights are characteristics of the lattice structure. The interface behaves very similar to pyrolusite and ramsdellite structures in terms of peaks, thus, Mn-O interaction is represented by the first highest peak of magnitude 15.0 followed by the O-O interaction. The first maximum peak almost occurs at 1.9 Å. The interatomic distances do not differ much from those of pyrolusite and ramsdellite. The RDFs for all these three pairs show an increase in peak broadening as the temperature is increased, which indicates a greater degree of disorder. At higher temperatures the RDFs become structureless, hence depicting the onset of the structure melting and eventually some of the peaks merge.

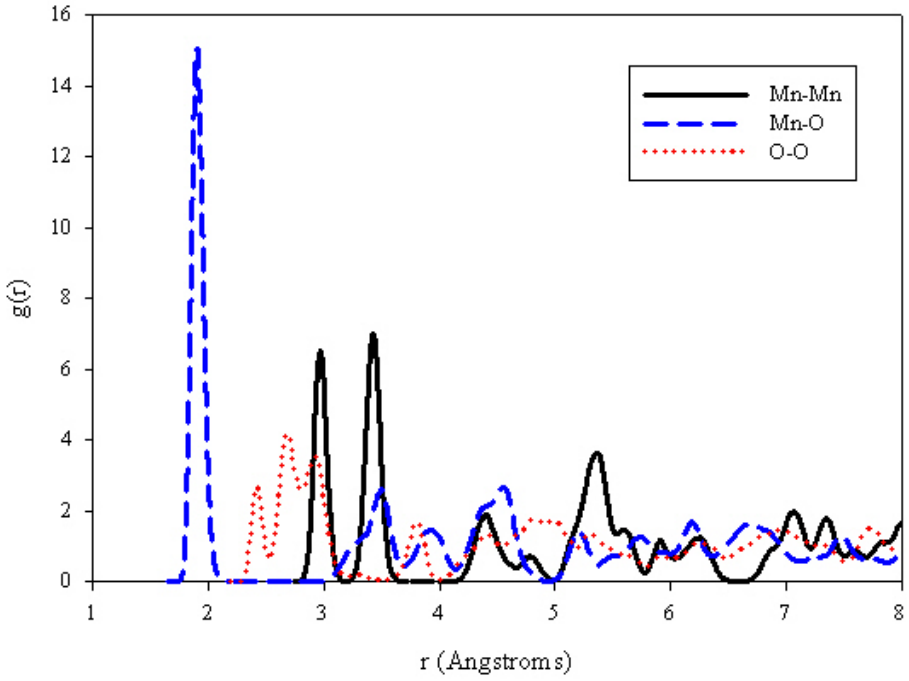

Figure 7.3: Radial distribution functions for R1P1 structure showing Mn-Mn, Mn-O and O-O interactions at 300K.

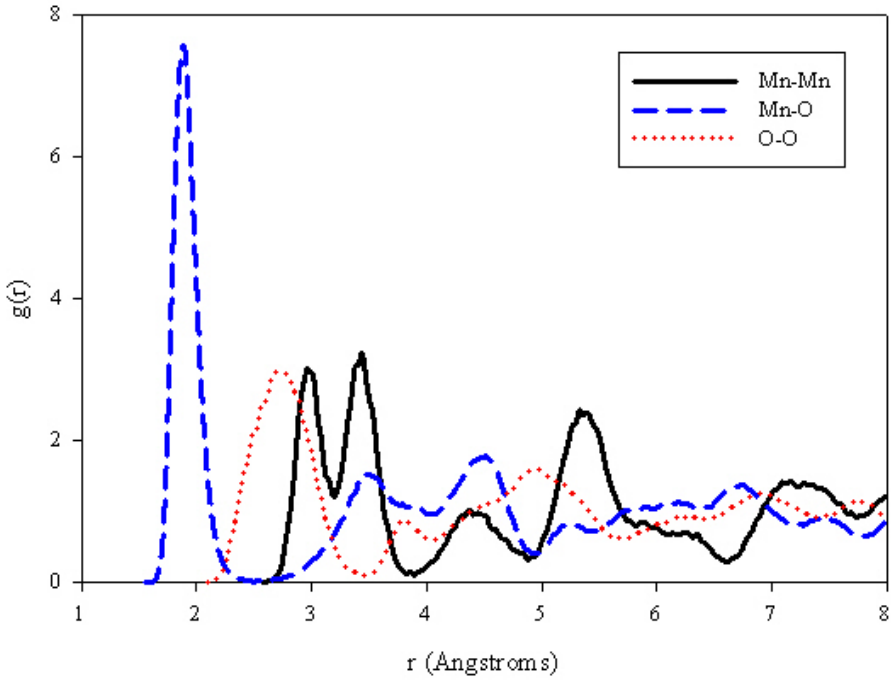

Figure 7.4: Radial distribution functions for R1P1 structure showing Mn-Mn, Mn-O and O-O interactions at 1500K.

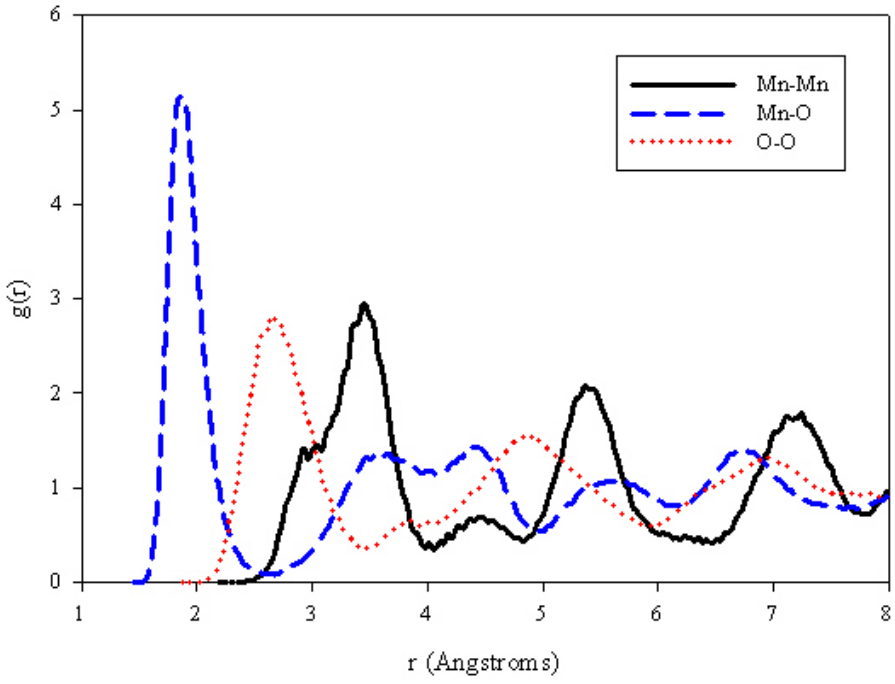

Figure 7.5: Radial distribution functions for R1P1 structure showing Mn-Mn, Mn-O and O-O interactions at 3500K.

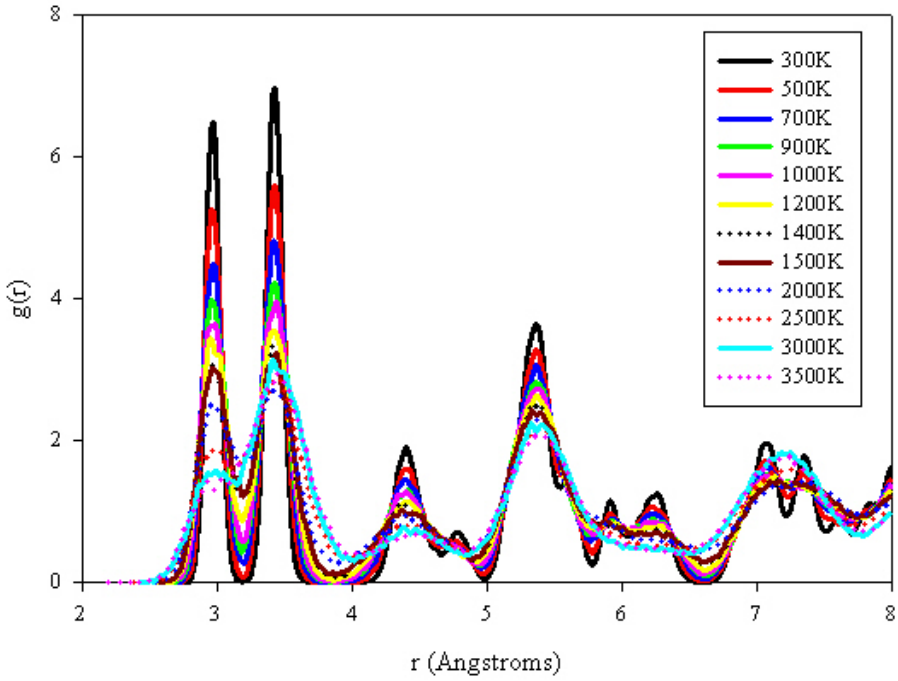

Figure 7.6: Radial distribution functions for R1P1 structure showing Mn-Mn pair at different temperatures.

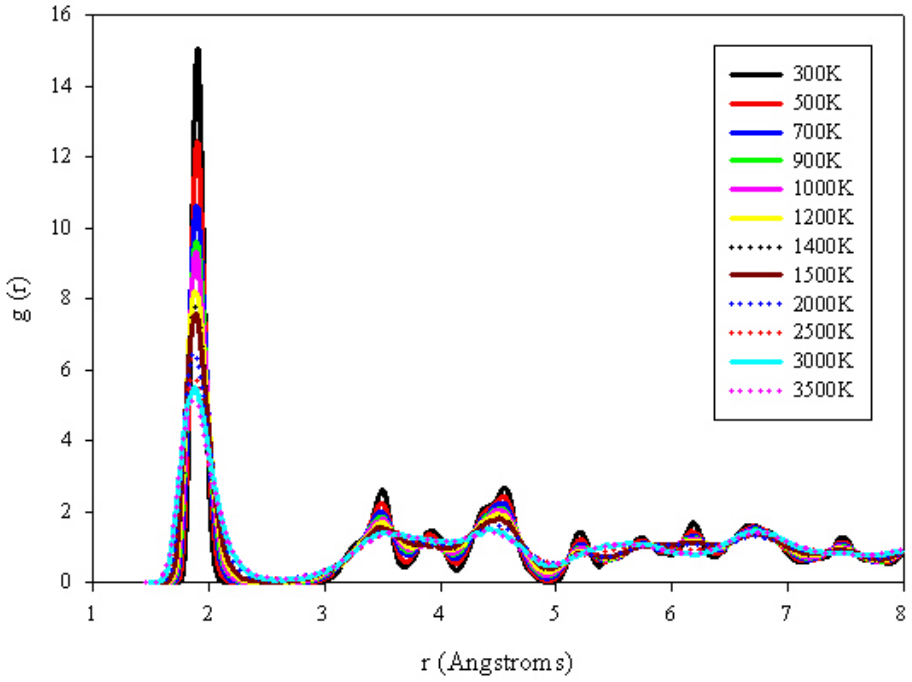

Figure 7.7: Radial distribution functions for R1P1 structure showing Mn-O pair at different temperatures.

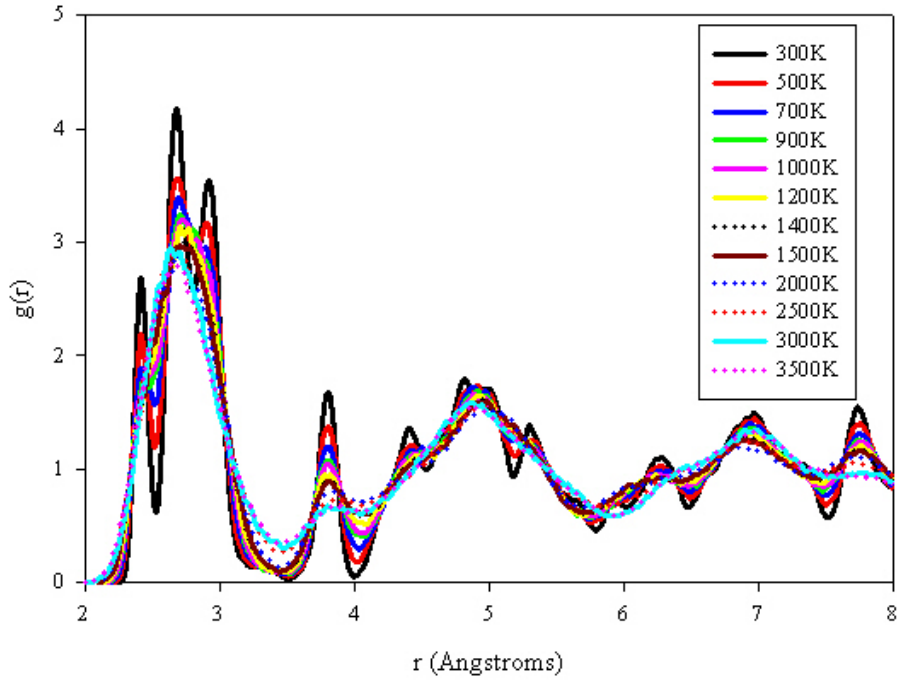

Figure 7.8: Radial distribution functions for R1P1 structure showing O-O pair at different temperatures.

7.3.2 R3P1(Three Ramsdellite-One Pyrolusite Interface)

R3P1 structure consisting of three ramsdellite and one pyrolusite unit cells is shown in figures 7.9 and contains 42 atoms. The oxygen atoms are represented by the red balls and manganese atoms are represented by the pink balls. Figure 7.10 presents a supercell of four R3P1 structure and depicts a smooth continuation of the interface. Table 7.4 shows that the relaxed lattice parameters do not differ much with the unrelaxed and substantial relaxation occurs in the x-direction. The radial distribution functions are given in figures 7.11 to 7.16. Figures 7.14-7.16 show the effect of the temperature on the Mn-Mn, Mn-O and O-O pair interactions. As expected, the radial distribution functions for all three pairs indicate that as the temperature is raised the heights of the peaks decrease and the peaks become broader. Mn-Mn pair exhibits the peak broadening more clearly

than the other two pairs. O-O pair possesses a double peak at lower radial distances, which collapses into a single peak as the temperature is increased; a complete loss of correlation is noted. The same behaviour is observed for Mn-O and O-O RDFs.

Lattice Parameter	Unrelaxed	Relaxed	Difference
a (Å)	32.9000	31.956	0.944
b (Å)	5.000	4.372	0.628
c (Å)	2.860	2.958	-0.098
α, β, γ (˚)	90.000	90.000	0.000

Table 7.4: Unrelaxed and relaxed lattice parameters for the R3P1 interface.

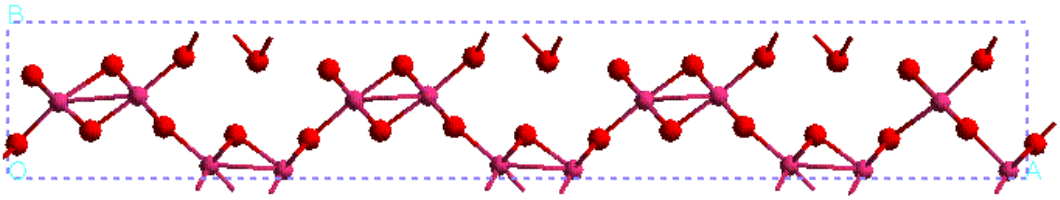

Figure 7.9: R3P1 crystal model represented in terms of balls and sticks.

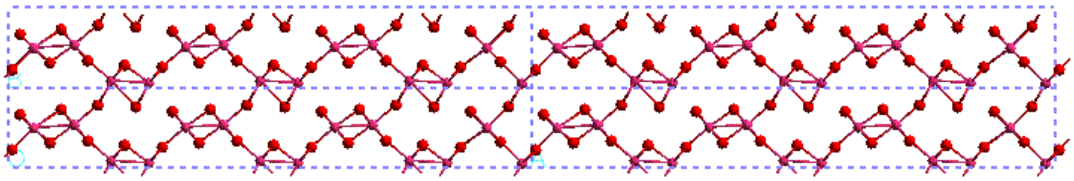

Figure 7.10: R3P1 visualized crystal model.

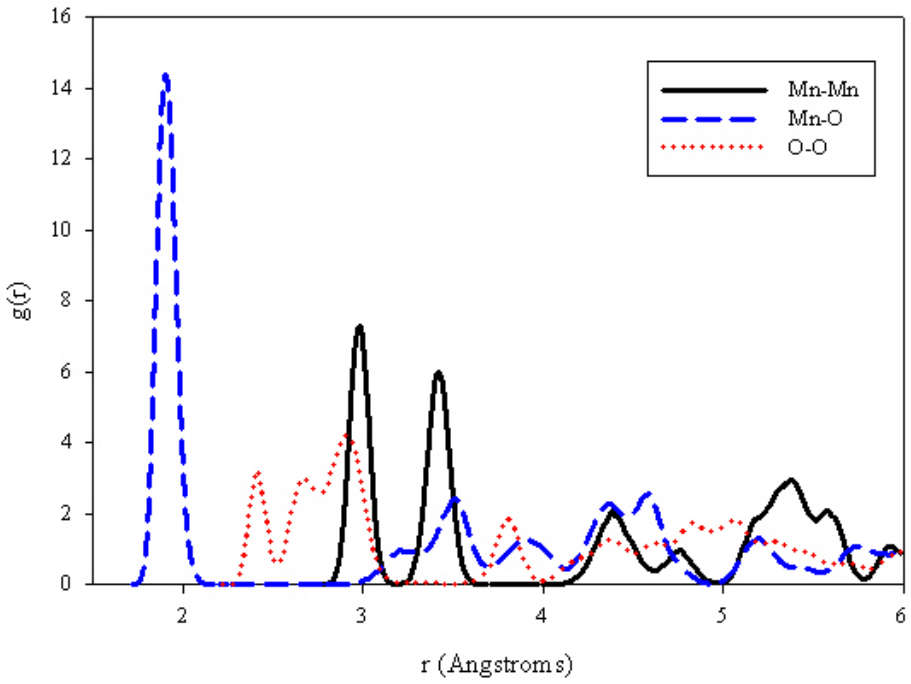

Figure 7.11: Radial Distribution Functions for R3P1 structure showing Mn-Mn, Mn-O and O-O interactions at 300K.

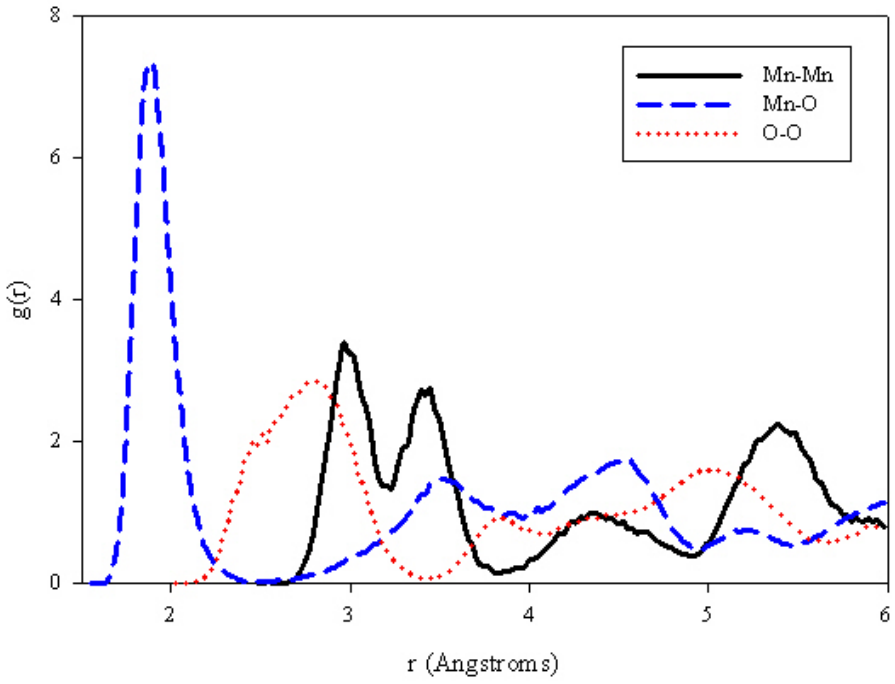

Figure 7.12: Radial Distribution Functions for R3P1 structure showing Mn-Mn, Mn-O and O-O interactions at 1500K.

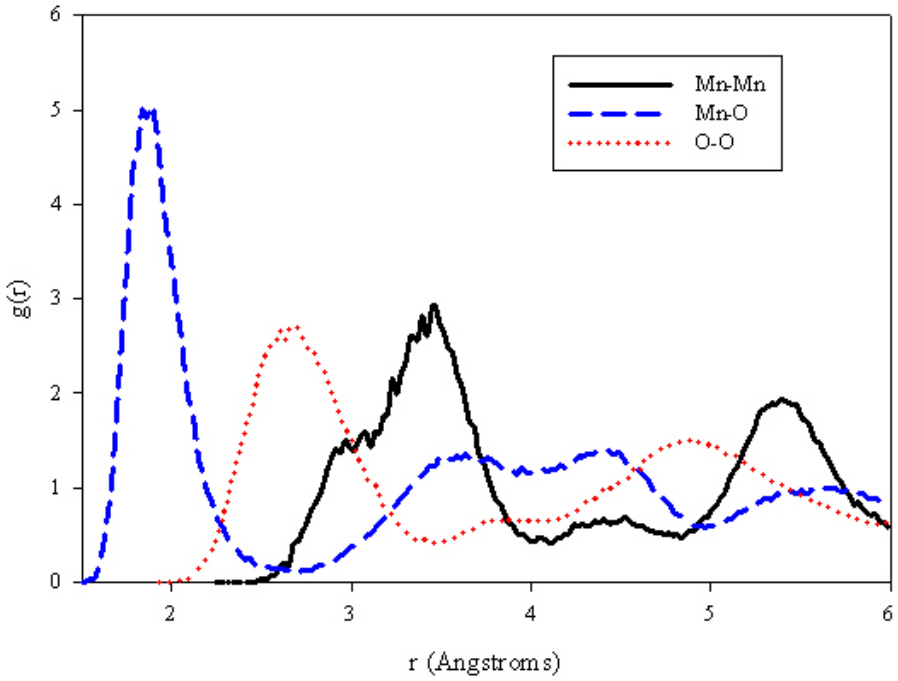

Figure 7.13: Radial Distribution Functions for R3P1 structure showing Mn-Mn, Mn-O and O-O interactions at 3500K.

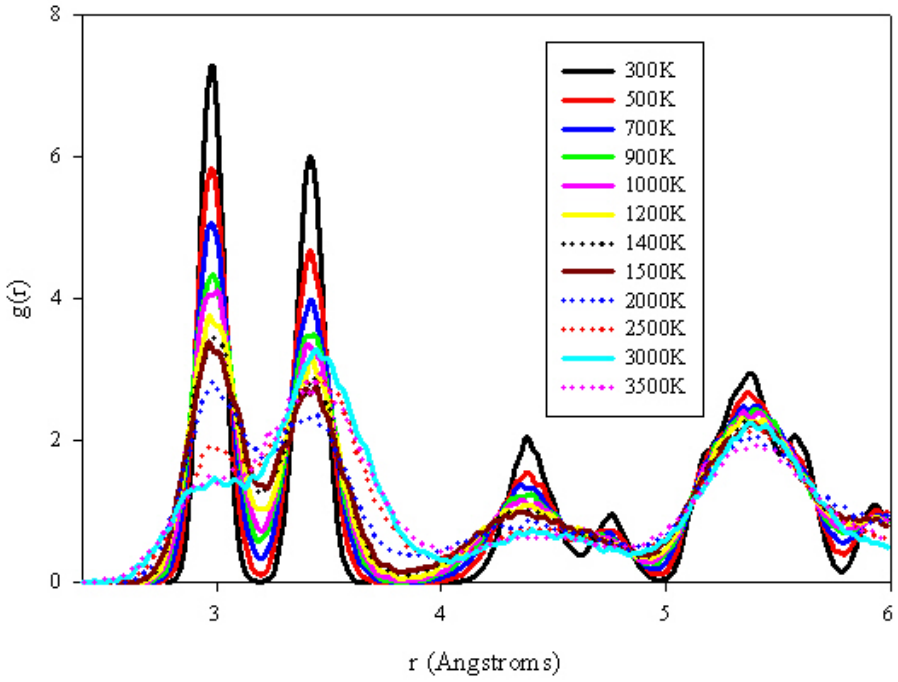

Figure 7.14: Radial Distribution Functions for R3P1 structure showing Mn-Mn pair at different temperatures.

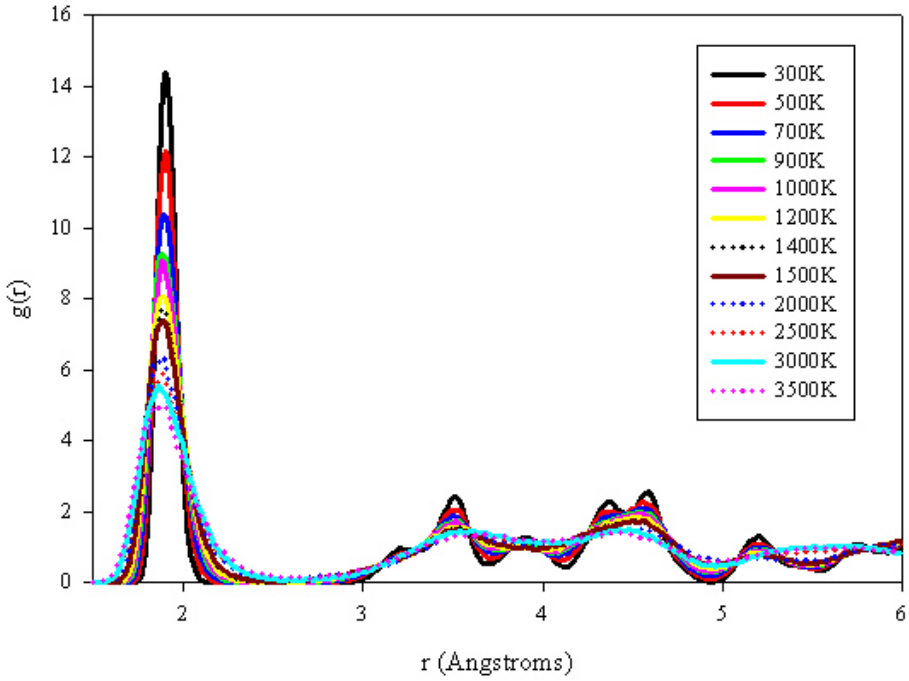

Figure 7.15: Radial Distribution Functions for R3P1 structure showing Mn-O pair at different temperatures.

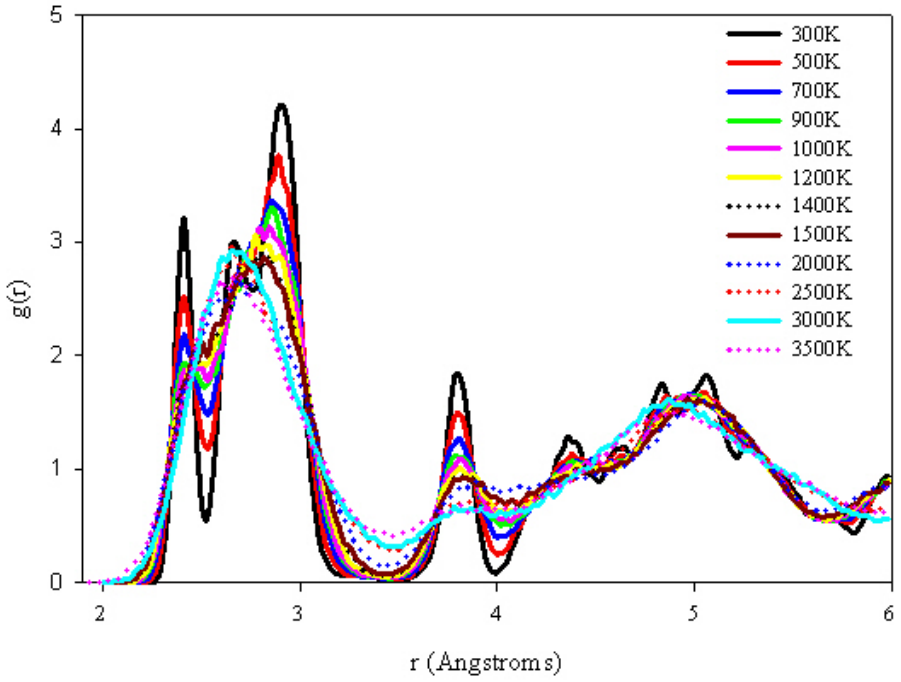

Figure 7.16: Radial Distribution Functions for R3P1 structure showing O-O pair at different temperatures.

7.3.3 R3P1R1

The R3P1R1 structure is composed of three ramsdellite, one pyrolusite and one-ramsdellite unit cells (RRRPR or R3P1R1), and is shown in figure 7.17 and it concicts of 54 atoms. The red balls represent the oxygen atoms and the pink balls represent the manganese atoms. From table 7.5 the relaxed lattice parameters of the interface are $a = 40.91Å$, $b = 4.35Å$, $c = 2.94$, $\alpha = 90°$, $\beta = 81.75°$ and $\gamma = 91.16°$. Accordingly the R3P1R1 interface relaxes more in the x-direction.

Lattice Parameter	Unrelaxed	Relaxed	Difference
a (Å)	41.66	40.91	0.75
b (Å)	4.23	4.35	-0.12
c (Å)	2.94	2.94	0.00
α (˚)	89.82	90.00	-0.18
β (˚)	83.96	81.75	2.21
γ (˚)	90.35	91.16	-0.81

Table 7.5: Unrelaxed and relaxed lattice parameters for the R3P1R1 interface.

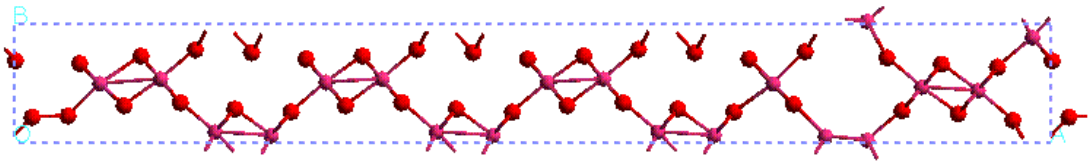

Figure 7.17: R3P1R1 interface structure.

Figures 7.18 (a)-(c) show the radial distribution functions for the interface at 300K, 1500K and 3500K respectively. At higher temperatures of 1500K and 3500K, the RDFs depict the peak broadening profile. Figures 7.18 (d)-(f) show the

RDFs for superimposed Mn-Mn, Mn-O and O-O interactions respectively at different temperatures. As the temperature is increased, the peaks broaden which indicates that there is a high degree of disorder at elevated temperatures. Figure 7.19 depicts how the RDF peak intensities change with temperature. In figure 7.19 Mn-Mn interaction corresponds to the first peak located at 2.94Å and has a magnitude of 5.03. The second maximum peak at 3.44Å has an intensity of 8.26. The results of Mn-O and O-O interactions are shown in figure 7.19 as well. All the interactions exhibit the steep decrease below 1000K and the reduced decrease above 1000K. The largest peak height for Mn-O indicates that there is more density for this particular interaction. The more the density the more are the atoms. The large peak heights have got narrow peaks; this is due to the clustering of the density. At higher temperatures with small peak heights, the density is distributed within the system and the atoms are apart from each other. Thus the peaks at higher temperatures are broader. Figure 19 depicts that Mn-O interaction is dominating within the system compared other interactions.

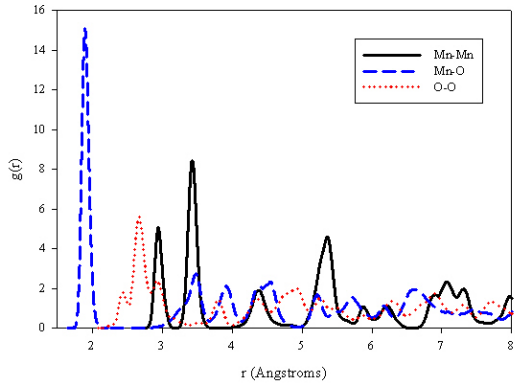

Figure 7.18 (a)

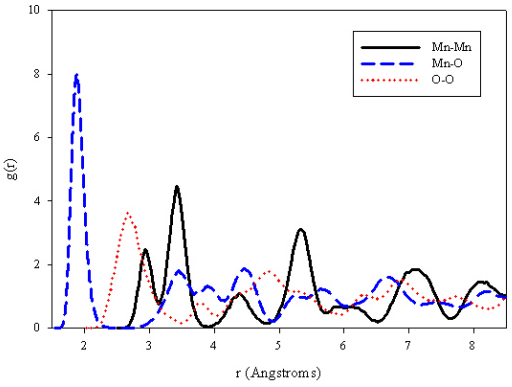

Figure 7.18 (b)

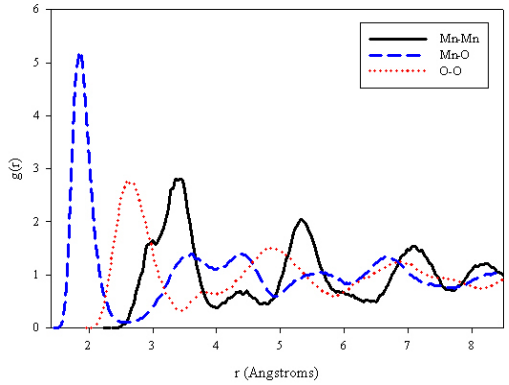

Figure 7.18 (c)

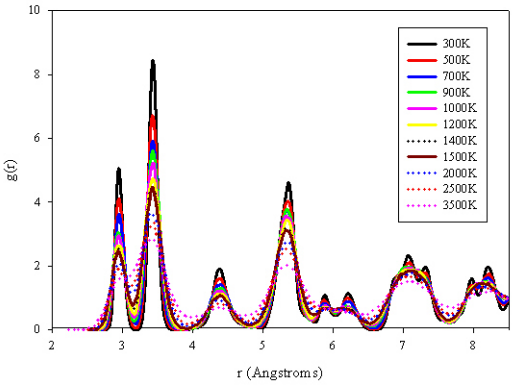

Figure 7.18 (d)

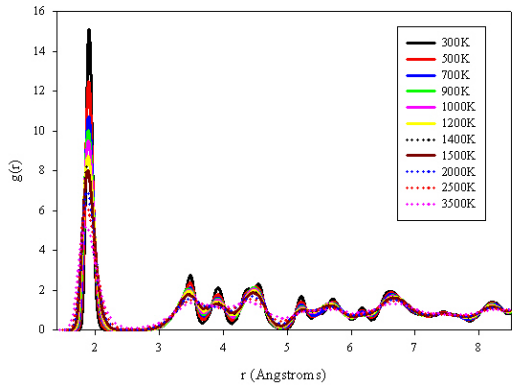

Figure 7.18 (e)

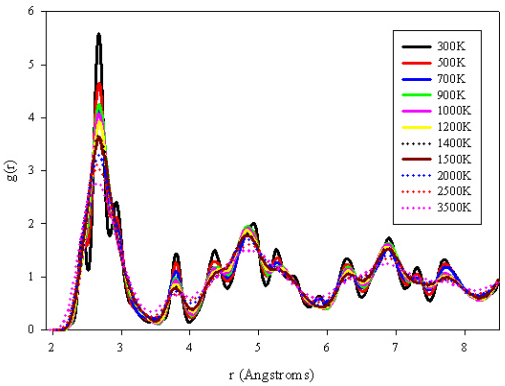

Figure 7.18 (f)

Figure 7.18 (a)-(f): Radial Distribution Functions for R3P1R1 structure showing Mn-Mn, Mn-O and O-O interactions at (a) 300K, (b) 1500K, (c) 3500K, and (d) Mn-Mn pair, (e) Mn-O pair and (f) O-O pair at different temperatures.

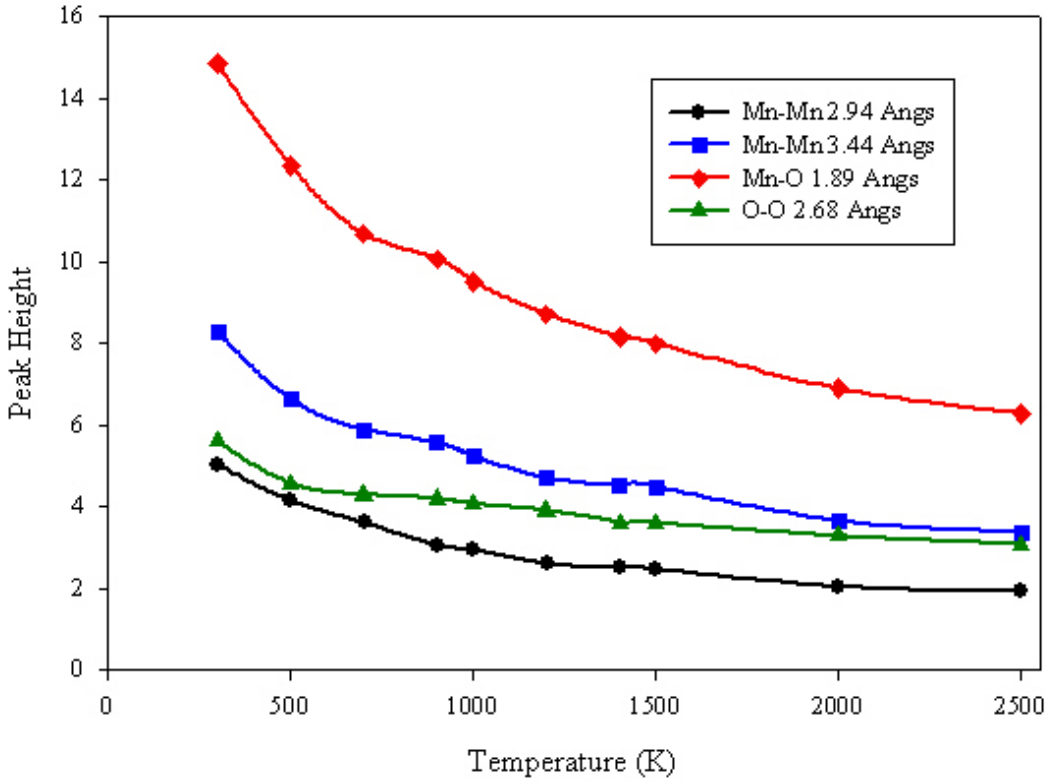

Figure 7.19: The variation of peak heights with temperature for R3P1R1 interface.

7.3.4 R3P1R1P1

The R3P1R1P1 structure is made of three ramsdellite, one pyrolusite, one ramsdellite and one pyrolusite (RRRPRP or R3P1R1P1) and is depicted in figure 7.20. The interface has got 56 atoms. The unrelaxed and relaxed lattice parameters are shown in table 7.6. The interface relaxes more in the x-direction. Radial distribution functions are not shown for this structure since they behave similarly to those in sections 7.3.2 and 7.3.3.

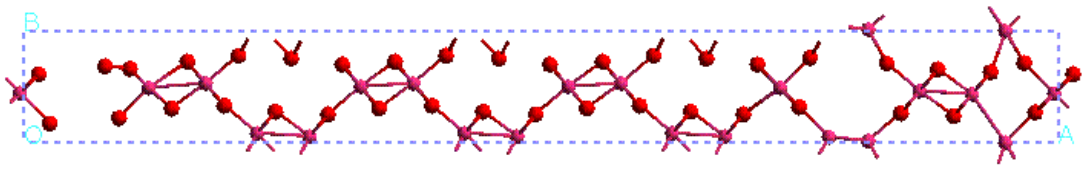

Figure 7.20: R3P1R1P1 interface structure.

Lattice Parameter	Unrelaxed	Relaxed	Difference
a (Å)	46.68	41.30	5.38
b (Å)	5.00	4.49	0.51
c (Å)	2.94	2.94	0.00
α (˚)	90.00	89.66	0.34
β (˚)	90.00	87.80	2.20
γ (˚)	90.00	94.86	-4.86

Table 7.6: Unrelaxed and relaxed lattice parameters for the R3P1R1P1 interface.

7.3.5 P12 (Twelve pyrolusite)

P12 is an intergrowth made up of only pyrolusite crystal unit cells and has twelve pyrolusite structures. The balls and stick and polyhedra represented structures are shown in figures 7.21 and 7.22 respectively, The lattice parameters are listed in table 7.7, and the relaxed and unrelaxed lattice parameters do not differ much.

Lattice Parameter	Unrelaxed	Relaxed	Difference
a (Å)	52.90	52.81	0.09
b (Å)	5.00	4.40	0.60
c (Å)	2.86	2.92	-0.06
α (˚)	90.00	90.00	0.00
β (˚)	90.00	90.00	0.00
γ (˚)	90.00	90.00	0.00

Table 7.7: Unrelaxed and relaxed lattice parameters for the P12 interface.

The RDFs graphs are shown in figures 7.23 (a)-(c); where (a), (b) and (c) illustrate the RDFs at 300K, 1500K and 3500K respectively. The graphs corresponding to the RDFs of Mn-Mn, Mn-O and O-O pairs at different temperatures are given in figures 7.23 (d)-(f). As expected, the RDFs peaks decrease in height and broaden with temperature increase. The radial distribution functions for Mn-Mn, Mn-O, and O-O interactions presented graphically in figure 7.24. The reduction of peak height with temperature for Mn-Mn, Mn-O and O-O is shown in figure 7.24. The figure depicts the decrease below 1000K and linear decrease above this temperature.

As described in the methodology, an interface made up of the same crystal structures is suitable for the introduction of microtwinning. The disordered arrangement of fully twinned pyrolusite is not known. However, regular twinning of rutile yields α–PbO_2 structure which is found for high pressure polymorph of TiO_2. Twinning is common in rutile TiO_2 and cassiterite SnO_2, where it occurs with a very low probability (macrotwinning). This is in contrast to ramsdellite which Chabre [1995] have shown to be very prone to microtwinning. Pyrolusite is the most stable form of MnO_2, but microtwinning destabilizes both ramsdellite and, to a large extent, pyrolusite. It is expected that when annealing defective samples of manganese dioxide at moderate, they are brought closer to equilibrium by increasing the amount of de Wolff disorder. Thus reducing the amount of edge-sharing octahedral of the lattice and transforming the double chains of ramsdellite into single chains. Then, decreasing the amount of microtwinning yield defectless pyrolusite.

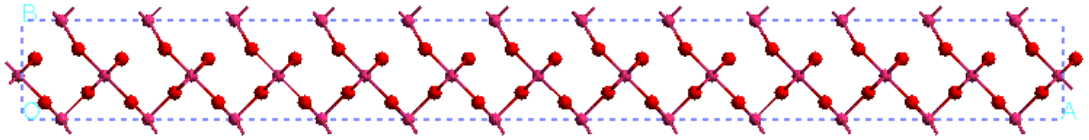

Figure 7.21: P12 interface structure represented by balls and sticks.

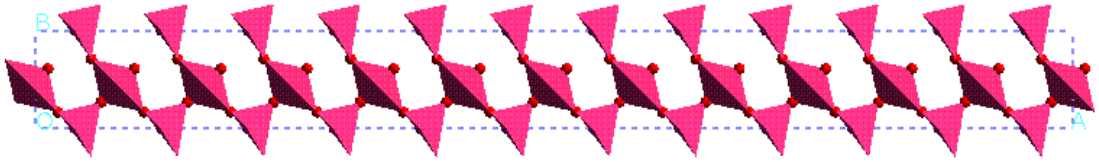

Figure 7.22: P12 crystal structure represented by the polyhedra.

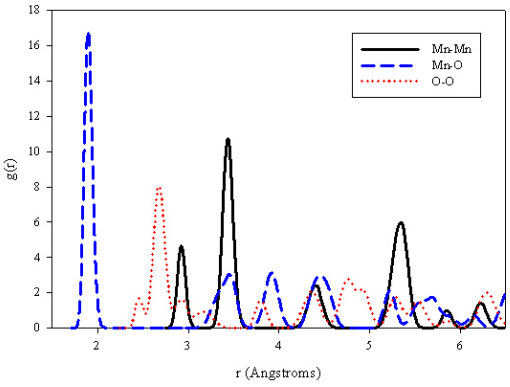

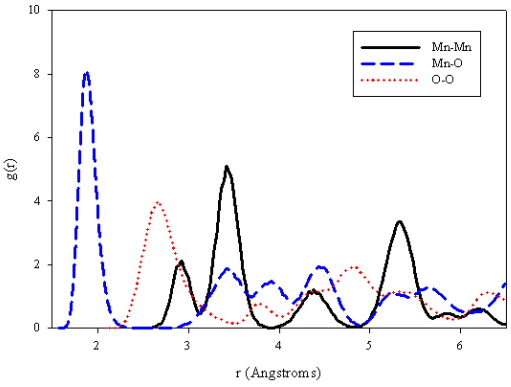

(a) (b)

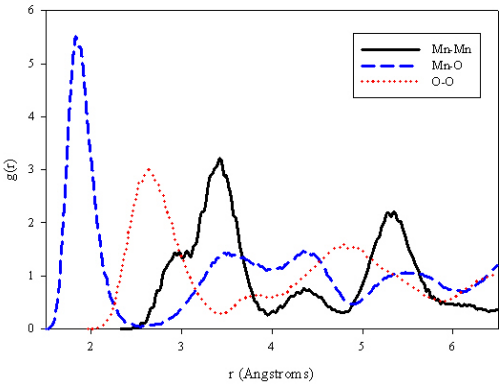

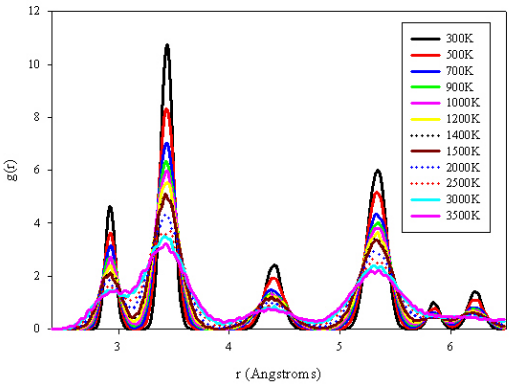

(c) (d)

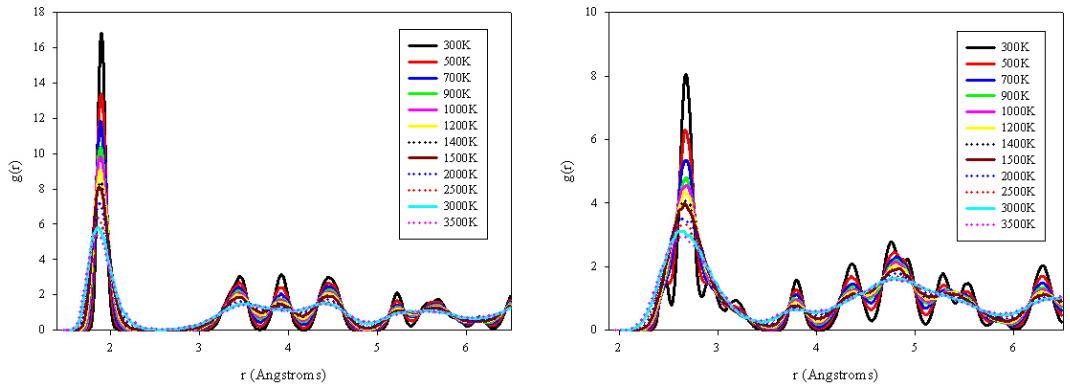

(e) (f)

Figure 7.23 (a)-(f): Radial Distribution Functions for P12 structure showing Mn-Mn, Mn-O and O-O interactions at (a) 300K, (b) 1500K, (c) 3500K, and (d) Mn-Mn pair, (e) Mn-O pair and (f) O-O pair at different temperatures.

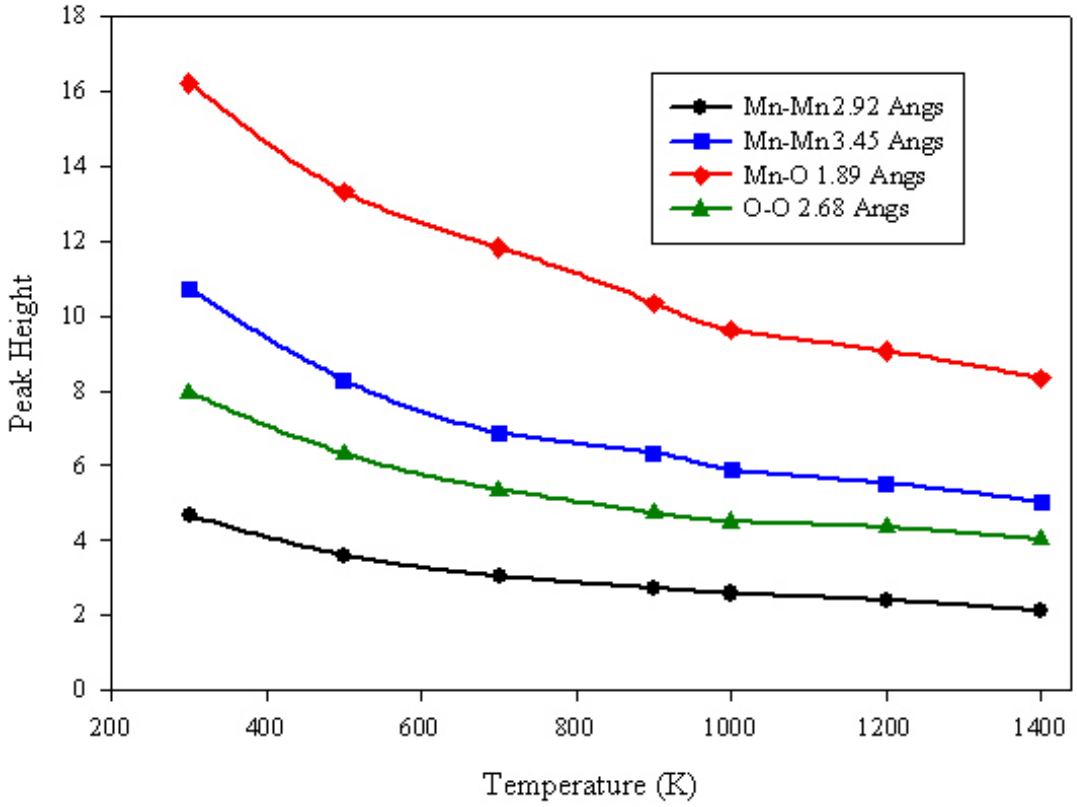

Figure 7.24: Graph of peak heights versus temperature for P12 interface.

7.3.6 P1R1P2R1P5

The P1R1P2R1P5 intergrowth is shown in figure 7.25 and it is comprised of one pyrolusite, one ramsdellite, two pyrolusite, one ramsdellite and five pyrolusite structures (PRPPRPPPPP or P1R1P2R1P5) and consists of 72 atoms. The relaxed and unrelaxed lattice parameters are listed in table 7.8. There is an outer relaxation of the interface in the x and z directions, and contrary to previous intergrowths predominant relaxation is noted in the y-direction. The RDFs results are shown in figures 7.26 (a)-(f). Figure 7.27 gives the change of peak heights with temperature. The peak height is decreasing as expected, but in this case the curvature decrease is to 1500K and the linear decrease is noted above this temperature. The Mn-O interaction at 1.89Å dominates the system.

Lattice Parameter	Unrelaxed	Relaxed	Difference
a (Å)	54.32	54.43	-0.11
b (Å)	5.00	4.41	0.59
c (Å)	2.86	2.93	-0.07
α (˚)	90.00	90.00	0.00
β (˚)	90.00	82.26	7.74
γ (˚)	90.00	96.99	-6.99

Table 7.8: Unrelaxed and relaxed lattice parameters for the P1R1P2R1P5 interface.

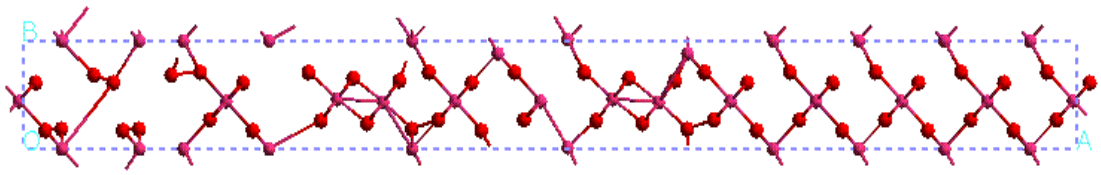

Figure 7.25: P1R1P2R1P5 interface structure.

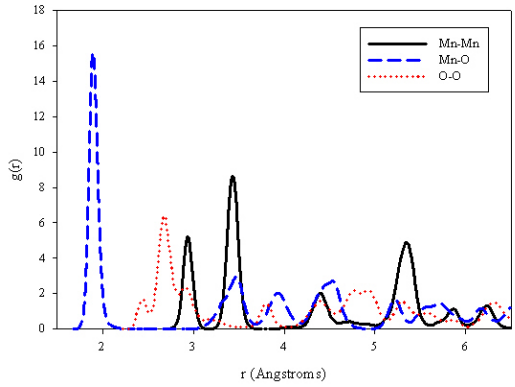

(a)

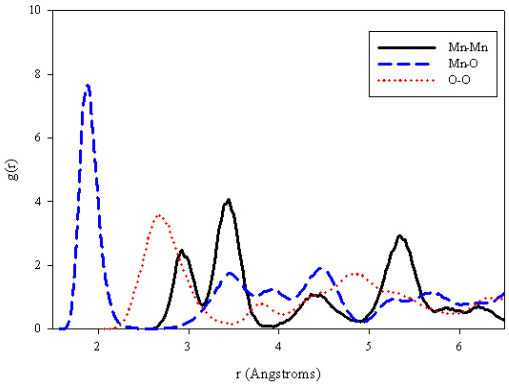

(b)

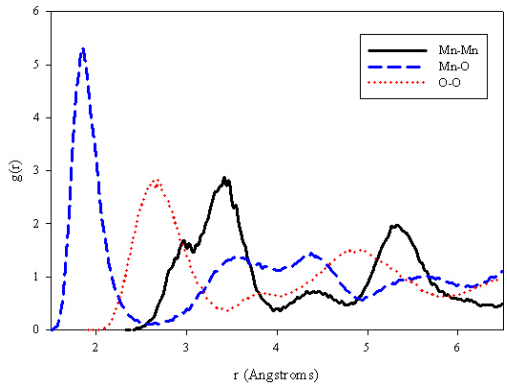

(c)

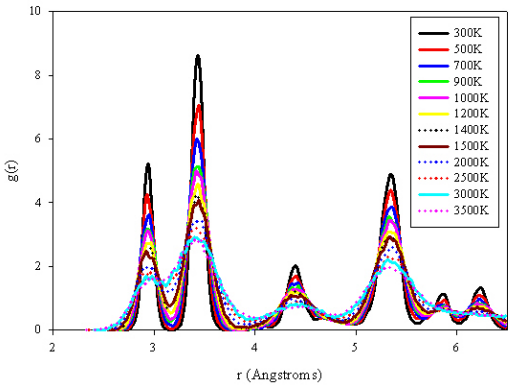

(d)

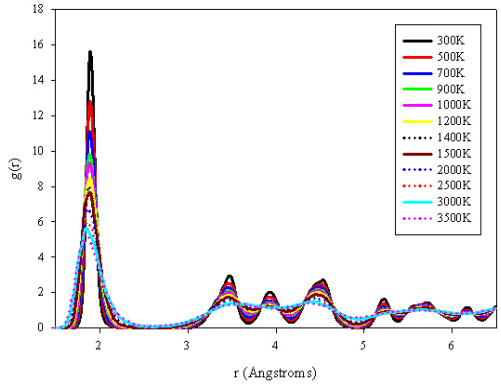

(e)

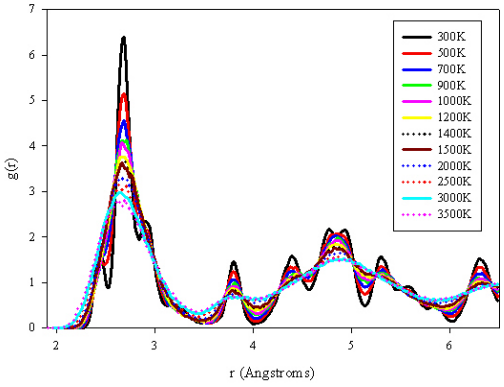

(f)

Figure 7.26 (a)-(f): Radial Distribution Functions for P1R1P2R1P5 structure showing Mn-Mn, Mn-O and O-O interactions at (a) 300K, (b) 1500K, (c) 3500K, and (d) Mn-Mn pair, (e) Mn-O pair and (f) O-O pair at different temperatures.

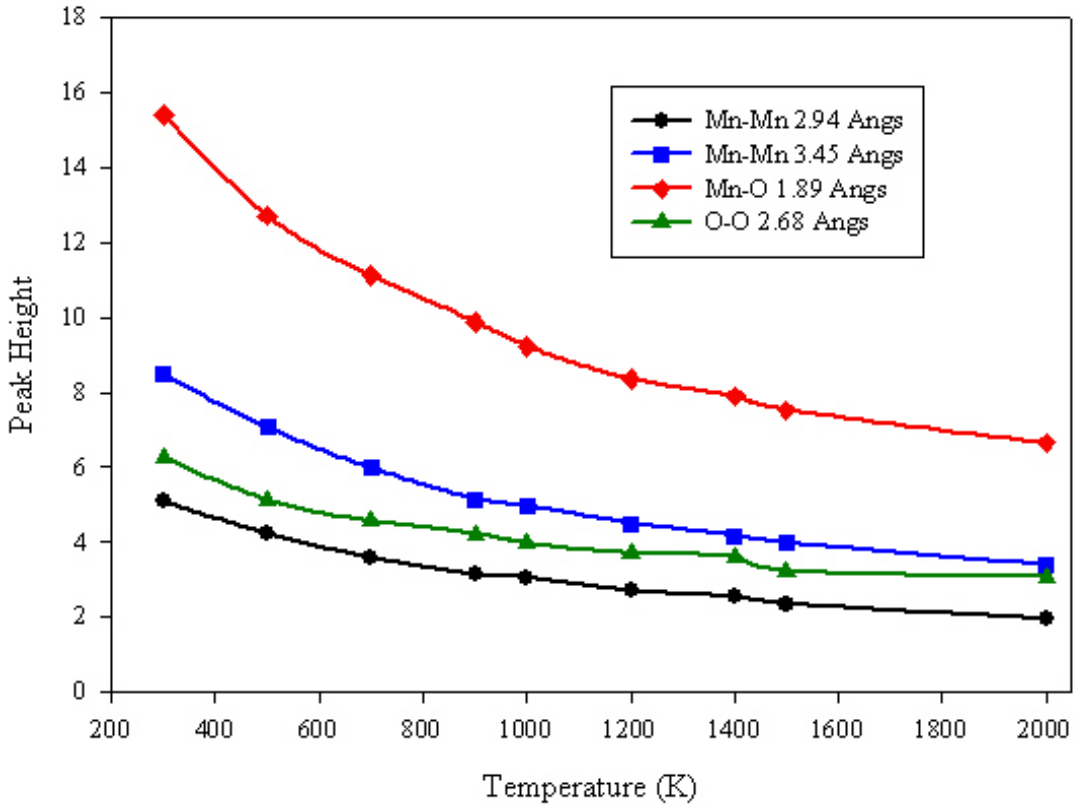

Figure 7.27: The change of peak heights with temperature for R1P2R1P5 interface.

7.3.7 Defects

An introduction of defects in the systems has been initiated where one manganese ion, Mn^{4+}, is removed from the structure (pyrolusite, ramsdellite or mixture of the two) and charge compensated by four hydrogen atoms. Hydrogen atoms are connected to oxygens atoms, that is, they form OH^- in the system. For a start, we introduced the defects in pyrolusite, ramsdellite, and an intergrowth made up of one-ramsdellite and one-pyrolusite (R1P1). Figures 7.28, 7.29 and 7.30 show the structures of pyrolusite, ramsdellite and R1P1 intergrowth with the defects respectively. In all structures, pink balls represent the manganese atoms, red balls represent the oxygen atoms and blue balls represent the hydrogen atoms. The

systems were optimized using the planewave pseudopotential method (see section 7.2)

The hydrogens are connected to four oxygens, which surrounded the manganese atom before it was removed. Orientations of hydrogens differ from structure to structure. Chabre and Pannetier [1995] showed that intercalated protons are always covalently bonded to oxygen atoms in both pyrolusite and ramsdellite. Pyrolusite contains one type of oxygen whereas ramsdellite contains two chemically different oxygen atoms, that is, $O_{pyramidal}$ and O_{planar} according to their coordination to Mn. Since the two oxygens are at different lattice potentials $O_{pyramidal}$ is less stabilized by the lattice potential while O_{planar} is more stabilized, that is, more likely to be hydroxylated. Hydrogen atoms were placed at various locations in both structures. Using pseudopotential planewave method the structures were optimized. The O-H bond was found to be 1.9Å.

7.4 Conclusion

Energetically equivalent surfaces of pyrolusite and ramsdellite were identified from the atomistic simulation results and were used in building pyrolusite-ramsdellite interfaces. Interface builder was used successfully to construct different intergrowths made up of pyrolusite and ramsdellite crystal structures. Since the intergrowths are based on two known polymorphs of MnO_2, we assessed the validity of the potentials used for calculations on those two pure crystals by

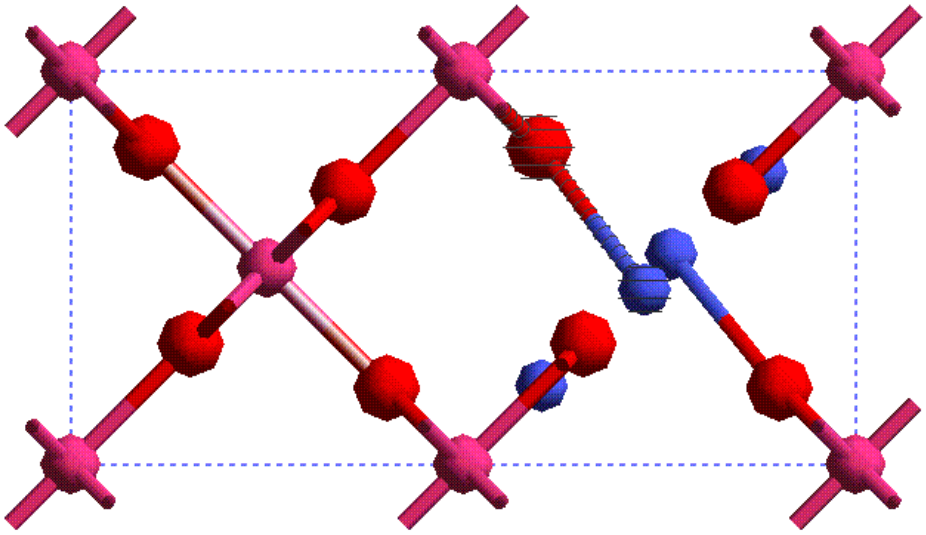

Figure 7.28: Pyrolusite structure with defects.

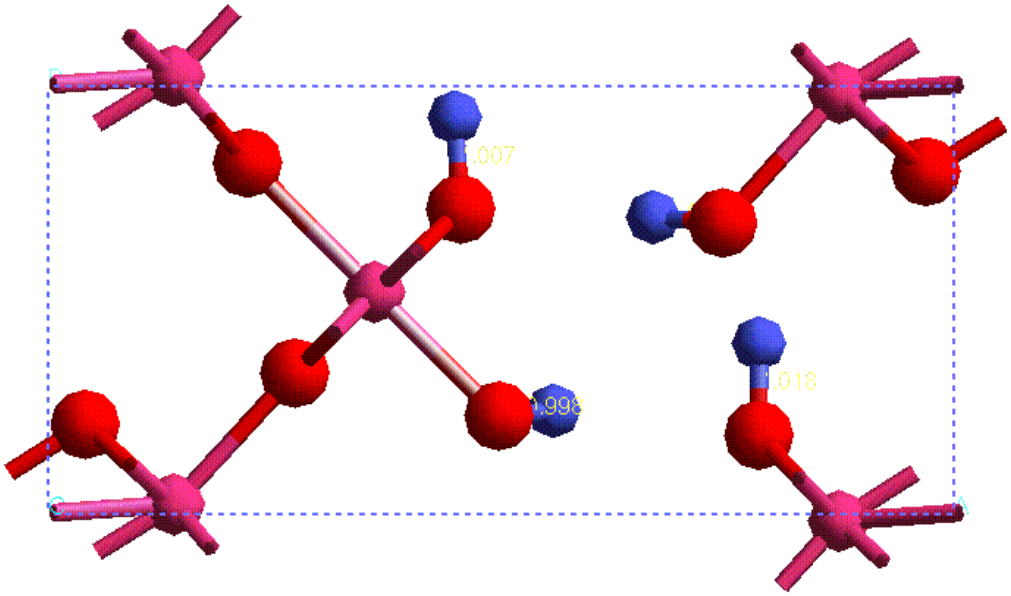

Figure 7.29: Ramsdellite structure with defects.

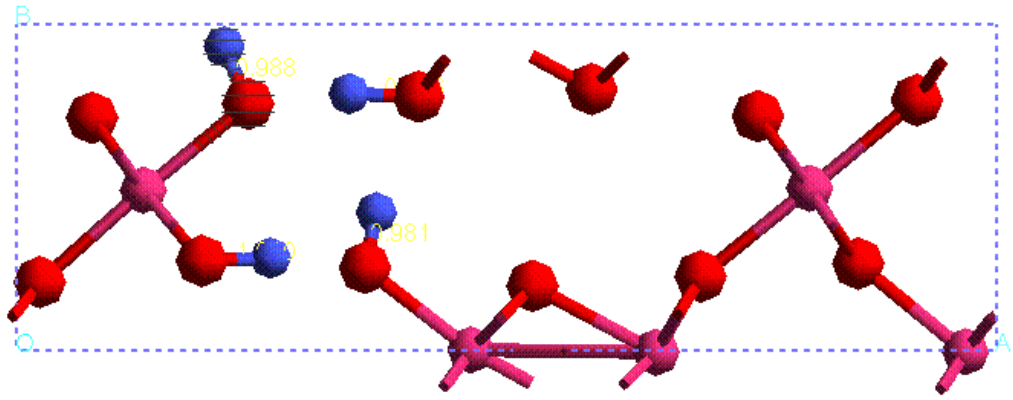

Figure 7.30: R1P1 interface structure with defects.

checking how they reproduce the lattice parameters of the intergrowths built. Indeed, they performed very well on all the interfaces. Furthermore, molecular dynamics calculations on interfaces were carried out and compared with the results obtained using the EXAFS spectroscopy (Chapter 6). The calculated radial distances compare very well with the experimental results. In all intergrowths peak heights reduced with increase temperature. However, the peak locations appear almost unperturbed by temperature change. Lastly, the location of Mn-Mn, Mn-O and O-O peaks is not significantly changed in the various types of intergrowths.

Chapter 8

Amorphization and Recrystallization Technique

8.1 Introduction

In this Chapter, a simulated amorphization and recrystallization methodology [Sayle 2000a and 2001] is employed to generate MnO_2 interface models and also to test whether the method can indeed generate pyrolusite-ramsdellite intergrowths of γ-MnO_2. Amorphization and recrystallization method is a potential method of generating a structure without any user intervention - perhaps the structure generated is more 'realistic'. Simulated amorphous and recrystallization in this work involves the straining on MnO_2 thin film under a considerable pressure and placing it on top of MnO_2(001) and MnO_2(100) supports for both pyrolusite and ramsdellite polymorphs respectively. Dynamical simulation is then applied to the systems (pyrolusite and ramsdellite) at high temperatures upon which MnO_2 thin film undergoes amorphization. Under prolonged dynamical simulation, MnO_2 thin film recrystallizes, revealing a wealth of structural modifications that evolve as the systems endeavour to accommodate the lattice misfit, whilst the maximizing interfacial interactions. To make sure that the thin film recrystallizes from an amorphous structure, no influence on the compromise between minimizing the lattice misfit whilst maximizing the interfacial interactions is introduced

artificially into the simulation [Maicaneanu 2001ab]. Central to this methodology is that the dynamical simulation, as applied to an amorphous structure, allows a more comprehensive exploration of the configurational space due to the high energy amorphous starting point and the conformational freedom this gives rise to. The associated calculated radial distribution functions are calculated and compared with experimental results.

In this chapter we generate models for MnO_2 interfaces and nanoparticles, which will give information pertaining to nanoparticle morphologies and exposed surfaces, epitaxial relationships, defects, dislocations and grain boundaries. At this moment, it is extremely difficult, to elucidate such information experimentally [Sayle 2002b]. Accordingly, computational simulation is well positioned as a complimentary technique. The simulation enables us to generate low energy structures; the various structural features and configurations will be energetically viable [Sayle 2003]. The construction of the MnO_2 interfaces and nanoparticles were generated using cube-on-cube approach and explored using a simulated amorphization and recrystallization methodology. The evolution of the amorphization and recrystallization process was monitored using radial distribution functions of the ions during the dynamical simulation.

8.2 Methodology

The force field used to describe the interaction within the materials are described in Chapter 2 and listed in Table 4.1. Simulation codes and amorphization and recrystallization technique (see sections 2.5-2.7) are used to construct different interfaces studied in this Chapter.

The DL_POLY code [Smith 1999] was used in this study to perform all the dynamical simulations. Since the code utilizes three-dimensional periodic boundary conditions the surface is simulated using a periodic array of slabs with a void introduced perpendicular to the interfacial plane to represent the vacuum above the surface of the thin film. The size of the void is, of course, suitably large to ensure that the interactions between the slabs are negligible. In the current study, the simulations were performed on a Silicon Graphics O2 workstation with R10000 processor for GULP calculations and Silicon Graphics Origin 2000 with R12000 processors for MARVIN and DLPOLY calculations. The simulations were performed using 26 processors of Origin, and the simulation procedure took three weeks for each system to complete.

8.2.1 MnO_2/MnO_2 Interfaces Construction

Several interfaces were generated; in this section a summary of how they were constructed is given for only two systems. All other systems were generated similarly unless otherwise stated. For pyrolusite, stable surfaces {001} and {100} were considered as substrates for supporting thin films whereas {100} surface was considered as substrate for supporting ramsdellite thin film. The MnO_2/MnO_2(001)

system was generated by placing four layers of MnO_2 thin film on top of a six $MnO_2(001)$ support, which corresponds to 23922 atoms or surface area of 14123Å^2 for pyrolusite and twelve layers of $MnO_2(100)$ thin film on top of twelve $MnO_2(100)$ support, which corresponds to 22068 atoms or surface area of 4179Å^2 for ramsdellite. The $MnO_2(001)$ and $MnO_2(100)$ substrates were maintained at their natural lattice parameters, whilst MnO_2 thin films were constrained initially to lie coherent with respect to the underlying $MnO_2(001)$ and $MnO_2(100)$ substrates, which required 10% and 13% compression for pyrolusite and 6% tension for ramsdellite lattices respectively. The constrained equation (lattice misfit, F) for both pyrolusite and ramsdellite is given by equation 8.1 below

$$F = \left[\frac{(a_1 xn) - (a_2 xn)}{(a_1 xn)} \right] \tag{8.1}$$

where a_1 is the lattice parameter of the thin film, a_2 is the lattice parameter of the support and n is the number of MnO_2 units. Owing to the considerable strain within pyrolusite and ramsdellite systems, dynamical simulations, performed at a high temperature of 1300K, resulted in the desired initial partial amorphization of the MnO_2 thin film, which then recrystallized during the subsequent prolonged application of the dynamical simulation at reduced temperatures of 800K, 400K, 200K and 0K. Specifically, dynamical simulation was performed on the systems with the time step of 0.005 ps for up to 500 000 cycles at 1300K. Velocity scaling performed at every time step was used throughout to prevent the rapid and large build up of excess kinetic energy. Figure 8.1 shows an example of schematic

representation of MnO_2 simulation cell, composed of ten layers of MnO_2 support and seven layers of MnO_2 thin film. Also shown are the layers, starting from the bottom to the top of the interfaces. Two different lattice misfits were used for pyrolusite to explore the influence of the lattice misfit on the final structure, which is the partial amorphization induced by either 10% or 13%.

8.2.2 MnO_2 Nanoparticles Construction

To generate MnO_2 nanoparticles, amorphization and recrystallization technique was employed. Nanoparticles comprised of 11340 and 8982 atoms for pyrolusite and ramsdellite respectively were generated from the {100}, {101}, {110}, {001} {010} and {011} Miller index planes for both systems. Dynamical simulation was performed on the nanoparticles at 900K for 0.005 ps. The procedure resulted in the formations of an amorphous MnO_2 nanoparticles after several timesteps. Then the dynamical simulation was prolonged on the systems to give a recrystallized nanoparticles at temperatures 900K for 500 000 cycles, 600K, 300K and 0K for 10 000 cycles each temperature, the latter acts effectively as an energy minimization step. For each temperature, dynamical simulation was performed until the system was no longer evolving structurally or energetically. The amorphization and recrystallization technique generates models which reveal the atomistic structures present on the surfaces of reactive faces of MnO_2 and provides details of defects (vacancies, interstitials and substitutionals) and grain boundary structures. The models are important in understanding the active sites at the surface of a material. All the nanoparticles simulations were performed within the NVE ensemble.

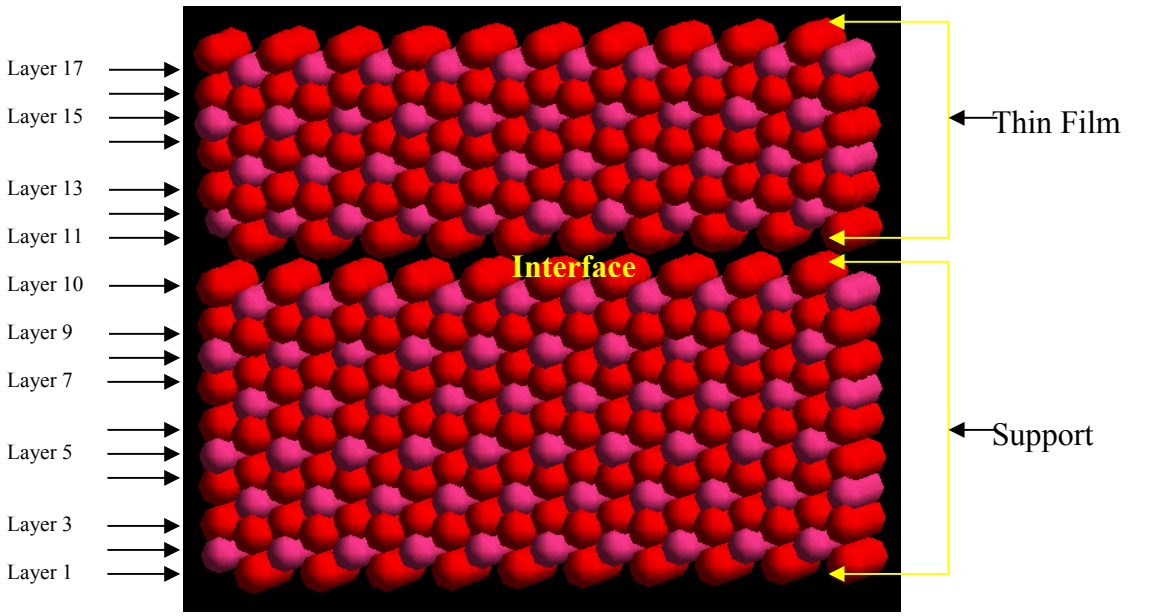

(a)

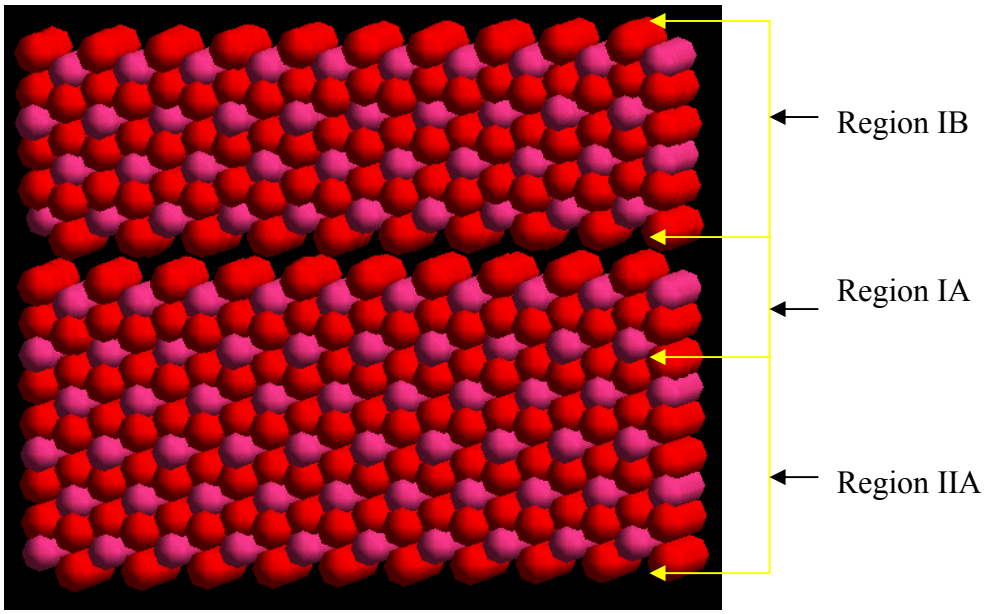

(b)

Figure 8.1: Schematic representation of MnO_2 simulation cell, (a) is showing the thin film and the support and (b) is showing regions I and II of the simulation cell.

8.3 Results and Discussions

Structural configuration, radial distribution functions and directional densities were calculated, to define structural properties of MnO_2 interfaces. Not all the RDFs graphs are shown, but the discussions and conclusions concerning the RDFs are given for all the systems. From the calculated structures, graphical techniques were used to provide a visual display of the evolving structures during dynamical simulations. The starting configuration, amorphous state and recrystallized state of the thin films and nanoparticles were looked at.

8.3.1. Pyrolusite $MnO_2/MnO_2(001)$ 10% lattice misfit

(a) Start

The partial radial distribution functions (RDFs) for Mn-O pair interaction of the pyrolusite $MnO_2/MnO_2(001)$ interface (10% compression) is shown in figure 8.2 at 1300K after first cycle (0.005ps) of dynamical simulation. In a crystal, a radial distribution function has an infinite number of sharp peaks whose separation and heights are characteristics of the lattice structure. The figure reveals a series of well-defined peaks corresponding to successive nearest neighbour distances.

The directional density plot of pyrolusite $MnO_2/MnO_2(001)$ interface for Mn and O atoms is shown in figure 8.3. The density of the simulation cell gives the information about the layers of the thin film and the support. The density graphs reveal distinct peaks corresponding to Mn and O densities. It reveals four layers of the thin film and six layers of the support. There is a breakdown between the thin film layers and the support layers at the start of the simulation.

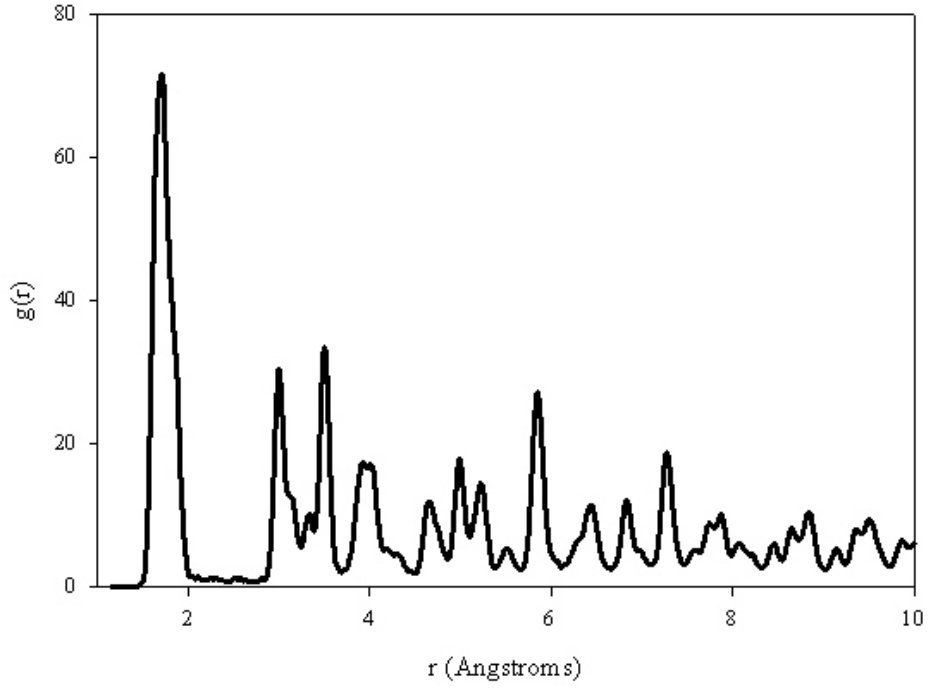

Figure 8.2: Pyrolusite MnO_2/MnO_2(001) interface (10% compression) Mn-O RDF at 1300K after 0.005 ps.

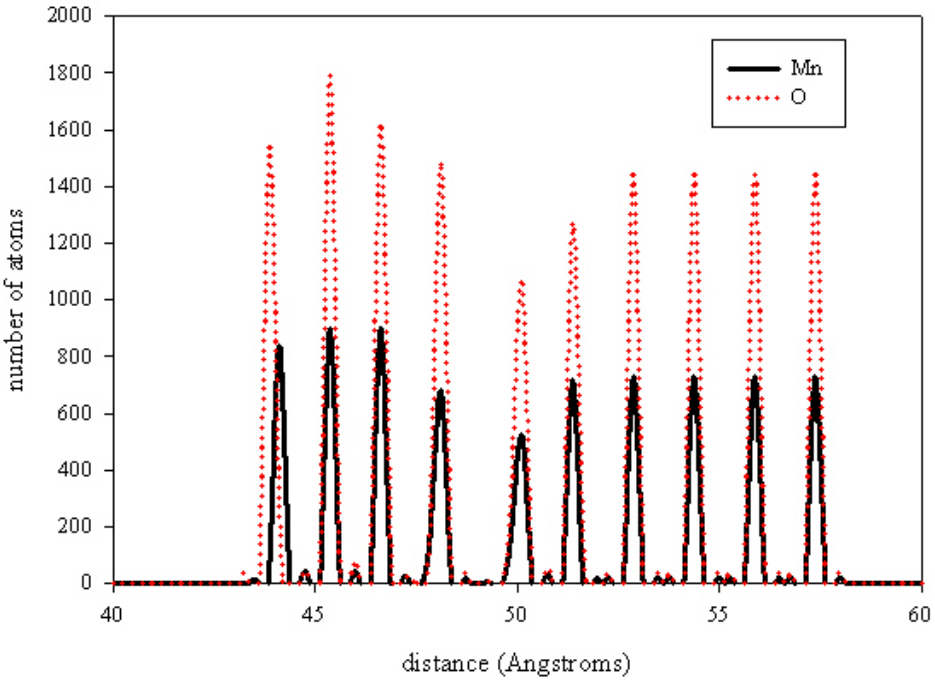

Figure 8.3: Pyrolusite MnO_2/MnO_2(001) interface (10% compression) Mn- and O densities at 1300K after 0.005 ps.

In figure 8.4 the picture of a simulation cell, with 23922 atoms after first cycle of the simulation is shown. The picture depicts MnO_2 thin film forced on top of MnO_2(001) support, that is the thin film being compressed by 10%.

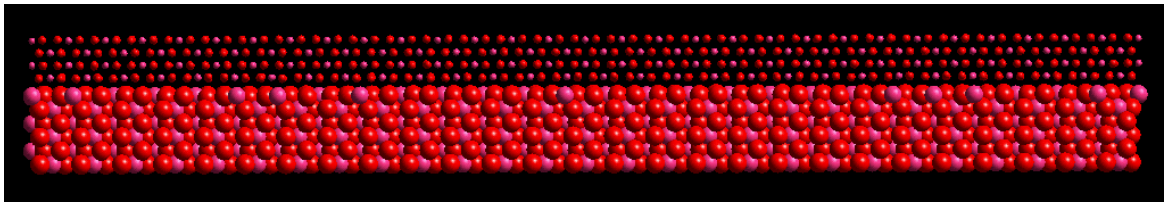

Figure 8.4: Pyrolusite MnO_2/MnO_2(001) interface (10% compression) at 1300K after 1 cycle. Manganese atoms are represented by the pink balls and oxygen atoms are represented by red balls.

(b) Amorphous

The simulation cell has undergone partial amorphization soon after the dynamical simulation was applied to the system. Amorphization occurred after approximately 2.5 ps of the dynamical simulation. The RDFs, densities and the picture of the simulation cell in partial amorphous state are shown in 8.5-8.7. The RDFs exhibit broad peaks for Mn-O pair. The first maximum peak, in figure 8.5, corresponding to the nearest neighbour distances occur at ≈ 1.88Å. The broad peaks from the RDFs graph shows that the system has lost its crystallinity, as it retains some short-range order but no long-range orders. The density pictures show that the layers of the thin film are amorphous.

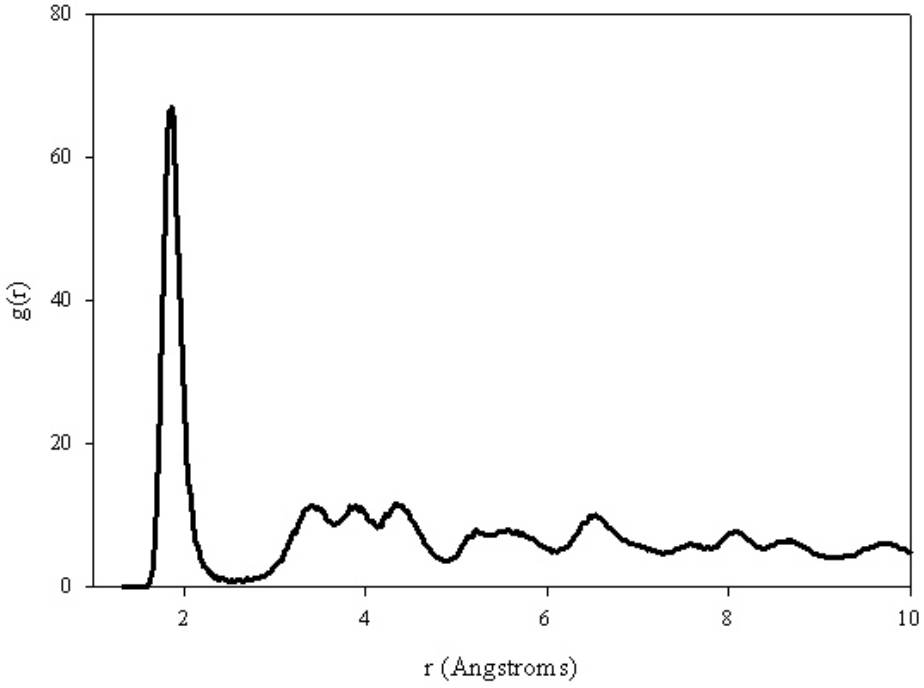

Figure 8.5: Pyrolusite $MnO_2/MnO_2(001)$ interface (10% compression) Mn-O rdf at 1300K after 2.5 ps.

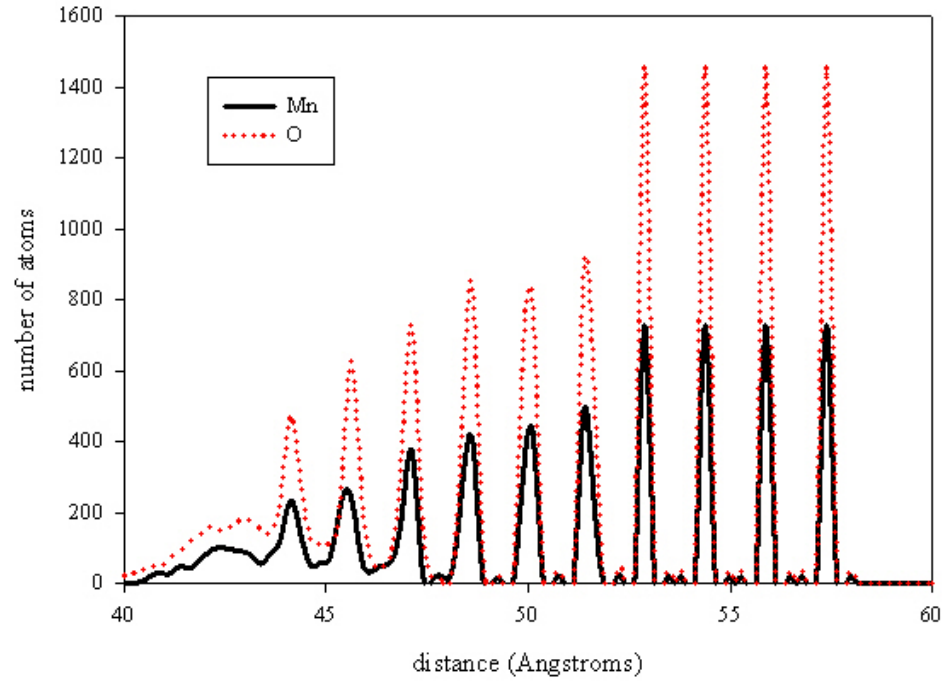

Figure 8.6: Pyrolusite $MnO_2/MnO_2(001)$ interface (10% compression) Mn- and O densities at 1300K after 2.5 ps. Mn density is represented by black colour and O density by red colour.

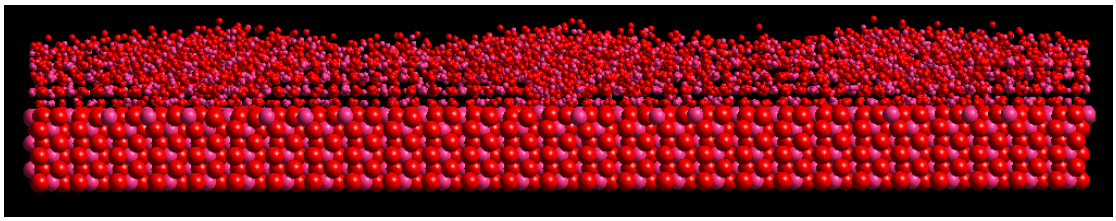

Figure 8.7: Pyrolusite MnO_2/MnO_2(001) interface (10% compression) at 1300K after 2.5 ps. Manganese atoms are represented by the pink balls and oxygen atoms are represented by red balls.

(c) Final

After prolonged dynamical simulation the thin film has recrystallized after 250 ps at 1300K. Figure 8.10 shows the picture of the simulation cell after it has recrystallized at a lower temperature of 200K, the picture looks different from the pictures at the starting point and at the amorphous state. Most importantly, the picture is completely different from the picture at the starting point; this confirms that the amorphization and recrystallization methodology removes any memory of the starting configuration. In addition, the thin film and interfacial structures have evolved because of the misfit induced at the start of the simulation. The RDF plot in figure 8.8 shows that the thin film is now recrystallized, as it has the short-range and the long-range order form. The first maximum peaks corresponding to the nearest neighbour distances occur at ≈ 1.88 Å for Mn-O pair. The density plot is shown in figure 8.9. Both manganese and oxygen densities show that the system has ten layers and one incomplete layer at the top of the thin film with the smallest peak. Fixed four layers of the support have the highest peaks at the higher densities. Top side view of the interface structure is shown in figures 8.11-8.12 (b) for the starting, partial amorphous and final structure respectively. Further analysis on the final structure is depicted in figures 8.13-8.14. Due to lattice misfit

structural evolution includes the formation of Mn interstitials within the system. This is clearly seen in figure 8.14.

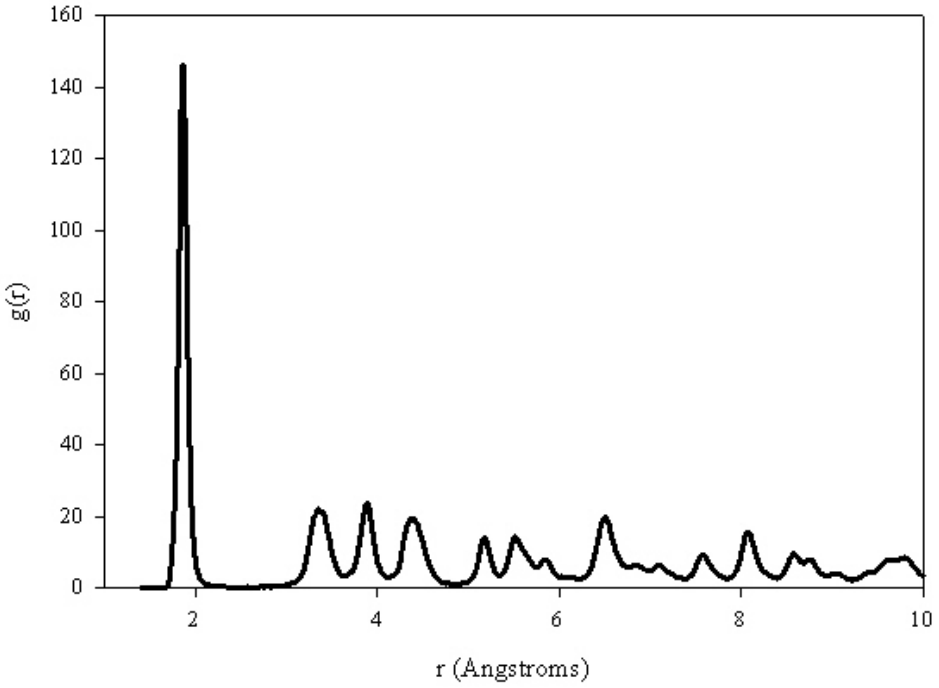

Figure 8.8: Pyrolusite MnO_2/MnO_2(001) interface (10% compression) Mn-O rdf at 200K after 400 ps.

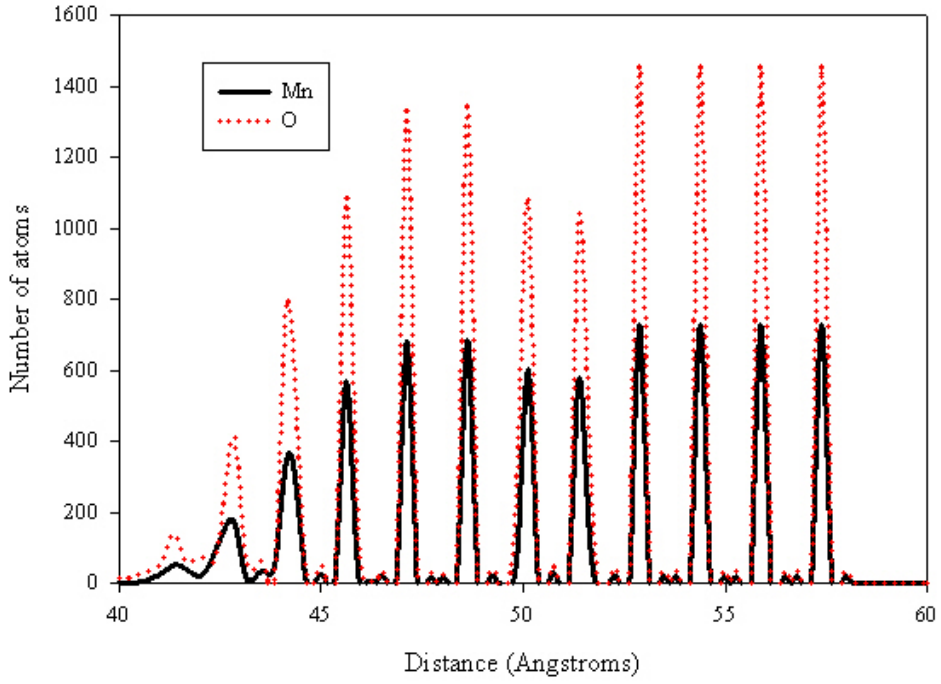

Figure 8.9: Pyrolusite MnO_2/MnO_2(001) interface (10% compression) Mn and O densities at 200K after 400 ps.

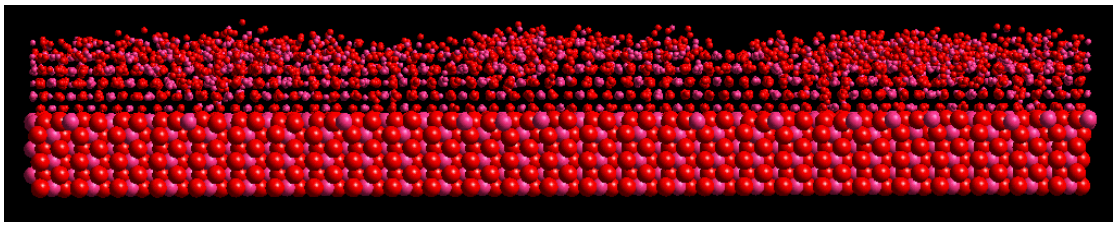

Figure 8.10: Pyrolusite MnO_2/MnO_2(001) interface (10% compression) at 200K after 400 ps. Manganese atoms are represented by the pink balls and oxygen atoms are represented by red balls.

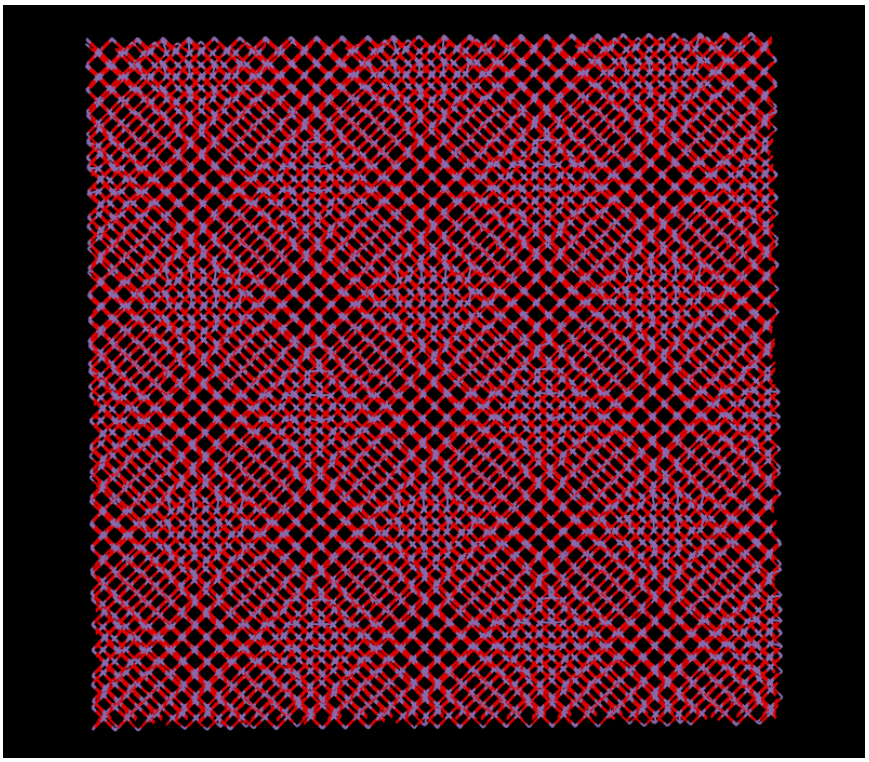

Figure 8.11: Starting configuration of the system viewed from the top side

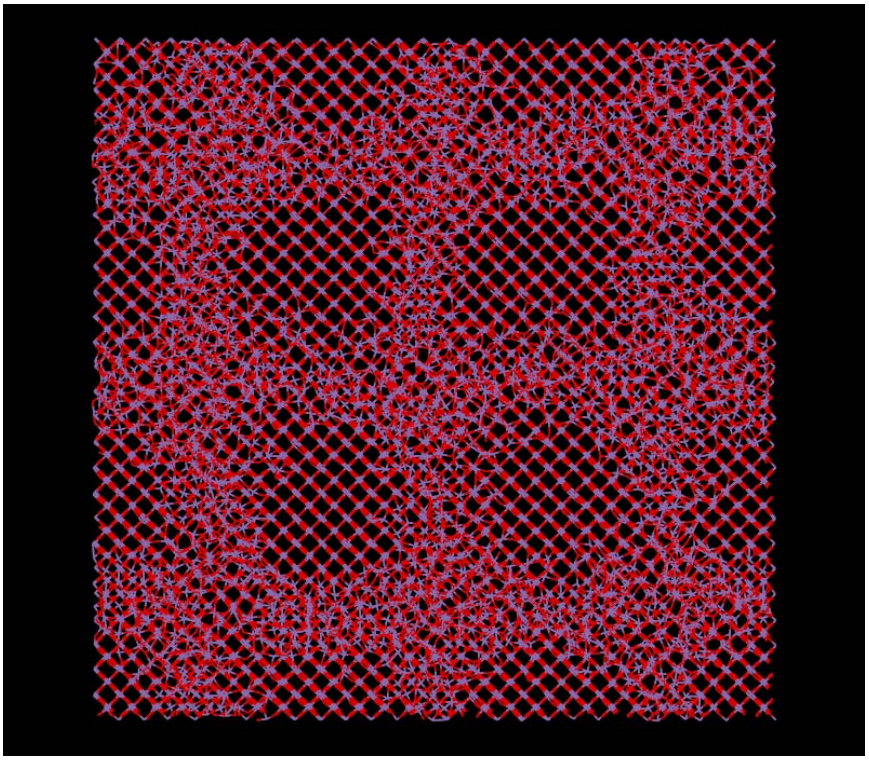

(a) Partial amorphous structure

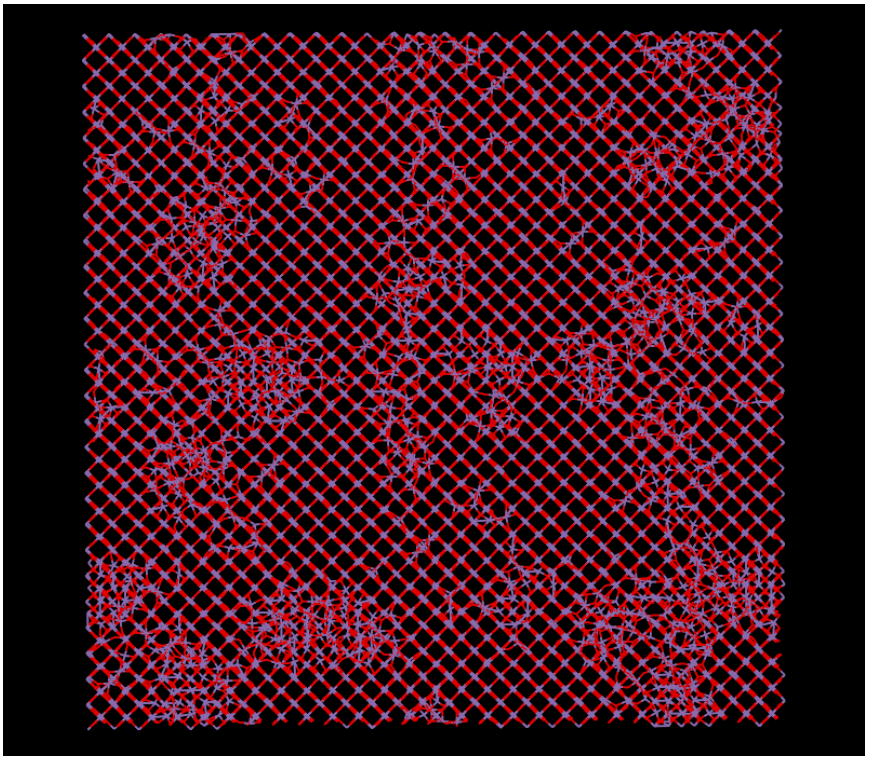

(b) Final structure

Figure 8.12 (a) and (b): Top side view of structures of the interface (a) partial amorphous and (b) final.

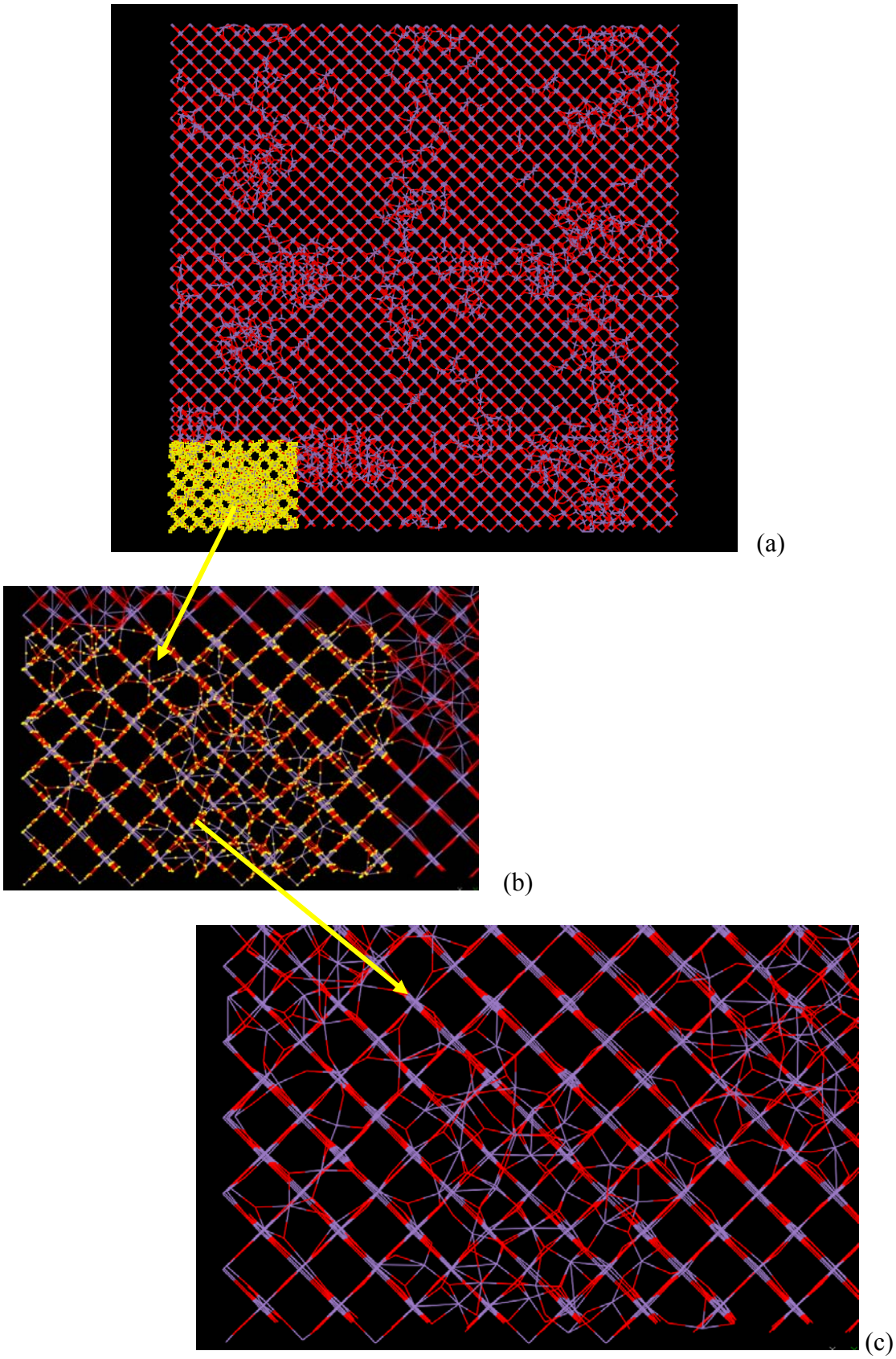

Figure 8.13 (a)-(c): Enlarged structures of figure 8.14 (b), final structure. Figure (a) is the final structure, (b) is the bottom left hand corner of the final structure and (c) is showing a clear picture of (b).

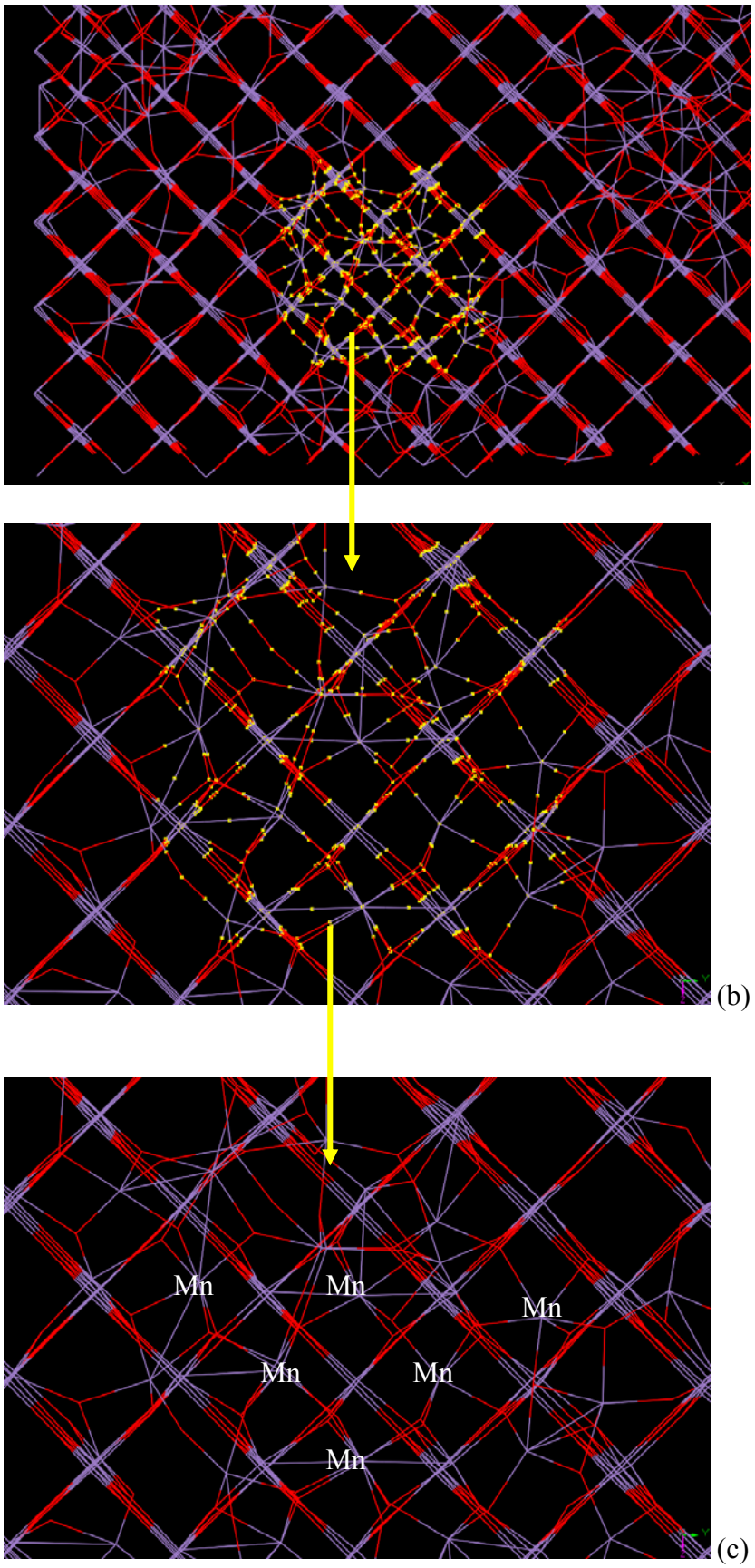

Figure 8.14 (a)-(c): Enlarged structures of figure 8.15 (c). Figure (c) is showing manganese interstitial atoms.

A variety of structural features have evolved within the MnO_2 thin film. The graphical techniques were used to analyze the system layer-by-layer and it reveals there are vacancies, substitutions and interstitials atoms within the system. However, neither vacancies nor interstitials were observed in the support and the interfacial layer (layer 5 and 6 shown in picture 8.15(a) and (b). Figure 8.16 shows the O vacancies within the first thin film layer from the interfacial plane, together with random distribution of Mn ions (interstitials and substitutions). The evolution oxygen vacancies within the system disrupt the charge neutrality. Accordingly, Mn substitutions are present to restore charge balance. Also further inspection of each layer revealed that the density of O vacancies within the thin film increases within the planes further from the interface. Figure 8.17 showing the further away layers from the interface are having more defects compared to layers closer to the interface. Manganese ions were observed to occupy their lattice sites and interstitial positions within the thin film.

Further inspection of the thin film layers (figure 8.16) shows the presence of network of edge dislocations in the system. Figure 8.17 shows manganese and oxygen vacancies, associated vacancies Mn and O pairs, triplets and a larger vacancy clusters. The latter can be described as a void or a cavity within the thin film layer. The layers reveal a wealth of voids located at the layers further away from the interfacial layer. Their evolution is due to greater relaxational freedom of ions in the local environment thereby relieving the stress within the system. Closer inspection of the thin film in the same picture reveals several Mn and O interstitials.

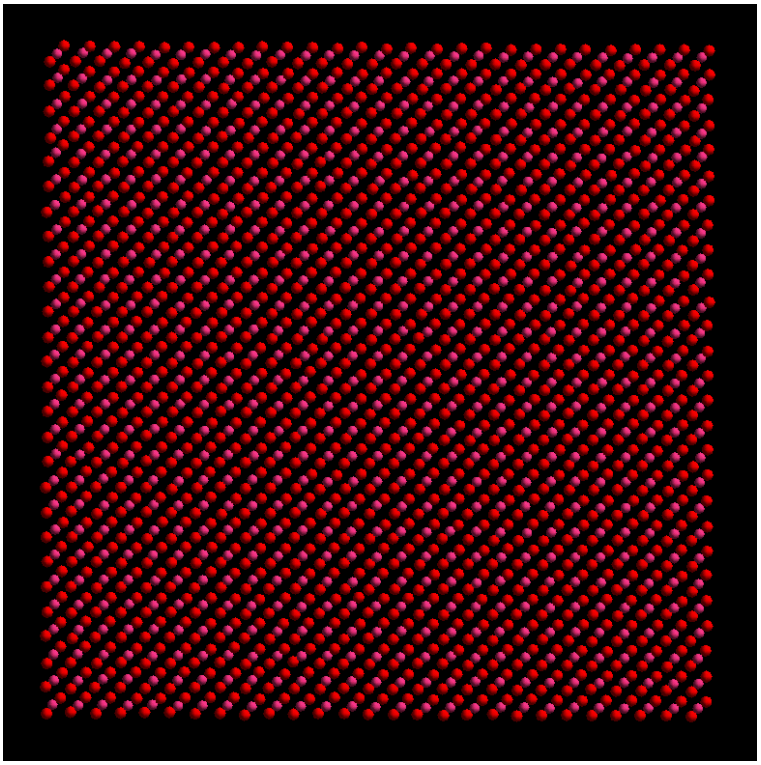

(a) Layer 5

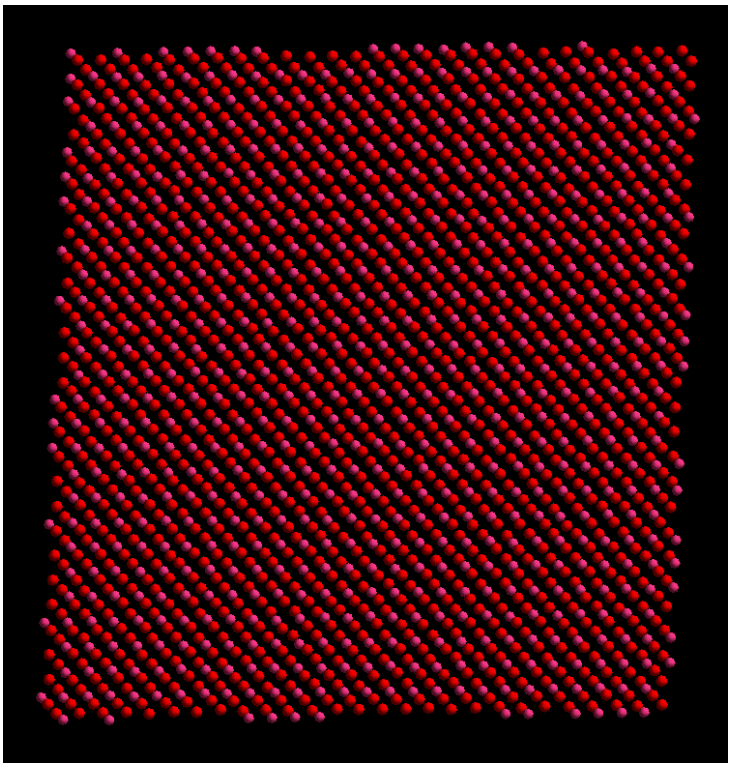

(b) Layer 6

Figure 8.15 (a) and (b): Structural characterization on layer by layer analysis of the interface. Figure (a) is showing support layer (layer 5) of the interface and (b) is showing interfacial (layer 6), both layers are showing a regular periodic arrangement of the atoms.

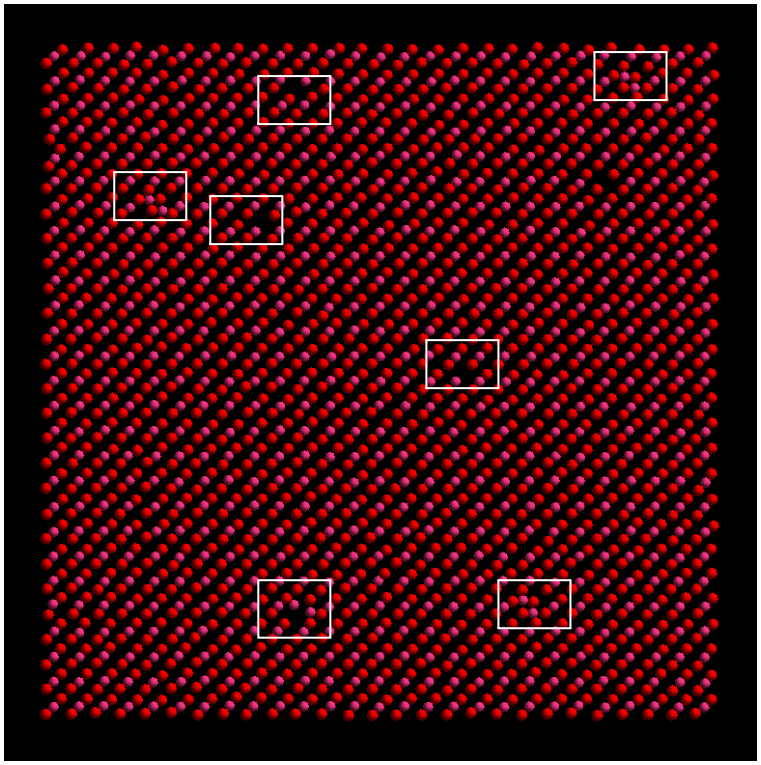

(a) Layer 7

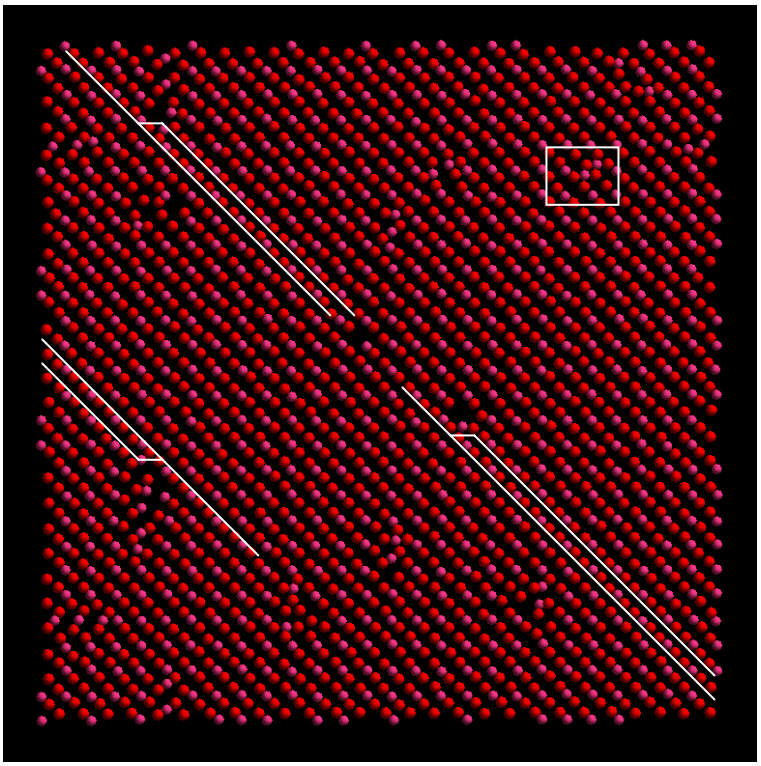

(b) Layer 8

Figure 8.16 (a) and (b): Structural characterization on layer by layer analysis of the interface. Figure (a) is showing thin film layer (layer 7) of the interface and (b) is also showing thin film layer (layer 8), both layers are showing interstitials and vacancies of Mn and O defects found within the thin film.

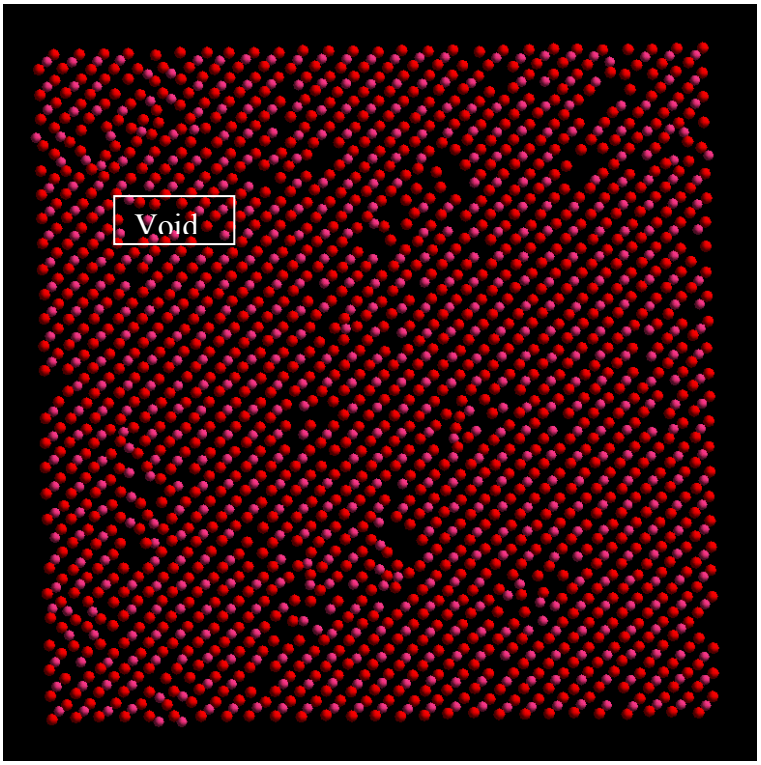

(a) Layer 9

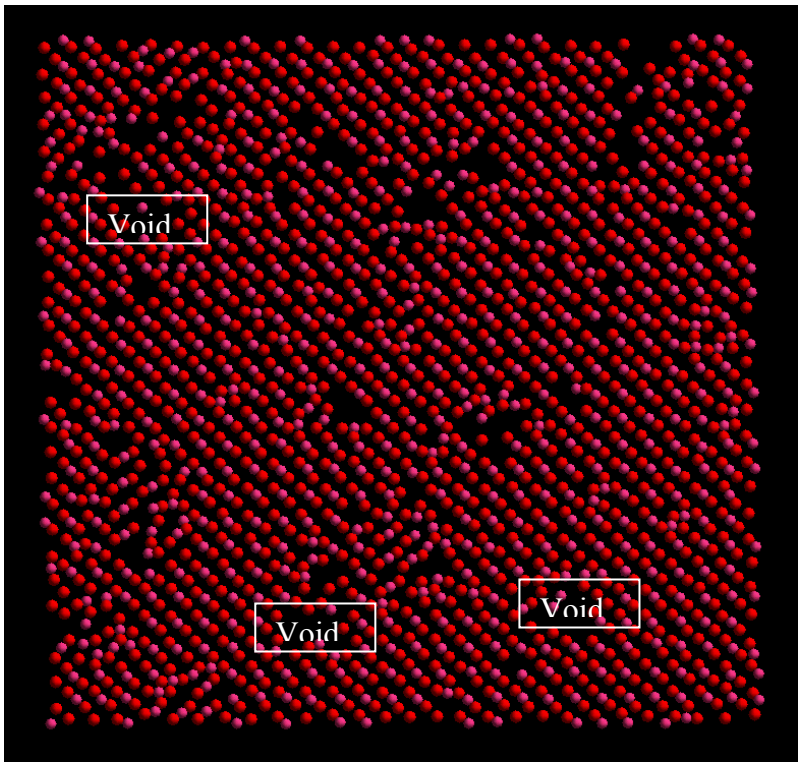

(b) Layer 10

Figure 8.17 (a) and (b): Structural characterization on layer by layer analysis of the interface. Figure (a) is showing thin film layer (layer 9) of the interface and (b) is also showing thin film layer (layer 10), both layers are showing that the number of defects increases as we go deeper into the thin film region.

8.3.2 MnO_2/MnO_2(001) 13% lattice misfit

Structural evolution of the amorphization and recrystallization, induced via +13% (compression) lattice misfit of MnO_2 pyrolusite is shown in figure 8.18 (a)-(c) for the starting, partial amorphous and final structures of the thin film respectively. Figure 8.18 (a) shows the starting structure with the thin film constrained under considerable pressure and placed on top of the support. The thin film responds, under dynamical simulation, to this huge initial pressure and relieves it via a transition of the thin film from a crystalline to an amorphous structure. Prolonged dynamical simulation results in the recrystallization of the thin film together with the evolution of structural modifications as the system responds to the lattice misfit and interaction potential of the support. From the RDFs pictures, the figures reveal that after 0.005 ps, the MnO_2 thin film loses partially the long-range order, suggesting an amorphous transition without melting. At 2.5 ps, the thin film starts to regain long-range order, indicating recrystallization of the thin film. The RDF graph for the final structure depicts broad peaks indicating poor crystallinity. In addition, inspection of the atom positions for the final structure (figure 8.18 (c)), reveals the presence of large crystalline regions separated by amorphous regions. Figure 8.19 shows the starting configuration, partial amorphous and final structure of the interface, viewed from the top side in sticks and polyhedron notations. The starting structure (a) shows the lattice mismatch clearly, partial amorphous structure (b) shows the non crystalline form of the interface and final structure (c) is showing the crystalline form with some defects. The interface final structure is showing significant structural modifications of manganese interstitials in figure 8.20.

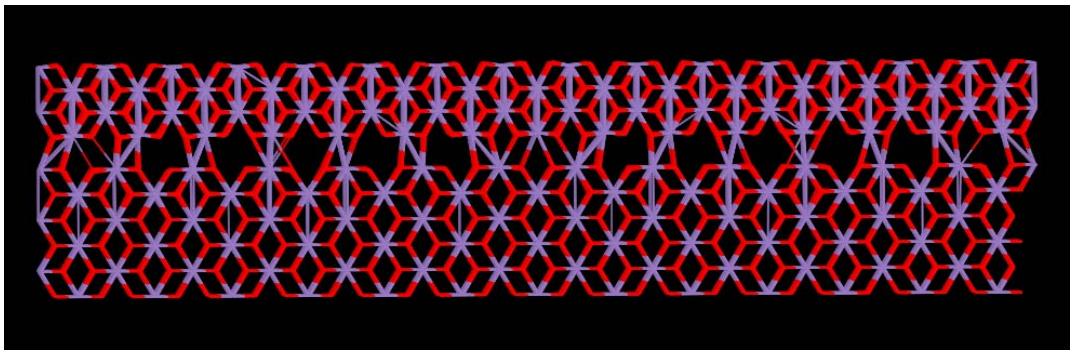

(a) Start

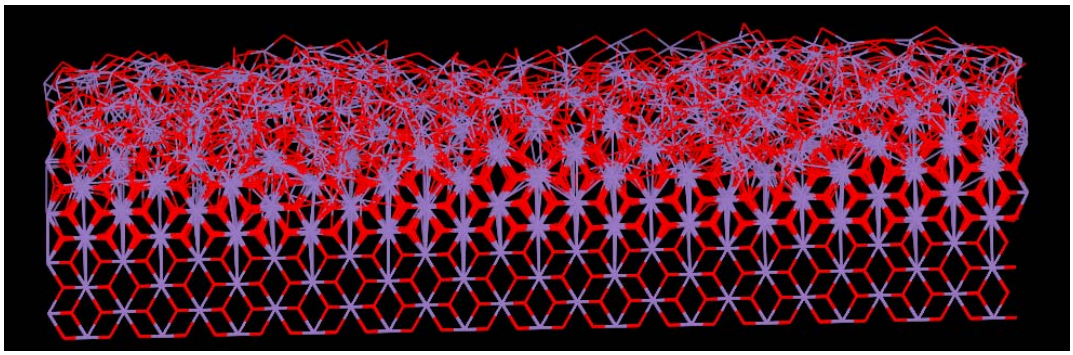

(b) Partial amorphous

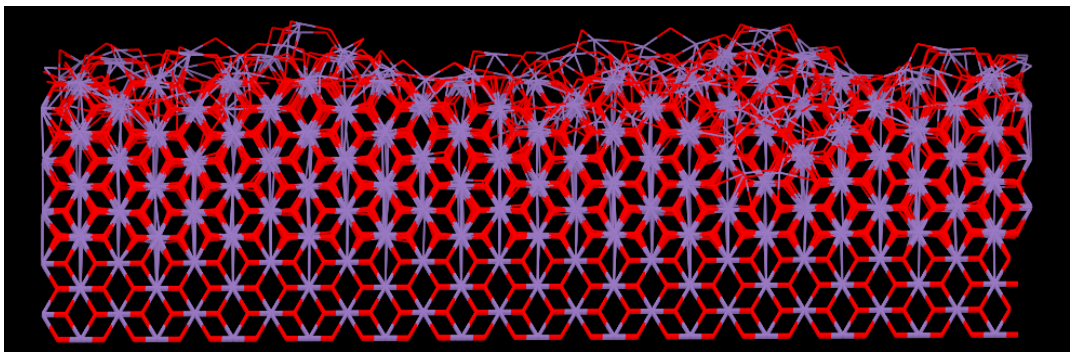

(c) Final

Figure 8.18: Pyrolusite MnO_2/MnO_2(001) interface (13% compression) at 1300K after 1 cycle. Manganese atoms are represented by the purple sticks and oxygen atoms are represented by red sticks.

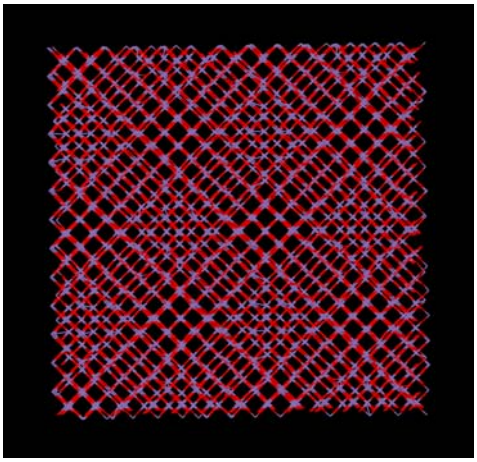

(a) Starting structure in stick notation

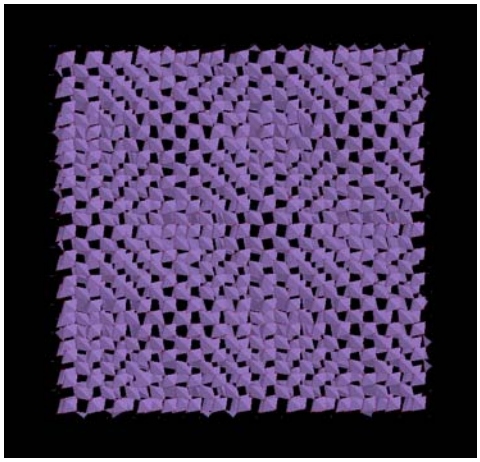

polyhedron notation

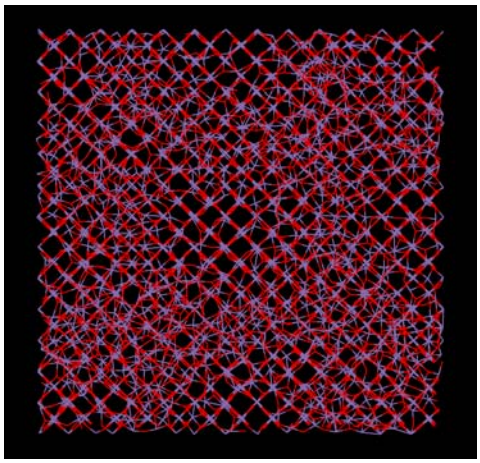

(b) Partial amorphous structure in stick notation

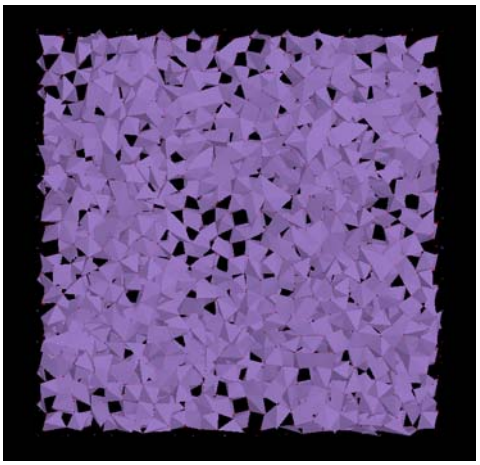

polyhedron notation

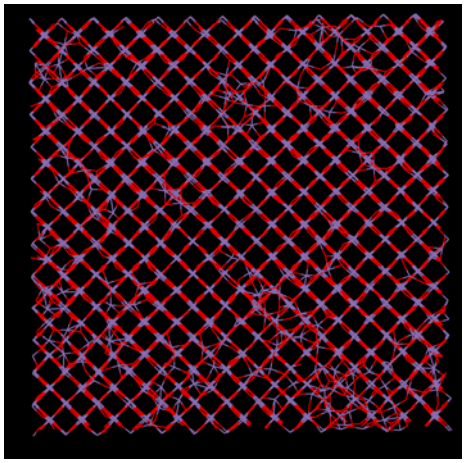

(c) Final structure in stick notation

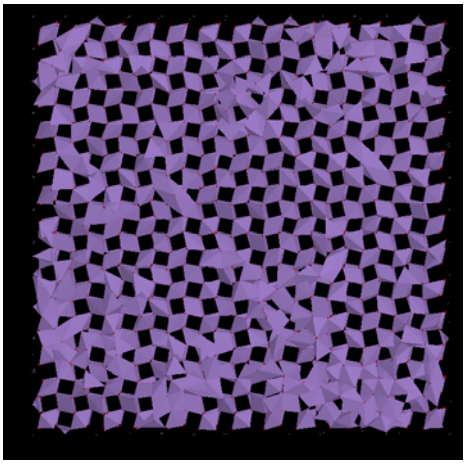

polyhedron notation

Figure 8.19: Pyrolusite MnO_2/MnO_2(001) interface (13% compression) at 1300K after 1 cycle.

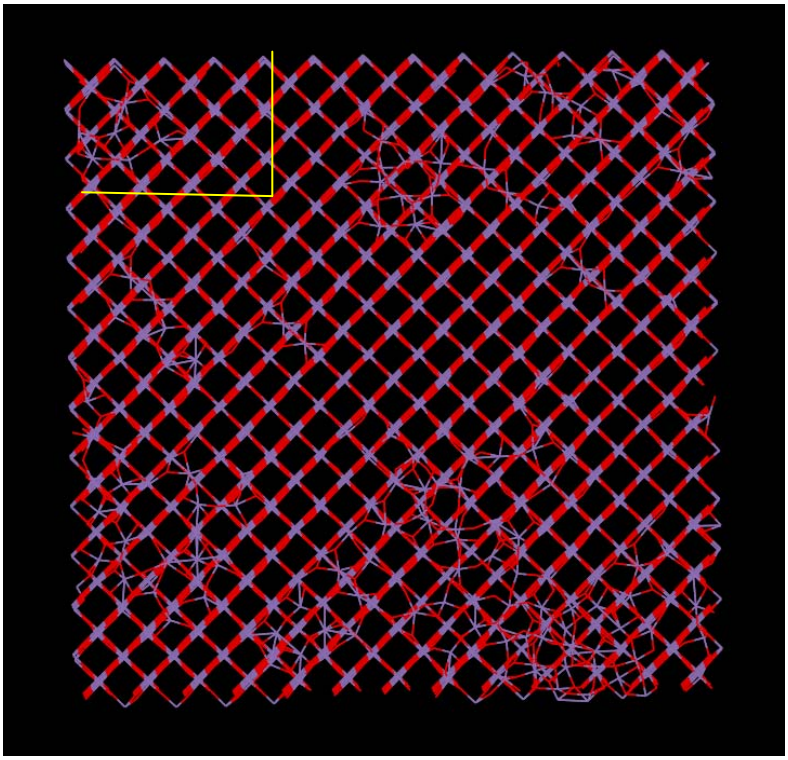

Left top corner enlarged

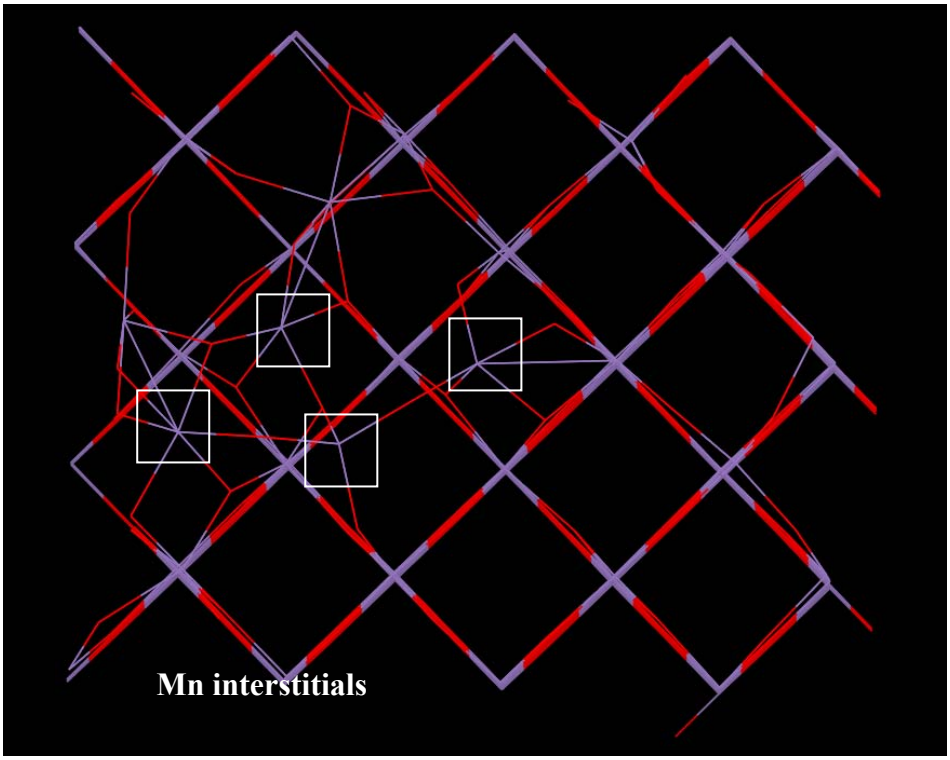

Figure 8.20: Structural characterization of the system showing defects (manganese interstitials indicated by white boxes) evolved during dynamical simulation.

8.3.3 $MnO_2/MnO_2(100)$ 10% lattice misfit

The $MnO_2/MnO_2(100)$ system, was created by placing MnO_2 thin film directly above $MnO_2(100)$ support. Both the thin film and the support are made up of six layers each. The MnO_2 was then compressed by 10% to ensure that the thin film fitted exactly within the simulation cell. Dynamical simulation, with a time step of 0.005ps, was then applied to the system at 1300K, figure 8.21(a). After 2.5ps the thin film has undergone partial amorphous transition figure 8.21(b). After prolonged dynamical simulations, the thin film started to recrystallize, figure 8.23(c). The system was the cooled down to lower temperatures, 800K, 400K, 200K and 0K, the latter acts effectively as an energy minimisation and was performed until the energy converged. For each temperature, the dynamical simulation was performed until the system was no longer evolving either structurally or energetically.

Figure 8.21(a) depicts the starting structure with the thin film constrained under considerable pressure. As the dynamical simulation progresses, the thin film expands along the surface normal in an attempt to eliminate the considerable strain present in the initial structure and causes the thin film to amorphise. At the partial amorphous state, after 2.5 ps, the corresponding Mn-O RDF exhibit the absence of long-range orders within the system. After prolonged dynamical simulation, the thin film starts to recrystallize. The RDF graph exhibits a well defined peaks, thus a crystalline state is obtained. The success of the simulated amorphization and recrystallization methodology in generating the MnO_2 structure from a partial

amorphous solid suggests that the methodology is applicable to study supported structured systems.

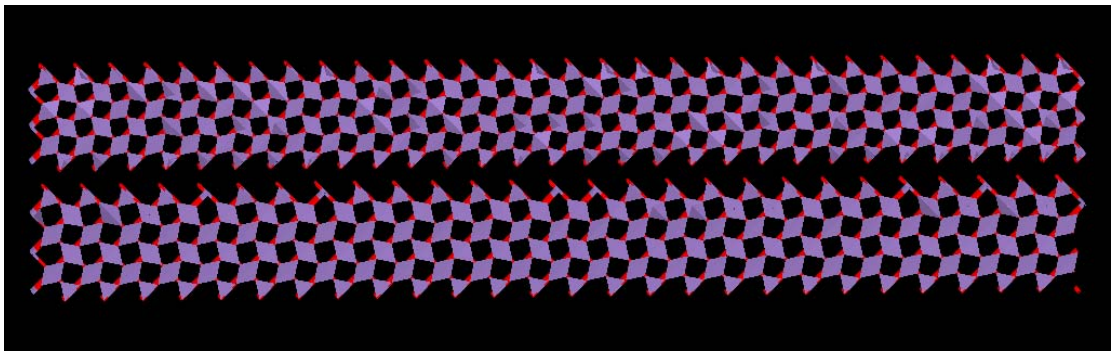

(a) Start

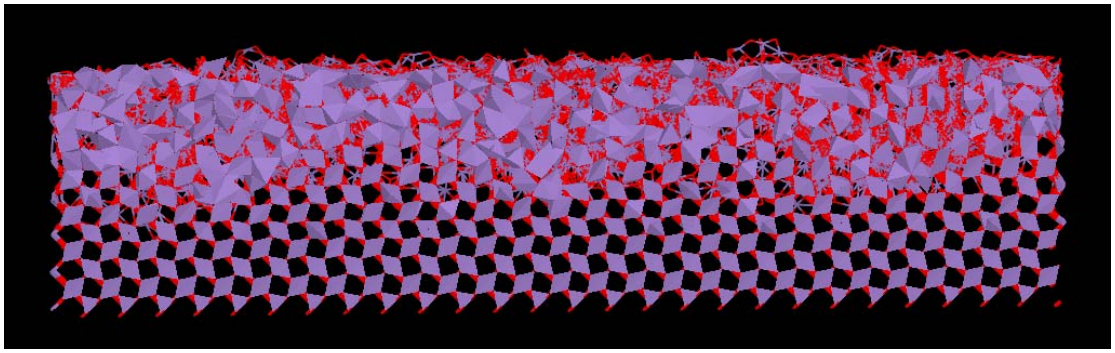

(b)Partial amorphous

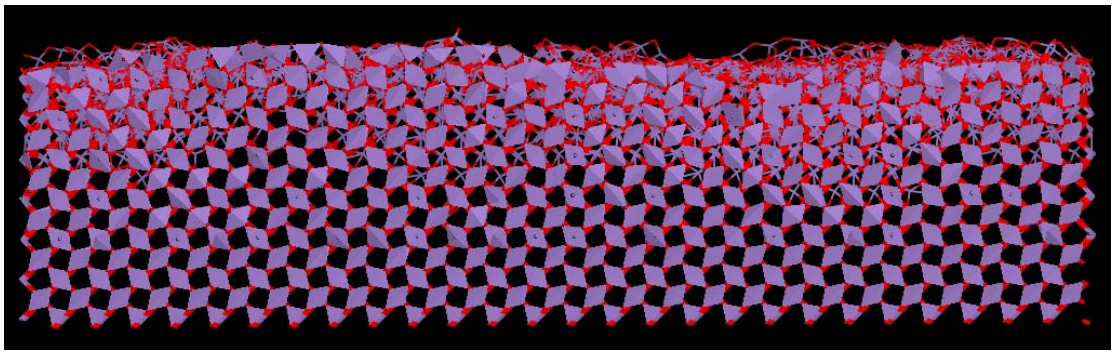

(c) Final

Figure 8.21: Pyrolusite MnO_2/MnO_2(100) interface (10% compression) at 1300K.

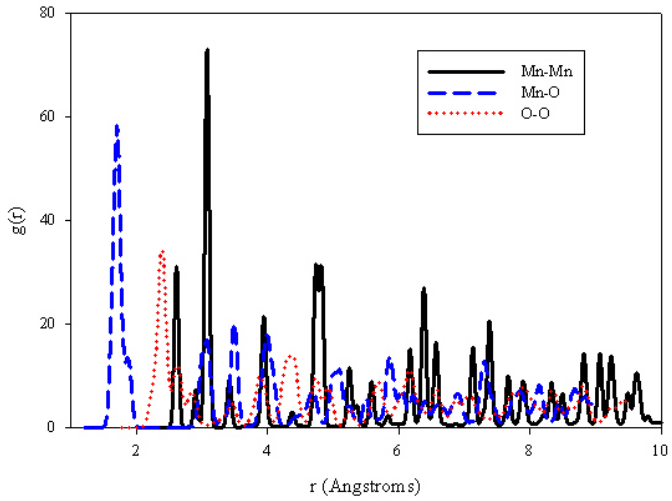

(a)

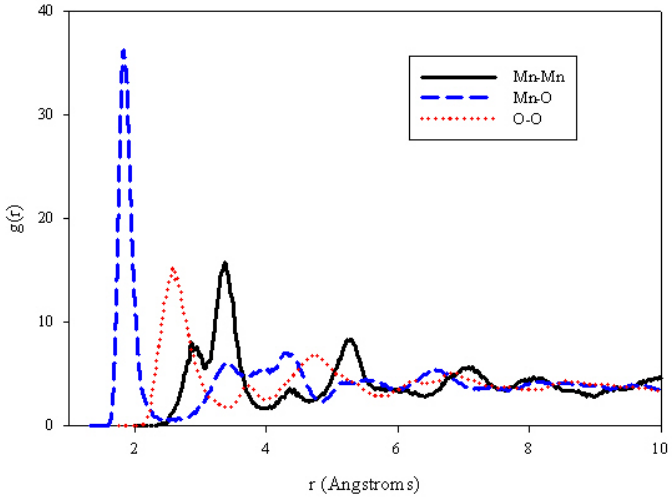

(b)

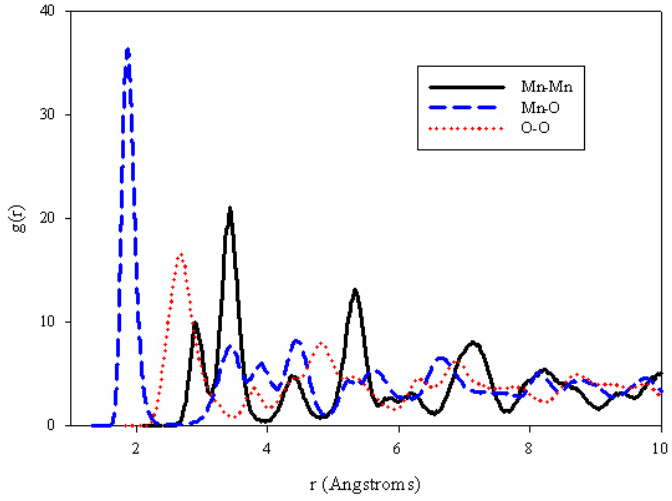

(c)

Figure 8.22: RDFs for $MnO_2/MnO_2(100)$ interface 10% lattice misfit, (a) start, (b) partial amorphous and (c) final structures.

8.3.4 MnO_2/MnO_2(100) 13% lattice misfit

The effect of temperature on the interfaces is discussed in this section. As in all other interfaces, the starting configuration was generated by applying dynamical simulation at 1300K for 0.005ps. Owing to the influence of the lattice misfit in the system the thin film had undergone partial amorphous transition after 2.5ps. The dynamical simulation was then prolonged, where the thin film started to recrystallize. Figure 8.23 (a)-(c) depicts this different stages graphically, where (a) is showing starting configuration in polyhedron notation, (b) is showing the partial amorphous state and (c) the final structure of the interface. The calculated Mn-Mn, Mn-O and O-O RDFs within the MnO_2 thin film during dynamical simulation performed at different temperatures are shown in figure 8.25 (a)-(c) respectively. After one step the RDF shows dense peaks, which correspond to compressed crystalline structure. After 2.5 ps, the MnO_2 thin film loses the some long-range order, indicating an partial amorphous transition. At the end of the simulation the thin film has regained some long-range order; two additional peaks have started to evolve, indicating that the system has regained its crystallinity.

The RDFs in figure 8.25 exhibit that as the low temperature is applied to the system, the height's of the peaks increases and the broadness of the peaks decreases, which indicates that the system is becoming more ordered at lower temperatures. This is again confirmed by the graphical representation of the atom positions shown in figure 8.26, the system at lower temperatures are more ordered compared to those at higher temperatures.

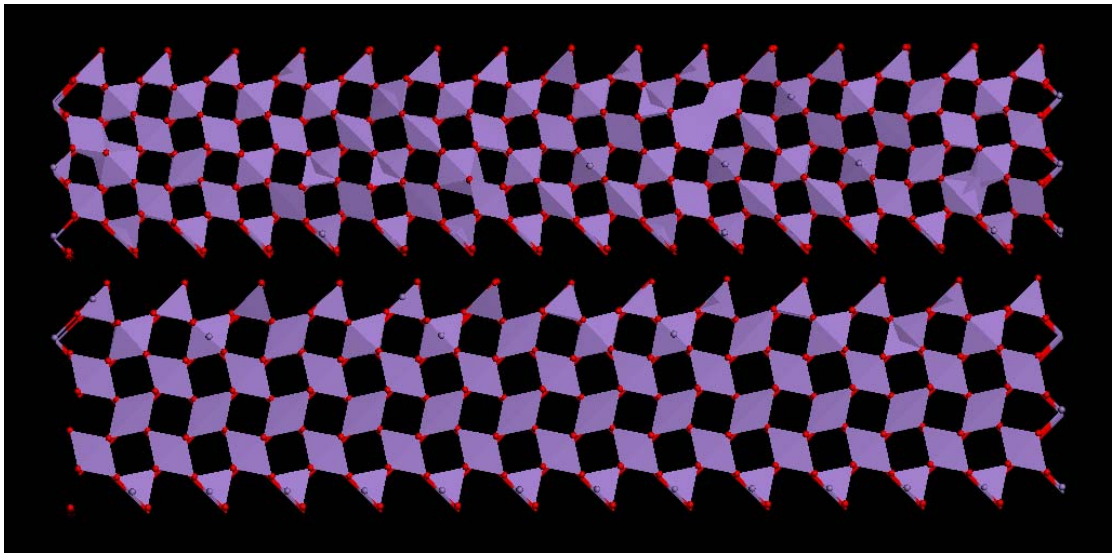

(a) Start

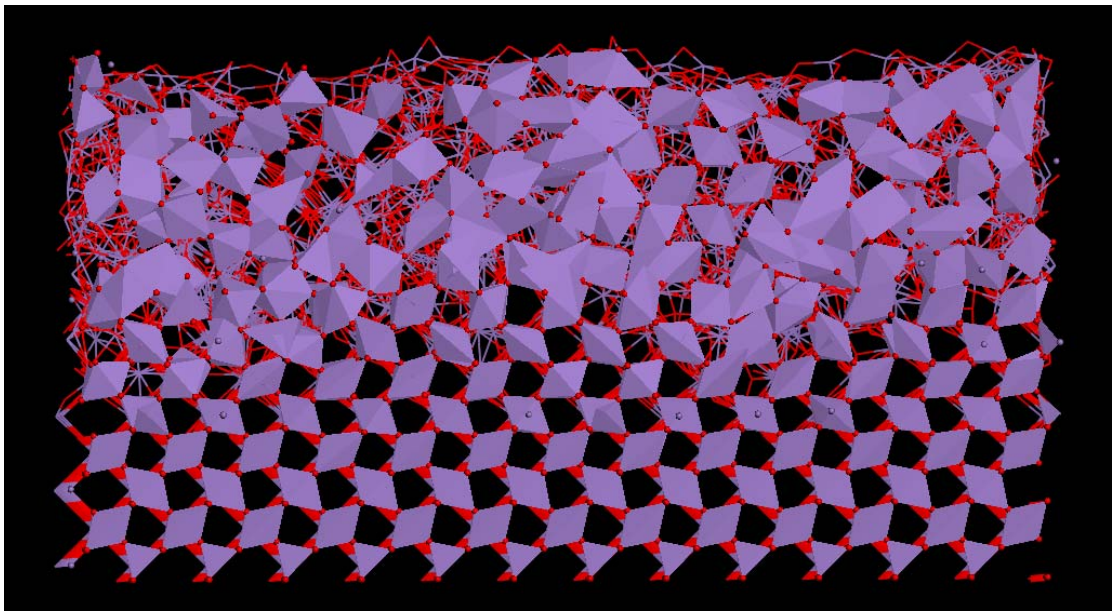

(b) Partial amorphous

Figure 8.23 (a) and (b): Structures of pyrolusite MnO_2/MnO_2(100) interface 13% lattice misfit, (a) starting configuration and (b) partial amorphous structure.

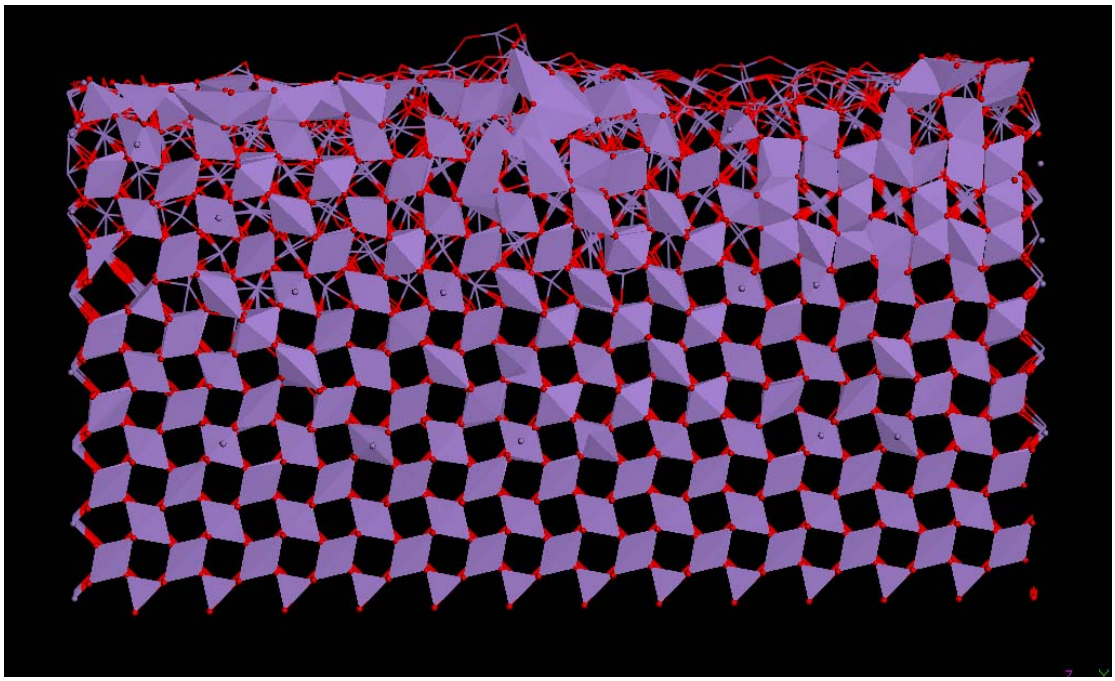

Final

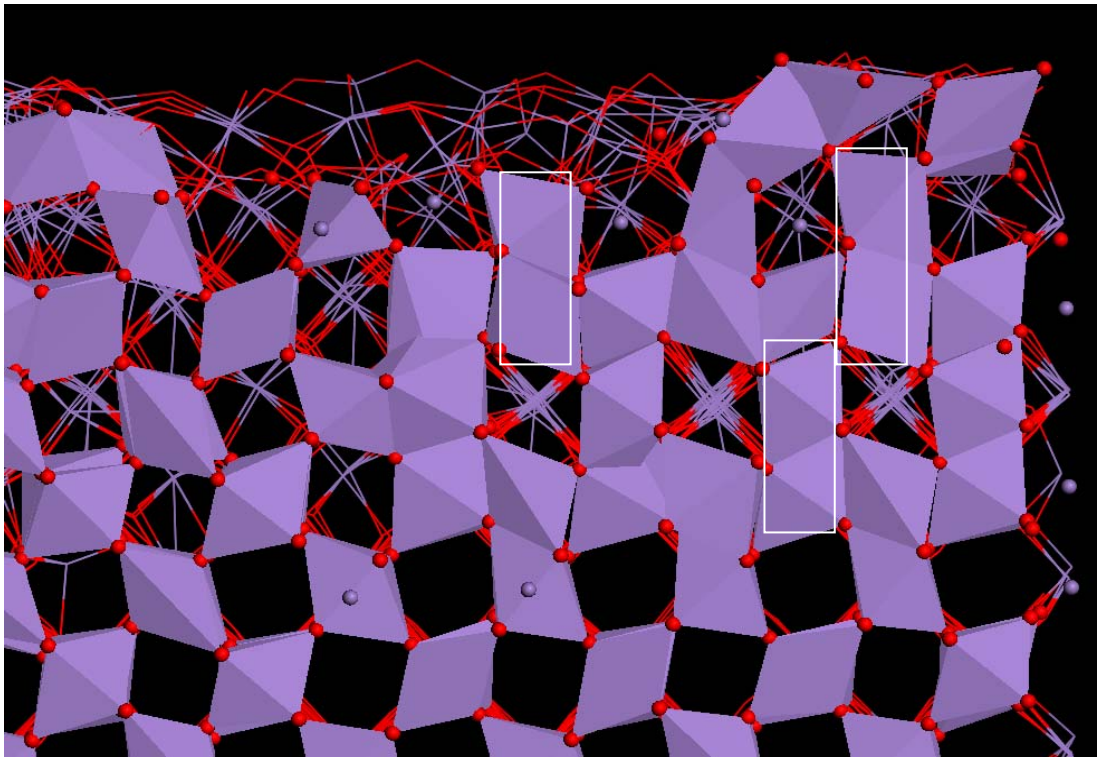

Enlarged top right hand corner

Figure 8.24: Final structures of pyrolusite MnO_2/MnO_2(100) interface 13% lattice misfit, also shown is the enlarged top right hand corner of the interface showing the stacking fault within the system.

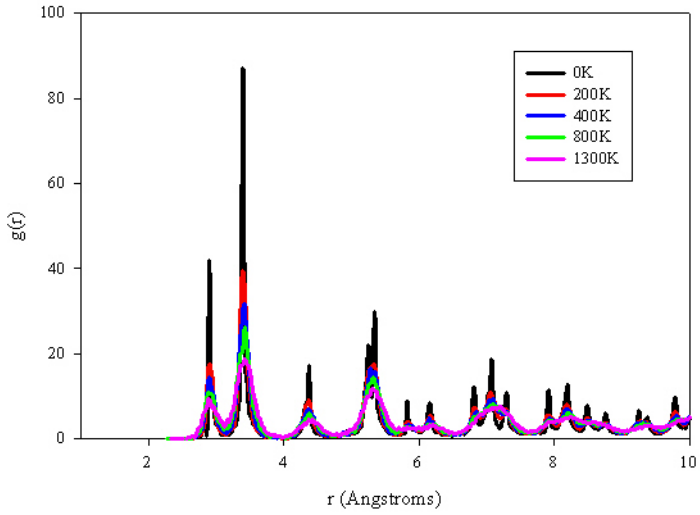

(a)

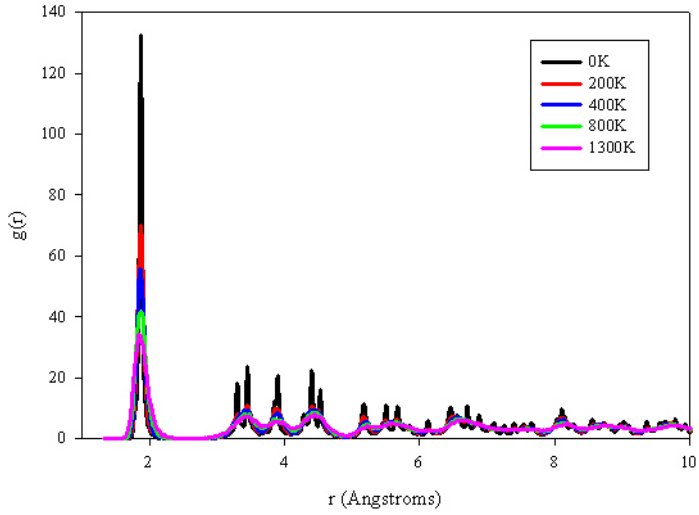

(b)

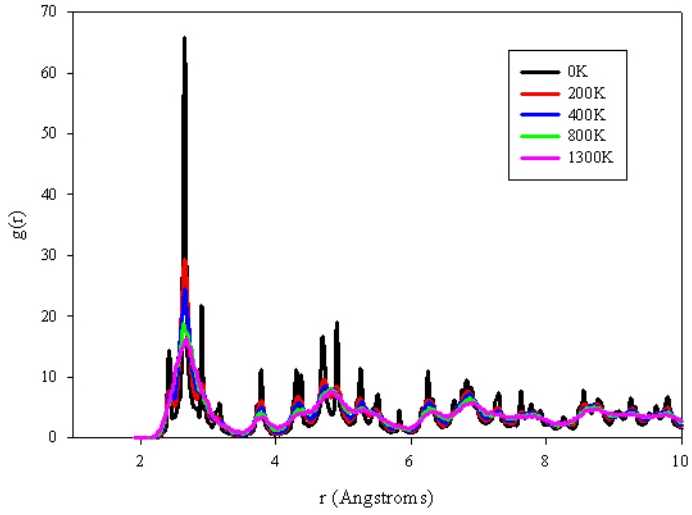

(c)

Figure 8.25: RDFs for $MnO_2/MnO_2(100)$ interface 10% lattice misfit, (a) Mn-Mn, (b) Mn-O and (c) O-O pairs.

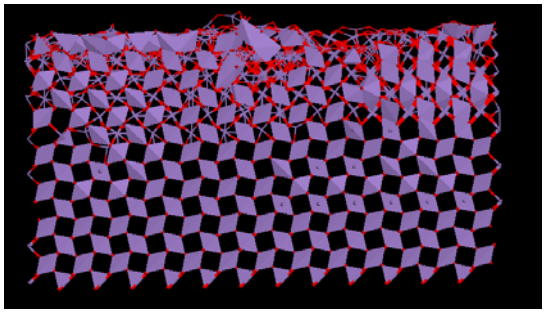

0K

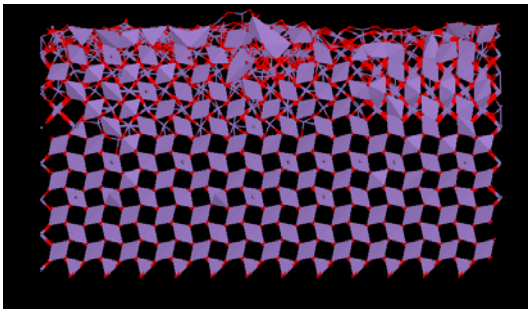

200K

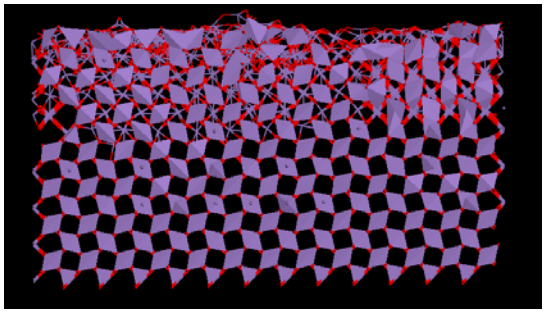

400K

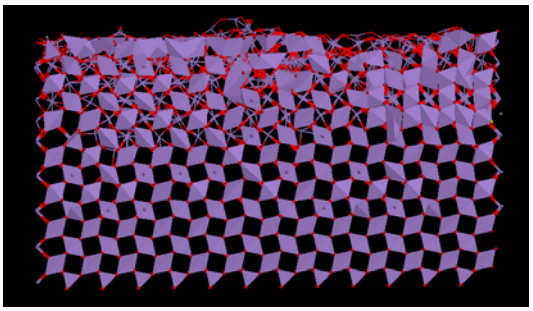

800K

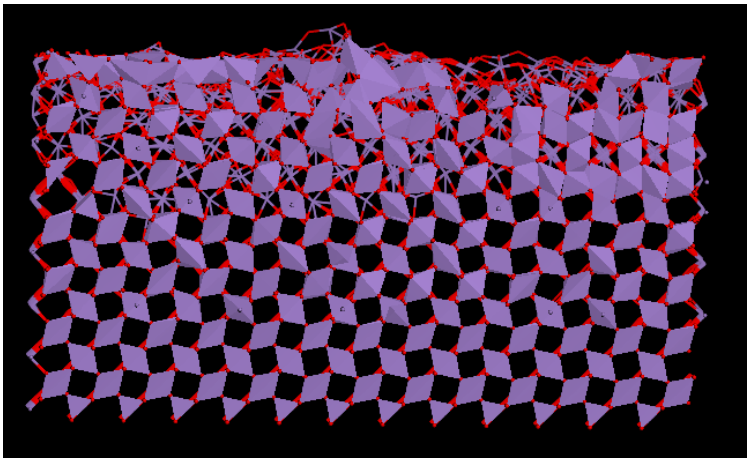

1300K

Figure 8.26: Pyrolusite MnO_2/MnO_2(100) interface 13% lattice misfit showing structures at different temperatures.

8.3.5 Ramsdellite MnO_2/MnO_2(100) -6% lattice misfit, NVE

(a) Start

Radial distribution function picture corresponding to the atom positions after 0.005 ps is shown in figure 8.27 for Mn-O pair. The RDFs picture is showing well-defined peaks of the starting structure corresponding to a crystalline structure. The first maximum peak corresponding to the nearest neighbour distance of Mn-O is located at 1.97 Å with a peak of height of approximately 27.98.

Figure 8.28 shows the directional densities of manganese and oxygen at the starting point of dynamical simulation. The peaks correspond to the layers of the thin film and the support. The system is composed of twenty-five layers, twelve-five layers of the thin film and twelve-five layers of the support.

The calculated atom positions, after the time step of 0.005 ps of the dynamical simulation are shown in figure 8.29. The misfit of –6% was applied to the system, that is the tension of 6% was applied to the thin film. The simulation cell is composed of 22068 atoms.

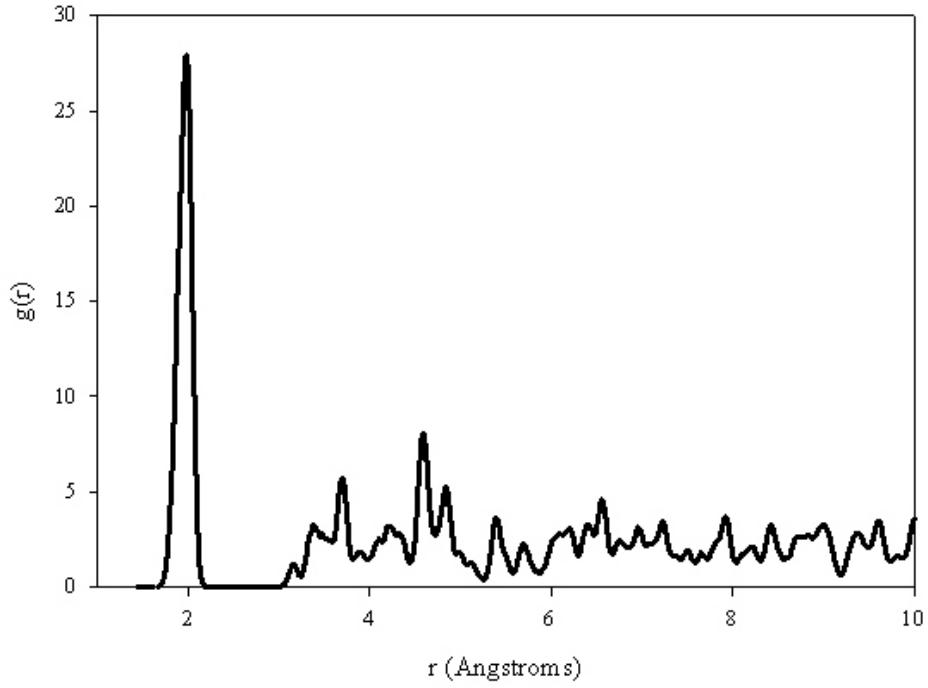

Figure 8.27: Ramsdellite MnO_2/MnO_2(100) interface (6% tension) NVE, Mn-O rdf at 1300K after 0.005 ps.

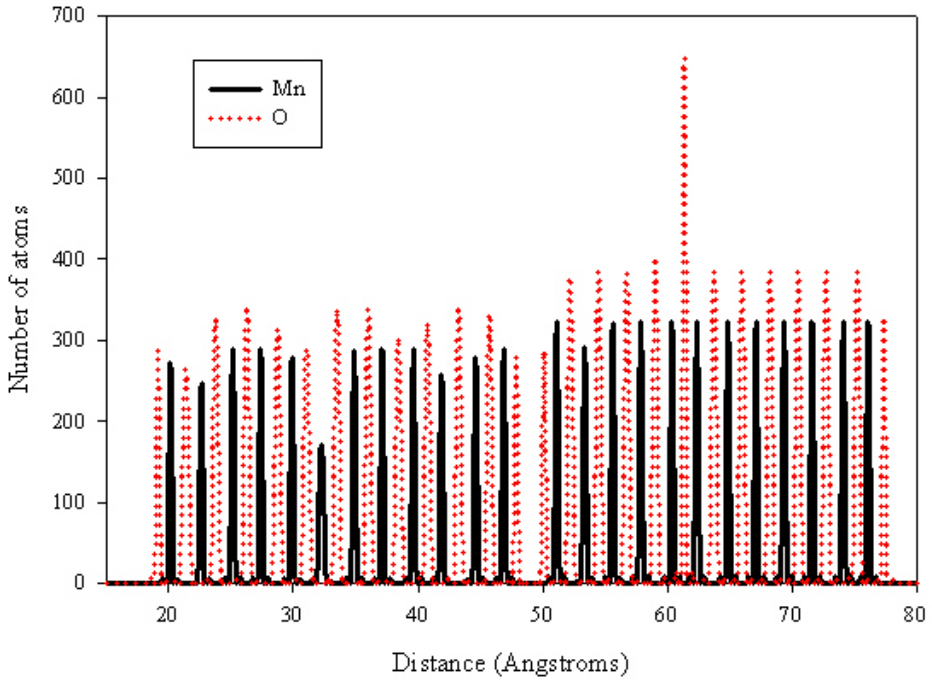

Figure 8.28: Ramsdellite MnO_2/MnO_2(100) interface (6% tension) NVE, Mn- and O densities at 1300K after 2.5 ps.

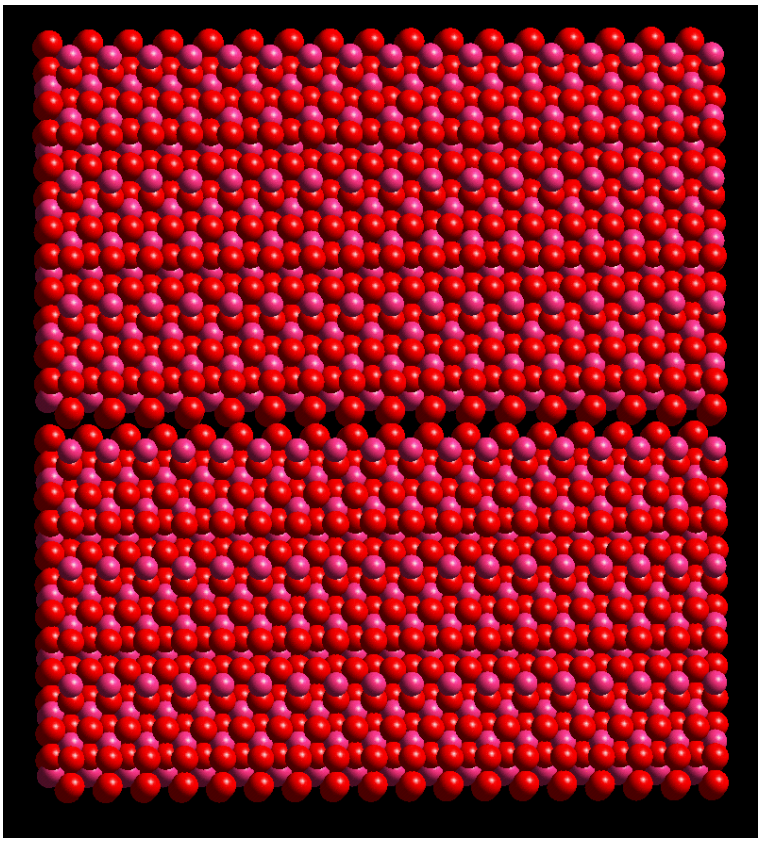

Figure 8.29: Ramsdellite interface (6% tension) NVE, at 1300K after 0.005 ps. Manganese atoms are represented by the pink balls and oxygen atoms are represented by red balls.

(b) Amorphous

The RDF of the partial amorphous structure, depicting Mn-O pair, is shown in figure 8.30. The graph shows that some long-range order is being lost in the system. The first maximum peak corresponding to the nearest neighbour distances of Mn-O is now at approximately 1.88Å. The density plot given in figure 8.31 shows that the system is partially amorphous, since some layers (in particular, layers of the thin film), are no longer represented by sharp peaks, as it was at the beginning of the simulation. Figure 8.32 shows graphical representation of calculated atom positions after 1500 cycles. As it can be noted from the picture, at this stage the MnO_2 thin film is partially amorphous.

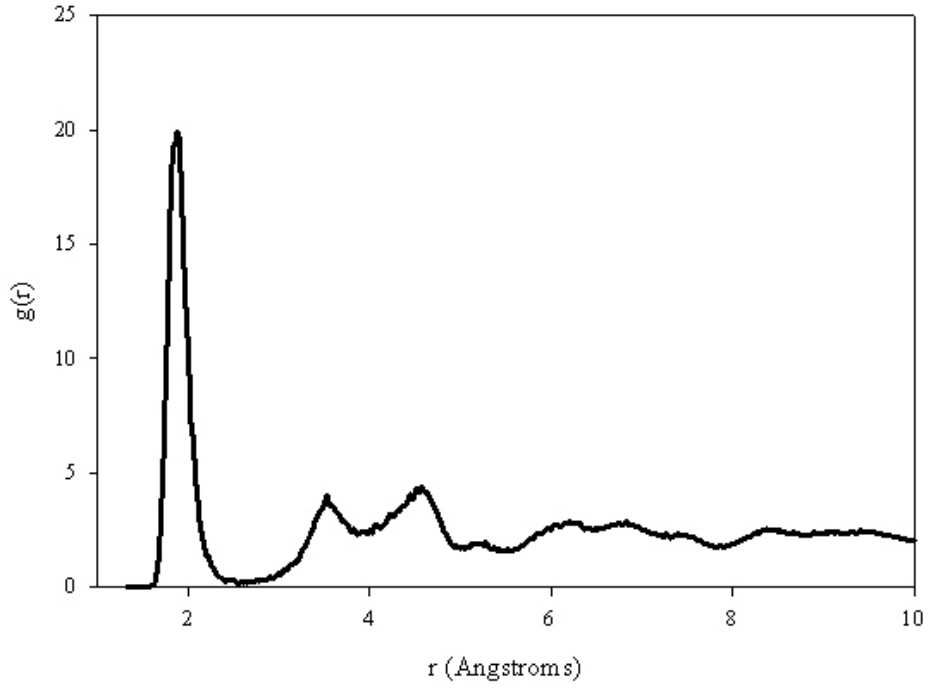

Figure 8.30: Ramsdellite MnO_2/MnO_2(100) interface NVE, (6% tension) Mn-O rdf at 1300K after 7.5 ps.

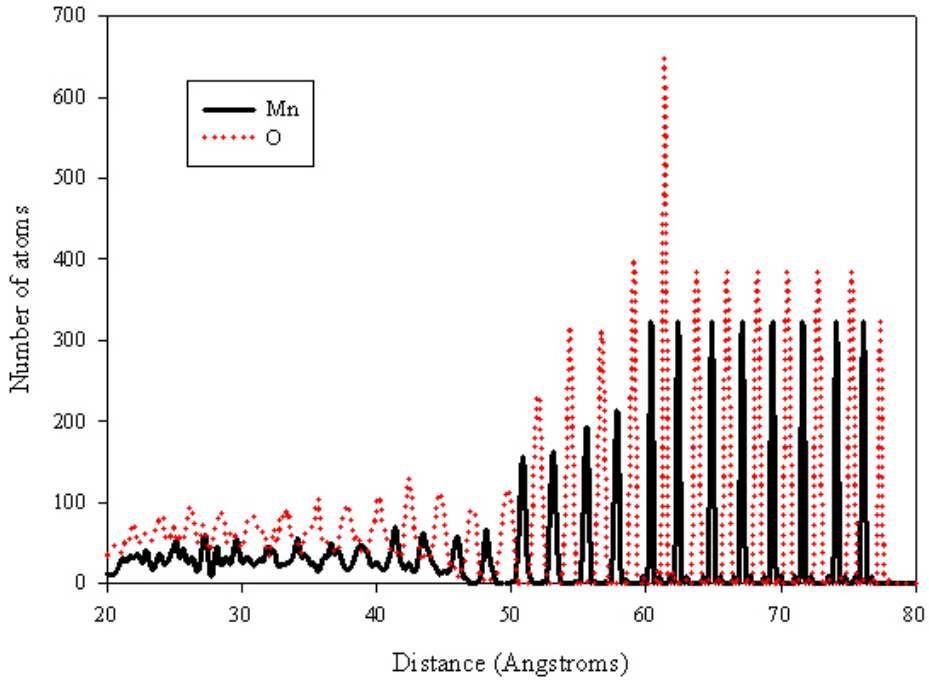

Figure 8.31: Ramsdellite MnO_2/MnO_2(100) interface (6% tension) NVE, Mn and O densities at 1300K after 7.5 ps.

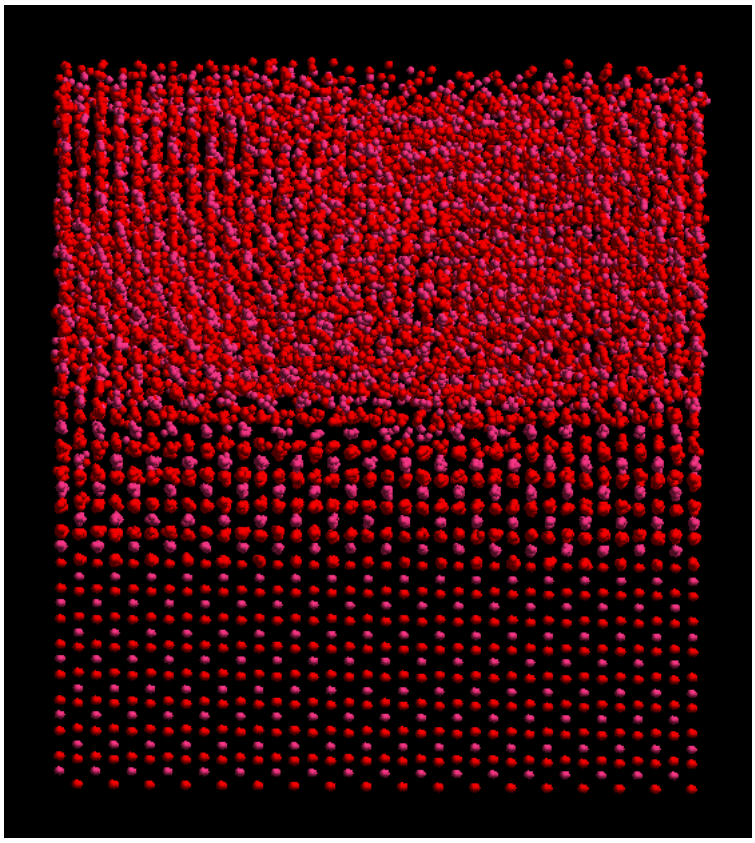

Figure 8.32: Ramsdellite interface (6% tension) NVE, at 1300K after 7.5 ps.

(c) Final

The RDFs corresponding to Mn-O pair interaction at 0K (lower temperature) is given in figure 8.33. Now the RDF is showing both the short-range order and the long-range order. This indicates that the thin film has now recrystallized. The Mn-O pair is represented by a first maximum peak, which has the nearest neighbour distance of 1.88Å. The directional densities also show that the thin film has recrystallized as evidenced in figure 8.34, for both manganese and oxygen atoms. After a prolonged dynamical simulation, MnO_2 thin film has recrystallized into pyrolusite and ramsdellite structures. The pyrolusite-ramsdellite interface has formed naturally, with no 'artificial' interventions on the system. The supported thin film, shown in figure 8.35, changed to a random distribution of pyrolusite layers formed from single chains and ramsdellite layers formed from double

chains. The width of pyrolusite and ramsdellite tunnels is similar in one dimension and these phases easily form a domain intergrowth. This type of random planar defect has been given the name de Wolff disorder by de Wolff [1959] and Pannetier [1992]. The EMDs and CMDs are generally poorly crystallized and the X-ray diffraction patterns may look different from one sample to another. Their structures are much more complicated and generally undetermined. Ripert et al [1991a] have proposed an extended de Wolff's model and in the model he described γ–MnO structure as a basic ramsdellite structure modified by the following:

- Stacking disorder of ramsdellite and pyrolusite slabs (de Wolff disorder [1959]) and
- Microtwinning in the ramsdellite lattice along (021) and (061) planes [Ripert 1991a].

However, experimental evidence confirming de Wolff model has been scarce [Godart 1992]. Research investigations turned to analytical methods that are sensitive to the short-range atomic order or medium-range atomic order, rather than the long-range order. Different techniques gave different results. Infra-red (IR) studies supported de Wolff's model [Potter 1979]. High Resolution Electron Microscopy (HREM) revealed a mixture of complex intergrowths patterns together with incoherent defects [Turner 1979]. The technique discovered intergrowths of multi-dimensional tunnels in natural occurring Mn(IV) oxides. Electron diffraction gave an experimental evidence of de Wolff's intergrowth structure in Electrolytic Manganese Dioxide [Charenton 1988]. Our calculations also confirmed the de Wolff' model.

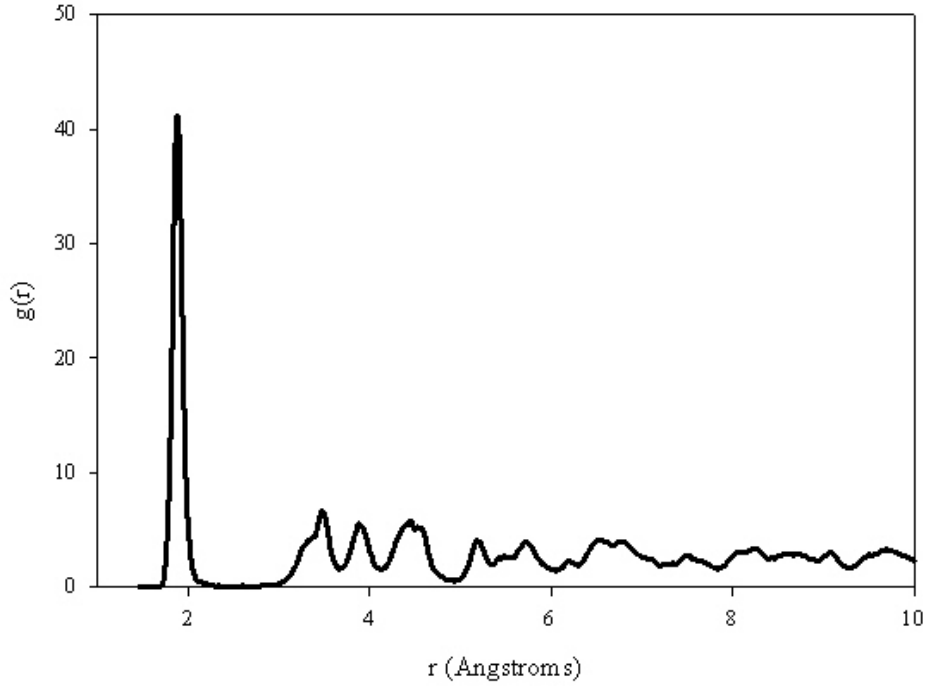

Figure 8.33: Ramsdellite MnO_2/MnO_2(100) interface (6% tension) NVE, Mn-O rdf at 200K after 2650 ps.

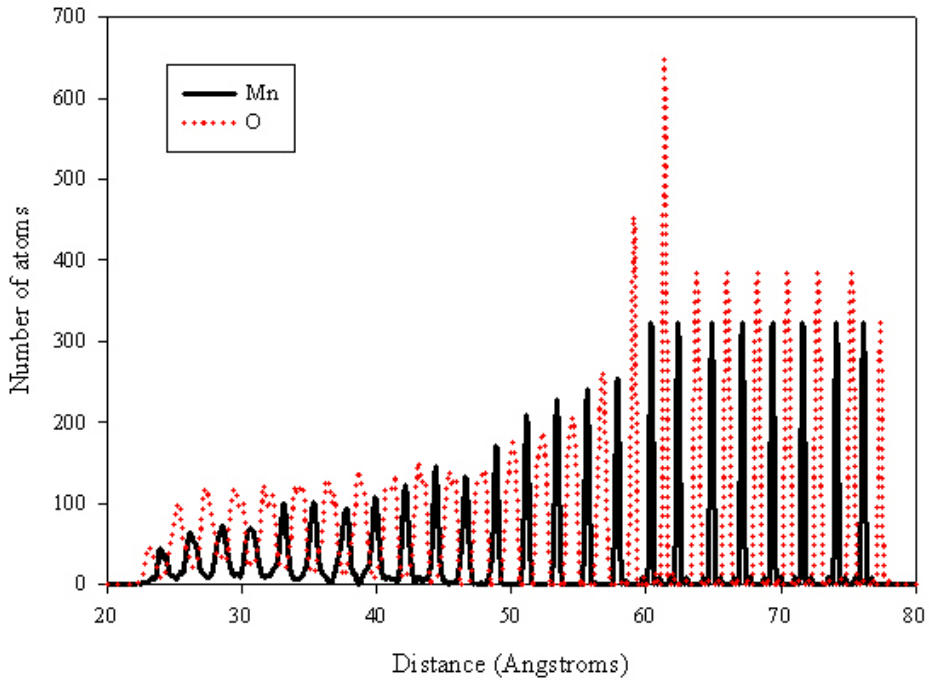

Figure 8.34: Ramsdellite MnO_2/MnO_2(100) interface (6% tension) NVE, Mn and O densities at 1300K after 2650 ps.

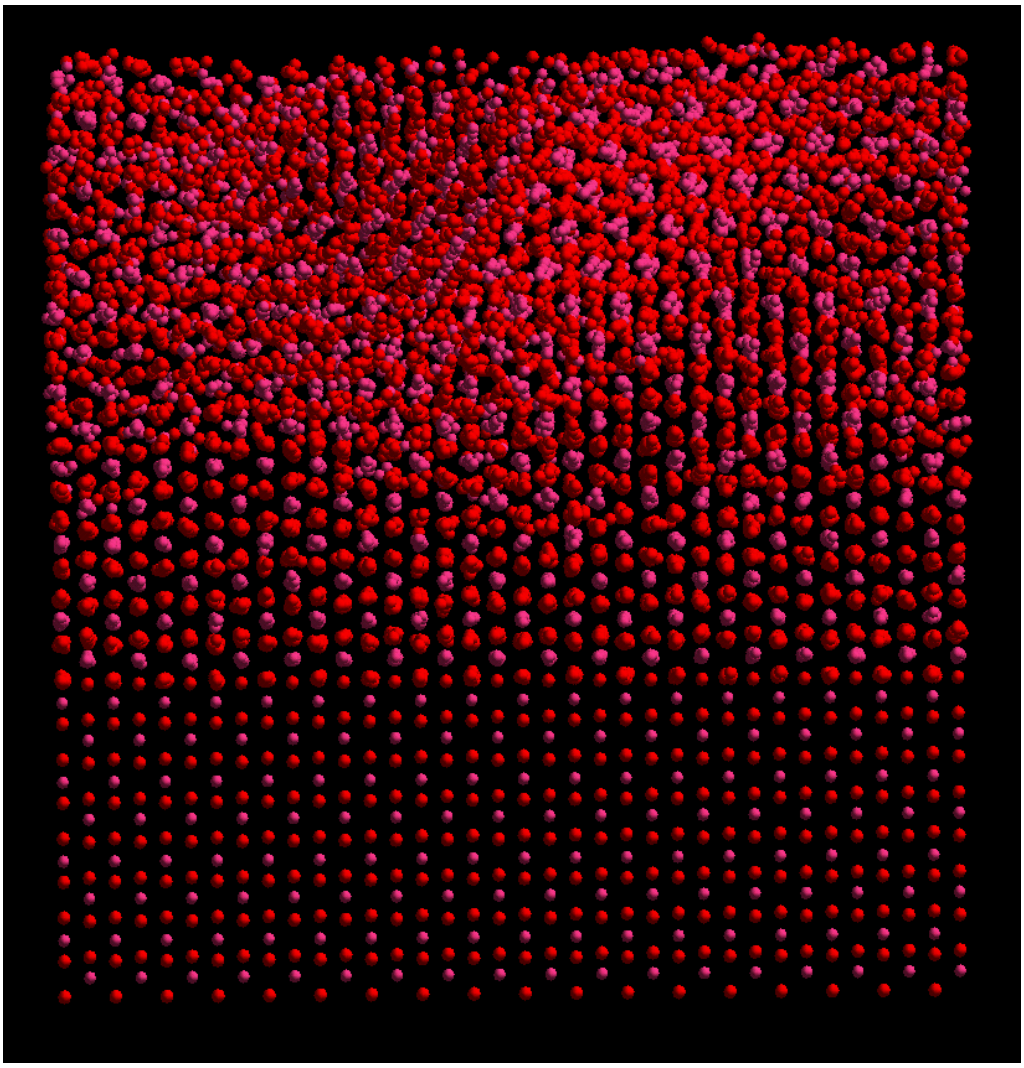

(a)

Figure 8.35 (a): Ramsdellite interface (6% tension) NVE, at 200K after 2650 ps.

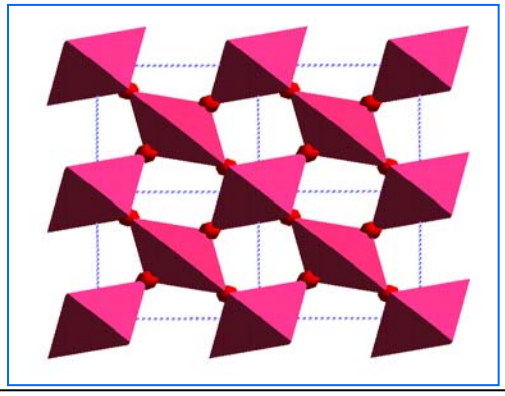

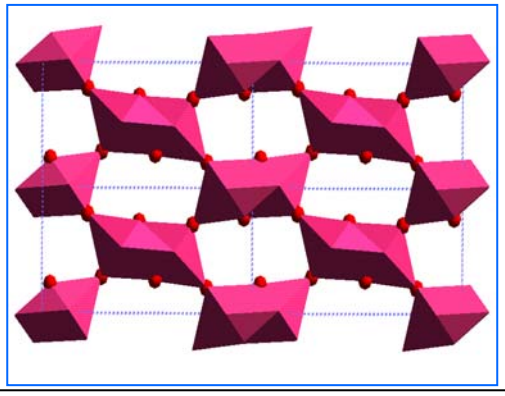

Pure pyrolusite (P) crystal model showing single chains connected to other single chains by corners	Pure ramsdellite (R) crystal model showing double chains connected to other double chains by corners

Pyrolusite-Ramsdellite intergrowth yielded from $MnO_2/MnO_2(100)$ ramsdellite thin film-support interface. The model is showing pyrolusite (single chains) and ramsdellite (double chains) structures and some defects (vacancies and substitutional atoms).

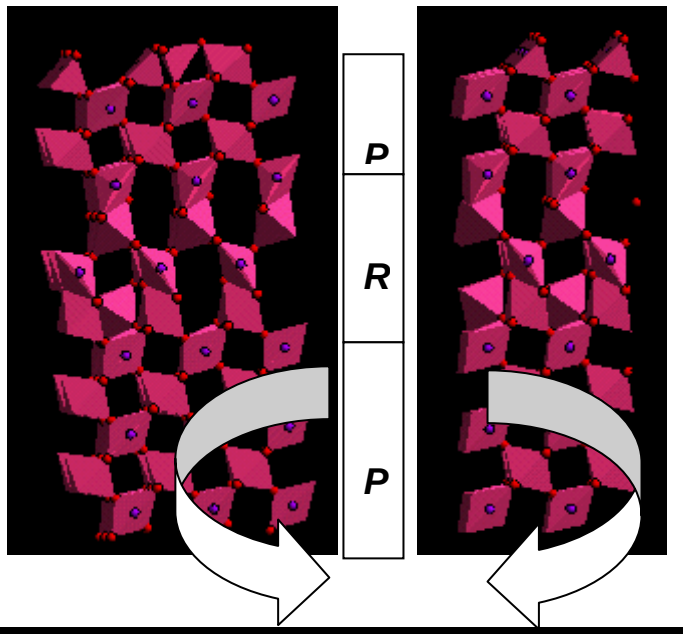

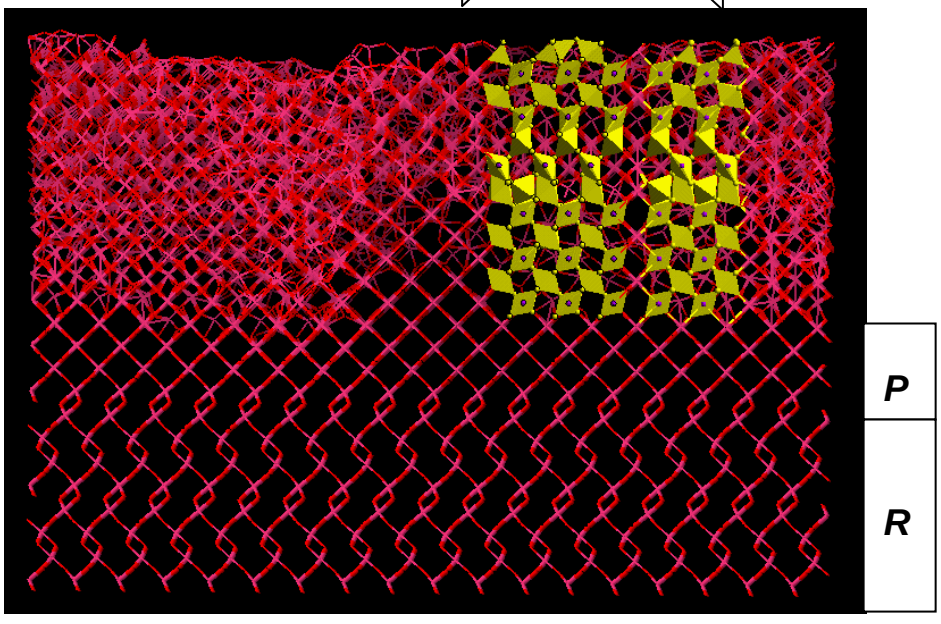

(b)

Figure 8.35 (b): Ramsdellite interface (6% tension) NVE, at 200K after 2650 ps.

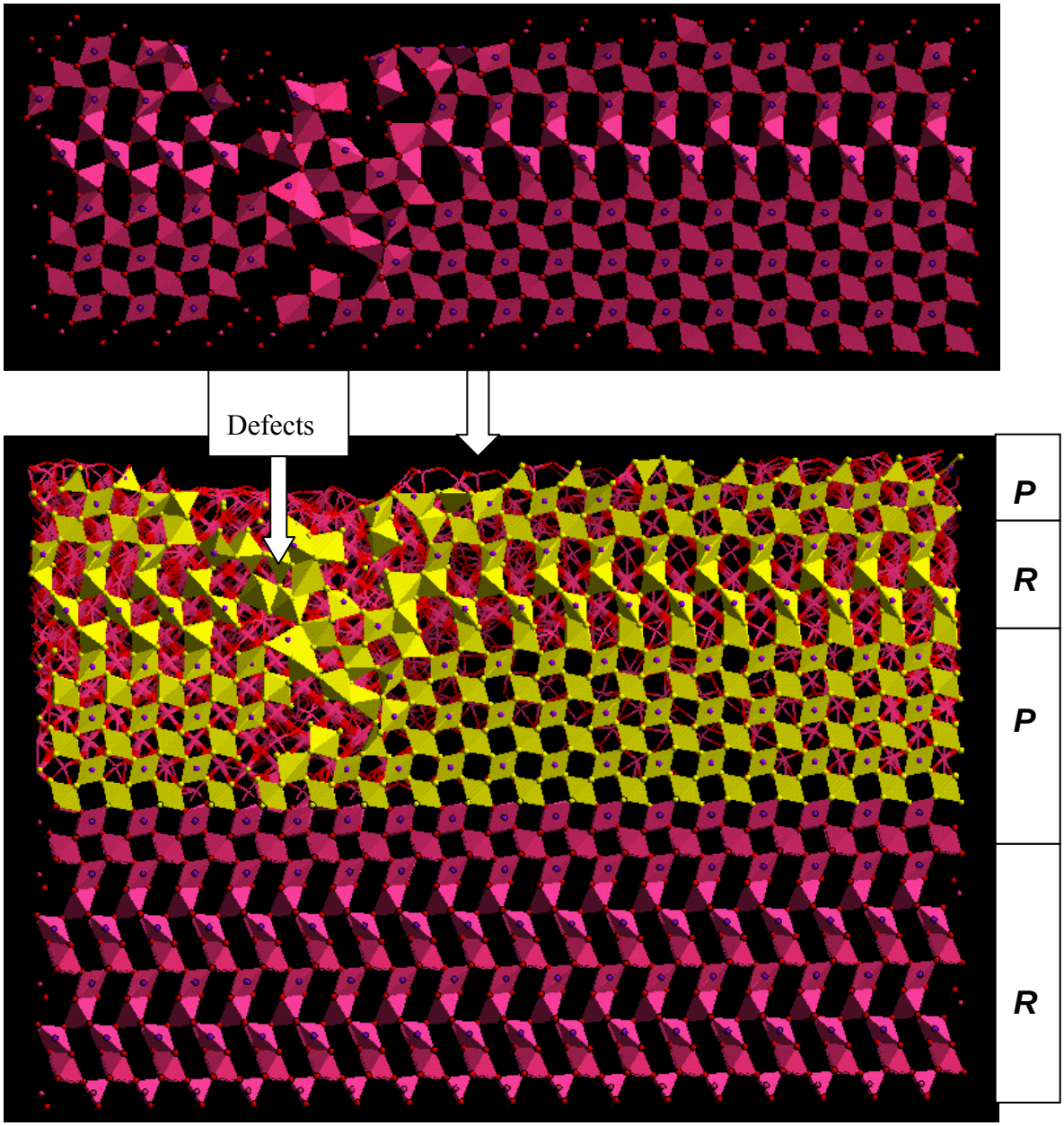

Figure 8.35 (c): Ramsdellite interface (6% tension) NVE, at 200K after 2650 ps.

Table 8.1 shows that partial amorphization and recrystallization technique gave results which are in good agreement with our EXAFS results, in particular in terms of radial distances. Moreover, our results compare very well with literature results [Petit 1993, Manceau 1988, Godart 1992 and Li 1988c].

THIS WORK'S RESULTS						
EXAFS	Pyrolusite	Ramsdellite	RC1	RC2	RG1	RG2
O	1.899	1.898	1.899	1.896	1.900	1.895
Mn	2.885	2.886	2.889	2.880	2.885	2.879
Mn	3.620	3.597	3.661	3.622	3.659	3.626
O	3.457	3.448	3.476	3.456	3.471	3.452
O	4.029	….	4.205		4.194	
Mn			4.533		4.634	
O			4.453		4.472	
MD	Pyrolusite	R1P1	R3P1	R3P1R1	P12	P1R1P2R1P5
O	1.911	1.914	1.910	1.891	1.891	1.891
Mn	2.954	2.924	2.917	2.973	2.916	2.961
Mn	3.937	3.437	3.436	3.780	3.447	….
O	3.445	3.491	3.534	3.445	3.449	3.449
A and R*	EMD1	EMD2	EMD3	EMD4	EMD5	EMD6
O	1.88	1.88	1.88	1.85	1.88	1.88
Mn	2.90	2.93	2.93	2.90	2.97	2.95
Mn	3.43	3.43	3.43	3.43	3.43	3.45
O	3.80	3.88	3.48	3.43	3.82	3.83

LITERATURE RESULTS					
Pyrolusite	Petit [1993]	Manceau [1988]	Godart [1992]	Li [1988c]	
O	1.9		1.90, 1.86	1.88	
Mn	2.8	2.88	2.87, 2.87	2.87	
Mn	3.4		3.40, 3.44		
O	3.4	3.45	3.44, 3.44	4.06	
Ramsdellite					
O			1.90, 1.88	1.894	
Mn	2.86	2.90	2.90, 2.88	2.833	
Mn			3.40, 3.46		
O	3.48	3.48	3.41, 3.42	4.082	
EMD					
O			1.86		
Mn			2.86		
Mn			3.43		
O			3.44		

Table 8.1: Comparison of EXAFS, molecular dynamics, A and R* and available radial distance results for pyrolusite, ramsdellite and their interfaces. P is pyrolusite, R is ramsdellite and A and R* is amorphization and recrystallization technique. For EXAFS the interfaces are represented by RC1, RC2, RG1 and RG2 samples. EMD 1-6 are the interfaces mentioned in Chapter 8, the order is as they are discussed in there.

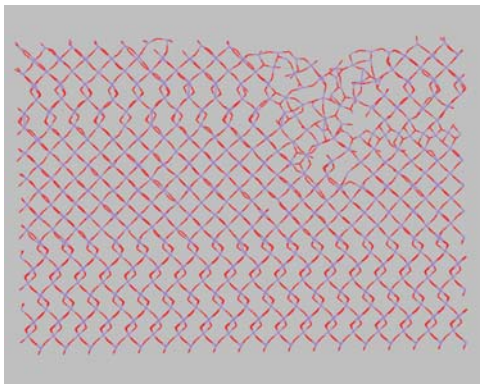

Slice 1

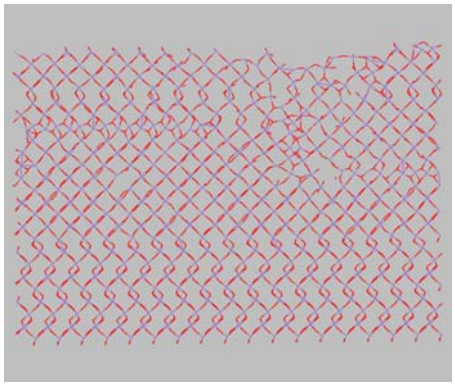

Slice 2

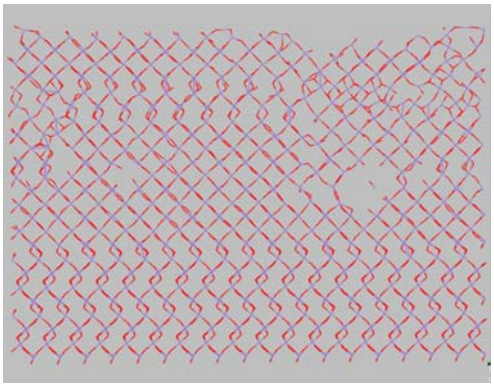

Slice 3

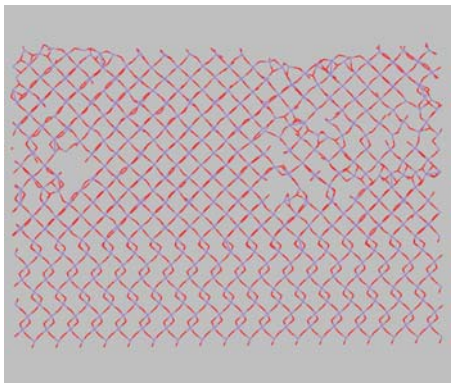

Slice 4

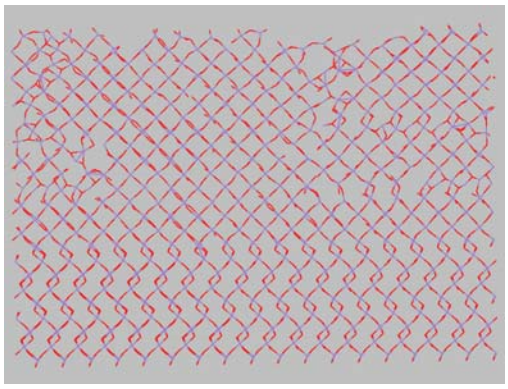

Slice 5

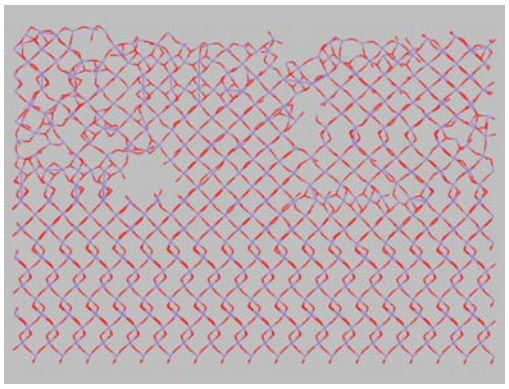

Slice 6

Figure 8.36 shows further structural characterization of ramsdellite interface which was cut into slices 1-12. The first slice corresponds to the face shown in the final structure of the interface (figure 8.35), and subsequent slices lie deeper in the interface. It is noted that each slice has a different defect pattern. This can be regarded as the stacking fault of the interface, which in turn will give rise to grain

boundaries within the system. The slices depict random distribution of single chains and double chains and defects (vacancies, interstitials, substitutionals, and voids).

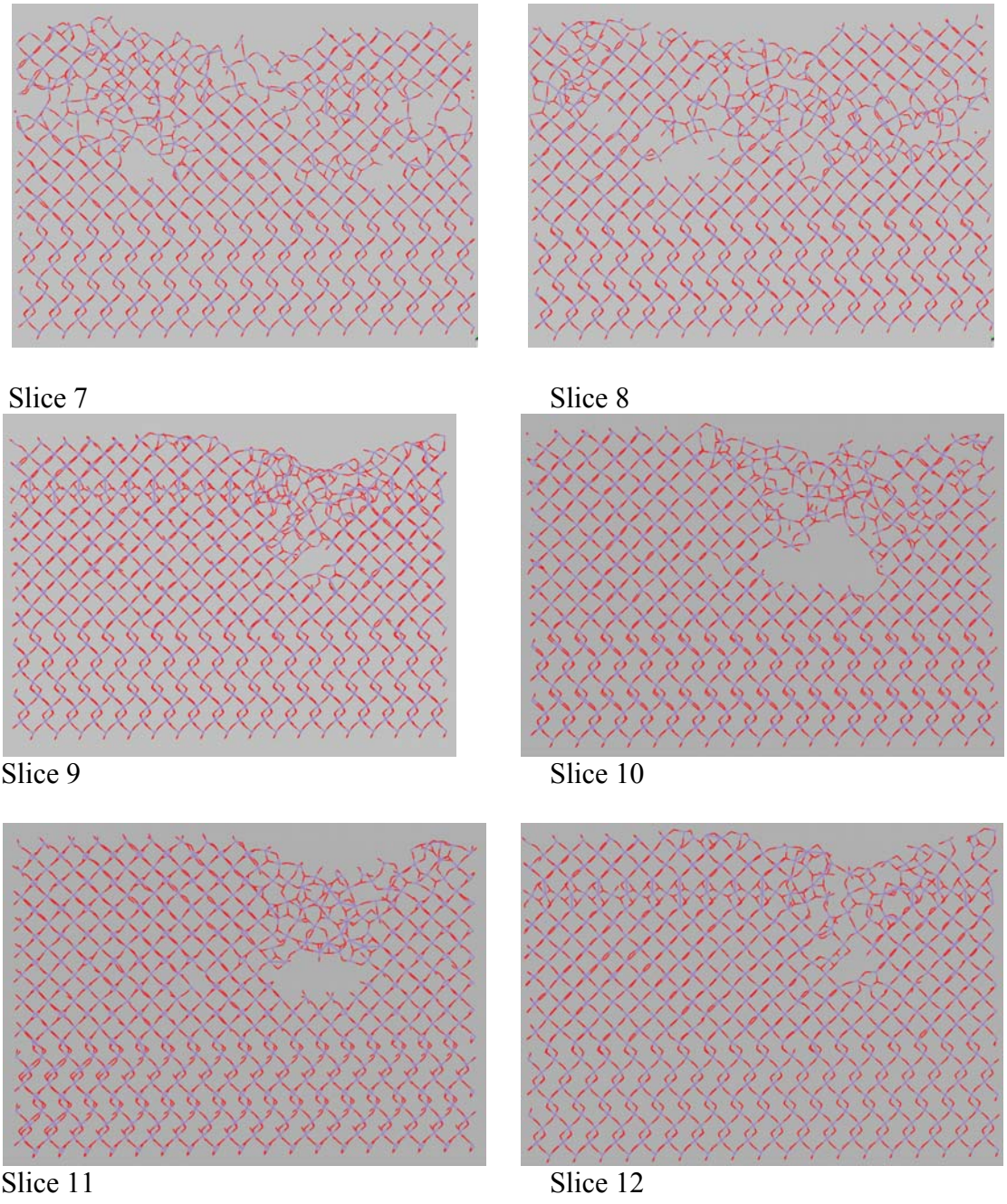

Figure 8.36: Structural characterization of ramsdellite interface (6% tension), indicating slice by slice analysis.

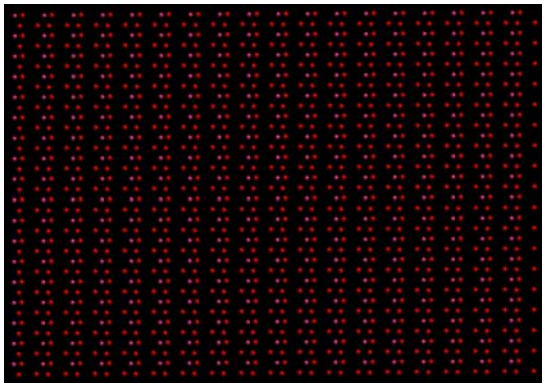

Layer 1(support)

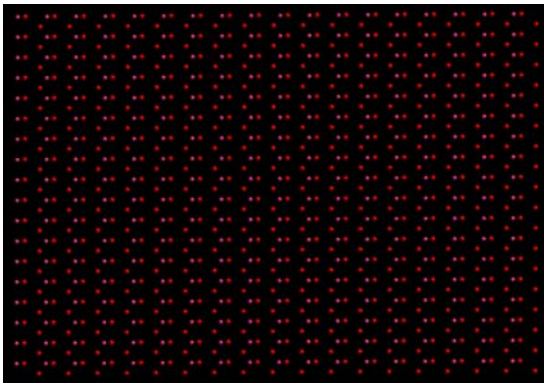

Layer 2 (support)

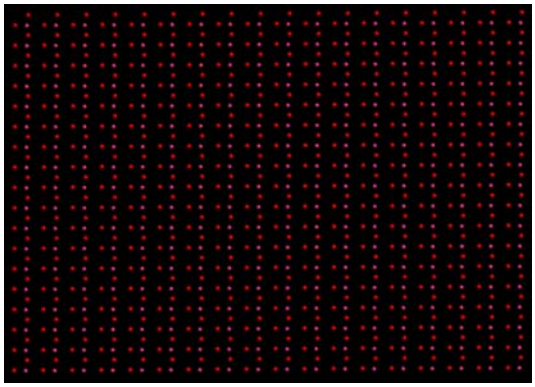

Layer 3 (support)

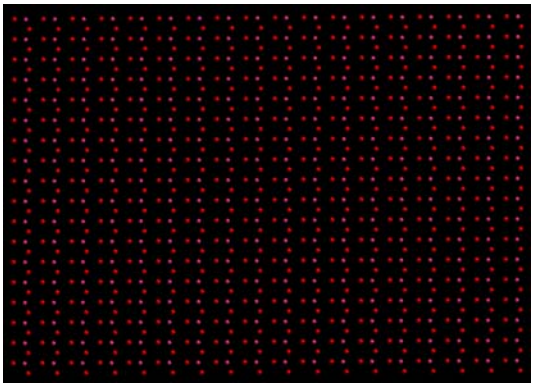

Layer 4 (support)

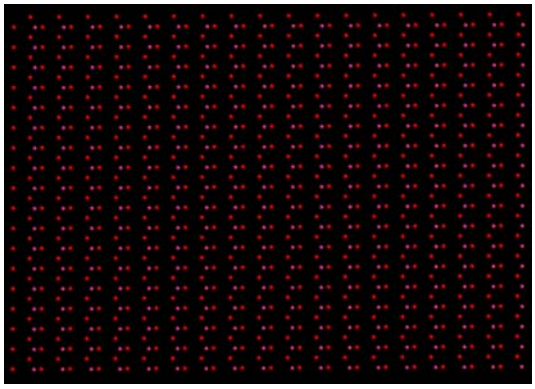

Layer 5 (support)

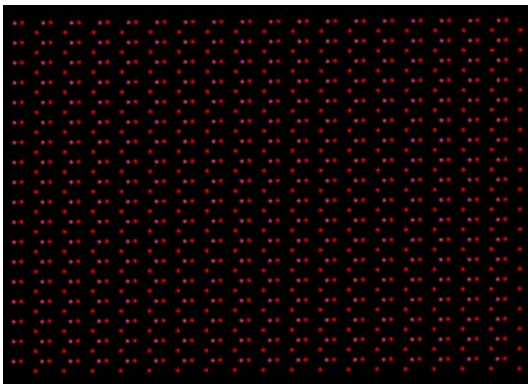

Layer 6 (support)

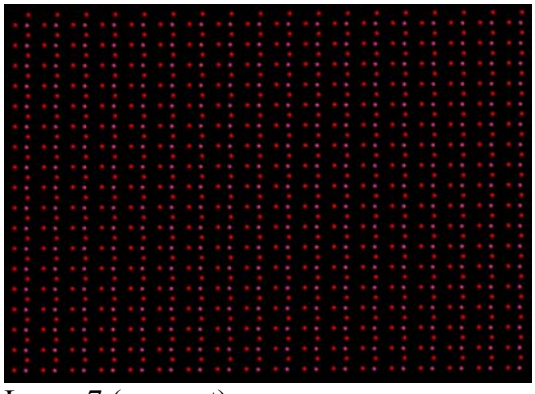

Layer 7 (support)

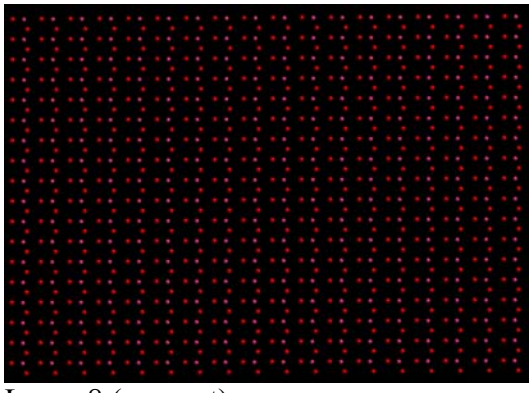

Layer 8 (support)

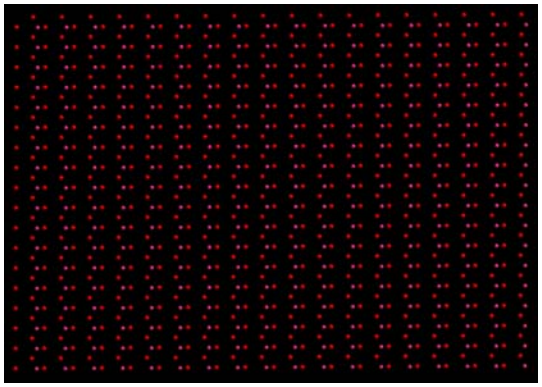

Layer 9 (support)

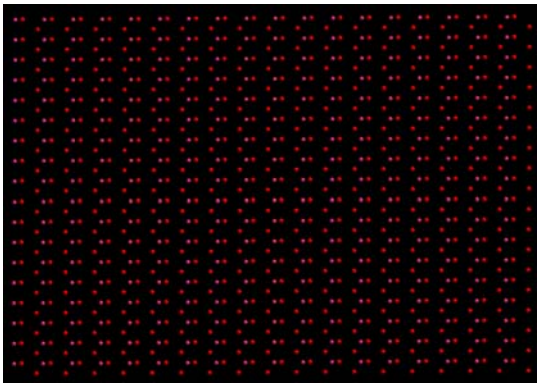

Layer 10 (support)

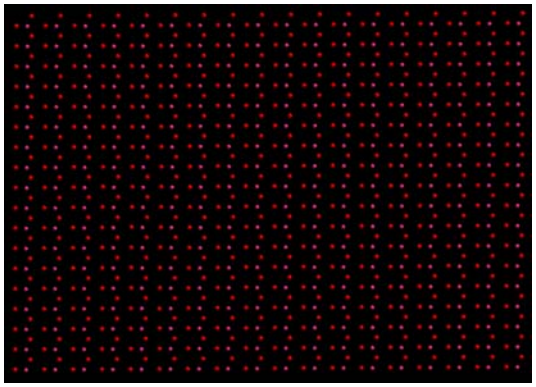

Layer 11 (support)

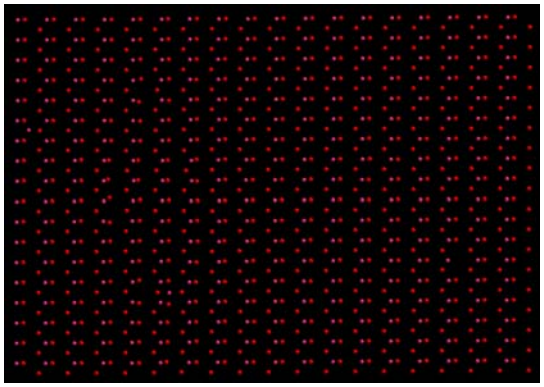

Layer 12 (interfacial)

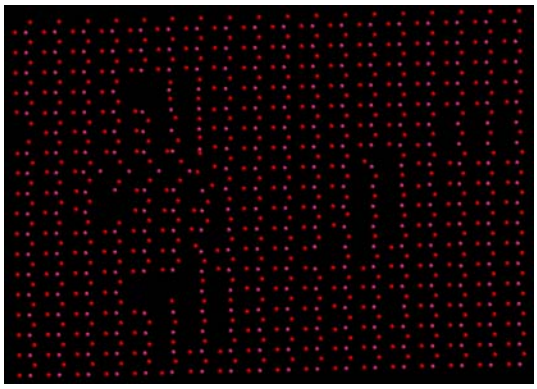

Layer 13 (thin film)

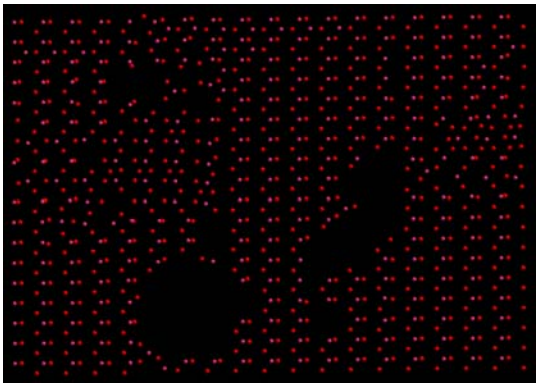

Layer 14 (thin film)

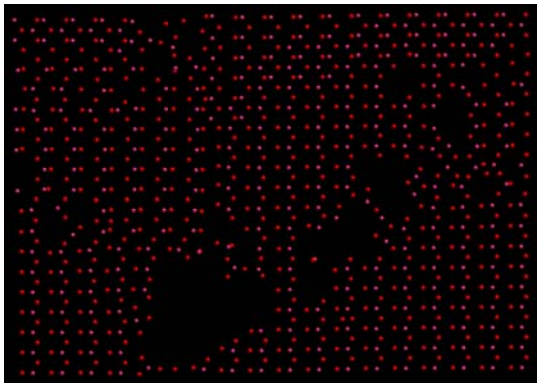

Layer 15 (thin film)

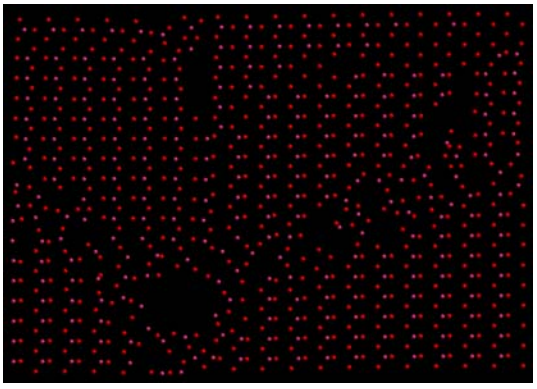

Layer 16 (thin film)

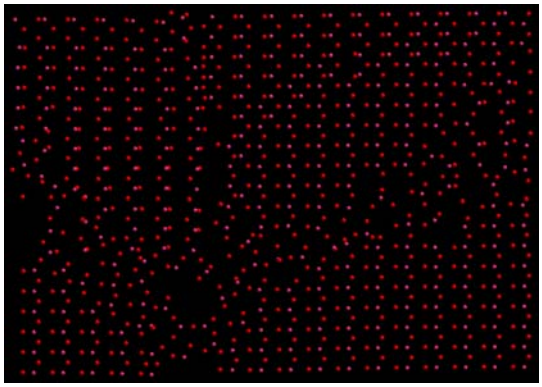

Layer 17 (thin film)

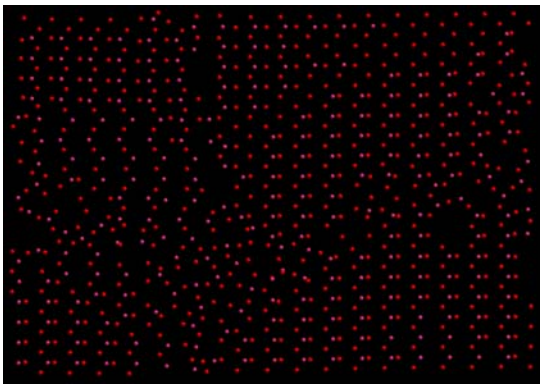

Layer 18 (thin film)

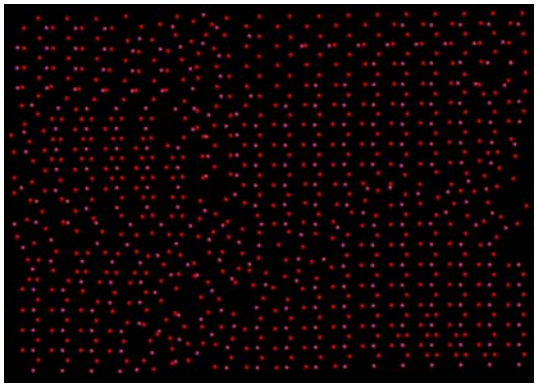

Layer 19 (thin film)

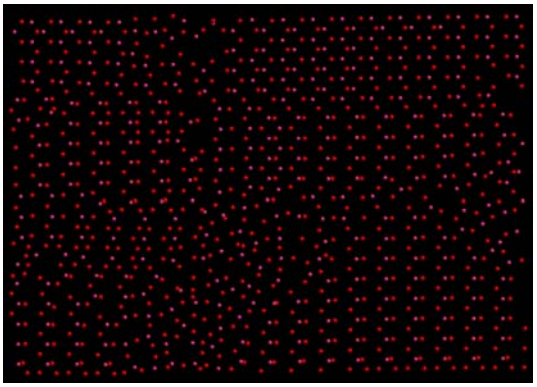

Layer 20 (thin film)

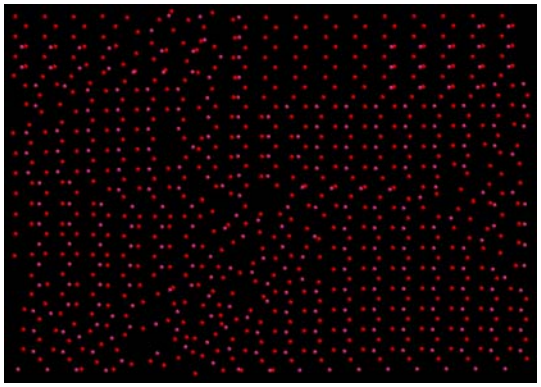

Layer 21 (thin film)

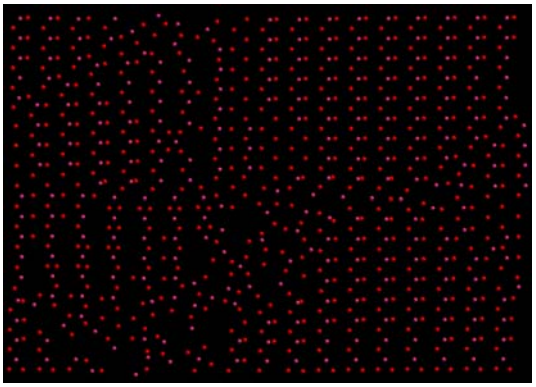

Layer 22 (thin film)

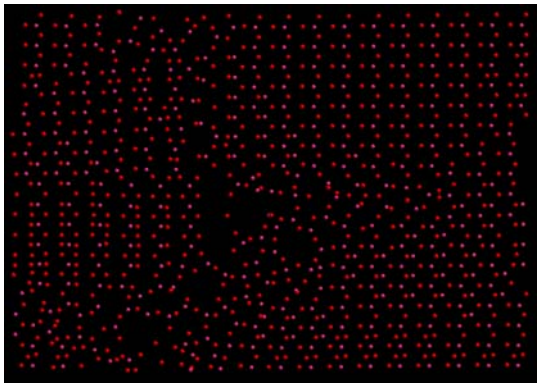

Layer 23 (thin film)

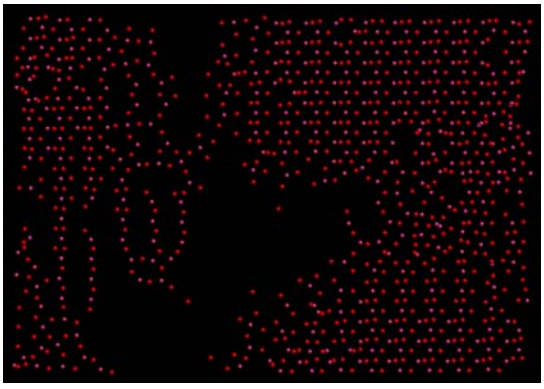

Layer 24 (thin film)

Figure 8.37: Structural characterization on layer by layer analysis of the interface. Shown are layers 1-24, depicting defects contained within the system.

In addition to slice analysis of the interfaces, layer-by-layer analysis was performed, as shown in figure 8.37. The first layer corresponds to the bottom cut of the final structure shown in figure 8.35. The subsequent layers are cuts from bottom to top. It was found that the support has a regular periodic arrangement of atoms. However, different layers of the support have got different patterns; this is owing to some part of the support having changed to pyrolusite layers after the dynamical simulation was applied to the system. There are several types of defects found within the system, namely, vacancies, interstitials, substitutions and voids. As in the case of pyrolusite, the number of defects increases as one moves further away from the interfacial layer, deeper into the thin film. The top layer has a significant number of defects and is usually termed incomplete layer. Pictures showing some preliminary analysis of the grain boundaries are depicted in figures 8.38 (a)-(c).

In summary, all this type of defects that were found within our systems, are amongst those mentioned by Burns [1975, 1983]. Burns and co-workers suggested that naturally occurring and synthetic γ–MnO_2 phases which are used in batteries might contain lattice defects such as stacking faults, dislocations, chain defects, multi-dimensional tunnels and other irregular voids. Also water and impurity ions may be accommodated in such lattice defects. Such defects may account for high electrochemical activity of this EMD.

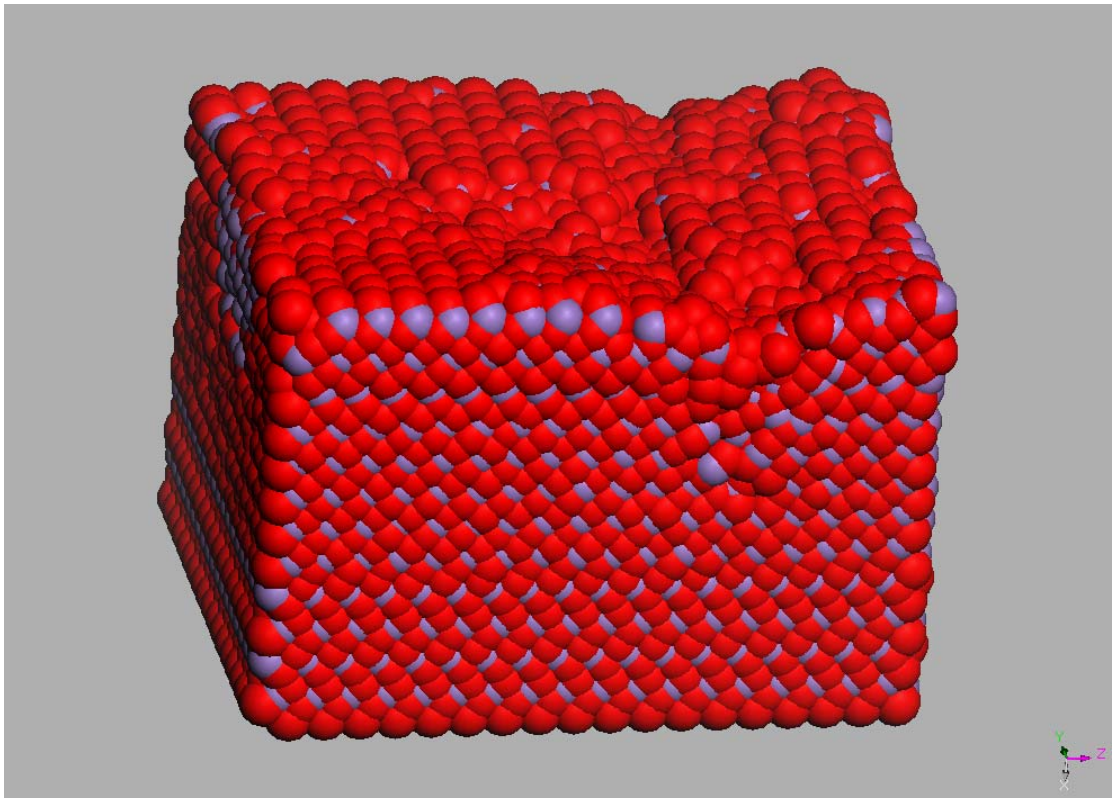

(a) along c-axis view

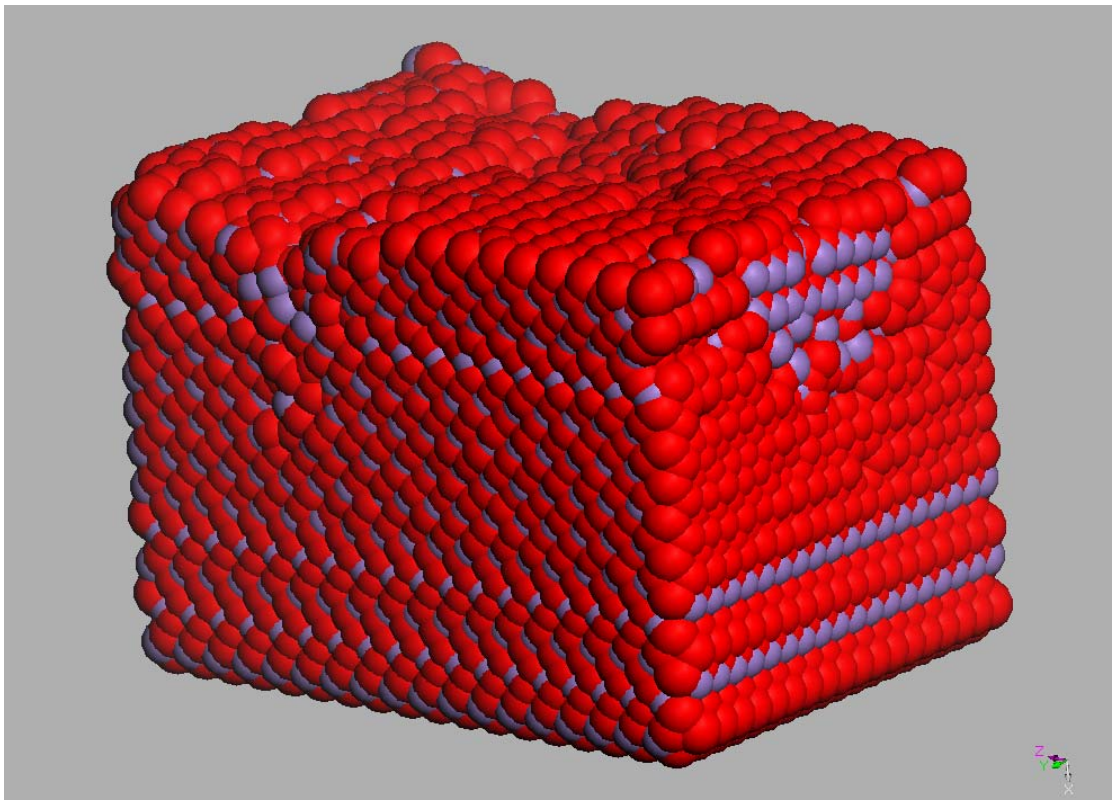

(b) a-, c-view

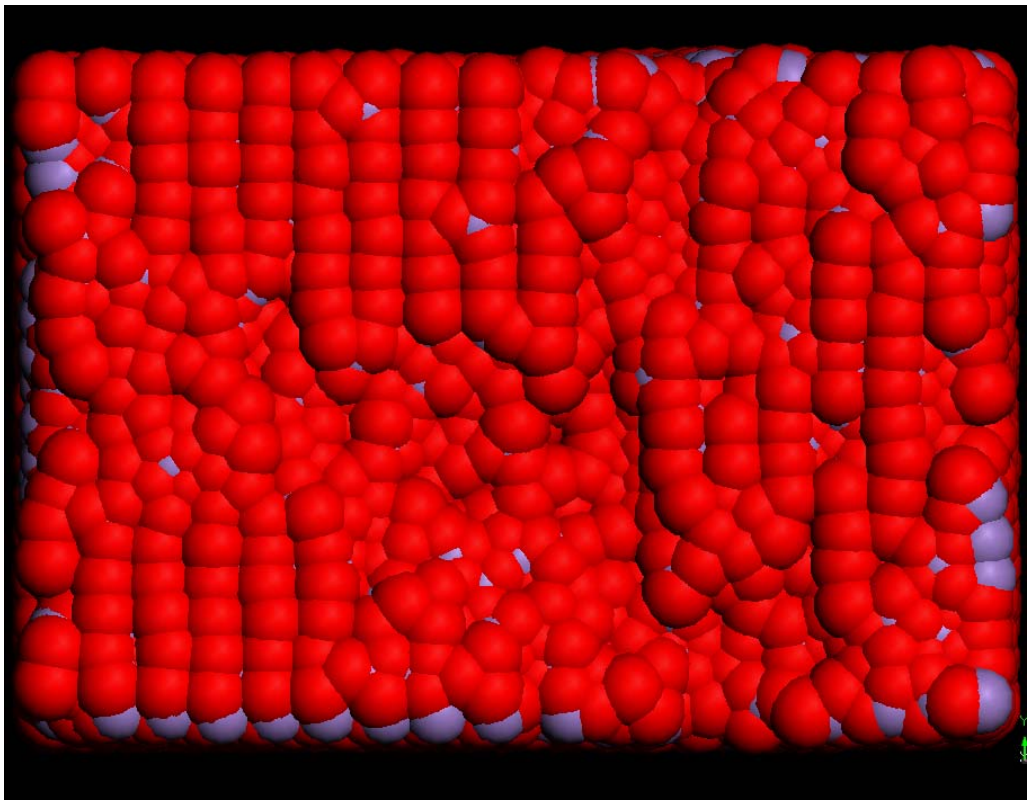

(c) top side view

Figure 8.38 (a)-(c): Reveals that the thin film comprises of disorientated crystals separated by grain boundaries. The whole system is shown in the top figure and the top side view of the interface by the bottom figure.

8.3.6 Ramsdellite MnO_2/MnO_2(100) -6% lattice misfit, NPT

The interface was synthesised using amorphization and recrystallization technique, employing DLPOLY code within NPT ensemble. The total number of particles (N), pressure (P) and temperature (T) were kept constant. A block of MnO_2 thin film was placed on top of MnO_2(100) substrate (cube-on-cube approach) using periodic boundary condition to generate a layered structure. To amorphise the system, the thin film was then strained by -6% (tension). Molecular dynamics simulation was performed at 1300K for 1 cycle (picture same as figure 8.29), under which the tensile strain results in the partial amorphization of the thin film (same as figure 8.32). Prolonged dynamical simulation resulted in the

recrystallized thin film. The simulation was then continued at lower temperatures to recrystallize the system further. Specifically at 800K, 400K, 200K and 0K, the latter acts as an energy minimization. Graphical techniques were used extensively to help understand and characterize the various structural features comprising the system. The picture of the final structure is shown in figure 8. 39. Unlike in the case of NVE ensemble, all the ions (Region I and II ions) are allowed to move during the dynamical simulation. The duration of the dynamical simulation 2500ps (500 000 cycles) was sufficient to ensure that the recrystallization was complete and the structure was no longer evolving (energy of the system had converged). Velocity scaling, performed at every step, was used throughout to prevent the rapid and large build up of excess kinetic energy as the thin film evolves via an amorphous transition.

Close inspection of the system reveals that the system has recrystallized into random distribution of pyrolusite and ramsdellite layers, as obtained in the case of NVE. But the pattern of two different ensembles is different because the conditions under which the simulations were performed are different. In NPT ensemble, the bottom part of the system has recrystallized into pyrolusite layer, because all the ions in the system were interacting. This type of random planar defect has been given the name de Wolff disorder [1959] and Pannetier [1992] as mentioned in section 8.3.5. Also this agrees with the literature that EMDs and CMDs are generally poorly crystallized and the X-ray diffraction patterns may look different from one sample to another. Their structures are much more complicated and generally undetermined.

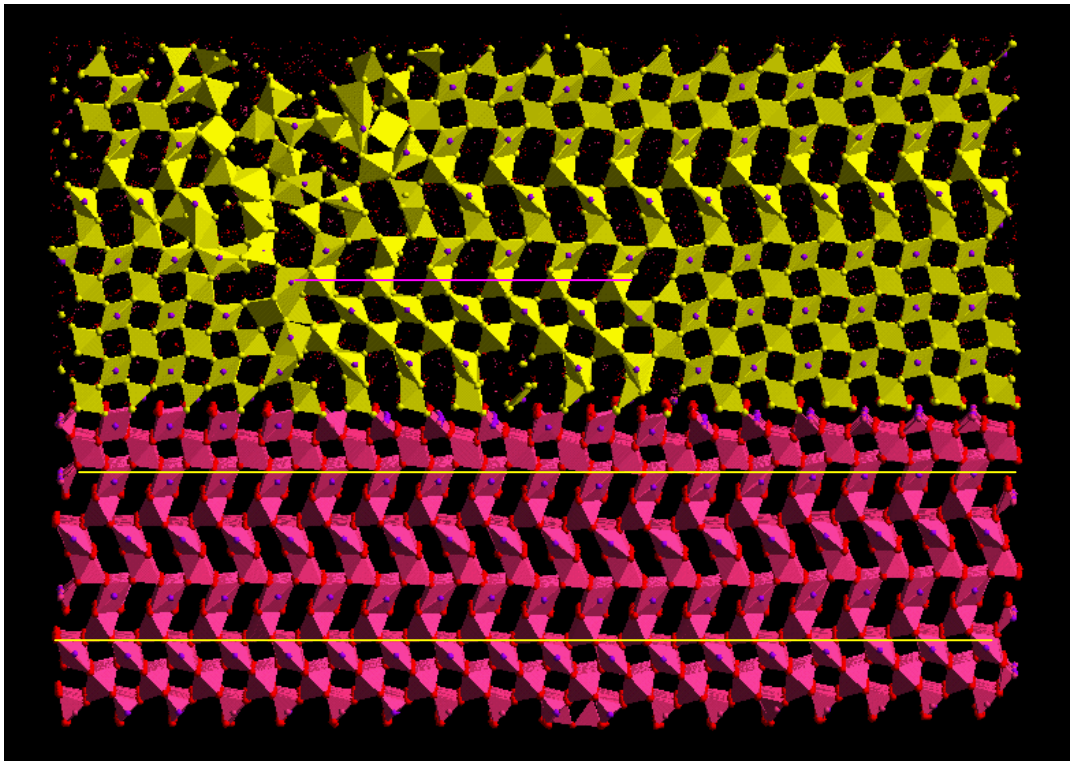

(a)

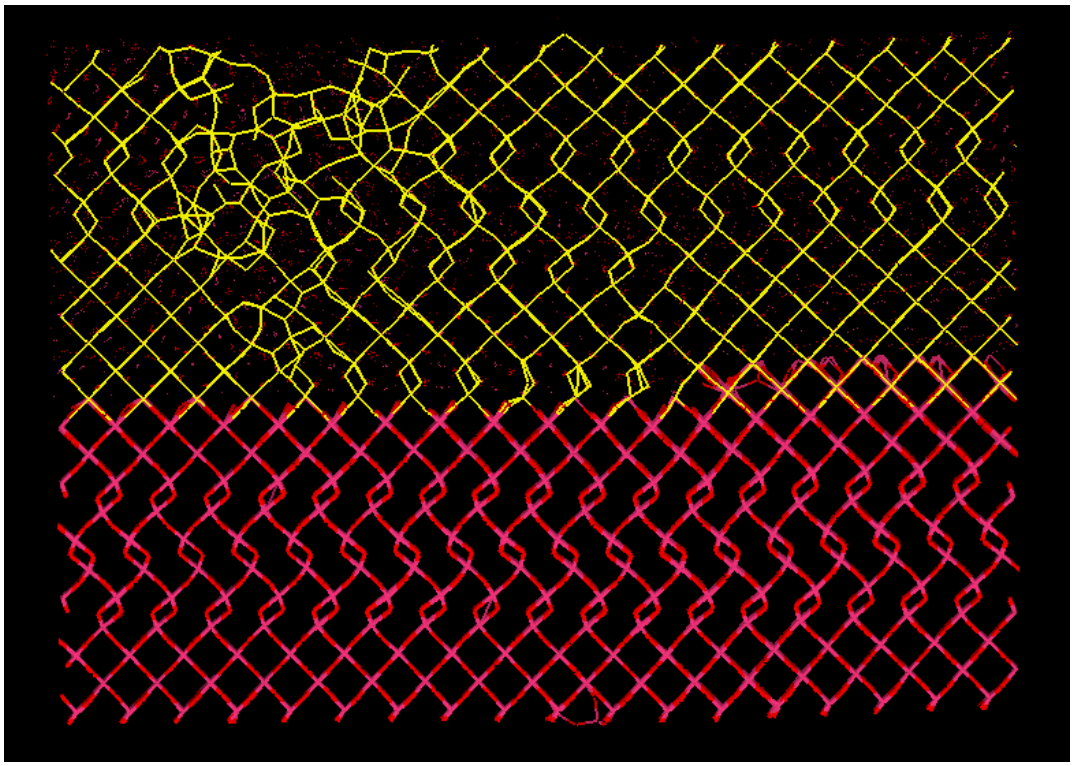

(b)

Figure 8.39: Ramsdellite MnO_2/MnO_2(100) interface (6% tension) NPT at 200K after 2650 ps, (a) shows the polyhedron representation whilst (b) is showing the stick representation of the system.

8.3.7 MnO_2 nanoparticles

(a) Start

To determine the morphologies of pyrolusite and ramsdellite-MnO_2 nanoparticles, graphical techniques were employed to visualize and manipulate the atoms and surfaces comprising the nanoparticles. The atom positions (in graphical representation) for pyrolusite and ramsdellite are shown in figures 8.40 and 8.41 respectively. The pictures are revealing a well-defined morphologies with the sizes of 112 x 112 x 112 Å for pyrolusite and 100 x 100 x 100 Å for ramsdellite. The {110} surface is dominating the morphology of pyrolusite nanoparticle, which is expected since {110} surface was found to be the most stable surface of pyrolusite

in our surface calculations. With ramsdellite {001}, {100} an {110} surfaces are exposed.

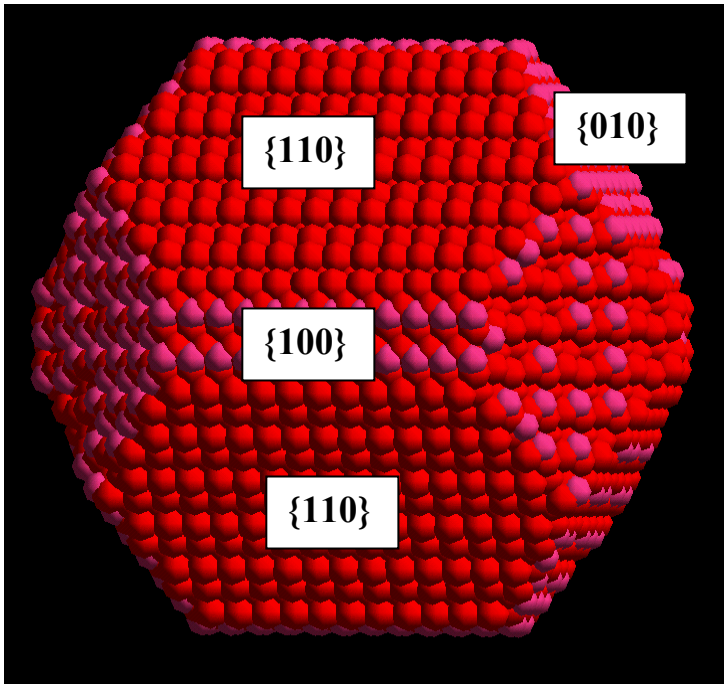

Figure 8.40: Pyrolusite nanoparticle at 900K after 0.005 ps. The red balls represent the oxygen atoms and the pink balls represent the manganese atoms.

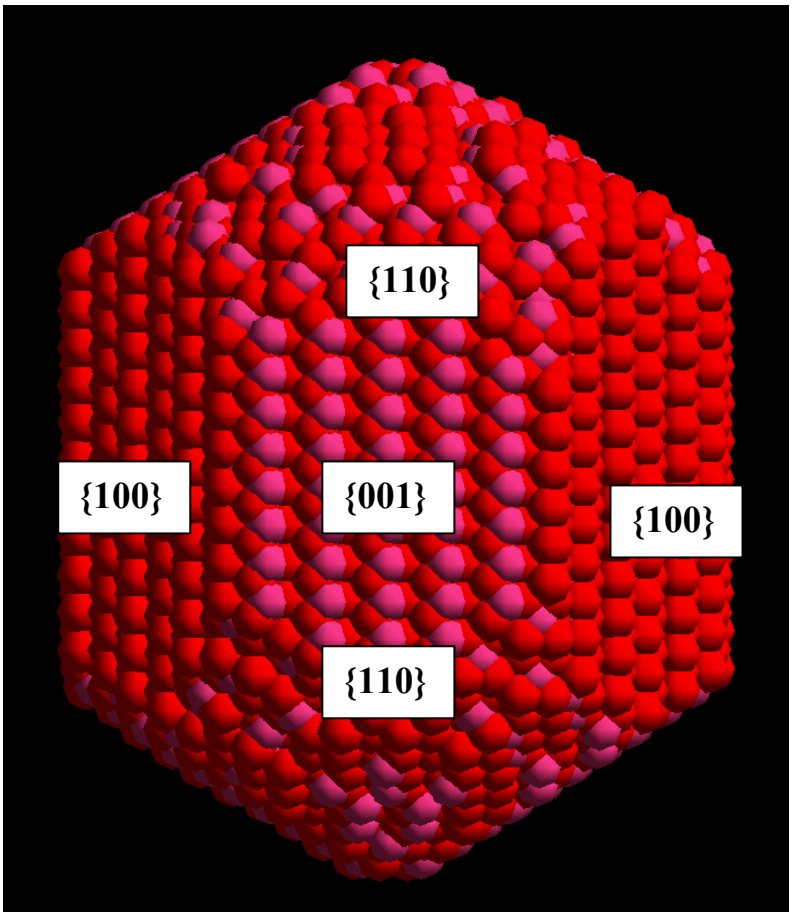

Figure 8.41: Ramsdellite nanoparticle at 900K after 0.005 ps.

(b) Amorph

After the dynamical simulation has been applied to the nanoparticles, the simulation cells became amorphous. For pyrolusite nanoparticle, amorphization occurred approximately after 2.5 ps whereas for ramsdellite nanoparticle it occurred approximately after 7.5 ps. The amorphous simulation cells of pyrolusite and ramsdellite nanoparticles are shown in figures 8.42 and 8.43 respectively. Unlike with the starting configuration cell where different surfaces were clearly defined, with the amorphous simulation cells no surfaces can be defined or detected, they are irregular.

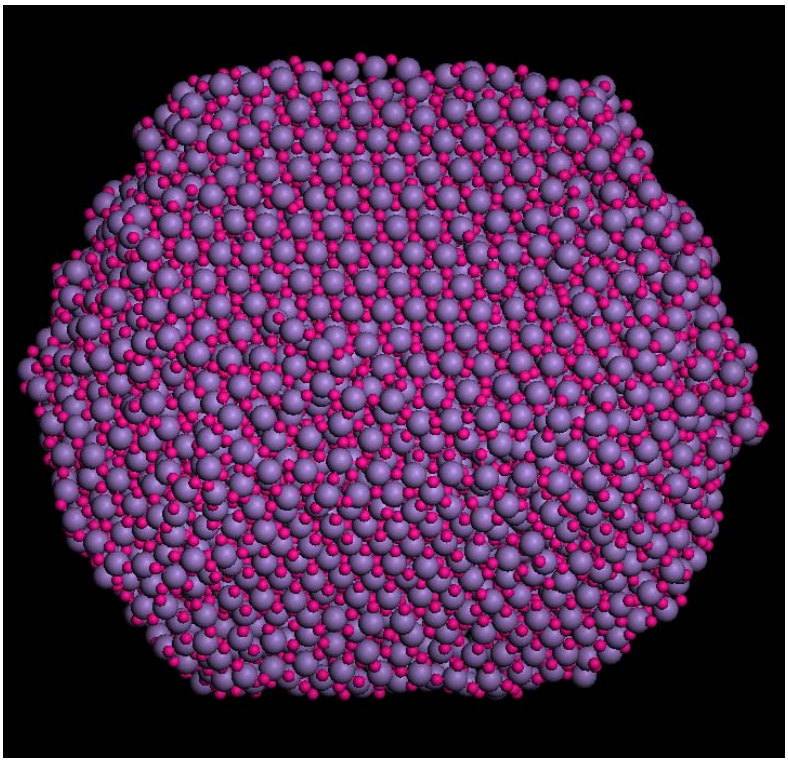

Figure 8.42: Pyrolusite nanoparticle at 900K after 2.5 ps

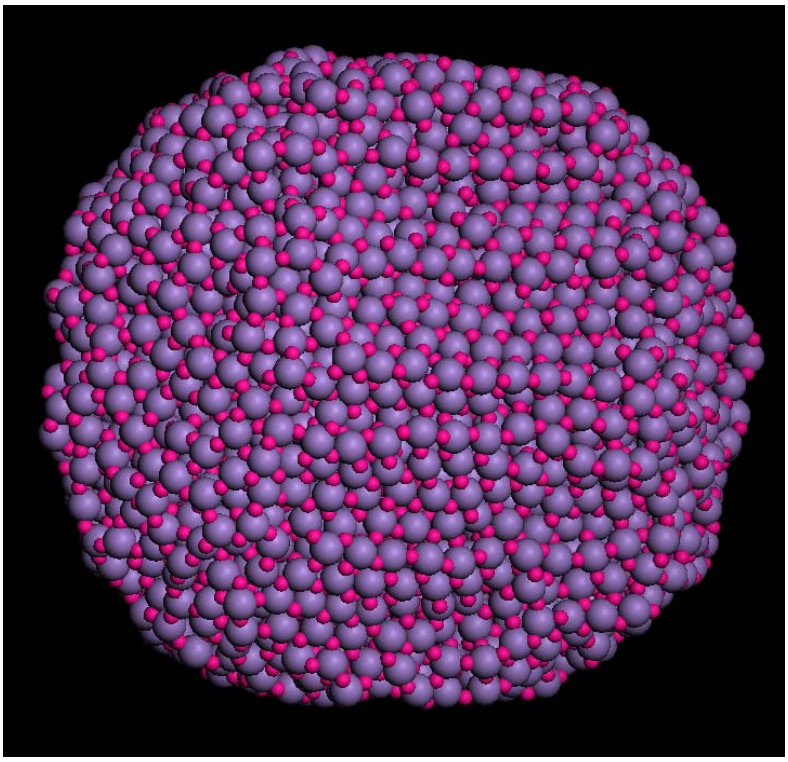

Figure 8.43: Ramsdellite nanoparticle at 900K after 7.5 ps.

(c) Final

After a prolonged dynamical simulation the nanoparticles have recrystallized. Figures 8.44 and 8.45 show the graphical representation of calculated atom positions, after 2000 ps and 2500 ps for pyrolusite and ramsdellite respectively. The atoms positions are represented by manganese and oxygen balls. In figures 8.44(b)-(e), we used another visualization technique to show the surfaces. The technique is called surface tool, which is used to enhance the model. It creates a soft surface coloured by electrostatic potential. Different orientations of the nanoparticles are shown. The pictures show that after the simulation cell has undergone amorphous transition, the surfaces start to form again, even though the surface cannot be easily defined because of the defects (vacancies and substitutional atoms) composed in the simulation cells. For example there are missing atoms (vacancies) at the top of the picture in the pyrolusite nanoparticles. Again the visualization technique used in figures (b)-(e) shows that there are some defects in the nanoparticles. The pictures are showing atom arrangements of different surface for both nanoparticles and boundaries contained therein.

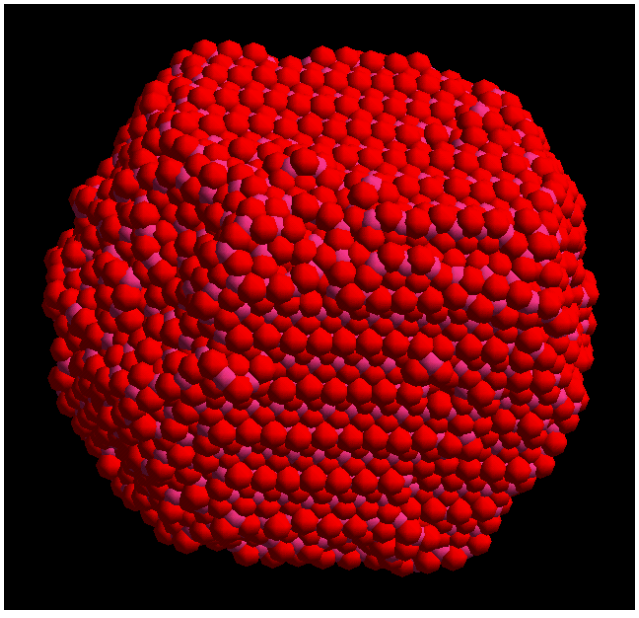

(a)

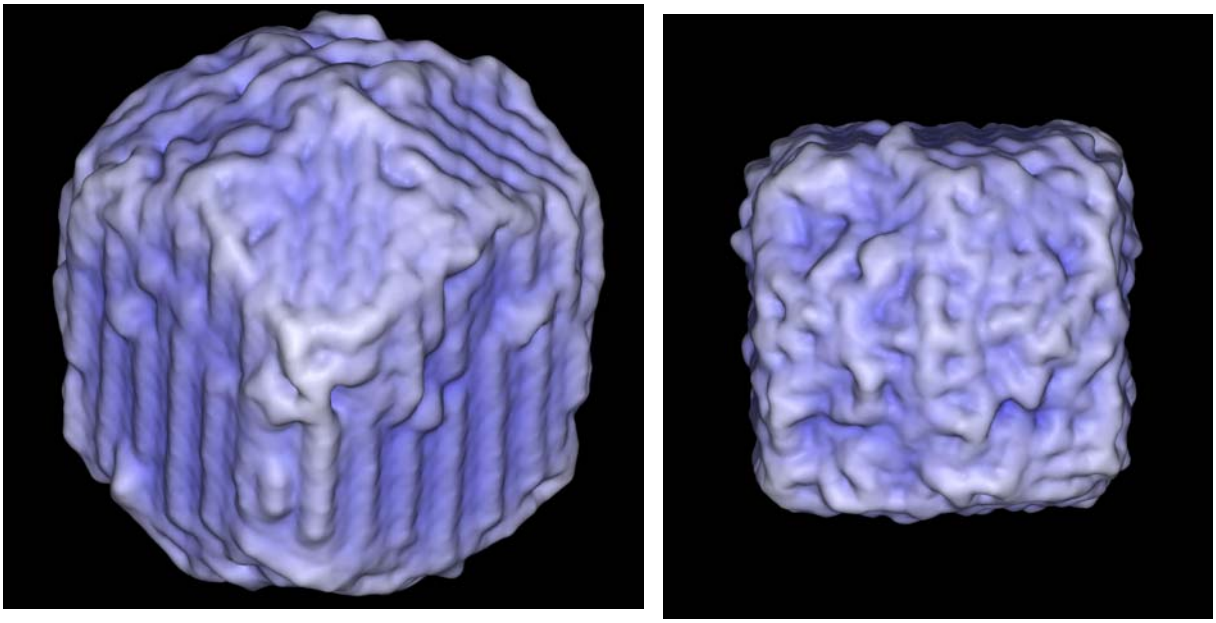

(b) (c)

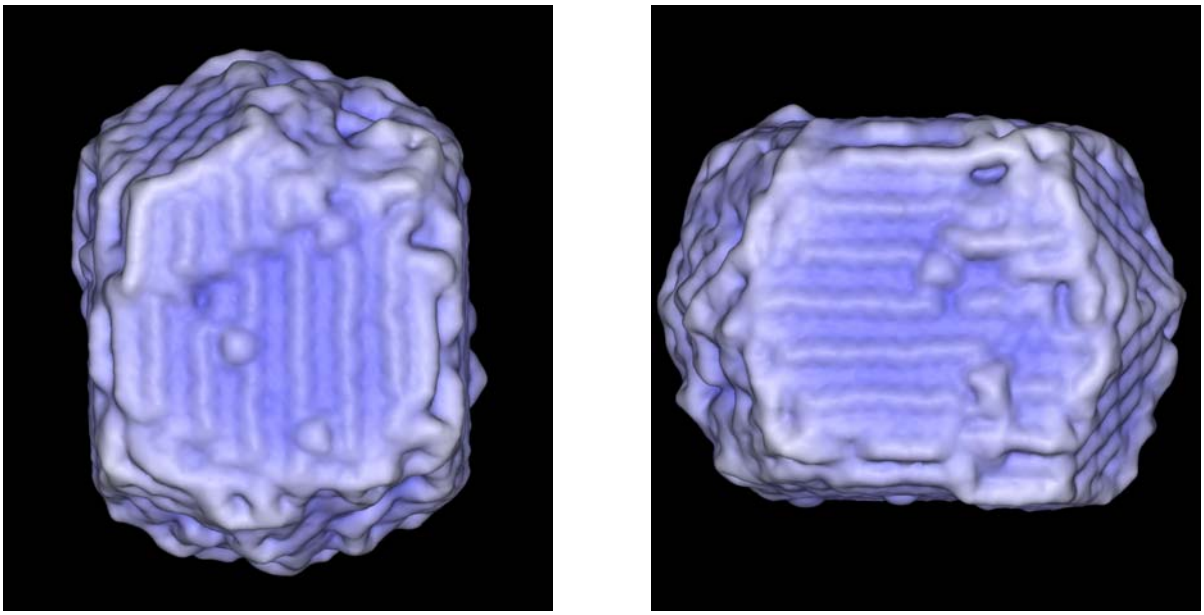

(d) (e)

Figure 8.44: Pyrolusite nanoparticle at 900K after 2000 ps.

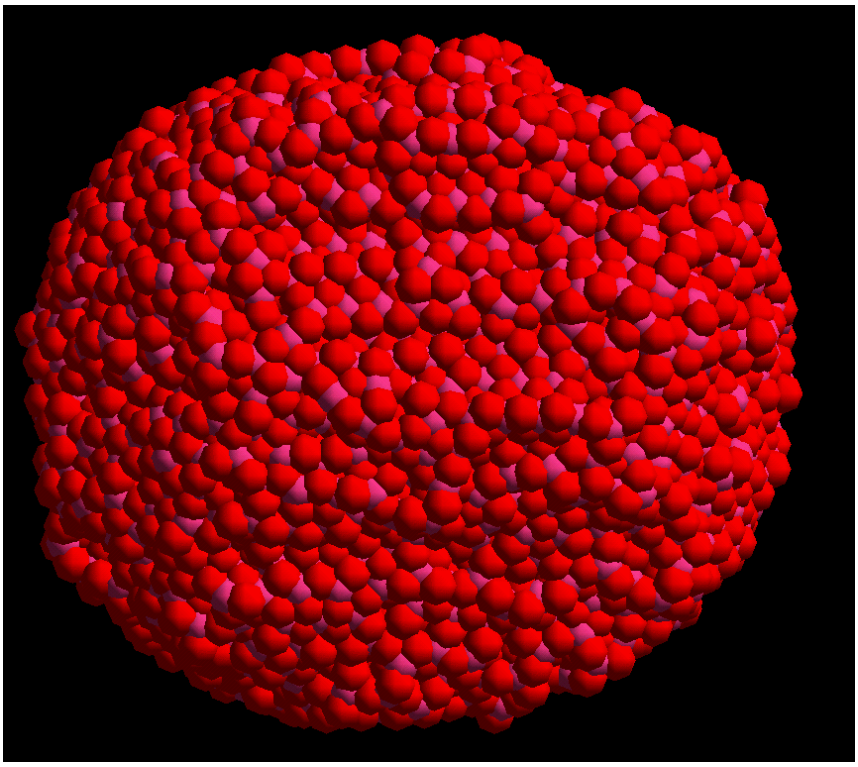

(a)

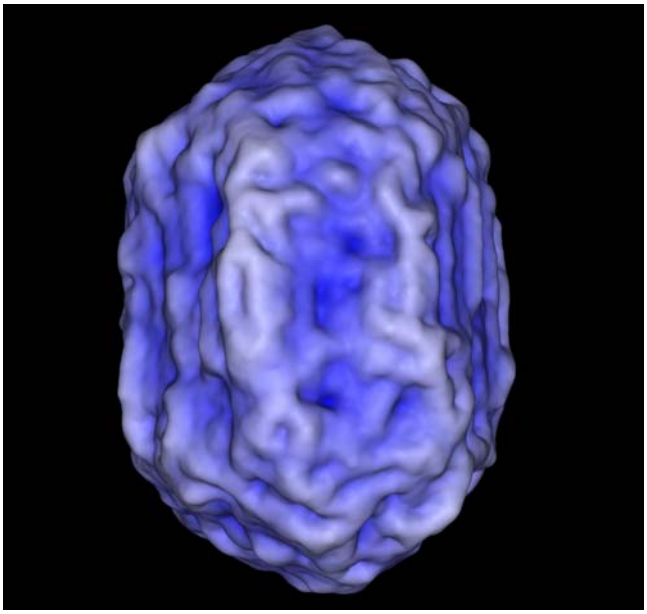

(b)

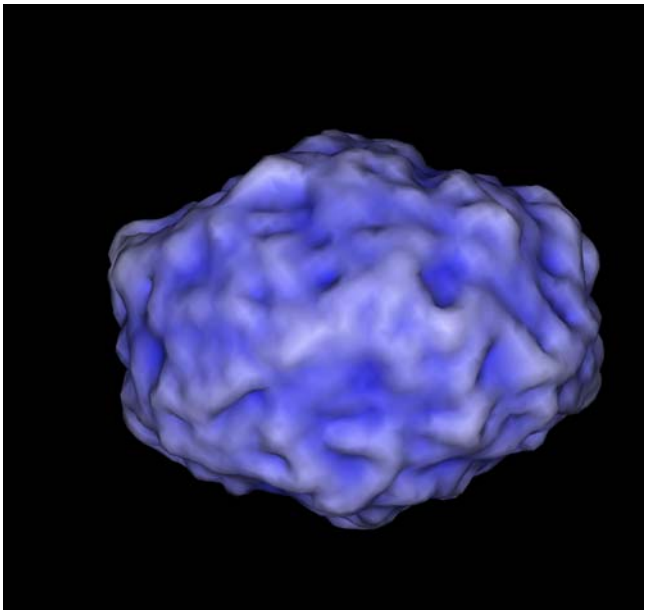

(c)

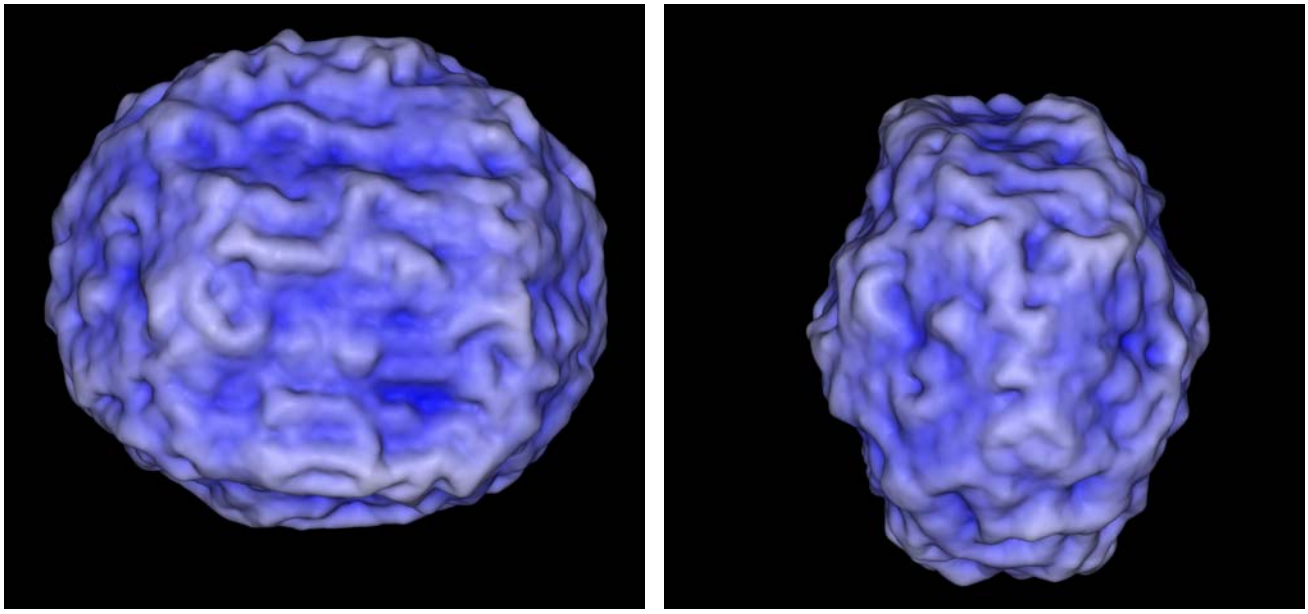

(d) (e)

Figure 8.45: Ramsdellite nanoparticle at 900K after 2500 ps

8.4 Conclusion

The amorphization and recrystallization methodology was successfully used to generate MnO_2 interface models. The methodology involves dynamical simulations at the starting configuration, amorphous state and recrystallized state of the systems. It enables the investigation of considerably large simulation cell, that is, simulation cell composed of 23922 atoms for pyrolusite structure and 22068 atoms for ramsdellite structure were studied. In addition this evolutionary methodology is designed to allow the system to accommodate a low energy configuration influenced solely by lattice rather than by any 'artificial' intervention based upon the intuition of the simulator. In this work we generated models for pyrolusite interface and ramsdellite interface using the evolutionary method. The success of the simulated amorphization and recrystallization methodology in generating MnO_2 structure from a partial amorphous solid

suggests that the methodology is applicable to study supported thin film systems. The simulated compression induced methodology was used to generate pyrolusite interface [10% MnO_2/MnO_2(100)] whereas the simulated tension induced methodology was used for ramsdellite interface [-6% MnO_2/MnO_2(100)], which yields an interface composed of ramsdellite and pyrolusite structures. Using the amorphization and recrystallization methodology, in conjunction with analytical (calculated RDFs and directional density profiles) and graphical techniques, we have generated models for pyrolusite-ramsdellite interfaces and studied their structural properties. Our results agree very well with experimental and literature results. In particular, in terms of the radial distances of the EMD and most importantly ramsdellite interface resulting in the model which is similar to the one suggested by Ripert et al [1991a]. Thus, basic ramsdellite structure turns into stacking disorder of ramsdellite and pyrolusite slabs (de Wolff's disorder) and microtwinning of ramsdellite structure. Understanding and characterization of pyrolusite-ramsdellite interfaces in MnO_2 structures will aid us in gaining better knowledge about their performances in batteries. Although amorphization and recrystallization technique can be used to study atomic structure of different oxides interfaces, this study is a first attempt on using the technique to study Electrolytic Manganese Dioxides. Further investigation of EMD structural properties (morphologies, dislocation networks, interfacial boundaries) using the technique is desired.

Amorphization and recrystallization methodology has also been successfully used to generate pyrolusite- and ramsdellite-MnO_2 nanoparticles. The objective of the study was to generate MnO_2 nanoparticle models using the calculated surface

energies from energy minimization technique (Chapter 4). As expected the morphologies exposed the more reactive and stable surfaces. The amorphization and recrystallization methodology was used in conjunction with graphical techniques to generate the models. At the starting configuration of the dynamical simulation the surface were clearly shown, the simulation cells were allowed to go amorphous and finally after a prolonged simulation the nanoparticle becomes recrystallized, showing the surfaces with some defects. The methodology enables a nanoparticle not to depend on the starting configuration and it takes the low-energy configuration. Tasker et al [1987] suggested that since low interfacial densities (associated with vacancies, interstitials and substitutionals) give rise to low energy configurations, such species are not defects as such; rather they form an integral part of the low energy configuration [Tasker 1987].

Chapter 9

Conclusions and Recommendations

9.1 Conclusions

In this study, computer simulations and EXAFS studies were combined to study the structural properties of EMD, which is used as the cathode materials for alkaline batteries. Structural calculations based on simulations lead to the following conclusions.

Planewave pseudopotential calculations based on density functional theory was used to perform structural and electronic properties of pyrolusite and ramsdellite polymorphs of MnO_2. The LSDA approach was implemented successfully to study the abovementioned properties. The calculated lattice parameters of both systems are in reasonable agreement with experimental values. The bond lengths have shown to be reducing with the increase of applied pressure. Bulk moduli were deduced from the equation of state. The partial density of states have been calculated and have predicted pyrolusite to be metallic at the ambient pressure and an insulator at 50GPa whilst ramsdellite was found to be an insulator at both 0 and 50GPa. However, as the system is subjected to more pressure, the band gap reduces. These results correlate with what we observed on charge density differences, where pyrolusite was found to be covalent at 0GPa and ionic at

50GPa. Furthermore, for ramsdellite, no change in nature of bonding was observed, it has the mixture of ionic and covalent bonding at both pressures.

The knowledge of surface structure is largely absent, even with the remarkable advances in microscopy that have been made recently. Therefore, as part of this study, MnO_2 surfaces were studied, where their energies, structures and reactivity were predicted. Energy minimization technique was used to investigate the surface properties of pyrolusite and ramsdellite. Two different potential models, shell and rigid ion potential models were considered. The properties studied include surface energies, structure and reactivity. The most stable low index surfaces were predicted. We investigated the surface properties by calculating the surface energies and compared the rigid ion and shell model results. A correlation was found amongst the surface energies of pyrolusite predicted by these two models. No correlation was found on ramsdellite results, as shell model predicted one of the surfaces to have a negative surface energy. From the rigid ion model results, we identified equivalent surface energies between pyrolusite and ramsdellite. The most reactive surfaces were calculated, where the surface was reduced by introducing oxygen vacancy in the system and the charge was compensated by replacing Mn^{4+} by Mn^{3+}. In summary, based on our findings, the rigid ion model is the favourable potential model for MnO_2 as compared to the shell model.

Molecular dynamics technique was used to study structural properties of pure pyrolusite, ramsdellite and mixture of the two (intergrowths). For pyrolusite bulk and surface structures were investigated whilst for ramsdellite only the bulk

structure was calculated. The radial distances were calculated and compared with EXAFS experimental results. Our calculated and experimental results showed a good agreement. For pyrolusite surface energies were calculated using MD and compared with those obtained using energy minimization method. The effect of temperature was investigated, and it was observed that as the temperature is increased, the system becomes more disordered. At higher temperatures, the system looses its crystallinity, thus, it does not have any long-range orders. As part of the study, EXAFS experiments were performed to investigate the short-range order of MnO_2. The structural properties (radial distances, coordination numbers and atom type) for pyrolusite, ramsdellite and mixture of the two were measured. The radial distances were compared with those obtained using MD, and the agreement was good.

Equivalent surface energies obtained were used to construct pyrolusite-ramsdellite intergrowths. The structural properties and temperature effect were studied using MD. The radial distances were calculated and used to describe the structure of the intergrowths. The results were compared with EMD results obtained from EXAFS experiments.

Amorphization and recrystallization technique proved successful in generating models of supported oxide-oxide thin films and nanoparticles, and established a strategy for generating systems, which include all the structural complexity expected within a real system. In this study, MnO_2/MnO_2(hkl) interfaces were generated using the technique. In contrast to most studies, the technique start by

defining the basic structure of the system, here the thin film is allowed to evolve naturally in response to the support. The methodology enables a variety of structural features to *evolve* within the system. The structural modifications observed in our interfaces include, vacancies, interstitials, voids, dislocations and grain boundaries. These were found within a single simulation cell. Our calculations suggest that ramsdellite-MnO_2/MnO_2(100) interface undergoes a remarkable structural changes, which yielded an interface composed of random distribution of pyrolusite and ramsdellite layers. The calculations suggest that ramsdellite interface demonstrates remarkable structural changes, including the formation of pyrolusite layers within the system, intermixing across the planes, crystal orientations and hence grain boundaries. In addition, nanoparticles exposed various facets at the surface; the morphology appearances of the nanoparticles were profound.

9.2 Recommendations

Computational modelling and EXAFS studies were combined to study the Electrolytic Manganese Dioxide. Computer simulations proved to be a successful tool for studying MnO_2, since it gave a key understanding on the structural and electronic properties of this system. The work undertaken to date, lays a foundation from which more understanding of EMD can be built. There are lots of EMD properties which can be investigated based on the findings of this study. To list some:

- Studying structural and electronic properties of protonated pyrolusite, ramsdellite and the mixture of two, experimentally it is been found that Mn vacancies can be compensated by addition of protons (Na^+, K^+, H^+, OH^-, Mg^{2+}), and they create local sites with higher discharge potential. This could be done using both ab initio and molecular dynamics simulations.
- More investigations on EMD surfaces are required; this will include surface hydration and different surfactants (probably protons).
- It will be very interesting to look at the X-ray diffraction of the models generated, and be compared to XRD data obtained experimentally on EMD samples.
- Using the amorphization and recystallization technique, more MnO_2 interface and nanoparticle models can be generated under different conditions, namely; temperature, lattice misfits, (hkl) plane or orientation, ensembles, etc. Also in this case addition of protons to the systems can be investigated.
- Another method of generating thin films called 'atom deposition' can be used to deposit protons to the MnO_2 substrate.
- Recently, nanotechnology has been the subject of most research; MnO_2 is not an exception in the nanotechnology. The nanoparticle study could be extended even further, looking at different properties of nano-MnO_2.

References

Abou-El-Sherbini K.S., (2002) *J. Solid State Chem.,* **166**, 371-381

Allan N.L., Barrera G.D., Purton J.A., Sims C.E. and Taylor M.B., (2000), *Phys. Chem. Chem. Phys.*, **2**, 1099-1111.

Allen M.P. and Tildesley D.J., (1989), '*Computer Simulation of Liquids', Clarendon Press, Oxford*

Ammunsden B., Roziere J. and Islam M.S., (1997), *J. Phys. Chem. B,* **101,** 8157

Ananth M.V., Pethkar S. and Dakshinamurthi K., (1998), *J. Power Sources,* **75,** 278

Azaroff L.V., (1963), *Rev. Mod. Phys.,* **35,** 1012

Balducci G., Kašpar J., Fornasiero P., Graziani M., Islam, M.S. and Gale J.D., (1997), *J. Phys. Chem. B*, **101**, 1750-1753.

Baur W.H., (1976), *Acta Cryst.,* **32,** 2200

Becke A.D., (1988), *J. Chem. Phys.,* **88,** 1053

Bell G.S. and Huber R.,(1964), *J. Electrochem. Soc.,***111,** 1

Benosman N., Amrane N., Mecabih S. and Aourag H., (2001), *Phys. B,* **304,** 214-220

Bertant F., (1958), *Comp. Rend.,* **246,** 3447

Biesiadecki J.J. and Skeel R.D., (1993), *J. Comp. Phys.,* **109,** 318-328

BigLiocca C., Giraidi F., Pauly J. and Sabioni E., (1967), *Analy. Chem.,* **39,** 1634

Binder L., Jantscher W., Hofen F. and Kothleitner G., (1998), *J. Power Sources,* **70,** 1

Binstead N., (1998), *Excurve98: CCLRC Daresbury Laboratory computer Program*

Boden D., Venuto C.J., Wisler D. and Wylic R.B., (1967), *J. Electrochem. Soc.,* **114,** 415

Born M. and Huang K., (1954), '*Dynamical Theory of Crystal Lattices', Oxford University Press*

Bowden W. Sirotina R., and Hackney S., (2000) IBA Manganese Oxide Symposium, Argonne, III, May 9-12 2000.

Brenet J., (1950), *C.R. Acad. Sci. Paris,* 230, 1360, Bull. Soc. France Min., **75,** 409

Brenet J.P, (1985), *3rd MnO_2 Symposium, Graz,* 16-18

Burns R., (1983), *Battery Material Symposium, Brussels,* **1,** 342-344

Burns R.G. and Burns .V.M., (1975), *IBA Manganese Symposium Cleveland,* **1,** 306-372

Byström A.M., (1949), *Acta Chem. Scand.,* **3,** 163

Byström A. and Byström A.M., (1950), *Acta Cryst.,* **3,** 146

Cahoon N.C. and Korver M.P., (1959), *J. Electrochem. Soc.,* **106,** 745

CASTEP Users Guide, (1998), *Molecular Simulation Inc.,* San Diego, CA

Catlow C.R.A., (1987) '*Computational techniques and simulation of crystal structures'* in *'Solid state chemistry techniques'*, eds. Cheetham, A.K. and Day, P., Clarendon Press, Oxford.

Catlow C.R.A. and Price, G.D., (1990), *Nat.*, **347**, 243.

Catlow C.R.A., (1994a), *Comp. Mat. Scie.*, **2**, 6-18.

Catlow C.R.A., Bell R.G. and Gale J.D., (1994b), *J. Mat. Chem.*, **4**, 781-792.

Catlow C.R.A., (1996) *Comp. Model. Inorg. Cryst.*

Catlow C.R.A., Ackermann L., Bell R.G., Corà F., Gay D.H., Nygren M.A., Pereira J.C., Sastre G., Slater B. and Sinclair P.E., (1997a,) *Faraday Disc.*, **106**, 1-40.

Catlow C.R.A., Ackermann L., Bell R.G., Gay D.H., Holt S., Lewis D.W., Nygren M.A., Sastre G., Sayle D.C. and Sinclair P.E., (1997b,) *J. Mol. Catal. A*, **115**, 431-448.

Chambers S.A. and Liang Y., (1999), *Surf. Sci.,* **420,** 123

Chambers S.A., (2000,) *Surf. Sci. Rep.*, **39**, 105-180.

Chabre Y. and Pannetier J., (1995), *Prog. Solid State Chem.,* **23,** 1

Charrenton J.C. and Strobel P., (1988), *J. Solid State Chem.,* **77,** 33

Clausen B.S. and Topsoe H., (1994) *Synchrotron Radiation news,* **7,** 32

Clausen B.S. and Topsoe H., (1996) in: Y. Iwasawa (Ed), '*X-ray Absorption Fine Structure for Catalysts and Surface', Chapter 8.2, World Scientific, Singapore*

Clausen B.S., Topsoe H. and Frahm R., (1998), *Adv. Catal.,* **42,** 315

Cohen M.L. and Heine V., (1970), *Solid State Phys.,* **24,** 37

Cole W.F., Wadsley A.D. and Wackley A., (1947), *Trans. Electrochem. Soc.,* **92,** 133

Cox P.A. Catlow C.R.A and Chadwick A.V., (1994), *J. Mat. Sci.,* **29,** 2725

David W.I.F., Bruce P.G. and Goodenough J.B., (1983), *J. Solid State Chem.,* **50,** 235

Davies R.A., Islam M.S., Chadwick A.V. and Rush G.E., (2000), *Solid State Ionics,* **130,** 118

de Leeuw N.H. and Parker S.C., (1998), *J. Phys. Chem. B,* **102,** 16, 2914-2922

de Leeuw N.H., Parker S.C., Sithole H.M. and Ngoepe P.E., (2000), *J. Phys. Chem. B,* **104,** 7969-7976

de Wolff P.M., (1959), *Acta Cryst.,* **12,** 341-345

Delta EMD (pty), Ltd., (1999) *Simulation Report*

Dick B.G. and Overhauser A.W., (1958), *Phys. Rev.,* **112,** 90

DL_POLY is a package of Molecular Simulation routines written by Smith W. and Forester T.R. Copyright by the council for the Central Laboratory of the Research Councils, Daresbury Laboratory, Daresbury, Warrington, UK, (1999), http://www.dl.ac.uk/TCSC/Software/DLPOLY

Donne S.W., Feddrix F.H, Glockner R., Marion S. and Norby T., (2002), *Solid State Ionics* 8540

Elliot S., (1998), *'The physics and chemistry of solids'*, J. Wiley & Sons, Chichester.

Ewald P.P., (1921), *Annalen der Physik,* **64,** 253

Fermi E.,(1928), Z. Phys., 48, 73

Fernandes J.B., Desai B.D. and Dalal V.N.K.(1985a), *J. Power Sources,* **15,** 209

Fernandes J.B., Desai B.D. and Dalal V.N. Kamat, (1985b), *J. Power Sources,* **28,** 224

Fernandes J.B., Desai B.D. and Dalal V.N. Kamat, (1985c), *J. Appl. Electrochem.,* **15,** 351

Fisher C.A.J. and Matsubara H., (1998), *Solid State Ionics*, **113-115**, 311-318.

Fleischer M., Richmond W.E. and Evans H.T., (1962) *American Mineralogist,* **47,** 47-58

Forester T.R. and Smith W., (1994), *DL_POLY manual*

Gale J.D., (1997), *J. Chem. Soc., Faraday Trans.,* **93,** 629

Gay D.H. and Rohl A.L., *J. Chem. Soc., Faraday Trans.,* (1995), **91,** 925

Giovanoli R., (1994), *Thermochim. Acta,* **234,** 303

Giovanoli R.,(1980), *Proceedings of the Manganese Dioxide Symposium, Tokyo,* (edited by Schumm J.B., Joseph H.M. and Kozawa A.), 113-133, I.C. Sample Office, Cleveland

Gleiter H., (2000), *Acta Mater.,* **48,** 1

Godart C., Latroche M., Fretigny C. and Levy-Clement C., (1992), *Phys. Stat. Sol.,* A132, 253

Gunnarson O. and Lundqvist B.I., (1976), *Phys. Rev. B,* **13,** 4174

Gurman S.J., Binstead N. and Ross I., (1984), *J. Phys. C,* **17,** 143

Hafner J., (2000), *Acta Materialia*, **48**, 71-92.

Harding J.H., Harris D.J. and Parker S.C., (1999), *Surf. Sci.*, **422**, L183-L187

Harris J. and Jones R.O., (1974), *J. Phys.,* **F4,** 1170

Hedin L. and Lundqvist S., (1969), *Solid State Phys.,* **23,** 1

Heifets E. and Kotonim E.A., (2000), *Thin Solid Films*, **358**, 1-5.

Henlein A., (1984), *Chem. Rev.,* **89,** 1861-1873

Herbert W.S., (1952), *J. Electrochem Soc.,* **19,** 190C

Herbert W.S., (1953), *US Patents:* 2,650,945

Herbert W.S., (1956), *US Patents:* 2,2,775,534 and 2,768,229

Heuer A.H., He A., Hughes P. and Feddrix F., (2000) IBA Manganese Oxide Symposium, Argonne, III, May 9-12 2000.

Hill J.R., Freeman C.M. and Rossouw M.H., (2004), *J. Solid State Chem*, **177**, 165-175

Hohenberg P. and Kohn W., (1964), *Phys. Rev.,* **136,** 864B

Jacobs P.W.M. and Rycerz Z.A., (1997), '*Molecular Dynamics Methods*' in '*Computer Modelling in Inorganic Crystallography*', ed. Catlow, C. R. A., Academic Press, London, 83-115.

Islam M.S., Cherry M. and Catlow C.R.A., (1996), *J. Solid State Chem.,* **124,** 230-237

Jantscher W., Binder L., Fiedler D.A., Andreause R. and Kordesch K., (1999), *J. Power Sources,* **79,** 9

Karakasidis T.E. and Evangelakis G.A., (1999), *Surf. Sci.*, **436**, 193-201.

Khan M. S., Islam M.S. and Bates D.R., (1998), *J. Mat. Chem.*, **8**(10), 2299-2307.

Khan M.I., (2000), *J. Solid State Chem.,* **152,** 105

Klingsberg C. and Roy R., (1959), *Amer. Mineral.,* **44,** 819

Kohn W. and Sham L.J., (1965), *Phys. Rev.,* **40,** 1133A

Konddrasev Lu d. and Zaslavskij A.I., (1951) *Izr. Akad. Nauk SSSR Ser., Fiz,* **15**, 179-186

Kordesch K.V. and Dekker M., (1974) *Batteries,* **1,** chapter 2

Kresse G. and Hafner J., (1994), *J. Phys.: Condens. Matter,* **6,** 8245

Kruis F.E., Fissan H. and Peled A., (1998), *J. Aerosol. Sci.,* **29,** 511

Langreth D.C. and Perdew J.P., (1977), *Phys. Rev.,* **B15,** 2884

Leach A. R., (1996), '*Molecular Modelling: Principles and Applications*', Addison Wesley Longman Ltd., Harlow.

Leach A.R., (1999), '*Molecular Modelling Principles and Applications', Glaxo Wellcome Research and Development and the University of Southampton*

Li J.B., Koumoto K. and Yanagida H., (1988a), *J. Mat. Sci.,* **23,** 2592-2600

Li J.B., Koumoto K. and Yanagida H., (1988b), *J. Ceram. Soc. Jpn.,* **96,** 74

Li J.B., Koumoto K. and Yanagida H., (1988c), *J. Mat. Sci. Lett.,* 331

Li, Q., Luo G., Li J. and Xia X., (2003), *J. Mater. Process. Technol.,* **137,** 25-29

MacLean L.A.H., and Tye F.L., (1996), *J. Solid State Chem.,* **123,** 0163, 150

Maicaneanu S.A., Sayle D.C. and Watson G.W., (2001a), *Chem. Comm.,* **289**

Maicaneanu S.A., Sayle D.C. and Watson G.W., (2001b), *J. Phys. Chem. B*, **105,** 12481-12489

Manceau A. and Combes J.M., (1988), *Phys. Chem. Minerals,* **15,** 28

Matsui M and Akoagi M., (1991), *Molecular Simulation,* **6,** 239

Meyer M. and Pontokis Kluwer Dordeche V., (1992) '*Computer Simulation in Materials Sciences: Interatomic Potentials Simulation Techniques and Applications' ed.*

Miura H, Kudou H. Choi J.H. and Hariya Y., (1990), *JFHGA,* **22,** 611-617

Netsisaulu T.T., Ngoepe P.E. and Chadwick A.V., (1999) *Mol. Sim.,* **22,** 1

Olivier P.M., Parker S.C. and Mackrodt W.C., (1993), *Modelling Simul. Mater. Sci. Eng.,* **1,** 755-760

Olivier P.M., Watson G.W., Kelsey E.T. and Parker S.C., (1997), *J. Mater. Chem.,* **7,** 3, 563-568

Pannetier J., (1991), *Proceedings of 5th IBA Meeting, Sydney, Progress in Batteries and Battery Materials*, **11,** 51, ITE-JEC Press Inc., 1992

Pannetier J., (1992), *Progress in Battery and Battery Materials, IBA Sydney Meeting,* **11,** 52

Pannetier J., (1993), *Proceedings of 8th IBA Meeting, Brussels, Progress in Batteries and Battery Materials,* **13,** 132, ITE-JEC Press Inc., 1994

Pardoe H., Chua-ausorn W., St. Pierre T.G. and Dobson J., (2001), *J. Magn. Magn. Mater.* **225,** 41

Parker S.C., Oliver P.M., de Leeuw N.H., Titiloye J.O. and Watson G.W., (1997), *Phase Transitions*, **61**, 83-107.

Parry D.E., (1975), *Surf. Sci.,* **49,** 433

Parry D.E., (1976), *Surf. Sci.,* **54,** 195

Petit F., Durr J., Lenglet M. and Hannoyer B., (1993), *Mat. Res. Bul.,* **28,** 959-966

Petroski J.M., Green T.C. and El-Sayed M.A., (2001), *J. Phys. Chem. A,* **105,** 5547

Perdew J.P. and Yue W., (1986), *Phys. Rev.,* **B 33,** 8800

Phillips J.C., (1958), *Phys. Rev.,* **112,** 685

Philos. Mag. (1996), **B73**, Special issue "Interatomic Potentials".

Pistoia G. and Antonini A., (1997), *J. Electrochem. Soc.,* **144,** 1553

Potter R.M. and Rossman G.R., (1979), *Amer. Mineralogist,* **64,** 1199

Punkkinen M.P.J., Kokko K. and Vayrynen I.J., (2001) *Solid State Comm.,* **117,** 583-588

Ripert M., Pannetier J., Charbe Y. and Poinsignon C., (1991a), *Mat. Res. Soc. Symp. Proceed. Series,* **210,** 359

Ripert M., Poinsignon C., Charbe Y. and Pannetier J., (1991b), *Phase Transitions,* **214,** 205

Ruetschi P. (1984), *J. Electrochem. Soc.,* **131,** 2737-2744

Sasaki K. and Kozawa A., (1957), *J. Electrochem. Soc. Japan,* **25,** 115 &253

Sayle D.C., Catlow C.R.A. and Perrin M.A., (1997), *Phys. Rev. B*, **56**, 15952-15961

Sayle D.C., (1998), *J. Mat. Chem.*, **8**, 2025-2032

Sayle D.C., (1999), *J. Mat. Chem.*, **9**, 2961-2964

Sayle D.C., Catlow C.R.A, Harding J.H., Healy M.J.F., Maicaneanu S.A., Parker S.C., Slater B. and Watson G.W., (2000a), *J. Mater. Chem.,* **10,** 1315-1324

Sayle D.C. and Watson G.W., (2000b), *Phys. Chem. Chem. Phys.*, **2**, 5491-5499.

Sayle D.C. and Watson G.W., *Surf. Sci.,* (2001), **473**, 97-107

Sayle D.C., Doig J.A., Maicaneanu S.A. and Watson G.W., (2002a), *Phys. Rev. B,* **65,** 245414

Sayle D.C., Catlow C.R.A., Dulamita N., Healy M.J.F., Maicaneanu S.A. Slater B. and Watson G.W., (2002b), *Mol. Sim.*, **28,** 683-725.

Sayle D.C. and Parker S.C., (2003), *J. Am. Chem. Soc.,* **125,** 8581-8588

Schnitker J. and Srolovitz D.J., (1998), *Model. Simul. Mater. Sci. Eng.*, **6**, 153-164.

Simon D.E., Anderson T.N. and Elliot C.D., (2000) IBA Manganese Oxide Symposium, Argonne, III, May 9-12 2000.

Smith W. and Forester T. R., (1999), *The DL_POLY Molecular Simulation Package*, URL: http://www.dl.ac.uk/TCSC/Software/DL_POLY.

Stephan A., Ravichandran K., Natarajan T. and Ananth M.V., (1997), *J. Solid State Electrochem.*

Suzuki K., Kubo M., Oumi Y., Miura R., Takaba H., Fahmi A., Chatterjee A., Teraishi K. and Miyamoto A., (1998a), *Appl. Phys. Lett.*, **73**, 1502-1504.

Suzuki K., Endou A., Miura R., Oumi Y., Takaba H., Kubo M., Chatterjee A., Fahmi A. and Miyamoto A., (1998b), *Appl. Surf. Sci.*, **130-132**, 545-548.

Tarascon J.M, (1993), *Mater. Technol.,* **8**, 39

Tasker P.W., (1978), *Technical report,* AERE (R9130)

Tasker P.W., (1979), *J. Phys. C, Solid State Phys.,* **12,** 4977

Tasker P.W. and Stoneham A.M., (1987), *J. Chemi. Phys.,* **84**, 149

Thomas L.H., (1926), *Proc. Camb. Philos. Soc.,* **23,** 542

Turner S. and Buseck P.R., (1979), *Science,* **203,** 456

Tye F.L., (1980), *Electrochemical Power Sources,* (edited by Barak M.), Peter Peregrinus, London, **50**

Vanderbilt D., (1990), *Phys. Rev. B,* **41,** 7892

Verlet L., (1967), *Phys. Rev.,* **159,** 2, 98-103

von Barth U. and Hedin L., (1972), *J. Phys. C5,* 1629

Wadsley A.D., (1950), *J. Amer. Chem. Soc.,* **72,** 1981

Watson G.W., Kelsey E.T., de Leeuw N.H., Harris D.J. and Parker S.C., (1996), *J. Chem. Soc., Faraday Trans.,* **92,** 433

Watson G.W., (2002), *MDPREP,* a computer program for the preparation and analysis of molecular dynamics simulations.

Wells A.F., (1984), '*Structural Inorg. Chem.' 5th edition,* 533

West R.A. and Bruce P.G., (1982), *Acta Cryst. B,* **38,** 1891

Wimmer E., (1998) *Molecular Simulation Inc. documentation*

Yin M.T. and Cohen M.L., (1982), *Phys. Rev. B,* **25,** 7403

Appendix A

A Surface Symmetry and Termination

A.1 {110} Pyrolusite surface showing different orientations of the surface

Miller Index: 1 1 0
Zone Axis 7.071067811865476E-001 7.071067811865476E-001 0.000000000000000E+000
PLDRAW: Code (1) with dipole = 7.435696502966493E-011

Height	charge	atom arrangement
.2	-1.1	O--
.4	.0	
.6	.0	
.8	.0	
1.0	.0	
1.2	.0	
1.4	2.2	MN--O--O--MN--
1.6	.0	
1.8	.0	
2.0	.0	
2.2	.0	
2.4	.0	
2.6	-1.1	O--

Miller Index: 1 1 0
Zone Axis 7.071067811865476E-001 7.071067811865476E-001 0.000000000000000E+000
PLDRAW: Code (4) with dipole = 7.435652094045508E-011

Height	charge	atom arrangement
.2	1.1	O--MN--
.4	.0	
.6	.0	
.8	.0	
1.0	.0	
1.2	.0	
1.4	-1.1	O--
1.6	.0	
1.8	.0	
2.0	-1.1	O--
2.2	.0	
2.4	.0	
2.6	.0	
2.8	.0	
3.0	.0	
3.2	1.1	MN--O—

A.2 {010} Pyrolusite surface showing different orientations of the surface

Miller Index: 0 1 0
Zone Axis 0.000000000000000E+000 1.000000000000000 0.000000000000000E+000
PLDRAW: Code (2) with dipole = 5.257838608940801E-011

Height	charge	atom arrangement
.2	-1.1	O--
.4	.0	
.6	.0	
.8	.0	
1.0	2.2	MN--
1.2	.0	
1.4	.0	
1.6	.0	
1.8	-1.1	O--
2.0	.0	
2.2	.0	
2.4	-1.1	O--
2.6	.0	
2.8	.0	
3.0	.0	
3.2	2.2	MN--
3.4	.0	
3.6	.0	
3.8	.0	
4.0	-1.1	O--

Miller Index: 0 1 0
Zone Axis 0.000000000000000E+000 1.000000000000000 0.000000000000000E+000
PLDRAW: Code (5) with dipole = 5.257749791098831E-011

Height	charge	atom arrangement
.2	-1.1	O--
.4	.0	
.6	.0	
.8	.0	
1.0	2.2	MN--
1.2	.0	
1.4	.0	
1.6	.0	
1.8	-1.1	O--
2.0	.0	
2.2	.0	
2.4	-1.1	O--
2.6	.0	
2.8	.0	
3.0	.0	
3.2	2.2	MN--
3.4	.0	
3.6	.0	
3.8	.0	
4.0	-1.1	O--

A.3 {101} Ramsdellite surface showing different orientations of the surface

Miller Index: 1 0 1
Zone Axis 4.277206751579510E-001 0.000000000000000E+000 9.039109602402365E-001
PLDRAW: Code (1) with dipole = -1.501021529293212E-013

Height	charge	atom arrangement
.2	-1.1	O--
.4	.0	MN--O--O--
.6	-1.1	O--
.8	.0	
1.0	.0	
1.2	2.2	MN--
1.4	2.2	MN--
1.6	.0	
1.8	.0	
2.0	-2.2	O--O--
2.2	1.1	O--MN--
2.4	-1.1	O--

Miller Index: 1 0 1
Zone Axis 4.277206751579510E-001 0.000000000000000E+000 9.039109602402365E-001
PLDRAW: Code (4) with dipole = -1.518785097687214E-013

Height	charge	atom arrangement
.2	-2.2	O--O--
.4	.0	
.6	.0	
.8	2.2	MN--
1.0	2.2	MN--
1.2	.0	
1.4	.0	
1.6	-1.1	O--
1.8	.0	O--O--MN--
2.0	-1.1	O--
2.2	.0	
2.4	.0	
2.6	.0	
2.8	.0	
3.0	.0	
3.2	.0	
3.4	.0	
3.6	-1.1	O--
3.8	2.2	MN--
4.0	-1.1	O--

Miller Index: 1 0 1
Zone Axis 4.277206751579510E-001 0.000000000000000E+000 9.039109602402365E-001
PLDRAW: Code (7) with dipole = -1.492139745096210E-013

Height	charge	atom arrangement
.2	2.2	MN--
.4	.0	

.6	.0	
.8	-2.2	O--O--
1.0	1.1	O--MN--
1.2	-1.1	O--
1.4	.0	
1.6	.0	
1.8	.0	
2.0	.0	
2.2	.0	
2.4	.0	
2.6	.0	
2.8	-1.1	O--
3.0	1.1	MN--O--
3.2	-2.2	O--O--
3.4	.0	
3.6	.0	
3.8	2.2	MN--

Miller Index: 1 0 1
Zone Axis 4.277206751579510E-001 0.000000000000000E+000 9.039109602402365E-001
PLDRAW: Code (10) with dipole = -1.518785097687214E-013

Height	charge	atom arrangement
.2	1.1	O--MN--
.4	-1.1	O--
.6	.0	
.8	.0	
1.0	.0	
1.2	.0	
1.4	.0	
1.6	.0	
1.8	.0	
2.0	-1.1	O--
2.2	1.1	MN--O--
2.4	-2.2	O--O--
2.6	.0	
2.8	.0	
3.0	2.2	MN--
3.2	2.2	MN--
3.4	.0	
3.6	.0	
3.8	-1.1	O--
4.0	-1.1	O--

Appendix B

B 1 Ewald summation

The Ewald's approach for evaluating the long-ranged potentials uses the convergence properties of periodic arrays of Gaussian functions. It assumes that the lattice periodic in three-dimensions and the charge density ρ at point i is given by

$$\rho_i = \begin{cases} 1 : r_i = r_{lattice} \\ 0 : otherwise \end{cases} \tag{B.1}$$

If r_i does not correspond to a lattice site, the density takes the value of zero, and if does correspond it takes the value of one. Each ion can therefore be replaced by Gaussian charge distribution of equal magnitude but opposite sign, and mathematically is written as

$$\rho_i = \exp\left(\frac{\left(r_i - r_{lattice}\right)}{\eta^2} \right)^2 \tag{B.2}$$

where η is the half width of the Gaussian. A cancelling charge distribution of the same sign as the original charge is added. The original charge density is now given by

$$\rho(r) = \left[\delta(r_i, r_{lattice}) - \exp\left(\frac{\left(r_i - r_{lattice}\right)^2}{\eta^2} \right) \right] + \exp\left(\frac{\left(r_i - r_{lattice}\right)^2}{\eta^2} \right) \tag{B.3}$$

where $\delta(r_i, r_{lattice})$ is the direchelet delta function and is equivalent to equation B.1 above.

The first term is solved in real space using Poisson's equation, B.4, which relates the charge density $\rho(r)$ to the second derivative of the potential, ψ.

$$\nabla^2\psi = \rho(r) \tag{B.4}$$

This gives the potential of the first term as

$$\psi(r) = q_i \sum \frac{q_j \, erfc(\eta r_{i,j})}{r_{i,j}} \tag{B.5}$$

where $erfc(\eta r_{i,j})$ is the error function. This sums all possible interactions of ion *i* and *j* over the entire lattice.

The second term in equation B.3 is a Fourier transformed. In transform space the function converges rapidly to give a series of Gaussians of the form:

$$\rho(\bar{r}) = \sum_k \left(C_k \exp^{(i\bar{K}\bar{R})} \right) \tag{B.6}$$

where $\bar{K}$ is the reciprocal lattice vectors and $\bar{R}$ is $r_i - r_{lattice}$ for all the ions in unit cell. Using Poisson's equation, B.4, the potential of the second term becomes

$$\psi(\bar{r}) = q_i \sum_i \left[\frac{q_i}{\pi V_k} \sum_k \left(\frac{\exp(-\pi^2 k^2 \eta^2) \exp(i\bar{K}\bar{R})}{k^2} \right) \right] \tag{B.7}$$

When *k=0*, the second term summation would be undefined. This problem is overcome by assuming that the cell is always charge neutral, this means the sum of the charges is zero.

When summing a periodic array of Gaussians the self-interaction needs to be removed. This is done by combining the potentials of the first and the second terms of equation B.3 and including an extra term to describe the self interaction. Equation B.8 describes the total Coulombic energy of ion *i*.

$$\psi_i = q_i \left[\frac{q_i}{\pi V_k} \sum_{\substack{k \\ k \neq 0}} \left(\frac{\exp(-\pi^2 k^2 \eta^2) \exp(i\bar{K}\bar{R})}{k^2} \right) + q_i \sum_j \left(\frac{q_j \, erfc(\eta r_{i,j})}{r_{i,j}} \right) - \frac{2q_i^2 \eta}{\sqrt{\pi}} \right] \tag{B.8}$$

where the final term is the self-interaction.

B 2 Parry Summation

The Parry method is a special application of the Ewald method for a two-dimensional crystal. The crystal is assumed to consist of a series of charged planes of infinite size rather than a infinite lattice. When summing the electrostatic interactions the vectors are now divided into in-plane vectors, $p_{i.j}$ and vectors perpendicular to the plane, $u_{i,j}$. It can no longer be assumed that the total charge of a plane of atoms is zero as in the three-dimensional cell and hence *k=0* term has to be evaluated. The part of the summation in reciprocal space then becomes

$$\psi = \frac{\pi}{A}\left\{-2u_{i,j}erf(\eta u_{i,j}) - \frac{2\exp(-\eta^2 u_{i,j}^2)}{\sqrt{\pi}\eta} + \sum_{\substack{k \\ k\neq 0}} \frac{\exp(ikp_{i,j})}{k}\left[\exp(ku_{i,j})erfc\left(\frac{k}{2\eta} - \eta u_{i,j}\right) + erf(-ku_{i,j})erfc\left(\frac{k}{2\eta} - nu_{i,j}\right)\right]\right\} \tag{B.9}$$

where *k* is a two dimensional reciprocal lattice vector, *A* is the surface area, *erf* is the standard error function and *erfc* is the complementary error function.

Appendix C

C1 Types of Surfaces

The surfaces are classified according to the scheme identified by Tasker.

Type I

The surface has each plane consisting of anions and cations in a stoichiometric ratio and is shown in figure C1. Each plane has an overall zero charge and there is no dipole moment perpendicular to the surface.

Type II

The surface has a stacking sequence of charged planes, but the repeat unit consists of several planes which when considered together have no dipole perpendicular to the surface. The surface type is shown in figure C2.

Type III

The surface has alternating stacked charged planes and produces a dipole moment perpendicular to the surface if the surface is cut between any planes of atoms. A stoichiometric surface can be generated by removing half of the ions in the surface layer at the top of the repeat unit and transferring them to the bottom, thereby producing a highly defective surface structure. The surface is shown in figure C3.

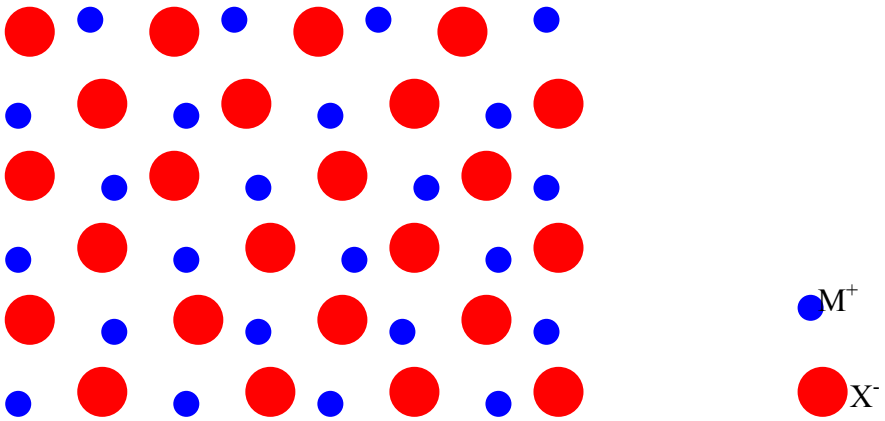

Figure C1: Type I stacking sequence surface.

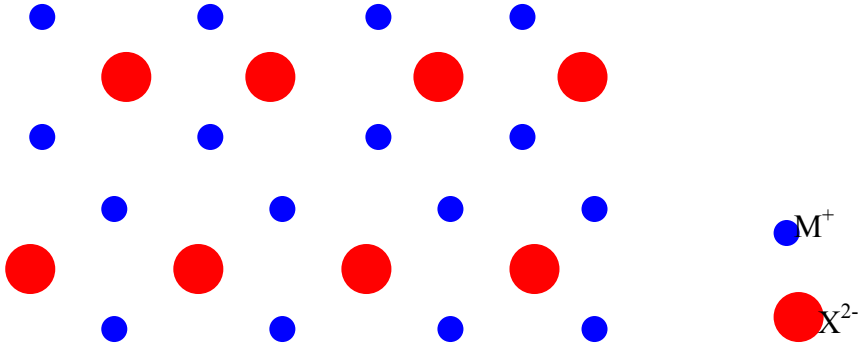

Figure C2: Type II stacking sequence surface.

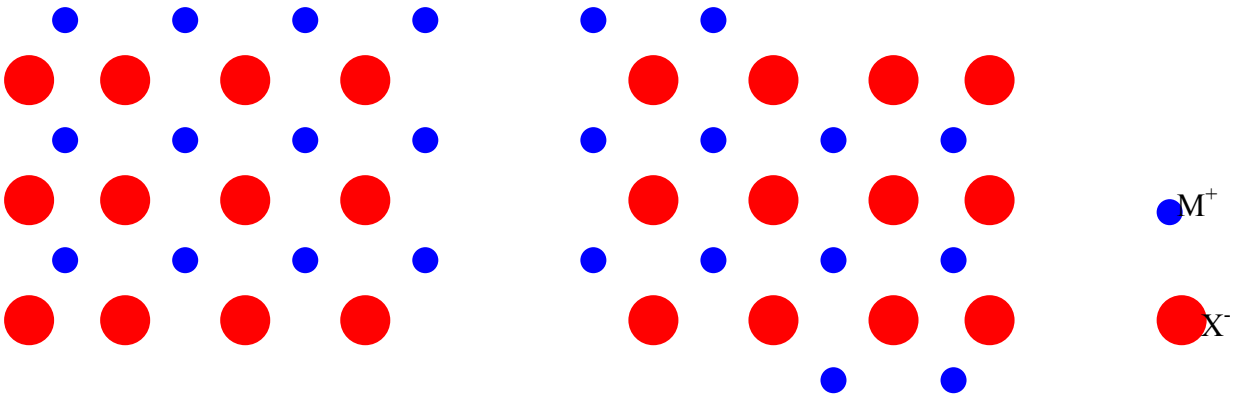

Figure C3: Type III (left) and reconstructed Type III (right) stacking sequence surface.

Appendix D

D 1 Presentations

D 1.1 Local

1. RR Maphanga and PE Ngoepe, "Calculations of Structural and Electronic Properties of Manganese Dioxide", Materials Modelling Meeting, 8-9th March 2001, University of the North, Sovenga.

2. RR Maphanga, SC Parker and PE Ngoepe, "Atomistic Simulation of the Surface Structure of Electrolytic Manganese Dioxide", Materials Modelling Meeting, 8-9th March 2001, University of the North, Sovenga.

3. RR Maphanga, PE Ngoepe and SC Parker, "Atomistic Simulation of the Surface Structure of Electrolytic Manganese Dioxide", South African Institute of Physics 46th Annual Conference, 3-6 July 2001, University of Natal, Durban.

4. RR Maphanga, PE Ngoepe, SC Parker and AV Chadwick "Structural and Electrolytic Manganese Dioxide: Computational Modelling…" South African Institute of Physics 47th Annual Conference, 25-27 September 2002, University of Potchefstroom, Potchefstroom.

5. RR Maphanga and PE Ngoepe, "Computational Studies of Pyrolusite Ramsdellite Interfaces", 7th Materials Modelling Meeting, 6th March 2003, University of the North, Sovenga.

6. RR Maphanga, PE Ngoepe, SC Parker and AV Chadwick, "Computational Studies of Pyrolusite-Ramsdellite Interfaces", South African Institute of Physics, 48th Annual Conference, 25-27th June 2003, University of Stellenbosch, Stellenbosch.

7. RR Maphanga, PE Ngoepe, SC Parker and AV Chadwick, "Structure Studies of Electrolytic Manganese Dioxide: Computational modeling and EXAFS", Interscience, 1-3rd October 2003, University of the North, Sovenga.

8. RR Maphanga, JA Doig, DC Sayle and PE Ngoepe, "Amorphization and Recrystallization Study of MnO_2 Interfaces", 8th Materials Modelling Meeting, 1st April 2004, University of the North, Sovenga.

9. RR Maphanga, JA Doig, DC Sayle and PE Ngoepe, "Amorphization and Recrystallization Study of MnO_2 Thin Films", South African Institute of Physics, 49th Annual Conference, 30 June -02 July 2004, University of the Free State, Bloemfontein.

10. TXT Sayle, CRA Catlow, Maphanga RR, DC Sayle and PE Ngoepe, "Amorphization and Recrystallization Study of MnO_2 Nanoparticles", 8th Materials Modelling Meeting, 16 March 2005, University of Limpopo, Sovenga.

11.TXT Sayle, CRA Catlow, Maphanga RR, DC Sayle and PE Ngoepe, "Simulating MnO_2 Nanoparticles using Amorphization and Recrystallization", South African Institute of Physics, 50th Annual Conference, 5-7th July 2005, University of Pretoria, Pretoria.

D 1.2 International

1. RR Maphanga, S.C. Parker and P.E. Ngoepe, "Surface calculations of Electrolytic Manganese Dioxide (EMD)", 14th International Battery Association –Battery Materials Symposium, 11-14th March 2001, Kwa-Maritane, SA.

2. RR Maphanga, P.E. Ngoepe, S.C. Parker and A.V. Chadwick, "Structural Studies of Manganese Dioxides", Europhysical Conference on Defects in Insulating Materials, 1-5th July 2002, Wrowclaw, Poland.

3. RR Maphanga, PE Ngoepe, SC Parker and AV Chadwick, "Computational Modeling and EXAFS Studies of EMD", 2nd International Conference of the African Materials Research Society, 8–11th December 2003, University of the Witwatersrand, Johannesburg, SA.

4. RR Maphanga, JA Doig, DC Sayle and PE Ngoepe, "Amorphization and Recrystallization Study of MnO_2 Interfaces.15th International Conference on Defects in Insulating Materials, 11-16th July 2004, University of Latvia, Riga.

D 2 Publications

D 2.1 Published

1. RR Maphanga, PE Ngoepe, SC Parker and AV Chadwick, "Computational Modeling and EXAFS Studies of Electrolytic Manganese Dioxide", Proceedings of the 2nd International Conference of the African Materials Research Society, Y. Ballim, AG Every, S Luyckx, DC Levendis (University of the Witwatersrand December) p. 229

2. TXT Sayle, CRA Catlow, RR Maphanga, PE Ngoepe and DC Sayle "Simulating MnO_2 Nanoparticles using Simulated Amorphization and Recrystallization", published in Journal of the American Chemical Society, August 2005.

D 2.2 To be submitted

1. RR Maphanga, PE Ngoepe and SC Parker, "Atomistic Simulation of the Surface Structure of Electrolytic Manganese Dioxide"

2. RR Maphanga, AV Chadwick and PE Ngoepe, "EXAFS Studies of Electrolytic Manganese Dioxide"

3. RR Maphanga, DC Sayle, Doig JA and PE Ngoepe, "Amorphization and Recrystallization studies of MnO_2 Interfaces"